Université de Toulouse

THÈSE

En vue de l'obtention du

DOCTORAT DE L'UNIVERSITÉ DE TOULOUSE

Délivré par :
Institut National Polytechnique de Toulouse (INP Toulouse)

Discipline ou spécialité :

Dynamique des fluides

Présentée et soutenue par :
Sebastian HERMETH

le : vendredi 28 septembre 2012

Titre :

Mechanisms affecting the dynamic response of swirled flames in gas turbines

---

Ecole doctorale :
Mécanique, Energétique, Génie civil et Procédés (MEGeP)

Unité de recherche :
CERFACS

Directeur(s) de Thèse :
Laurent GICQUEL
Gabriel STAFFELBACH

Rapporteurs :

Prof. Sebastian DUCRUIX, Ecole Centrale Paris
Prof. Jim KOK, University of Twente

Membre(s) du jury :

Prof. Matthew JUNIPER, University of Cambrigde, Président
Prof. Wolfgang POLIFKE, University TU Munich, Membre
Prof. Thierry POINSOT, University of Toulouse, Membre
Vyacheslav ANISIMOV, Ansaldo Energia S.p.A., Membre

Mechanisms affecting the dynamic response of swirled flames in gas turbines

Abstract:
Modern pollutant regulations have led to a trend towards lean combustion systems which are prone to thermo-acoustic instabilities. The ability of Large Eddy Simulation (LES) to handle complex industrial heavy-duty gas turbines is evidenced during this thesis work. First, LES is applied to an academic single burner in order to validate the modeling against measurements performed at TU Berlin and against OpenFoam LES simulations done at Siemens. The coupling between acoustics and combustion is modeled with the Flame Transfer Function (FTF) approach, and swirl number fluctuations are identified changing the FTF amplitude response of the flame.
Then, an industrial gas turbine is analyzed for two different burner geometries and operating conditions. The FTF is only slightly influenced for the two operating points but slight modifications of the swirler geometry do modify the characteristics of the FTF, showing that a simple model taking only into account the flight time is not appropriate and additional mechanisms are at play. Those mechanisms are identified being the inlet velocity, the swirl and the inlet mixture fraction fluctuations. The latter is caused by two mechanisms: 1) the pulsating injected fuel flow rate and 2) the fluctuating trajectory of the fuel jets. Although the diagonal swirler is designed to provide good mixing, effects of mixing heterogeneities at the combustion chamber inlet do occur. Mixture perturbations phase with velocity (and hence with swirl) fluctuations and combine with them to lead to different FTF results. Another FTF approach linking heat release rate to inlet velocity and mixture fraction fluctuation (MISO model) shows further to be a good solution for complex systems. A nonlinear analysis shows that the forcing amplitude not only leads to a saturation of the flame, but also to changes of the delay response. Flame saturation is only true for the global FTF and the gain increases locally with increasing forcing amplitude. Both, the linear and the nonlinear flames, are not compact: flame regions located right next to each other exhibited significant differences in delay meaning that at the same instant certain parts of the flame damp the excitation while others feed it.

Keywords: Combustion instabilities, Large Eddy Simulation, Gas turbine engines

Contents

Part I

Introduction and context

Chapter 1

Introduction

"The Stone Age Didn't End Because We Ran Out of Stones." **Ahmed Zaki Yamani.** Former OPEC oil minister (born 30 June 1930).

Contents

1.1 Energy consumption

United Nations population forecast projects the world population of currently 7 billion to reach 9 billion people by 2050 and to exceed 10 billion in the next ninety years [111], following a medium projection variant (Fig. 1.1). Obviously, people need energy and the energy consumption is estimated to grow from 13 terawatts today, to 28 TW in 2050 and 46 TW in 2100 [99] (Fig. 1.2). Even with an extremely fast increase of alternative energies, this global consumption increase will not be possible if energy production by combustion does not increase rapidly too. This leads to an increased demand of resources, and especially of fossil fuels providing 85% of the worlds energy [69]. However, fossil fuels are limited, not evenly distributed over the world, giving concerns to energy security and geopolitical tension and they are associated to global warming and pollution [184]. Despite these drawbacks, it is out of reach today, to replace fossil fuels and it is therefore crucial to efficiently use them on the way to new technologies.

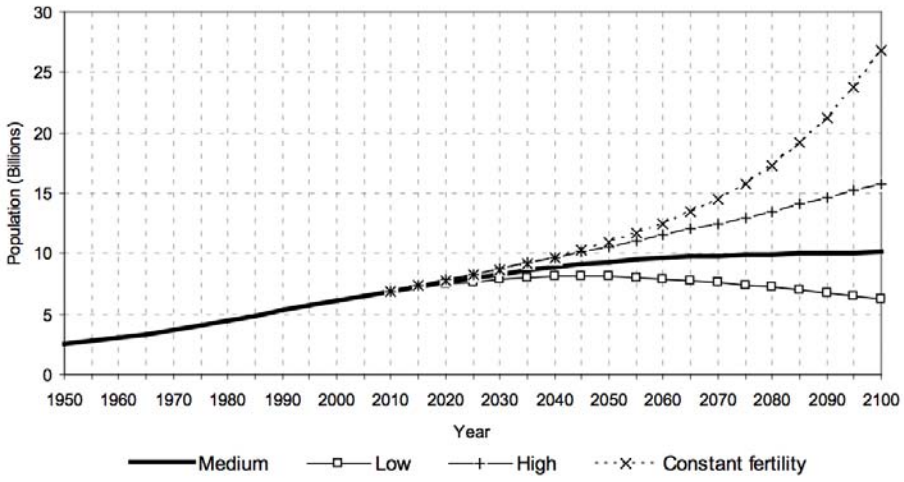

Figure 1.1: Population of the world, 1950-2100, according to different projections and variants [111].

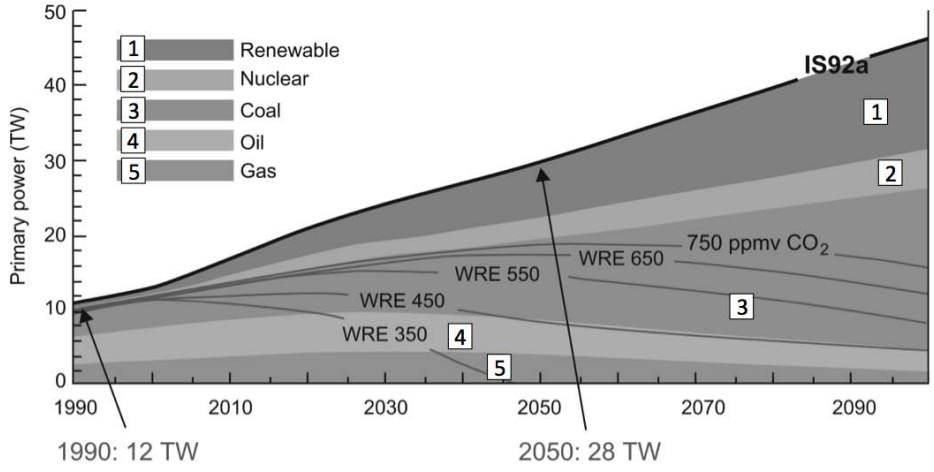

Figure 1.2: World energy consumption and projection [99].

1.2 Combustion and environment

Fossil fuels contain high percentages of carbon. The combustion of those hydrocarbon fuels produce greenhouse gases like carbon dioxyde CO_2 and pollutants like unburnt hydrocarbons HC, nitric oxides NO_x and carbon monoxides CO [141]. Greenhouse gases absorb energy which is radiated from the earth's surface and keep it in the atmosphere leading to a higher temperature on earth. This is essential for life as it exists, since the temperature would be around 15°C lower in the absence of greenhouse gases [61]. However, the intense use of fossil fuels over the last 200 years have led to a significant increase in greenhouse gases with a severe impact on the global climate. Compared to the past 1 to 2 millennia the late 20th century warmth is unprecedented and results from anthropogenic forcing of the climate [72]. An increase in temperature has been observed with beginning of the industrialization and the average temperature from 1960-1990 is $0.5°C$ warmer than in the past millennia as Fig 1.3 shows. Furthermore, the global average surface temperature increase since 1950 is almost doubled per decade ($0.13°C \pm 0.03$) compared to the last 100 years [162]. Future projections show an ongoing increase of temperature of around $1.5°C$ until 2030 and around $3.5°C$ until 2100 [162]. The effects of global warming are numerous:

- Physical impact:
  The physical impact implies effects on the rain fall and extreme weather with drought and cyclone activity, glacier retreat and disappearance, volcano activity, earthquakes and effects on the oceans as acidification, rise of the sea level and its temperature [162].

- Regional effects:
  Global warming changes the regional climate e.g. the forming and melting of ice, the currents in oceans and air flows and the hydrological cycle. With rising sea level coastal regions are heavily affected [162].

- Social system:
  An increasing temperature has furthermore effects on the food supply, water resources and the health of human people as infectious diseases might spread [121].

- Ecosystems:
  Plants and animals are responding (extinction or movement) to temperature changes having strong effects on biological systems [121].

The rapid growth of CO_2 in the atmosphere is mostly due to the combustion of fossil fuels [134].
Combustion also produces pollutants such as HC, NO_x and CO. Air pollution increases the risk to human health and can cause respiratory infections, heart disease and lung cancer according to the WHO (World Health Organization).
The depletion of fossil fuel resources is another critical point. Figure 1.4 shows that

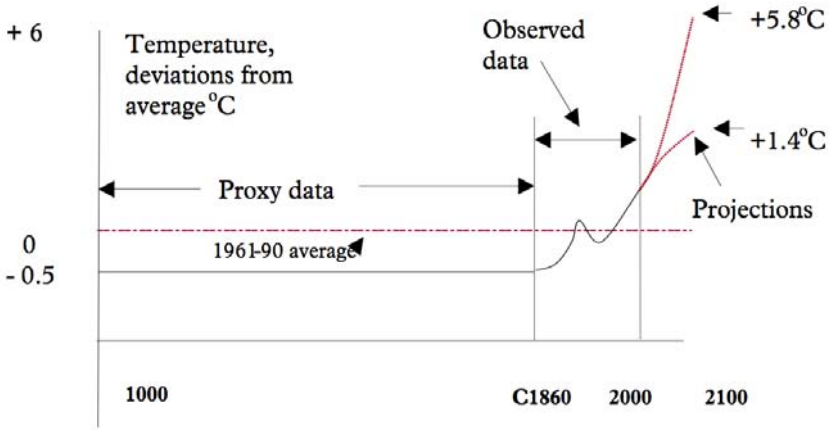

Figure 1.3: Temperature deviations over the pas millenia [72].

resources are limited and especially gas and oil is densely distributed in the Middle East and in Russia. In the near future, this will not only lead to a lack of fossil fuels but also to geopolitical and economical tensions [184].

For all these reasons, it is crucial to efficiently use fossil fuels and to decrease

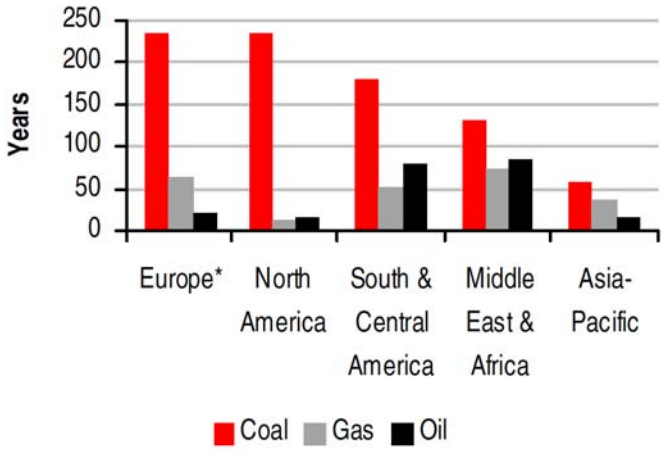

Figure 1.4: Fossil fuel resources estimation for different world regions [184].

pollutants and greenhouse gases. To face these challenges, the international community has introduced regulation policies on emissions, *"which presently include stationary sources (including energy plants and industry), mobile sources and products, national emissions ceilings to cap total emissions and air quality standards as well as policies on transport modes such as shipping"* (UN Department of Economic and Social Affairs: Division for Sustainable Development, CSD-14 National Reporting Guidelines: Page 7 of 43).

1.3 Gas turbines

Gas turbines are used in a broad range of applications including power generation, compressor stations at gas pipelines, oil production, water and sewage pumping stations and engines for aircrafts or ships. They exist for a wide range of power outputs with up to 375 MW for one of the largest turbines today (Siemens SGT5-8000H). Considering the increasing demand of energy and fossil fuels and the associated pollutant emissions, an efficient design of gas turbines is of great importance. Gas turbines are the only propulsion method for most aircraft and helicopters. They are also mandatory on the energy market to complete other sources which are either very slow to start up (nuclear power plants) or unpredictable (wind or sun). A gas turbine can be started in less than an hour and modern systems can operate over the whole power range efficiently to adjust to the power delivered by other sources, as proposed by GE or Siemens.

1.3.1 History

The first mentioned turbine was Hero's aeolipile around the year 150. It was a steam turbine whose potential was not understood since it was only used as a toy. First in 1500, Leonardo da Vinci drew the Chimney Jack (Fig. 1.5), in which hot air rises from a fire and passes through an axial turbine in the exhaust duct and turns a roasting spit through a mechanical connection. The first patent was given to John Barber in 1791 for the first gas turbine designed to power a horseless carriage. His design failed in practice but it already used most elements of modern gas turbines. It took a hundred more years (at the end of the 19th century) for a gas turbine to produce more power than needed to sustain its own motion (Egidius Elling in 1903). In 1932 the Swiss company BBC first started selling gas turbines for commercial purposes. Their design still followed the historical patent of John Barber in 1791.

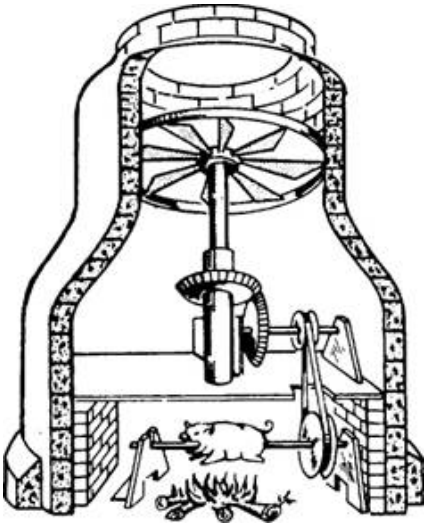

Figure 1.5: Chimney jack from Da Vinci.

1.3.2 Operation theory

A gas turbine is an internal combustion engine operating with rotary motion. It essentially consists of three major components: a compressor, a combustion chamber and a turbine as shown in Fig. 1.6. The working fluid follows the Brayton cycle (Fig. 1.7): Air passes the compressor and is isentropically compressed (1-2). It is then mixed with fuel and burnt in the combustion chamber at constant pressure (2-3) with a following isentropic expansion in the turbine back to the starting pressure (3-4). Energy is transmitted by the turbine as shaft power or propulsion. To increase the efficiency, most turbines recover the exhaust heat which is otherwise lost energy. It can be passed to the compressed air before entering the combustion chamber or used in combined-cycle designs, where a steam turbine uses the heat. Another possibility is to use the heat for hot water production (cogeneration).

Key advantages of gas turbines are their high power to weight ratio, their size

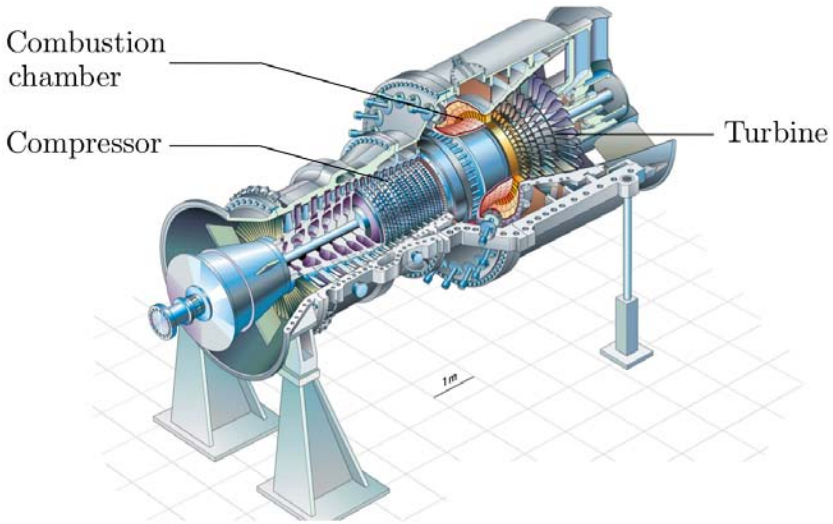

Figure 1.6: Siemens gas turbine. Model V84.3A/V94.3A. (www.siemens.com).

and their reliability due to less moving parts compared to reciprocating engines. They can furthermore operate on a wide variety of fuels and exist for a wide range of applications with different power outputs. However, they are costly, less efficient at part load conditions and show a longer transition between operating points. The combustion process is one of the key elements in a gas turbine. Most modern combustion chamber designs are of annular type. One distinguishes between annular and can-annular systems (Fig. 1.8). An annular combustor has one single continuous chamber around the turbine axis, whereas can-annluar systems have several can-shaped combustion chambers. The conception and design possibilities of combustors underlay certain limitations [97]. In order to achieve a high efficiency, the pressure loss through the burner has to be minimized and a high combustion temperature is needed. The ability of materials (e.g. ceramic, steel) to withstand

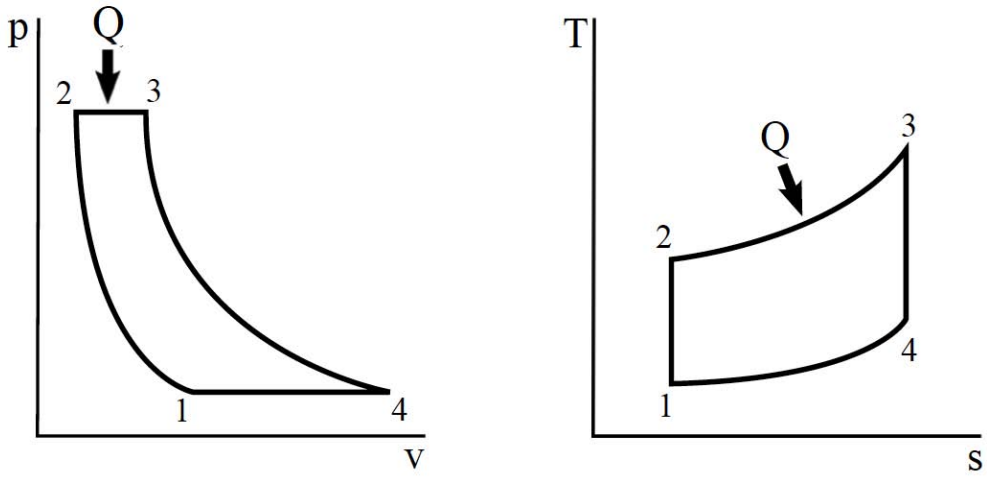

Figure 1.7: Brayton cycle in a gas turbine: P-v and T-s diagram.

the heat are nevertheless limited and cooling has to be applied to ensure a high life time. Additionally, the temperature profile of the combustor outlet influences strongly the life-time of turbine blades and has to be optimized. High operation performances under a variety of fuels has to be guaranteed and extinction limits as well as altitude reignition are a crucial factor for the safety of an aircraft. Especially in aviation the weight and size of the turbine and hence the combustion chamber is also important for the efficiency. In the last decades, the reduction of pollutant emissions as NO_x, CO_2 and CO have become an major issue for the design of gas turbines since regulation policies are increasingly demanding.

A great challenge for engineers is to improve the gas turbine efficiency while reducing the emissions since both are conflicting goals. A higher burning temperature

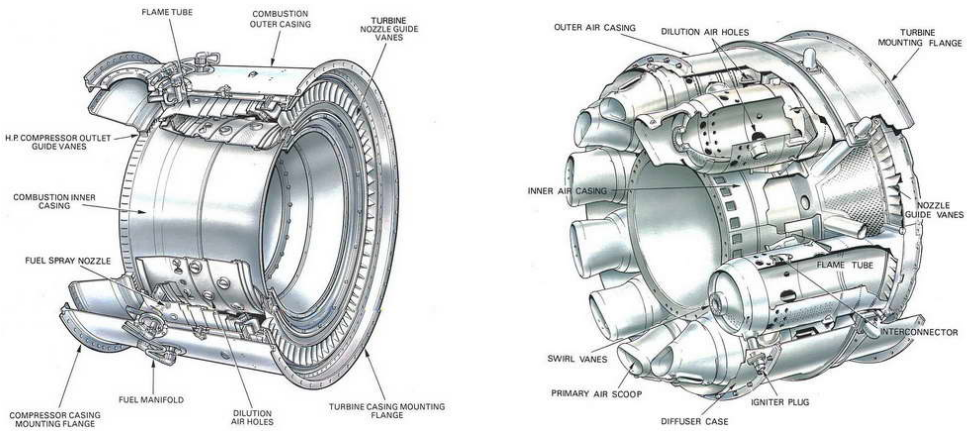

(a) Annular type (b) Can-annular type

Figure 1.8: Combustion chamber designs. (Source: The jet engine , Rolls-Royce plc.)

increases the efficiency but leads to problems for the structure as well as to a higher formation of NO_x. On the other hand NO_x can be reduced by reducing the available oxygen but this leads to an increase in carbon monoxide CO and unburnt hydrocarbon emission due to incomplete combustion. To overcome this problem, gas turbine manufacturers introduced the so-called lean (technically) premixed combustion systems. Here, air and fuel are premixed before they enter the combustion chamber so that the air acts as a diluter in order to reduce the combustion temperature and therefore the NO_x formation. Due to a higher combustion efficiency, a reduction of formed CO is also achieved. Nevertheless, these low-emission gas turbines are known to be particularly susceptible to thermo-acoustic instabilities [97, 126], which are characterized by large pressure amplitudes and heat release oscillations and controlled by non-linear effects [2, 3, 101]. These instabilities can lead to severe problems like noise emission, heat flux enhancement on duct linings, global extinction of the flame, structural vibrations or fatigue of burner and liner parts and even the failure of the turbine [174]. The prediction of this phenomenon at an early design stage has become an important task, but it remains still a great challenge today in terms of scientific modeling. This is the general framework of this PhD.

1.4 Objectives and organization of the present work

1.4.1 Objectives

The present work is placed in the framework of thermo-acoustic instabilities focussing on different mechanisms affecting the stability of gas turbine chambers. Large Eddy Simulation (LES) has been widely used for the numerical simulation of turbulent flows and is recognized as a powerful tool to study thermo-acoustic instabilities [126]. Complex industrial configurations can be successfully described by LES [136, 153] and thermo-acoustic instabilities can be captured for academic configurations [116, 176] and in complex industrial aeronautical combustion chambers [188, 189]. Nevertheless less information is available for large scale industrial gas turbines, which are typically ten times bigger than aeronautical engines and where the Reynolds numbers easily reach 1.000.000.

The objectives of this thesis can be summarized as follows:

- Is LES capable of handling such complex large industrial size geometries?
- Is LES modeling advanced enough to be used in industry as a design tool for gas turbine combustion chambers?
- Which mechanisms are causing thermo-acoustic instabilities? In systems with multiple inlets for air and fuel, how can models derived for simple burners be extended?
- Thermo-acoustic instabilities are controlled by non-linear effects due to heat release fluctuation [2, 3, 101]. What is the effect of nonlinearity on the flame

and on stability compared to a linear flame behaviour?

The approach to apprehend thermo-acoustic instabilities in complex geometries is to first analyze the state-of-the-art in literature and to introduce the LES modeling used. Then, LES is applied to a fully premixed swirled burner in order to validate the LES against experiments and to analyze the mechanisms influencing the flame on a simpler geometry. Finally, an industrial gas turbine operating at technically premixed conditions under high pressure is analyzed in detail. Different effects on the flame dynamics are highlighted and insight into a complex field is given.

1.4.2 Organization of this work

Part I The current part places this dissertation in a global context. Growing energy demand and environmental issues lead to challenges in the gas turbine design process. Lean premixed combustion systems are state of the art today and are particularly prone to combustion instabilities. Preventing these instabilities at an early design stage is an important task.

Part II The next part introduces the underlying physics leading to thermo-acoustic instabilities and shows possibilites used today to control them. A literature review deals with the different methods used to study those instabilities and gives the particular mechanisms influencing the flame behaviour. Finally on overview of the physical models for LES and the numerical tools used is given. The Navier-Stokes equations and their derivation for compressible reacting LES are discussed. The LES solver AVBP is presented.

Part III Part III aims to validate the LES modeling used against experiments performed at TU Berlin [142–144] and a second LES code OpenFoam [1] where the calculations were performed at Siemens [89] on an academic swirled burner. Mechanisms affecting the flame response to perturbations are investigated in this simplified single-sector configuration where detailed experimental data is available.

Part IV In Part IV the LES code is applied to an industrial gas turbine operating at high pressure. Two different operating conditions and burner configurations are considered. First, the four different flow fields are compared and analyzed. Then, the flame response to perturbations is investigated for the four cases in detail. Different mechanisms acting on the flame in the linear regime are identified. Finally, the nonlinear flame behaviour is analyzed and different mechanisms affecting the instability oscillation are given.

Part V The conclusion regarding the objectives of this thesis is provided and future work is discussed.

Part II

Theoretical background

Chapter 2

Thermo-acoustic instabilities

Contents

The first observation of combustion oscillation dates back to 1777, when Higgins discovered the so-called "singing flame" [179]. In 1858 John LeConte [96] described the interaction between acoustics and combustion when he observed synchronous flame movement to music:

> *"I happened to be one of a party of eight persons assembled after tea for the purpose of enjoying a private musical entertainment. Three instruments were employed in the performance of several of the grand trios of Beethoven, namely, the piano, violin and violoncello. Two 'fish-tail' gas burners projected from the brick wall near the piano. (...) Soon after the music commenced, I observed that the flame of the last-mentioned burner exhibited pulsations in height which were exactly synchronous with the audible beats. This phenomenon especially striking when the strong notes of the violoncello came in. It was exceedingly interesting to observe how perfectly even the trills of this instrument were reflected on the sheet of flame. A deaf man might have seen the harmony."*

Twenty years later in 1878, Lord Rayleigh discovered that not only the acoustics have an influence on the flame, but that a moving flame also excites acoustics [135]. Since then, the field of thermo-acoustic instabilities exists, but its interest for the research community was limited over a long time. It only became the center of attraction for a wider community with the development of high-intensity combustion systems, where suddenly unforeseen and undesired instabilities occurred. These instabilities are characterized by large pressure amplitudes and heat release oscillations which can lead to severe problems to the machine like noise emission, heat flux enhancement on duct linings, global extinction of the flame, structural vibrations or fatigue of burner and liner parts and even the failure of the turbine [174].

This chapter first introduces the physical mechanisms leading to thermo-acoustic instabilities in section 2.1. Then, in section 2.2 different possibilities to control those instabilities are discussed. Present methods to predict thermo-acoustic instabilites are described (section 2.3). Finally, methods based on LES extended to instabilities are discussed in more details (section 2.4) because they are the center of this PhD work.

2.1 Causes of thermo-acoustic instabilities

Thermo-acoustic instabilities are the result of a resonant feedback between combustion, acoustic waves and flow [34] (Fig. 2.1). Gases travelling through the flame

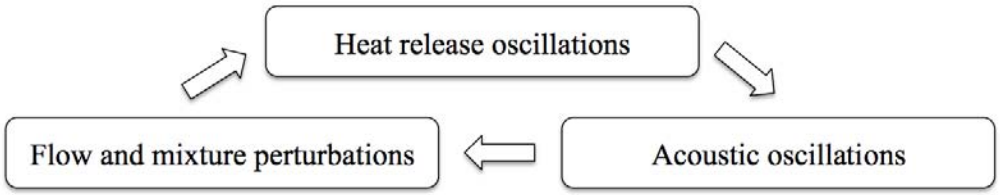

Figure 2.1: Feedback mechanism responsible for combustion instabilities [103].

front are heated up proportionally to the heat release rate. When the heat release fluctuates, the gases dilatation rate varies in time and the gases being heated up push the surrounding gases outwards as they expand. This leads to an increase in local pressure which then propagates as acoustic waves. The flame can be compared to an acoustic monopole [67, 170, 171] as it behaves locally as an inflating and deflating balloon radiating sound in all directions. These pressure waves propagate through the domain and are reflected (dependent on the impedance) at the turbine inlet and the combustor outlet, inducing perturbations of the flow and mixture. This leads to a perturbation of heat release which basically appears in two different ways [103]:

- **Variation of the flame surface area:**
  Acoustic waves induce velocity oscillations to the flow. The accelerated and decelerated mixture changes the flame shape accordingly, leading to variations in the total flame surface area and hence to oscillations in the total heat release.

- **Fluctuation of the heat of reaction:**
  Acoustic waves further induce oscillations to the air and fuel inlet mass flow rates leading locally to mixture heterogeneities. These mixture variations propagate to the flame front and influence the power released by unit of total mass.

The well-known Rayleigh criterion [113, 135] finally gives a condition for this closed feedback loop (Fig. 2.1) under which instabilities arise:

$$\int_V \int_T p'q' dV dt > 0 \tag{2.1}$$

where p' and q' are the pressure and heat release rate fluctuations respectively, V is the volume of the domain and T the oscillation period. The Rayleigh criterion states that pressure and heat release oscillations must be in phase to have a growing amplitude of instability. In other words, local pressure and heat release rate must increase or decrease at the same time. When gases expand against a growing pressure field, energy is transmitted to the acoustic field leading again to an increase in pressure. This happens when the phase between heat release rate and pressure is between $-\pi/2$ and $\pi/2$. Note that the Rayleigh criterion has to be integrated over the domain, which means that locally pressure and heat release oscillations can be in phase, but at the same time out of phase at a different position. The exchanged energy would thus cancel out and instabilities might be suppressed. When flames are "compact", i.e. when the acoustic wavelength is long compared to the flame thickness this problem disappears: since pressure fluctuations are homogeneous over the flame front, the Rayleigh criterion becomes

$$\int_T \iiint_V p'q' dV dt > 0 \text{ or } \int_T p' \iiint_V q' dV dt > 0 \text{ or } \int_T p'Q' dt > 0 \tag{2.2}$$

where Q' is the total heat release in the burner. Unfortunately, we will show that flames are not compact in the burners studied in this PhD, making their analysis more complex than suggested by Eq. 2.2.

Figure 2.2 shows the energy gain and the losses as a function of the perturbation in terms of the square of the acoustic velocity. The acoustic losses are assumed to be linearly increasing with the perturbation level [35] whereas the energy gain of the flame is linear for low perturbation amplitudes (region I) and saturates for larger perturbation levels (region II). Acoustics are linear in most cases where $p'/\bar{p}$ remains smaller than 1% explaining why the losses depend linearly on $\mid u' \mid^2$. On the other hand, combustion (Q') is expected to behave nonlinearly (and this is often observed [32, 123]): Q can not be negative and can not exceed values corresponding to the heat release associated to the total fuel mass introduced in the burner in one period.

Figure 2.3 shows a typical time evolution of growing pressure oscillations. When thermo-acoustic instabilities arise, first linear oscillations appear and grow exponentially since the energy gain is larger than the acoustic losses. An overshoot zone is often observed before the pressure amplitude reaches a plateau when the losses balance the energy gain. This oscillation state is called "limit cycle". However, instability does not necessarily occur when the Rayleigh criterion alone is fulfilled because losses also play a role [24, 113]. The boundaries of the combustion

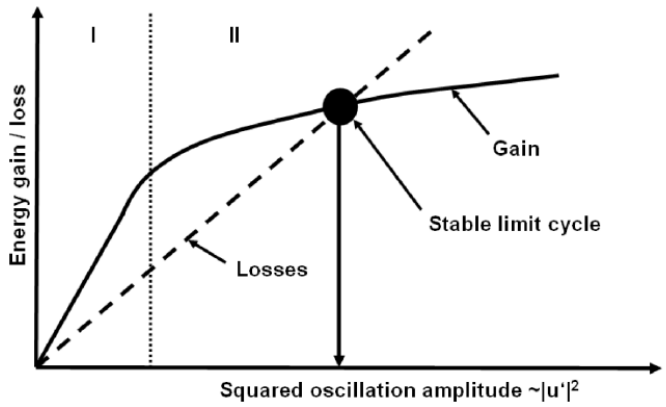

Figure 2.2: Interaction between between energy losses and gain with unsteady heat addition [101].

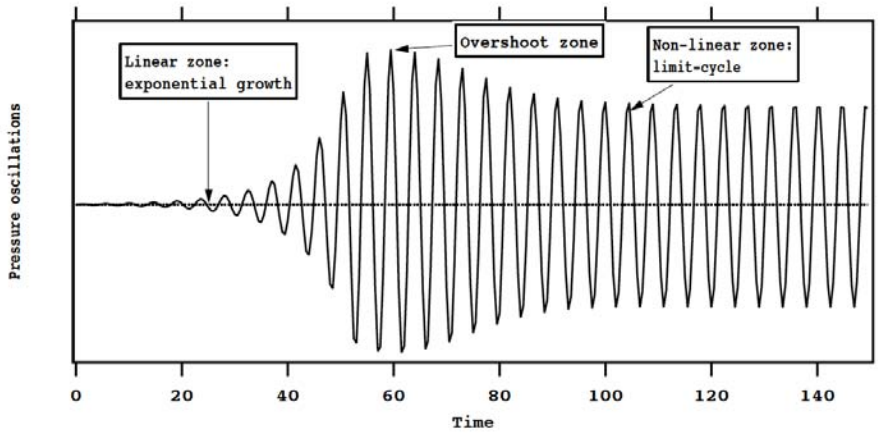

Figure 2.3: Growth of a combustion instability to limit cycle [126].

chamber (e.g. walls, compressor outlet, turbine inlet) and the turbulent flow damp the acoustic energy so that a proper instability criteria is that the Rayleigh term $\int_T \int \int \int_V p'q' dV dt$ must exceed all losses terms. Finally, even the Rayleigh term itself has been discussed by many authors. Chu [24] or Nicoud et al. [113] investigated an extension to the Rayleigh criterion integrating the fluctuation of pressure, velocity and entropy. This leads to a criterion where temperature and heat release (and not pressure and heat release) must be in phase for the instability to grow. They concluded that the extended version should be used for studies on combustion instabilities.

2.2 Control of thermo-acoustic instabilities

Thermo-acoustic instabilities should preferably be avoided at an early design stage. However, the prediction of flame-acoustic interactions is a great challenge today because all mechanisms leading to an unstable behaviour of the machine are not fully understood. It is therefore important, to have a posteriori methods to control and suppress thermo-acoustic instabilities. They can be classified in two categories, both having the goal to change the phase between pressure and heat release oscillations:

- **Passive Control [103]:**
  - Operating conditions: Changes in operating conditions can have an effect on the stabilization of the flame and therefore its time response as well as on the eigenmodes of the chamber due to a change in sound speed.
  - Design changes: Acoustic eigenmodes can also be changed by modifying the combustion chamber geometry. Furthermore, e.g. swirler positions or burner outlets have an impact on the time response.
  - Acoustic dampers [126]: Resonators can be used to damp eigenfrequencies. Nevertheless, frequencies encountered in most gas turbines are low and dampers with large volumes are needed. Since space is generally limited, the installation of these dampers is difficult in practice.
- **Active Control [103, 107]:**
  Active control techniques monitor the combustion system in order to detect the characteristics of the instabilities in terms of frequency and amplitude. The phase difference between acoustics and heat release can now be adjusted by attenuating e.g. the fuel mass rate. Thermo-acoustic instabilities are finally suppressed by a closed feedback loop. These systems need to be redundant since its failure risks an instability to grow and the machine to fail.

Despite multiple academic proofs of the efficiency of active control methods [9, 11, 92], active control has been used only a few times in real gas turbines [160]. The main reason for this is that the certification and the cost of these methods remain difficult

issues and that they do not control all unstable modes. Using passive methods, which means building systems which are naturally stable is the preferred path today for industry. This can be achieved only when mechanisms are understood: this explains why prediction methods must be developed first.

2.3 Study of thermo-acoustic instabilities

Preventing thermo-acoustic instabilities is an important task and their prediction at an early design stage remains a challenge, since their underlying mechanisms are not fully understood yet. Generally, two methods exist to study instabilities in combustors [126](Fig. 2.4):

- **Forced response:**
  The feedback loop leading to thermo-acoustic instability is removed and the flame is excited in a forced controlled mode to measure its response. Thermo-acoustic instability models give then information about stability and limit cycle oscillation amplitudes.
- **Self-excited modes:**
  The feedback loop is closed and the flow resonates on its own. The configuration is dominated by its own instability mode.

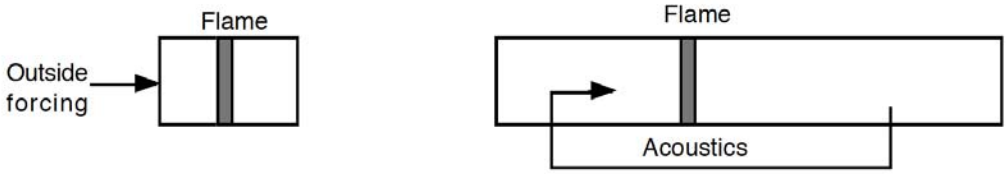

Figure 2.4: Forced (left) and self-excited (right) strategies to study thermo-acoustic instabilities [126].

2.3.1 Forced response method

In the **forced response** method a perturbation is introduced to the flame and its response is analyzed. To do so, a common approach for acoustically compact flames can be found in the literature which was first introduced by Crocco [29, 30]. In this approach, the Flame Transfer Function (FTF) is the key parameter and is defined as the ratio of the relative heat release fluctuation $(\hat{q}/\bar{q})$ to the relative inlet velocity perturbation $(\hat{u}/\bar{u})$ issued by the acoustic field. In the frequency domain it writes

$$F(\omega) = \frac{\hat{q}/\bar{q}}{\hat{u}/\bar{u}}. \tag{2.3}$$

with ω being the angular frequency. The FTF is generally expressed in terms of gain $n = |F(\omega)|$ and time delay $\tau = Arg(F(\omega)/(2\pi f))$. The shape of the FTF depends

on the flame shape [79] as well as on the operating conditions [85]. Flame Transfer Functions have been extensively studied in laminar and turbulent flames where only the axial velocity perturbation is at play. Investigations of laminar conical flames performed by Durox et al. [38] and Karimi et al. [76], inverted conical by Durox et al. [38] and multi-slit conical flames studied by Kornilov et al. [85] revealed that the FTF gain shows a low pass filter behaviour. Schuller et al. [150] observed from laminar flames and Armittage et al. [2] from turbulent V-flames an overshoot in gain and associated this to vortex roll-up at the flame base. In all cases, the gain is unity in the limit of zero frequency as derived by Polifke and Lawn [127] from the global conservation laws. The phase of the FTF evolves in these cases in an almost linear way with the frequency, indicating that the axial velocity perturbations propagate convectively from the burner outlet to the flame. Concerning different operating conditions, Kornilov et al. [85] showed that with increasing inlet velocity the gain decreases at higher frequency and that phase saturation occurs at higher frequency. Kim et al. [79] and Palies et al. [116] used the Strouhal number as dimensionless parameter instead of the frequency.

Industrial configurations use swirlers in order to create a vortex breakdown [106] which stabilizes the flame. The gain of swirled flames plotted versus frequency usually shows a second peak. Straub and Richards [173] first noticed a strong impact of the swirler position on the combustion oscillations. Hirsch et al. [59] hence investigated the effect of swirler designs and found that an additional time lag is responsible for changes in the FTF. Komarek et al. [84] investigated the influence of several swirler positions on the FTF and concluded that disturbances propagate at a convective and an acoustic speed downstream the swirler position. Finally, Palies et al. [117, 119] have shown that the acoustic perturbations reaching the swirler generate transverse velocity fluctuations which are convected by the flow. As a results, swirl number perturbations occur and effect the flame angle. When both components are in phase, the swirl number perturbations are small and the flame angle is less affected leading to an overshoot in gain since axial and azimuthal component are acting simultaneously on the flame. Vice versa, high swirl fluctuations occur when both components are out of phase leading to a low flame response.

The academic configurations mentioned above run under perfectly premixed conditions: fuel and air are mixed far upstream of the combustion chamber. However, industrial combustion systems operate for security reasons under technically premixed conditions meaning that fuel and air are mixed just prior to combustion. Thus, in technically premixed configurations another mechanisms, the perturbation of mixture, occurs and changes the shape of the FTF gain [104]. Schuermans et al. [148] compared the measured transfer matrix of a turbulent flame for a technically premixed and a fully premixed system and found the maximal amplitude to increase for the technically premixed case where equivalence ratio perturbations are present. Kim et al. [82] also found a phase difference between equivalence ratio and velocity at the combustor inlet. Following Kim et al. [82] this has an impact on the

amplitude response of the flame: when the two perturbations are out of phase richer mixtures enter the combustion chamber with low velocity, and mixtures with lower equivalence ratio reach the flame front with high velocity. The flame sees nearly the same amount of fuel during a cycle of oscillation. Therefore, the heat release rate does not vary significantly and a low amplitude response results. Furthermore, they showed that this phase difference is a function of frequency, fuel injection location, fuel injector impedance and the mean velocity in the nozzle.
In the case of technically premixed burners, Huber [64] proposed a different FTF approach including the fluctuations of equivalence ratio. He considers the differential of the heat release dQ following

$$dQ = \frac{\delta Q}{\delta Z} dZ + \frac{\delta Q}{\delta \rho_u} d\rho_u + \frac{\delta Q}{\delta \dot{V}} d\dot{V} \tag{2.4}$$

with the unburnt density ρ_u, the mixture fraction Z and the volume flow $\dot{V}$. The fluctuation Q'/Q_0 can now be written as

$$\frac{Q'}{Q_0} \approx \frac{Z'}{Z_0} + \frac{\rho_u'}{\rho_{u0}} + \frac{\dot{V}'}{\dot{V}_0} \tag{2.5}$$

Neglecting the density fluctuations (a reasonable approximation for most cases since p'/p_0 remains small) yields the FTF:

$$\frac{Q(\omega)}{Q_0} = F_u(\omega)\frac{u(\omega)}{u_0} + F_\phi(\omega)\frac{\phi(\omega)}{\phi_0} \tag{2.6}$$

where the mixture fraction fluctuations are replaced by the equivalence ratio fluctuations. In system identification terms the expression 2.6 for the FTF is a MISO-model (Multiple Inlet Single Outlet), whereas Eq. 10.1 is called a SISO-model (Single Input Single Output). One outcome of his work was that a unique FTF can only be achieved by using the MISO approach with an uncorrelated excitation signal while pulsating both the air and the fuel inlet. Note that the equivalence ratio is linked to the mixture fraction through: $\phi = Z(1 - Z_{st})/(Z_{st}(1 - Z))$ with Z_{st} being the mixture fraction at stoichiometry.

Generally, the FTF can be determined experimentally, numerically and analytically and is mostly based on the SISO approach. Experimentally, FTFs are obtained using loudspeakers to excite the flow and velocity or pressure sensors combined with chemiluminescence as indicator for the heat release rate [37, 168]. Numerous experimental studies can be found in literature [63, 103] for laminar and turbulent flames. Nevertheless, the experimental determination of the FTF for complex industrial configurations is very difficult to realize and costly since optical access into the combustion chamber is needed.

Another possibility is the analytical method. Fleifil et al. [42] introduced a model based on the kinematic analysis of the flame front evolution, a linearized version of

the G-equation, for conical flames at small perturbation amplitude. It was extended by Ducruix et al. [37] to any flame tip angle and Schuller et al [150] further developed this approach for high frequencies and applied it to a conical and a V-flame. Good agreement with experiments was found and the FTF could finally be determined by the use of reduced frequency depending on the flametube radius, the flame speed and the flame angle. This modeling has been extended to the nonlinear response of premixed flames by Lieuwen [100]. For more complex flames, Palies et al. [119] recently extended this approach to premixed swirled flames. Two additional parameters are introduced in his model accounting for swirl number fluctuations which can not be determined analytically: they need experiments or an adjustment process.

Another theoretical model is based on the analysis of the unit impulse response of the flame and has been formulated by Komarek and Polifke [84] for a premixed swirled flame. The response of the flame to an axial perturbation is modeled as a Gaussian time lag distribution $F(\omega)_{axial} = e^{-i\omega\tau_1 - 1/2\omega\sigma_1^2}$ and the response to a fluctuation of swirl with $F(\omega)_{swirl} = e^{-i\omega\tau_2 - 1/2\omega\sigma_2^2} - e^{-i\omega\tau_3 - 1/2\omega\sigma_3^2}$. The FTF is finally $F(\omega) = F(\omega)_{axial} + F(\omega)_{swirl}$. The values for n_i, τ_i and σ_i were determined via fitting to experimental data. Schuermanns et al. [148] used the same approach to account for mixture fluctuations in a non-swirled configuration and introduced one additional Gaussian time lag. Although good agreement is found for the fitted FTF with experiments, an a priori determination of the FTF is not possible.

Alternatively, the FTF can be determined from a computational fluid dynamics (CFD) simulation [51, 85, 175]. In this approach an unsteady CFD calculation is performed and controlled excitations are imposed in order to generate time series of velocity and heat release rate oscillation. Then, the data is post-processed using system identification techniques to obtain the FTF [64, 74, 105].

Once the FTF is determined, it serves as input to linear thermo-acoustic instability models in order to determine the stability of the system. One approach is to model the relevant configuration as a 1D network of acoustic elements and to determine the acoustic pressure and velocity through each element via a transfer matrix [50, 80, 129, 149]. The linearized conservation equations are solved in the frequency domain and the complex eigenfrequencies give finally the growth rates, hence information on the stability, of the different modes. A second 1D possibility is to solve the thermo-acoustic problem in the time domain with the modified Galerkin approach [31, 33, 36, 88, 190] which is essentially based on the use of Green's functions. The acoustic mode shapes are determined from a homogeneous Helmholtz equation and they are then perturbed in the time domain. This leads finally to a temporal solution with growing or decaying oscillations. Eigenmode shapes and growth rates can also be determined in 3D while solving the inhomogeneous Helmholtz equation on 3D meshes [112, 152, 164]. In this method, a local FTF is used as input and is linked to the global FTF with amplitude n and time

delay τ through:

$$ne^{-i\omega\tau} = \iiint_V n_l(\vec{x})e^{-i\omega\tau_l(\vec{x})} \tag{2.7}$$

with the local amplitude $n_l(\vec{x})$ and the local time delay $\tau_l(\vec{x})$. The local FTF field allows as well to obtain further insight into the flame dynamics as it illustrates how the flame reacts in different regions. The inhomogeneous Helmholtz equation can also be solved in 3D directly in the time domain [120]. Similar to the approach in the frequency domain, the mode shapes are finally determined.

The limit cycle is controlled by non-linear effects due to heat release [2, 3, 101]. In order to predict limit cycle pressure amplitudes, the classical FTF approach has first to be adjusted to account for nonlinear effects. In the presence of high perturbation amplitudes, when the acoustic velocity reaches a magnitude of the order of the mean flow velocity, the flame is observed to saturate [2, 3, 101, 118] (compare also region II in Fig. 2.2). Hence, the flame response is not only a function of the frequency any more but also of the perturbation amplitude. An extended version of the linear FTF approach has been introduced by [35]: The so-called Flame Describing Function (FDF) is defined as

$$F(\omega, \hat{u}) = \frac{q'/\bar{q}}{u'/\bar{u}}. \tag{2.8}$$

and accounts for the perturbation amplitude dependence $\hat{u}$.

The saturation mechanism has been investigated by several reviewers. Studies on V-flames and swirling flames [3, 40, 118] showed that the flame sheet and the vortices shed from the injector interact non-linearly and that the flame surface area evolves non-linearly with increasing excitation amplitude. Durox et al. [40] found experimentally that the response is dependent on the amplitude. Lieuwen et al. [101] state from investigations on a swirled flame that vortex roll-up and unsteady flame lift-off decrease the flame surface area and lead therefore to saturation at higher amplitudes. Thumuluru et al. [178] showed that the flame shape is strongly influenced by the excitation level as well as the position and strength of the vortex breakdown region. Schimek et al. [142, 143] found that the flame saturation mechanisms were flame quenching due to local extinction and re-ignition. Kim et al. [81] investigated the effects of equivalence ratio fluctuations in a swirled flame and showed that the response of the flame depends on the phase difference between velocity and equivalence ratio fluctuations and can be either linear or non-linear.

Linear thermo-acoustic instability tools only provide the stability criteria, but a nonlinear description is required to investigate limit cycles, instability triggering and mode switching. The FDF is the key element determining those phenomena and is used as input for nonlinear models. A Galerkin type model is proposed by Selimefendigil and Polifke [151] to predict the pressure oscillation amplitude in a Rijke tube.

Another model based on the wave equation from Portillo et al. [87, 132] yields to time evolution of the perturbation and thus the modal growth rates, modal frequencies and the oscillation amplitude. Studies from Ecole Centrale Paris [13, 114, 115, 118] insert the FDF in the system dispersion relation and solve for the complex eigenfrequency to become zero in order to determine the modal growth rates and frequencies as a function of the perturbation level. Like this, it is possible to interpret mode switching phenomena in terms of growth rate evolution with respect to the perturbation amplitude. When the amplitude reaches a value for which the growth rate curve of one mode becomes larger than that of the mode existing until this moment, the frequency changes [114]. With respect to the FDF, operating points can be linearly stable but nonlinearly unstable as the FDF changes not only in amplitude but also in phase. Recently, Krebs et al. [87] found the limit cycle amplitude to increase with increasing growth rate.

Although FDF approach and nonlinear analysis allow to capture bifurcations and triggering points, these methods assume that harmonics have no effect on the FDF and exclude the non-normal nature of thermo-acoustic interactions. Nicoud et al. [112] showed that the eigenvectors of the linearized thermo-acoustic system are non-normal under unsteady heat release or when complex impedance boundary conditions are used. Figure 2.5 illustrates that the resultant vector R of two decaying not orthogonal eigenvectors EV_1 and EV_2 (i.e. in a non-normal system) can grow in the short term over time (t_1 to t_3), whereas in the case of decaying orthogonal eigenvectors R decays as well. This means that in a linearly stable system, transient growth may trigger nonlinearities when exceeding a certain threshold level leading to combustion instabilities [4, 73]. Balasubramanian et al. [4, 5] showed that even small initial amplitudes can trigger thermoacoustic instabilities. Juniper [73] determined the lowest initial energy for this to happen in a Rijke tube being 1% to 10% of the oscillation energy. Further he found that over almost half the linearly stable range, self-sustained oscillations can arise. In the present work, non-normality was not considered.

2.3.2 Self-excitation method

The second method to study thermo-acoustic instabilities is to allow the flame to interact with the acoustics until self-excited modes occur. In this way, the exact modes in terms of frequency and amplitude can be obtained both experimentally and numerically without further need of any thermo-acoustic instability model. There are numerous studies which experimentally investigate self-excited instabilities, e.g. [18, 35, 39, 56, 93, 102, 109, 143] and successful numerical studies e.g. [22, 54, 55, 75, 153].

Despite its obvious potential, simulation based on self-excited modes is in most cases, not mature and faces multiple difficulties: a) it does not yet incorporate all physical models required to capture instabilities with precision in real combustors

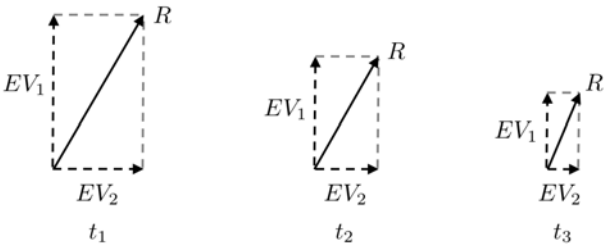

(a) Normal eigenvectors

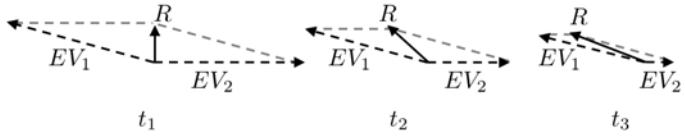

(b) Non-normal eigenvectors

Figure 2.5: Decaying eigenvectors in a normal (a) and non-normal (b) system.

(acoustics, geometrical complexity, two-phase flows, wall phenomena, radiation, etc) because present solvers simply do not have the power to do so in the absence of recent HPC tools, b) each simulation is only one realization of a short time period for one regime (one inlet temperature, one pressure, one fuel, one injection type, etc) in one combustor which depends on the boundary conditions, especially on the acoustic impedances imposed at the inlet(s) and outlet(s) of the combustion chamber. Simulation results change as soon as one of these parameters changes, exactly like the real combustor would. In that sense, numerical studies of self-excited modes in itself does not bring new insight into the reasons why a given chamber is unstable and does not tell which change will lead to a stabilization. In other words, simulation of self-excited modes will provide a result which is very similar to a perfectly instrumented experiment: it can help us understand instabilities if we have a theory to guide us but it can not replace this theory.

In the present work, no numerical simulation of self-excited modes will be performed: we will focus on the forced response of flames using FTF formulations. To determine FTFs we will use simulation methods and especially LES as discussed in the next section.

2.4 CFD as a tool to study thermo-acoustic instabilities

In Computational Fluid Dynamics (CFD) of turbulent combustion processes, three main approaches exist [126]:

- **Direct Numerical Simulation (DNS):**
  A DNS solves the full instantaneous Navier-Stokes equations explicitly on fine meshes without any modeling. All turbulent scales are captured and can act

on the combustion process leading to high numerical costs.

- **Large Eddy Simulation (LES):**
  A LES resolves the turbulent large scale structures and models the small scale ones by applying a filter. Unsteady features are represented and the modeling impact is reduced. Lower numerical costs than DNS.

- **Reynolds-Averaged-Navies-Stokes (RANS):**
  RANS simulations compute only averaged values without solving turbulent quantities. Coarse grids can be used and the numerical costs are reduced compared to LES.

LES is an intermediate approach which includes unsteady features with a reduced impact of the required modeling and acceptable computational costs. Numerous LES have been performed for laboratory and industry-scale configurations and have proved the capability of this approach [74, 153, 166, 176, 189]. Another advantage of LES is that it is well suited to unsteady phenomena such as forced flames required for FTFs. Therefore, the LES approach is used throughout this thesis.

Thermo-acoustic instabilities can be studied with the forced response method or as self-excited modes. For both approaches, the LES needs to meet special requirements. In the forced response method, first a stable regime has to be attained before a controlled excitation signal is introduced. The size of the forced domain needs to be reduced in order to exclude any possible resonant frequencies arising from the geometry. Specific boundary conditions are also needed to avoid unnatural resonant modes [78, 154]. One drawback is that transverse acoustic modes can not be predicted as they are created inside the chamber itself. For the self-excitation method the whole combustor geometry has to be taken into account. In order to generate resonance, the acoustic boundary conditions at the in- and outlet need to be well defined, something which is difficult in a real turbine. With this method, the limit cycles (modal frequency and amplitude) are determined from the LES exactly as they appear in experiments and all modes are captured. Nevertheless, if only one boundary condition is not accurately set, no limit cycle or a different one could be predicted.

In terms of computational costs the forced response method is the better choice. Self-excited oscillations may require a long computing time, first because the simulation domain has to describe the entire combustor and second because limit cycles need to be simulated over several periods to reach convergence. Furthermore, hysteresis and transition from stable to unstable operation condition can take a long physical time which is out of reach of present CPU power. Moreover, some combustors are linearly stable but non-linearly unstable meaning that a perturbation has to be added in order to start a growing oscillation. The choice of the initial condition for such LES is difficult and CPU intense as many tests are required. The forced response method is much faster to compute since the computational domain

(a) Self-excitation method

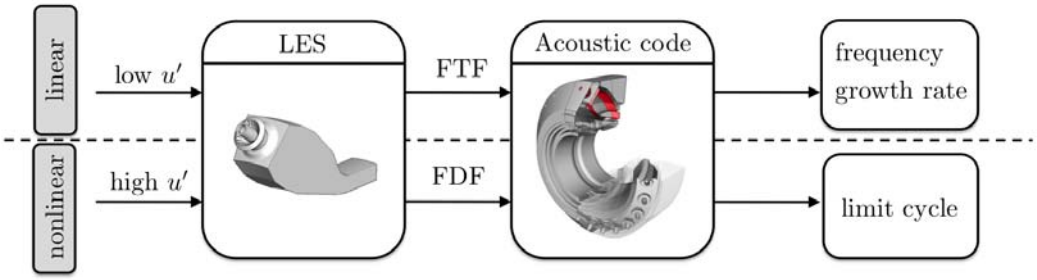

(b) Forced response method

Figure 2.6: Schematic drawing of self-excited and forced response method.

is smaller and less oscillation periods need to be calculated. The CPU time for a subsequent analysis with any thermo-acoustic instability code is negligible compared to the LES computations. Figure 2.6 summarized both methods.

During this dissertation, the flame transfer function and the mechanisms at play leading to stable or unstable combustor behaviour are determined with the forced response method. The LES code AVBP [110, 145, 157][1] is used and is described in the next chapter.

[1] http://www.cerfacs.fr/

Chapter 3

Numerical method

Contents

The present part is organized as follows: This chapter describes the governing equations solved by the LES code AVBP used throughout this thesis. AVBP is a massively parallel LES code solving the filtered, compressible, reacting Navier-Stokes equations on three-dimensional unstructured grids [26, 139, 146]. The code is only shortly described here, since no specific developments have been made during this work. The interested reader is referred to [110, 145, 157].
The next chapter deals with specific details of the analysis of thermo-acoustic instabilities. In particular, the excitation signals used for flame identification (FTFs) are discussed and the system identification process is described.

3.1 Governing equations

The evolution of a compressible and reacting flow is defined by the momentum, energy and species balance equations and can be written as:

$$\frac{\partial \rho u_i}{\partial t} + \frac{\partial \rho u_i u_j}{\partial x_j} = -\frac{\partial}{\partial x_j}\left[p\delta_{ij} - \tau_{ij}\right] \tag{3.1}$$

$$\frac{\partial \rho E}{\partial t} + \frac{\partial \rho E u_j}{\partial x_j} = -\frac{\partial}{\partial x_j}\left[u_i\left(p\delta_{ij} - \tau_{ij}\right) + q_i\right] + \dot{\omega}_T \tag{3.2}$$

$$\frac{\partial \rho Y_k}{\partial t} + \frac{\partial \rho u_j Y_k}{\partial x_j} = -\frac{\partial}{\partial x_j}\left[J_{j,k}\right] + \dot{\omega}_k \tag{3.3}$$

where ρ, u_i, p and E are respectively the mass density, the i-th component of the velocity vector, the thermodynamic pressure and the energy per mass unit (specific internal and kinetic energy). The index notation is adopted (Einstein summation convention) for almost all the variables and equations. The exception concerns the index k that is related to species and traditional summation symbol is used in this case, and N is the related number of species. Y_k is the mass-fraction of species k. The Kronecker's delta is δ_{ij}. Assuming the fluid to be Newtonian (viscous stress tensor is linearly dependent of the strain rate tensor) and neglecting the bulk viscosity, the viscous stress tensor τ_{ij} results:

$$\tau_{ij} = 2\mu\left(S_{ij} - \frac{1}{3}S_{ll}\right) \tag{3.4}$$

with μ the shear dynamic viscosity and S_{ij} the strain rate tensor defined as:

$$S_{ij} = \frac{1}{2}\left(\frac{\partial u_i}{\partial x_j} + \frac{\partial u_j}{\partial x_i}\right) \tag{3.5}$$

The heat and molecular diffusion fluxes are q_j and $J_{j,k}$ respectively. The source term $\dot{\omega}_T$ is related to the heat release rate and $\dot{\omega}_k$ to the production rate of the species k.

E is the total (non-chemical) energy per unit mass calculated as $E = H - P/\rho$. H represents the total enthalpy calculated as $H = h_s + \frac{1}{2}u_i u_i$, where $\frac{1}{2}u_i u_i$ is the kinetic energy of the gases and $h_s = \int_{T_0}^{T} C_p dT$ is the sensible enthalpy, C_p and T being the heat capacity and temperature of the mixture respectively.

3.1.1 Equation of state

The equation of state follows the ideal gas law:

$$P = \rho T \frac{R^0}{\overline{W}} \tag{3.6}$$

where R^0 is the universal gas constant and $\overline{W}$ is the mean molecular weight of the gas mixture.

3.1.2 Species transport

The conservation of mass has to be satisfied and follows:

$$\sum_{k=1}^{N} Y_k V_i^k = 0 \tag{3.7}$$

where V_i^k is the diffusion velocity of species k in directions $i = 1, 2, 3$ for the number of N species. The determination of diffusion velocities for all species requires a complex non-linear system of equations [10, 41, 126, 185] and the solution is time consuming. Therefore a simplified approach is used in AVBP to solve the chemical species transport following the Hirschfelder and Curtiss approximation [60]:

$$Y_k V_i^k = -D_k \frac{W_k}{\overline{W}} \frac{\partial X_k}{\partial x_i} \tag{3.8}$$

with D_k, W_k and X_k being the averaged diffusion coefficient into the mixture, the molar weight and the molar fraction of species k respectively. Since this approximation is not mass conservative, a correction velocity V_i^c is added in the conservation equation for each species (Eq. 3.7) resulting in the species diffusion flux for species k:

$$J_{i,k} = -\rho \left(D_k \frac{W_k}{\overline{W}} \frac{\partial X_k}{\partial x_i} - Y_k V_i^c \right) \tag{3.9}$$

where the diffusivity $D_k = D_{th}/Le_k$, with D_{th} being the thermal diffusivity of the mixture. Le_k is the Lewis number of species k and is assumed to be constant [126].

3.1.3 Chemistry modeling

The chemistry is determined for M reactions and N reactants $\mathcal{M}_k$:

$$\sum_{k=1}^{N} \nu'_{kj} \mathcal{M}_k \rightleftharpoons \sum_{k=1}^{N} \nu''_{kj} \mathcal{M}_k, \qquad j = 1, M \tag{3.10}$$

where ν'_{kj} and ν''_{kj} are the stoichiometric coefficients. The reaction rate progress $\mathcal{Q}_j$ of reaction j is

$$\mathcal{Q}_j = K_{f,j} \prod_{k=1}^{N} \left(\frac{\rho Y_k}{W_k} \right)^{\nu'_{kj}} - K_{r,j} \prod_{k=1}^{N} \left(\frac{\rho Y_k}{W_k} \right)^{\nu''_{kj}} \tag{3.11}$$

with the forward and reverse rate $K_{f,j}$ and $K_{r,j}$ of reaction j respectively.

The reaction rates follow the Arrhenius law

$$K_{f,j} = A_{f,j} exp \left(-\frac{E_{a,j}}{R^0 T} \right) \tag{3.12}$$

with $A_{f,j}$ and $E_{a,j}$ denoting the pre-exponential constant and the activation energy of reaction j. The reverse reaction rate writes

$$K_{r,j} = K_{r,j}/K_{eq} \tag{3.13}$$

using the equilibrium constant K_{eq} [90]. The reaction rate of species k finally follows

$$\dot{\omega}_k = W_k \sum_{j=1}^{M} \left(\nu'_{kj} - \nu''_{kj}\right) \mathcal{Q}_j \tag{3.14}$$

and the formation enthalpy of species k, $\Delta h^0_{f,k}$ can be written as:

$$\dot{\omega}_T = -\sum_{k=1}^{N} \dot{\omega}_k \Delta h^0_{f,k} \tag{3.15}$$

3.2 Large-Eddy Simulation

Large Eddy Simulation (LES) [130] is a widely recognized approach to compute the characteristics of turbulent flows. It is compared to the Direct Numerical Simulation (DNS) and the classical Reynolds Averaged Navier-Stokes (RANS) and intermediate approach. Figure 3.1 illustrates the different concepts of DNS, LES and RANS showing the spectral density of the turbulent kinetic energy $E(K)$ over the turbulent wave number k. DNS resolves the entire range of turbulent length scales and does not need any models but is expensive in terms of CPU cost. For RANS and LES new governing equations are derived by introducing operators to the set of compressible Navier-Stokes equations whereby unclosed terms arise. Hence, models are needed in order to solve the equations. The major differences between RANS and LES result from the operator used for the derivation. The RANS approach uses a temporal or ensemble average over the studied flow [21, 130] and the unclosed terms represent the physics taking place over the entire range of frequencies. In other words, the entire range of turbulent length scales is modeled. The operator in LES is a spatially localized time independent filter of given size Δ. This "spatial average" separates the large scales (greater than the filter size) from the small scales (smaller than the filter size) so that the unclosed terms represent the physics associated with the small structures at high frequencies. LES represents the dynamic large scale motions which are critical in complex gas turbine engines [126]. It is therefore the best approach considering CPU cost and accuracy for combustion instabilities.

3.2.1 Filtered Navier-Stokes equations

To obtain the new set of equations a spatial filtering operator is introduced [126]

$$\overline{f}(\mathbf{x}) = \int f(\mathbf{x}')F(\mathbf{x} - \mathbf{x}')d\mathbf{x}' \tag{3.16}$$

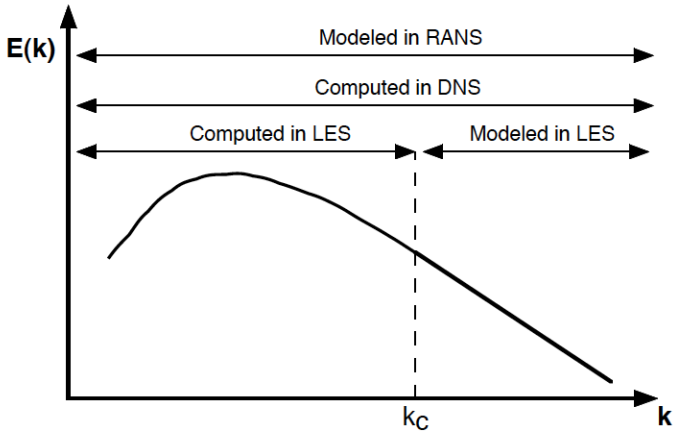

Figure 3.1: Conceptual differences between DNS, LES and RANS.

with F defining the LES filter. To account for density variations, a Favre filtered variable $\widetilde{f}$ is used as

$$\overline{\rho}\widetilde{f} = \overline{\rho f} \tag{3.17}$$

Variables can be decomposed in a Favre averaged part $\widetilde{f}$ and a fluctuating part f'' so that:

$$f = \widetilde{f} + f'' \tag{3.18}$$

The balance equations for LES are obtained by filtering the instantaneous balance equations 3.1, 3.2 and 3.3 and write:

$$\frac{\partial \overline{\rho}\widetilde{u}_i}{\partial t} + \frac{\partial \overline{\rho}\widetilde{u}_i\widetilde{u}_j}{\partial x_j} = -\frac{\partial}{\partial x_j}\left[\overline{P}\delta_{ij} - \overline{\tau_{ij}} + \underbrace{\overline{\rho}\left(\widetilde{u_i u_j} - \widetilde{u}_i\widetilde{u}_j\right)}_{SGS\ term}\right] \tag{3.19}$$

$$\frac{\partial \overline{\rho}\widetilde{E}}{\partial t} + \frac{\partial \overline{\rho}\widetilde{E}\widetilde{u}_j}{\partial x_j} = -\frac{\partial}{\partial x_j}\left[\overline{u_i\left(P\delta_{ij} - \tau_{ij}\right)} + \overline{q_{ij}} + \underbrace{\overline{\rho}\left(\widetilde{u_j E} - \widetilde{u}_j\widetilde{E}\right)}_{SGS\ term}\right] + \overline{\dot{\omega}_T} \tag{3.20}$$

$$\frac{\partial \overline{\rho}\widetilde{Y}_k}{\partial t} + \frac{\partial \overline{\rho}\widetilde{u}_j\widetilde{Y}_k}{\partial x_j} = -\frac{\partial}{\partial x_j}\left[\overline{J_{j,k}} + \underbrace{\overline{\rho}\left(\widetilde{u_j Y_k} - \widetilde{u}_j\widetilde{Y_k}\right)}_{SGS\ term}\right] + \overline{\dot{\omega}_k} \tag{3.21}$$

The total flux is composed of the inviscid flux, the viscous flux and sub-grid scale terms. The inviscid flux components write:

$$\begin{pmatrix} \overline{\rho}\widetilde{u}_i\widetilde{u}_j + \overline{P}\delta_{ij} \\ \overline{\rho}\widetilde{E}\widetilde{u}_j + \overline{u_i P}\delta_{ij} \\ \overline{\rho}\widetilde{u}_j\widetilde{Y}_k \end{pmatrix} \tag{3.22}$$

and the viscous flux is

$$\begin{pmatrix} -\overline{\tau_{ij}} \\ -\left(\overline{u_i \tau_{ij}}\right) + \overline{q_{ij}} \\ \overline{J_{j,k}} \end{pmatrix} \tag{3.23}$$

The convective terms introduce additional terms in the conservation equations during filtering due to their non-linear character.

$$\begin{pmatrix} -\overline{\tau_{ij}}^t \\ \overline{q_{ij}}^t \\ \overline{J_{j,k}}^t \end{pmatrix} = \begin{pmatrix} \overline{\rho}\left(\widetilde{u_i u_j} - \widetilde{u_i}\widetilde{u_j}\right) \\ \overline{\rho}\left(\widetilde{u_j E} - \widetilde{u_j}\widetilde{E}\right) \\ \overline{\rho}\left(\widetilde{u_j Y_k} - \widetilde{u_j}\widetilde{Y_k}\right) \end{pmatrix} \tag{3.24}$$

Those terms represent the contribution of the non-resolved turbulent scales which have to be modeled.

3.2.2 Sub-grid scale modeling

Filtering the transport equations yields a closure problem for the sub-grid scale (SGS) turbulent fluxes. The influence of the SGS on the resolved motion is taken into account by a model based on the introduction of a turbulent viscosity ν_t following the Boussinesq hypothesis [14] assuming the SGS terms to behave as their laminar counterparts, except with the use of a turbulent viscosity ν_t instead of the gas viscosity. The Reynolds tensor writes:

$$\overline{\tau}^t_{ij} = 2\overline{\rho}\nu_t \tilde{S}_{ij} - \frac{1}{3}\delta_{ij}\overline{\tau}^t_{ll} \tag{3.25}$$

Note that this approach assumes that the SGS field has a purely dissipative effect. The heat and species turbulent flux terms, the turbulent thermal and species diffusivities are computed using constant turbulent Prandtl and Schmidt numbers.

The eddy viscosity is calculated using the Smagorinsky [161] turbulence model where ν_t is proportional to the resolved filtered strain tensor $\widetilde{S_{ij}}$ and the mesh size $\Delta = V_{cell}^{1/3}$. It is given through

$$\nu_t = (C_S \Delta)^2 \sqrt{2\tilde{S}_{ij}\tilde{S}_{ij}} \tag{3.26}$$

C_S is the model constant and takes typically values between 0.1 and 0.18 and is fixed during this work to 0.18. The Smagorinsky model was developed in the 1960's [161] and is extensively tested over a wide range of flow configurations. It is easy to implement and performs sufficiently well for flows away from solid walls at low computational cost. Furthermore, it supplies the right amount of kinetic energy dissipation in homogeneous isotropic turbulent flows. However, locality is lost and only global quantities are maintained. and it is known as being too dissipative. Particularly, the simulation of wall-bounded flows combined with no-slip boundary conditions leads to an over prediction of the fluid friction on walls. The reason is that ν_t is proportional to the velocity gradients and is over predicted. The use of

slip-wall-law boundary conditions avoids this problem and justifies the use of the Smagorinsky model.

3.2.3 Combustion modeling

One problem occurring in LES is that the flame thickness is generally smaller than the mesh size and cannot be resolved. For this reason, the Dynamic Thickened Flame Model (DTFM) introduced by Légier [98, 145, 156] is used to model turbulent combustion. It is based on a classical dimensional analysis of premixed flames [185] showing the dependence of the flame front thickness δ

$$\delta \propto \sqrt{\frac{D}{A}} \tag{3.27}$$

and the laminar flame speed S_L

$$S_L \propto D \cdot A \tag{3.28}$$

on the reaction rate pre-exponential constant A and the diffusion coefficient D. This model is developed in order to resolve the flame front smaller than the mesh size by multiplying it with a thickening factor $\mathcal{F}$ while preserving the flame speed S_L. The constant A is therefore divided and D multiplied by $\mathcal{F}$. The thickening reduces the ability of the vortices to wrinkle the flame front. This results in a reduced reaction rate since the flame surface is decreased which is shown in Fig. 3.2. The efficiency

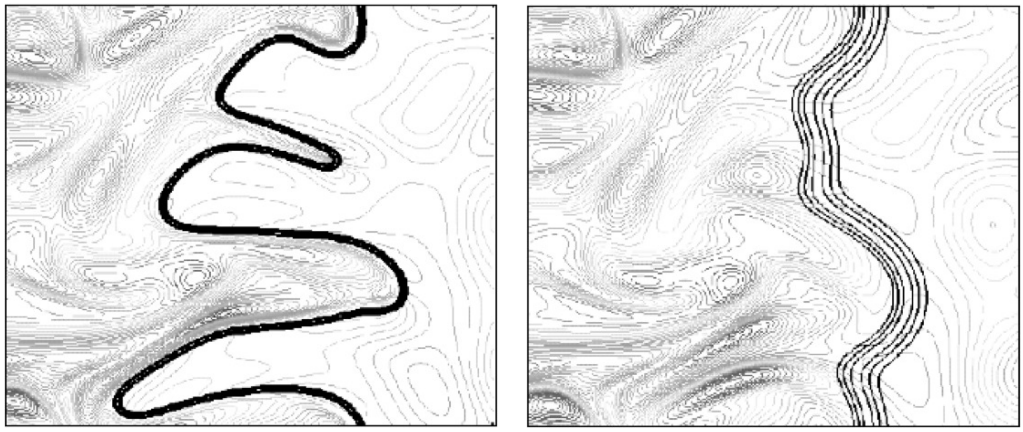

(a) Non-thickened flame (b) Thickened flame

Figure 3.2: Direct Numerical Simulation of flame/turbulence interaction [126].

function E by Charlette et al. [20] is used to account for these effects and multiplies the diffusion and reaction terms by the factor E:

$$E = \left(1 + min\left[\frac{\Delta}{\delta_l^0}, \Gamma\left(\frac{\Delta}{\delta_l^0}, \frac{u'_\Delta}{s_l^0}, Re_\Delta\right)\right]\right)^\beta \tag{3.29}$$

Here, Δ defines the implicit filter size of the LES, u'_Δ the SGS root-mean-square velocity. The propagation velocity and the thickness of the corresponding laminar flame are s_l^0 and δ_l^0. The Reynolds number follows $Re_\Delta = s_l^0 \delta_l^0 \nu$, with ν being the viscosity of the fresh gases and the model parameter is β.

3.3 Discretization

The LES code AVBP is used for simulations performed during this work. It is a highly massively parallel code which solves compressible Navier-Stokes equations on a unstructured grids [147, 165]. This section presents shortly the cell-vertex method and the numerical schemes used in this thesis. Details about the numerics can be found in [91].

3.3.1 Cell-vertex method

AVBP is based on the "finite volume" (FV) method wich can be implemented in three different ways: cell-centered, vertex-centered and the cell-vertex method. Only the latter is discussed here, since it is used in AVBP. In the cell-vertex technique the discrete values of the conserved variables are stored at the cell vertices and the mean values of the fluxes are obtained by averaging over the cell edges. The first step of the cell-vertex method consists of calculating the cell residuals. Then, information is sent to the mesh nodes in order to obtain as many equations as degrees of freedom and the nodal residual is calculated. Finally, the solution is advanced in time and the differential formulations of the Navier-Stokes are approximated [138, 140, 146].

3.3.2 Time advancement

Time advancement is explicit and based on a Runge-Kutta scheme [71, 187]. To avoid numerical instabilities the time step has to be below the critical CFL (convective scheme) and Fourier (diffusive scheme) number. Since the code is fully compressible, the CFL number is based on the sum of the acoustic and convective speeds. An AVBP, the usual CFL number is 0.7. In the case of source terms, the timestep also has to be small enough to avoid negative values e.g. of pressure or mass fraction. The timestep is finally chosen to be the smallest so that the three criteria are fulfilled.

3.3.3 Convection scheme

The Lax-Wendroff scheme [95] is used during this work. It is second order accurate in space and time and presents reasonable diffusive and dispersive properties at a fairly low computational cost. It is based an a Taylor expansion in time [58].

Boundary condition	Reflection coeffcient	Angle $\omega/\kappa \to 0$	Angle $\omega/\kappa \to \infty$
Relaxation p	$-\frac{1}{1-i\omega/\kappa_p}$	π	$+\frac{\pi}{2}$
Relaxation u	$+\frac{1}{1-i\omega/\kappa_u}$	0	$-\frac{\pi}{2}$

Table 3.1: Reflection coefficients of the boundary conditions used in this thesis.

3.4 Boundary conditions

Boundary conditions are crucial in LES since the acoustics are present in the governing equations and special attention must be paid.

3.4.1 Inlet and outlet boundary conditions

In- and outlet boundary conditions follow the Navier Stokes Characteristic Boundary Conditions (NSCBC) formalism from Poinsot and Lele [125] which avoids acoustic reflection by the use of a reflection coefficient. Throughout this thesis only inlet boundary conditions based on the relaxation of the normal velocity u and outlet conditions for the relaxation of pressure p are used.
The NSCBC method is based on the decomposition into characteristic waves as presented in Thompson [177] for the Euler equations (Euler Characteristic Boundary Conditions (ECBC)). The boundary condition must separate the information going in or out of the computational domain: the outgoing waves are considered as correctly predicted since they are a result of the CFD computation. The ingoing waves (usually the convective wave at $u - c$) have to be determined and are given through the boundary condition. More detailed information about NSCBC can be found in [91, 125, 131].

3.4.1.1 Acoustic behaviour

The in- and outlet boundary conditions used throughout this work behave similarly. The reflection coefficients of these boundaries behave like first-order low-pass filters and have cut-off angular frequencies proportional to the relaxation coefficients κ [154]. Their acoustic behaviour is summarized in Table 3.1. Care has to be taken on the choice of the relaxation coefficient, since it controls the variation from the desired target value and at the same time the reflection of outgoing acoustic waves. When low frequency pulsation is applied, undesired reflection might occur when the relaxation coefficient is too high. The pulsation procedure is described in the following.

3.4.1.2 Pulsation procedure

Forcing is introduced by using the inlet wave modulation method [78]. This method allows accurate predictions of FTF because only the amplitude of the ingoing acoustic wave is forced. Forcing the inlet velocity would lead to excitation of eigenmodes in the burner preventing the correct prediction of FTF [78]. Two types of excitation signals are used in this thesis: a harmonic and a broadband excitation which will be described in more details in section 3.5.1.

3.4.2 Wall treatment

On solid walls wall-law formulation are used [16, 62, 163]. The normal velocity component with respect to the wall normal is set to zero, while the no-slip condition is relaxed to allow for a non-null velocity component parallel to the walls. Today, resolving the boundary layer in the context of LES for industrial applications is beyond the computational resources available [122] and the fluid friction on solid walls is therefore modeled with a law of the wall boundary condition. The walls of all configuration throughout this work are modeled following a wall law condition with either adiabatic treatment or combined with a heat flux through the wall [145].

3.4.2.1 Adiabatic wall law

The dimensionless variables for the wall-distance and the velocity in the boundary layer are defined as

$$y^+ = \frac{y_w u_\tau}{\nu_w} \tag{3.30}$$

and

$$u^+ = \frac{u_2}{u_\tau} \tag{3.31}$$

with y_w being the cell height perpendicular to the wall, the mean velocity u_2 and the viscosity on the wall ν_w. The wall shear stress is $\tau_w = \rho u_\tau^2$. The friction velocity u_τ follows either a linear relation $u^+ = y^+$ (for $y^+ \leq 11.445$) or the logarithmic law of the wall $y^+ = C^{-1} ln(Ey^+)$ (for $y^+ > 11.445$, with $C = 0.41$ and $E = 9.2$).

3.4.2.2 Heat flux wall law

Heat losses through the wall are crucial for the occurrence of thermo-acoustic instabilities since they can have an effect on the stabilization of the flame [156, 176]. A simple dual model is used for modeling the heat loss through the wall and follows the linear law

$$q_w = \frac{T_{ref} - T_w}{R_w} \tag{3.32}$$

where q_w describes the heat flux at the wall, T_{ref} an outside reference temperature, T_w the wall temperature and R_w the total heat resistance of wall conduction and convection outside the chamber. The heat resistance is $R_w = \frac{e}{\lambda} + \frac{1}{h}$ with the

material thickness e and the heat resistance e/λ and $1/h$ of the conduction through the chamber wall and outside convection respectively (Fig. 3.3). Convection from

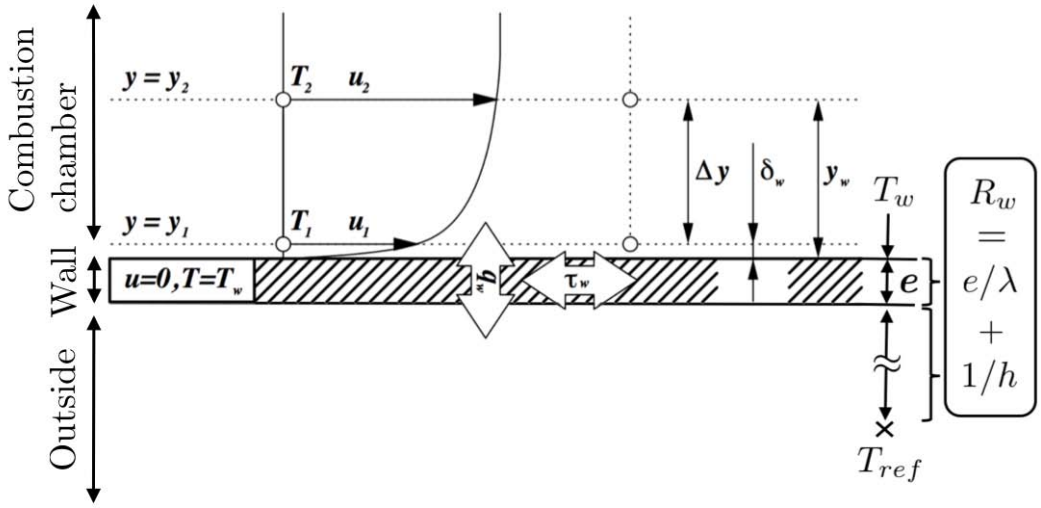

Figure 3.3: Typical velocity profile near the wall and notation used for near-wall quantities [145].

the fluid to the wall is modeled by the logarithmic law of the wall as:

$$T^+ = \frac{\rho_w C_{p,w} u_\tau (T_w - T_2)}{q_w} \tag{3.33}$$

The heat wall flux q_w follows (like u_τ) either a linear relation $T^+ = Pry^+$ (for $y^+ \leq 11.445$) or the logarithmic law of the wall $T^+ = C^{-1} Pr_t ln(Fy^+)$ (for $y^+ > 11.445$, with $C = 0.41$ and $F = 2.96$).

3.5 LES and System identification

System identification is a crucial step in LES in order to determine the FTF correctly. The process used here, follows the methods utilized and tested by TU Munich [43, 50, 64–66, 128] and are summarized in the following.

3.5.1 Excitation signal

Throughout this work, two different types of excitation signals are chosen:

- **Harmonic excitation**:
  A sinusoidal perturbation is introduced and one obtains the flame response in one LES for each frequency so that several simulations are needed to cover the frequency range. The harmonic excitation signal follows:

$$u(t) = u_0 sin(\omega t) \tag{3.34}$$

Postprocessing is performed with a Fast Fourier Transformation (section 3.5.2.1) of the velocity and heat release signals.

- **Broadband excitation**:
  This method allows the determination of the whole FTF in one single LES. Several broadband signals can be found in literature, as e.g. white noise, sinus overlay or a discrete random binary signal (DBRS). White noise is a pseudo-random signal distributed uniformly between 0 and 1 and the sinus overlay is generated by a superposition of sine waves. In this study a DBRS signal is chosen, which is a discrete random binary signal taking only two values $+u_0$ and $-u_0$. It is given through:

$$u(t) = u_0 sign(rand(m) - 0.5) \tag{3.35}$$

  where "sign" is the sign function taking the value 1 or -1 depending on the sign of the randomly generated number m which is between 0 and 1. DBRS is chosen as excitation signal because it has compared to the others the lowest crest factor [64–66]. The crest factor has been proposed by Ljung [105] and is defined as:

$$C_r = \sqrt{\frac{max_n(x_n^2)}{1/N \sum_{n=1}^{N} x_n^2}} \tag{3.36}$$

  It is equal to the peak amplitude of the waveform divided by the mean square of the zero mean signal allowing to judge the maximal amplitude distribution over a wide range of frequencies. A good signal waveform corresponds (following Ljung) to a small crest factor.

  In order to avoid reflection on the NSCBC boundary conditions (cf. section 3.4.1) in the low frequency range, the DBRS signal is high-pass filtered. Furthermore it is low-pass filtered to excite only the frequency range of interest and to achieve a higher power spectrum density [64–66].

  The FTF identification is performed with the Wiener Hopf method, which is presented in the next section.

3.5.2 System identification

The identification process must give the flame transfer function of an unknown configuration [43, 50, 64–66, 128]. Therefore the system is considered as a "black box" only knowing the input signal $s(t)$ and the system response $r(t)$ as illustrated in Fig. 3.4. For the FTF, the velocity just upstream of the flame is considered as input and the global heat release rate as output signal.

According to system identification theory [105], a linear time-invariant (LTI), causal system with an input signal s and a output response r at time t can be described

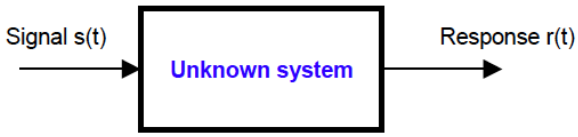

Figure 3.4: System identification: Black box.

by its impulse response h for every value $\tau = 0 \ldots \infty$ by:

$$r(t) = \int_{\tau=0}^{\infty} h(t)s(t-\tau)d\tau \tag{3.37}$$

Knowing the impulse response for each τ and the signal in the present and past, completely characterizes a system and allows for the determination of the system response [105].

Most practical systems, as well as LES, provide discrete signals: the signal is not continuous but sampled at times $t_n = n\delta t$ with $n = 1, 2, \ldots, n_{total}$. For such systems Eq. 3.37 becomes:

$$r_n = \sum_{k=0}^{\infty} h_k s_{n-k} + e_n \tag{3.38}$$

The additional term e_n represents undesired disturbances occurring in most systems. Dependent on the signal to noise ratio, this might have an important impact on the quality of the system identification. In LES, this term can be due to turbulence or acoustic modes in the chamber which affect the response of the flame and perturb the identification results.

For the two types of excitation signals (harmonic and broadband) different methods are used to determine the FTF $F(\omega)$ in the frequency domain:

$$F(\omega) = \sum_{k=0}^{L} h_k e^{-i\omega\delta tk} \tag{3.39}$$

3.5.2.1 Fast Fourier Transformation (FFT)

The transfer function for a harmonic excitation signal can be calculated by a FFT of $(u'/\bar{u})/(Q'/\bar{Q})$:

$$F(\omega) = FFT\left(\frac{Q'/\bar{Q}}{u'/\bar{u}}\right) = ne^{-i\omega\tau} \tag{3.40}$$

in order to obtain the amplitude response n and the time delay response τ of the system. To avoid spectral leakage, an integer number of cycles is used (6 cycles during this work). n and τ are both functions of ω.

3.5.2.2 Wiener Hopf Inversion (WHI)

The Wiener Hopf inversion is a method to reconstruct the transfer function between a signal and a response for a broadband excitation. This allows for the FTF determination over the whole frequency range with only one simulation. It has first been introduced to the CFD community by Polifke et al. [129] and Gentemann et al. [50]. The underlaying theory is briefly described here. Detailed information is given in [65, 66, 129].

For a broadband excitation it is difficult to separate which contributions of the flame response are due to the excitation signal and due to undesired disturbances represented by an error e_n in Eq. 3.38. The Wiener Hopf transformation minimizes e_n in a least-mean squared sense [105] and writes

$$\boldsymbol{\Gamma h} = \boldsymbol{c} \tag{3.41}$$

where Γ is the auto-correlation matrix of the input signals

$$\Gamma_{ij} = \frac{1}{N-L+1} \sum_{k=L}^{N} s_{k-i} s_{k-j} \text{ for } i,j = 0,\ldots,L \tag{3.42}$$

and $\mathbf{c}$ the cross-correlation vector of the input signals and the responses

$$c_{ij} = \frac{1}{N-L+1} \sum_{k=L}^{N} s_{k-i} r_k \text{ for } i,j = 0,\ldots,L \tag{3.43}$$

N denotes the number of considered time steps and L corresponds to the filter "memory". L has to account for the longest time lag of the system in order to capture all relevant physical effects [49]. In combustion instabilities this is usually the convective time scale [129]. The memory of the filter τ_{MEM} is given through $\tau_{MEM} = (L-1)\delta t$.

The so-called Wiener-Hopf Inversion

$$\boldsymbol{h} = \boldsymbol{\Gamma}^{-1}\boldsymbol{c} \tag{3.44}$$

and a subsequent z-transformation allow finally to determine the transfer function of the system. The identification procedure is illustrated in Fig. 3.5. The valid frequency range for the transfer function is determined by the time step δt through the Nyquist criterion $f_{max} = 1/(2\delta t)$ and the length of the time series (e.g. the simulation time) $T = n_{total}\delta t$ from $f_{min} = 1/T$.

The time step in LES is generally very small and a large filter length L would be needed in order to capture the longest time lag of the system. This leads to a high order of the auto-correlation matrix Γ_{ij} and to errors in the system identification during inversion due to bad conditioning [49]. In order to reduce the size of Γ

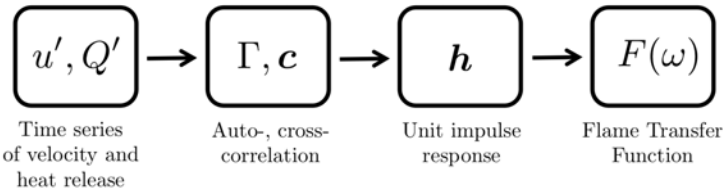

Figure 3.5: System identification process with Wiener-Hopf (adapted from [176]).

a factor m is introduced so that the auto-correlation matrix now writes:

$$\Gamma_{ij} = \frac{1}{N - Lm + 1} \sum_{k=Lm}^{N} s_{k-mi} s_{k-mj} \text{ for } i, j = 0, \ldots, L \tag{3.45}$$

The cross-correlation vector is in this case

$$c_{ij} = \frac{1}{N - Lm + 1} \sum_{k=Lm}^{N} s_{k-mi} r_k \text{ for } i, j = 0, \ldots, L \tag{3.46}$$

Of course, the valid frequency range for the identification procedure changes to $f_{max} = 1/(2m\delta t)$. A detailed analysis of this method can be found in [49].

Part III

Application to a perfectly premixed swirler combustor: the FVV burner

Chapter 4

Target configuration

Contents

The aim of this part is to validate the modeling for a lean premixed swirled burner at atmospheric pressure featuring a highly turbulent flow ($Re \approx 35000$) but also to estimate the uncertainties associated to a given LES approach to compute mean flows and FTFs in a swirled burner (FVV burner). Therefore the LES code AVBP is compared against experiments (performed at TU Berlin [142–144]) and to validate the modeling independently of the code used, against OpenFoam [1] LES simulations (performed at Siemens [89]). Thanks to the detailed data made available by LES, mechanisms can be identified influencing the dynamic behaviour of the flame.

This part is organized as follows: chapter 4 describes the FVV test rig, the operating point and the experiments used to characterize the flame and flow field. Then (section 4.2) the simulation domain, mesh, boundary conditions and numerical parameters are specified. Chapter 5 discusses the numerical results and validates them against experiments and the LES code OpenFoam (section 5.1.2). Furthermore the acoustically perturbed flame is analyzed and the FTF is validated in section 5.2.2. Finally the impact of different mechanisms influencing the dynamic flame response is analyzed (section 5.2.3).

4.1 The FVV test rig

The experimental test rig is located at the University of Berlin and operates under atmospheric conditions. All experimental results shown here have been provided by Schimek et al. [89, 142–144] who studied the swirl-stabilized premixed flame extensively. Figure 4.1 illustrates the experimental configuration. Preheated air

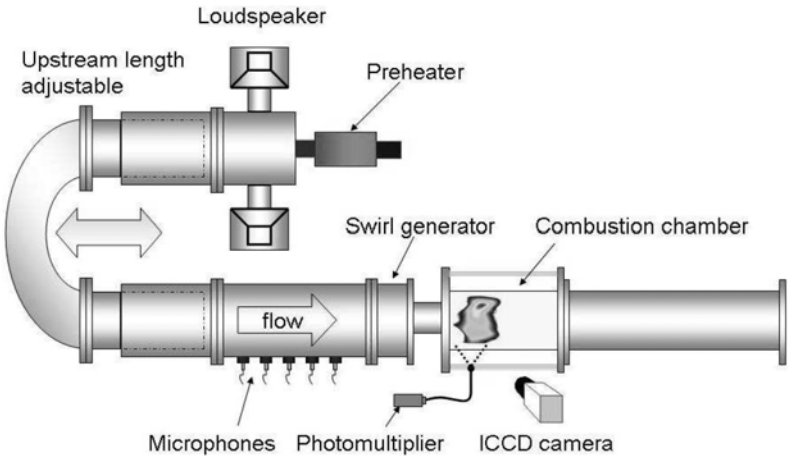

Figure 4.1: Experimental test rig [143]

passes the upstream duct, enters the swirl generator and reaches the combustion chamber through an annular duct. The flame is stabilized through an inner and outer recirculation zone resulting from the vortex breakdown due to the sudden geometrical expansion. The main parameters of the test rig are summarized in table 4.1. The upstream duct is variable in length in order to generate resonance in

Upstream duct	Length	2.0 to 2.7 m
	Diameter	0.1484 m
Annular duct	Length	0.171 m
	Diameter interior	0.0275 m
	Diameter exterior	0.055 m
Combustion chamber	Length	1.5 m
	Diameter	0.2 m

Table 4.1: Main parameters of the FVV configuration.

the combustion chamber when forcing is applied by the four loudspeakers mounted at the duct inlet (Fig. 4.1). The lowest resonance frequency is around 50 Hz and the second around 100 Hz with no resonance in between, whereas above 100 Hz multiple higher frequency modes appear. An acoustic forcing of up to 100 % of the mean velocity in the annular duct can be reached in order to meet desired excitation amplitudes at a given frequency. The swirl generator possesses movable blocks to apply for a wide range of swirl numbers from 0 up to approx. 2 (Fig. 4.2).

4.1.1 Experimental set-up

The acoustics of the duct are characterized via the multi microphone method, and the velocity fluctuation in the annular duct is obtained through reconstruction of

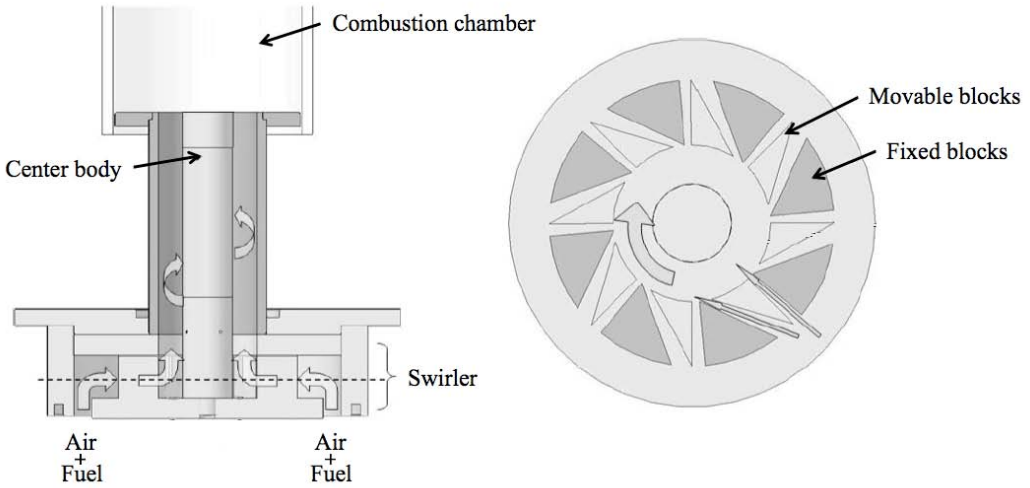

Figure 4.2: Cross-section of swirler, annular duct and combustion chamber [142].

the transfer matrix of the swirl generator. Fluctuations of heat release rate are measured with OH* chemiluminescence. Measurements are available for a variety of operating conditions including technically premixed (air and fuel are injected separately and mixed prior to combustion) and perfectly premixed operation, variation in swirl number, mass flow rates and equivalence ratios. In the technically premixed case, fuel is injected through sixteen holes in the swirl generator whereas for the perfectly premixed operating point, fuel and air is mixed far upstream of the swirler (Fig. 4.2). The reader is referred to [142, 143] for further information.

4.1.2 Operating point

This part focusses on the perfectly premixed operating conditions where fuel and air are mixed far upstream and a fully premixed mixture reaches the combustion chamber. This operating point is detailed in Table 4.2. The goal is to validate the LES methodology used against experimental mean flow fields and the flame transfer function and furthermore to obtain insight into the saturation mechanisms of the FTF amplitude.

4.2 Description of the numerical setup

This section presents first the computational mesh for the LES and the boundary conditions are given. The pulsation procedure for FTF determination is shortly described and finally the numerical parameters used for the calculation are explained.

Operating mode	Pre-premixed
Swirl number	1.2
Air mass flow rate	150 kg/hr
Air preheat temperature	493 K
Equivalence ratio	0.65

Table 4.2: Operating point

Number of cells	7.716.647
Number of nodes	1.400.323
Smallest cell volume	$4.699 \cdot 10^{-13} m^3$
Time step (CFL=0.7)	$8.742 \cdot 10^{-8} s$

Table 4.3: Parameters describing the mesh for the FVV burner.

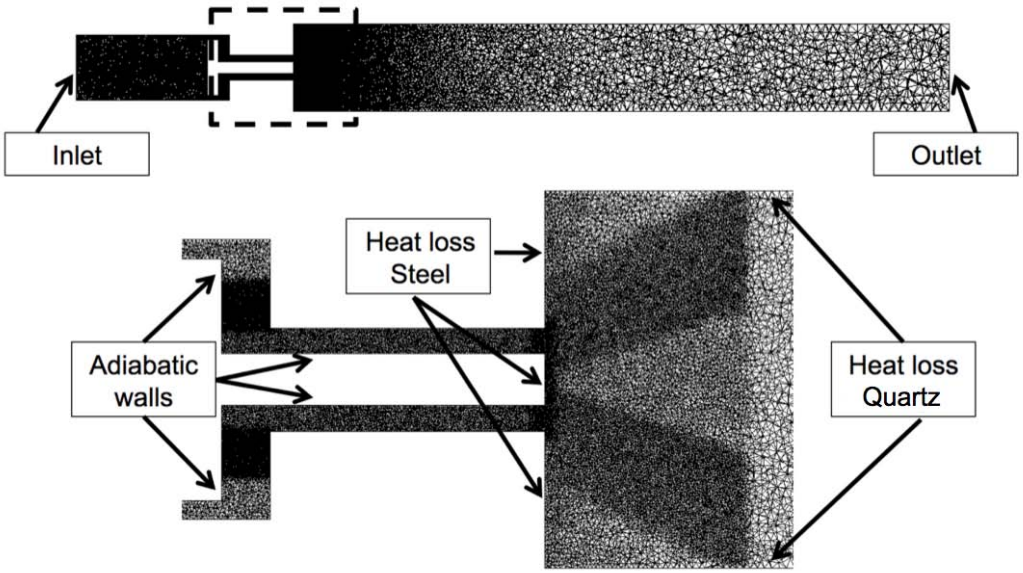

Figure 4.3: Mesh and computational domain

4.2.1 Computational mesh

The grid for the FVV configuration is three-dimensional and fully unstructured with 1.400.323 nodes corresponding to 7.716.647 tetrahedral elements. The time step is approx. $8.7 \cdot 10^{-8} s$ with the acoustic CFL number being fixed at 0.7 [124] for both cases. The mesh is refined in the flame region, in the annular duct and the swirler. Figure 4.3 shows the mesh on the middle cut plane in 2D and Table 4.3 summarizes its main parameters.

4.2.2 Boundary conditions

The inlet and outlet boundary conditions are imposed through the non-reflecting Navier-Stokes Characteristic Boundary Condition (NSCBC) formulation [125] which limits acoustic reflection. For the combustion chamber walls a logarithmic wall-law condition is set and additionally applies for heat loss effects since it is essential for flame stabilization and thus the correct prediction of FTF [176]. The model for heat loss through the wall follows the linear law presented in section 3.4.1:

$$q_{wall} = \frac{T_{ref} - T_{wall}}{R_{wall}} \tag{4.1}$$

where q_{wall} describes the heat flux at the wall, T_{ref} a reference temperature, T_{wall} the wall temperature and R_{wall} the combined heat resistance of conduction through the material and outside convection. The side walls of the combustion chamber are made out of quarzglas with a thickness of 6 mm resulting in a heat resistance of $1/R_{wall} = 500W/m^2K$ if the outside convection coefficient h is large. The end walls of the combustor, i.e. where the flame stabilizes, consist of steel 1.4301 with a thickness of 8 mm which results in $1/R_{wall} = 1875W/m^2K$. The reference temperature is set to 300 K. All other walls follow an adiabatic wall-law.
Flame transfer functions are determined via pure tone excitation for different frequencies. Therefore an harmonic perturbation is introduced through the inlet using the inlet wave modulation method [78] and the perturbation of the total heat release rate is measured.

4.2.3 Numerical parameters

The fully compressible explicit code AVBP is used to solve the reactive multi-species Navier-Stokes equations on unstructured grids using a cell-vertex approximation [147]. A second order finite element scheme is used for both time and space advancement [57, 94]. Sub-grid stress tensor is modeled by a classical Smagorinsky approach [161]. Chemistry is computed using a two step mechanism for Methane/Air flames [44–46] where the full chemistry is replaced by two reactions taking into account six species (CH_4, O_2, CO_2, CO, H_2O and N_2):

$$CH_4 + \frac{3}{2}O_2 \quad \longrightarrow \quad CO + 2H_2O \tag{4.2}$$

$$CO + \frac{1}{2}O_2 \quad \longleftrightarrow \quad CO_2 \tag{4.3}$$

The first reaction is irreversible and decribes the rate of reaction as follows:

$$q_1 = A_1 \left(\frac{\rho Y_{CH_4}}{W_{CH4}}\right)^{n_1^{CH_4}} \left(\frac{\rho Y_{O_2}}{W_{O_2}}\right)^{n_1^{O_2}} exp\left(-\frac{E_{a1}}{RT}\right) \tag{4.4}$$

The second reaction is reversible and leads to an equilibrium between CO and CO_2 in the burnt gases. Its rate of reaction is given through:

$$q_2 = A_2 \left[\left(\frac{\rho Y_{CO}}{W_{CO}}\right)^{n_2^{CO}} \left(\frac{\rho Y_{O_2}}{W_{O_2}}\right)^{n_2^{O_2}} \left(\frac{\rho Y_{CO_2}}{W_{CO_2}}\right)^{n_2^{CO_2}}\right] exp\left(-\frac{E_{a2}}{RT}\right) \tag{4.5}$$

Numerical scheme	Lax-Wendroff
Sub-grid scale model	Smagorinsky model
Artificial viscosity model	Colin Sensor ($\varepsilon_2 = 0.05$; $\varepsilon_4 = 0.01$)
Chemistry	Two-step BFER
Flame/turbulence interaction	Thickened flame model

Table 4.4: Numerical parameters used for the FVV simulation.

A_1	E_{a1}	$n_1^{CH_4}$	$n_1^{O_2}$	
$4.9 \cdot 10^9 cgs$	$35500 cal/mol$	0.5	0.65	
A_2	E_{a2}	n_2^{CO}	$n_2^{O_2}$	$n_2^{CO_2}$
$-2.0 \cdot 10^8 cgs$	$12000 cal/mol$	1.0	0.5	0.0

Table 4.5: Coefficients used in the reduced chemical scheme for CH_4/air flames.

This scheme was developed and fitted to match the full mechanism's behaviour for equivalence ratios between 0.4 and 1.5 [45, 46]. To capture flame/turbulence interactions, the dynamic thickened flame model is used. The flame sub-grid-scale wrinkling and interactions are supplied by an efficiency function [25, 27, 98]. The numerical parameters are summarized in Table 4.4 and the coefficients for the reduced chemical scheme can be found in Table 4.5.

Chapter 5

LES of the reacting unforced and forced flows in the FVV setup

Contents

5.1 Reacting flow fields

The following section describes first the averaged and instantaneous flow field obtained with AVBP for the turbulent unforced cases. In the second section a comparison of simulation results obtained with AVBP and OpenFoam at different axial cuts in the combustion chamber is performed and compared to PIV measurements obtained by TU Berlin. The reader is referred to [142–144] and [89] for detailed information about the PIV measurements and the OpenFoam simulation respectively.

5.1.1 Mean reacting flow fields with AVBP

A first impression of the flow field can be obtained by plotting the instantaneous axial velocity field in the middle cut plane and a three-dimensional iso-surface of the flame ($T = 1200$ K) in Fig. 5.1. A highly turbulent flow develops in the annular flame tube and a wrinkled flame is stabilized by the inner and outer recirculation zones resulting from the vortex breakdown and the sudden expansion. The averaged axial velocity field (Fig. 5.2) shows that the flow is accelerated at the chamber inlet and that a large inner recirculation zone and strong outer recirculation zones are formed. The velocity at the outlet of the annular flame tube is higher at the outer

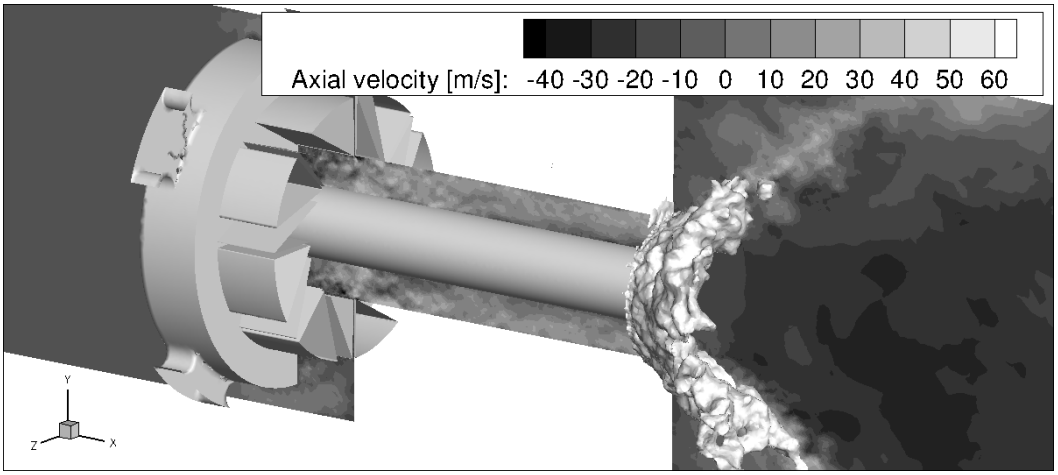

Figure 5.1: Instantaneous axial velocity field on middle cut plane and temperature iso-surface ($T = 1200$ K).

walls because the flame already stabilizes right at the inner side of the annular tube (Fig. 5.3) and acts as a surface reduction. The highest heat release (Fig. 5.4) appears on the inner side of the flame at the chamber inlet. The flame is stabilized slightly upstream of the dump plane. It is slightly lifted from the outer walls due to the imposed heat loss boundary conditions on the dump plane wall (Fig. 4.3). The time averaged flow field of has been obtained by averaging the converged simulation over 102 msec corresponding to 30 flow-through times of the flame region.

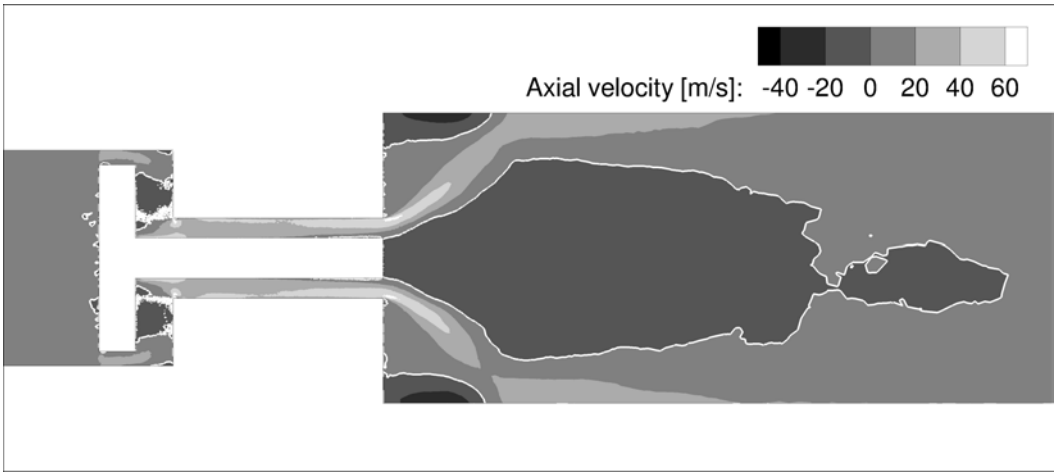

Figure 5.2: Averaged axial velocity field on middle cut plane.

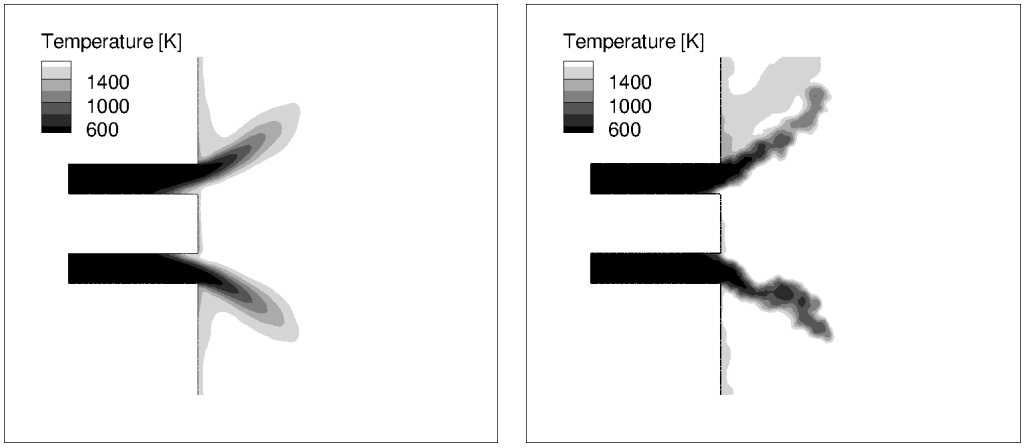

(a) Averaged solution (b) Instantaneous solution

Figure 5.3: Temperature field on middle cut plane.

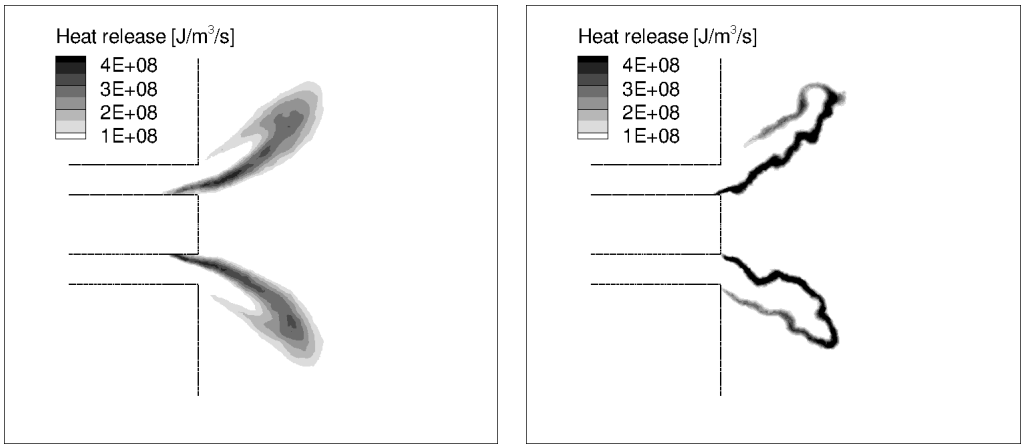

(a) Averaged solution (b) Instantaneous solution

Figure 5.4: Heat release field on middle cut plane.

5.1.2 Comparison Between AVBP, Openfoam and PIV

Particle image velocimetry experiments and averaged results are compared here to the LES computations performed with AVBP and OpenFoam. Figure 5.6 illustrates the mean temperature field for both codes at position $x = 0.01, 0.02, 0.03, 0.04, 0.05$ and 0.1 m from the combustion chamber entrance corresponding to $x = 0$ as illustrated in Fig. 5.5.

AVBP and Openfoam show good overall agreement. The maximal temperatures in the chamber predicted by the two solvers agree although a different approach is used with OpenFoam: i.e. iso-thermal wall conditions against a heat flux through the wall with AVBP. These differences partly explain the different temperatures directly at the wall. Axial velocity profiles are compared with PIV data in Fig. 5.7. The inner recirculation zone is well represented by both codes. The outer recirculation zone is over predicted. The results of AVBP are slightly closer to the measurements compared to OpenFoam but both codes overestimate the recirculated flow rate.

The radial and tangential velocity profiles (Fig. 5.8 and 5.9) reproduce well the location and magnitude of extrema for the inner recirculation zone. Room for improvement is still present compared to experiments for the outer recirculation zone. Again, the simulation with AVBP is slightly closer to PIV. Note that following [89], measurement errors might be present due to window contamination in this region. Considering that both LES codes agree very well away from these regions, errors in PIV measurements are possible.

Although temperature and velocity profiles agree well, differences between AVBP and OpenFoam are observed for the RMS fluctuations. RMS temperature profiles (Fig. 5.10) are similar at the chamber inlet, but almost double in AVBP at

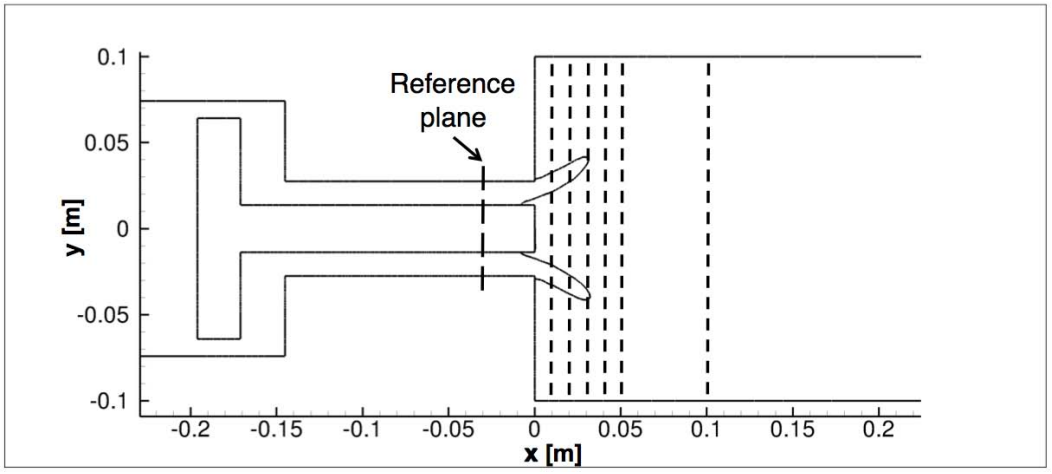

Figure 5.5: Reference plane for FTF determination, location of cuts at $\Delta x = 0.01, 0.02, 0.03, 0.04, 0.05$ and 0.1 m and iso-line of temperature ($T = 1200$ K).

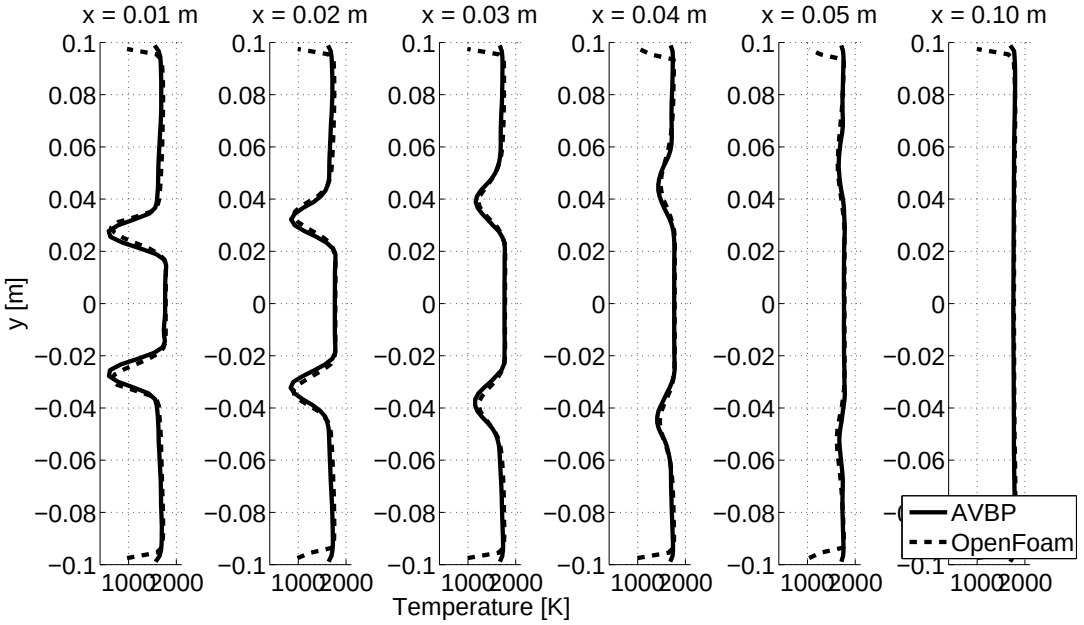

Figure 5.6: Temperature profiles at $x = 0.01, 0.02, 0.03, 0.04, 0.05$ and 0.1 m for AVBP and OpenFoam.

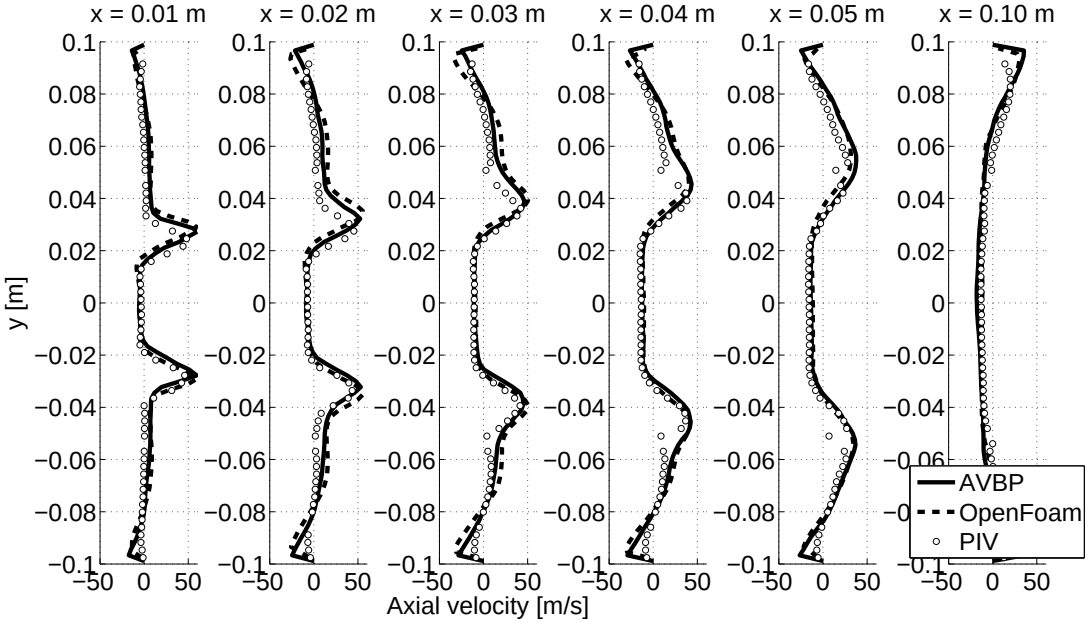

Figure 5.7: Axial velocity profiles at $x = 0.01, 0.02, 0.03, 0.04, 0.05$ and 0.1 m for AVBP, OpenFoam and PIV.

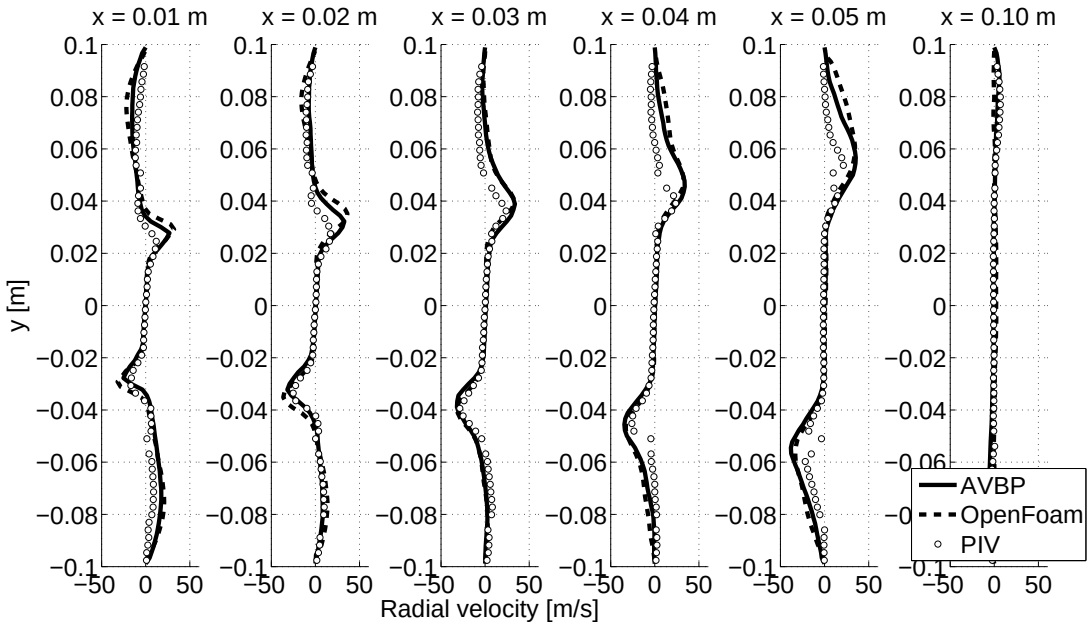

Figure 5.8: Radial velocitiy profiles at $x = 0.01, 0.02, 0.03, 0.04, 0.05$ and 0.1 m for AVBP, OpenFoam and PIV.

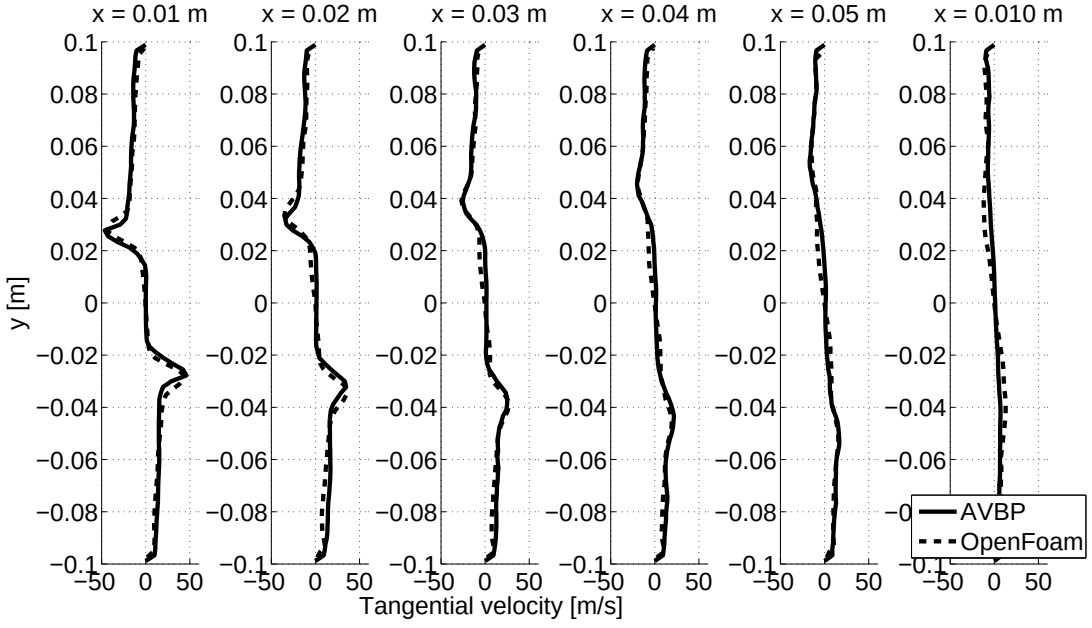

Figure 5.9: Tangential velocitiy profiles at $x = 0.01, 0.02, 0.03, 0.04, 0.05$ and 0.1 m for AVBP and OpenFoam.

$x = 0.04$m. Since no PIV data is available, it is difficult to conclude here that AVBP is better. However, the smaller RMS values obtained with OpenFoam are consistent with the larger dissipation observed in this solver.

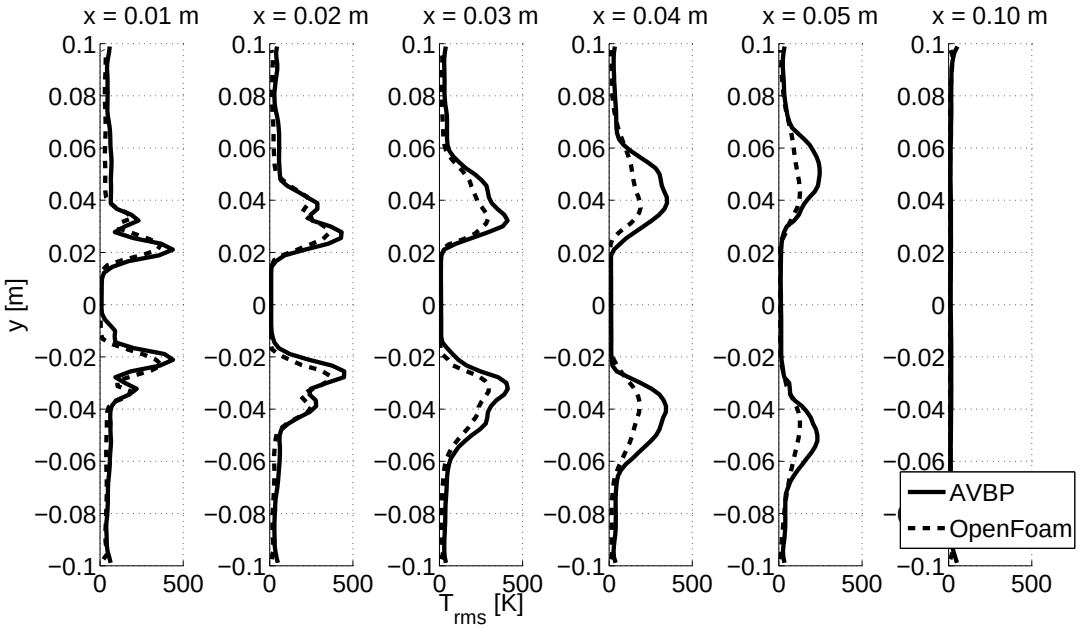

Figure 5.10: RMS temperature profiles at $x = 0.01, 0.02, 0.03, 0.04, 0.05$ and 0.1 m for AVBP and OpenFoam.

5.2 Forced reacting flow

5.2.1 Pulsation procedure

For this configuration, only harmonic forcing has been applied for velocity excitation and results for u' and q' are post-processed using FFT described in Section 3.5. The velocity amplitude applied at the boundary inlet (Fig. 4.3) is of 40 % the mean velocity in order to obtain a velocity fluctuation in the annular tube of 10% the mean velocity. The simulation has been performed with a fixed time step of $9 \cdot 10^{-8}$ sec. The gain and the phase of the FTF can be reconstructed from the time series of measured relative flow velocity perturbation $(u'/\bar{u})$ at a reference plane and the relative heat release rate perturbation $(q'/\bar{q})$. The reference plane is located in the annular duct (Fig. 5.5). The FTF is finally obtained by using a Fast Fourier Transformation (FFT). Six cycles of oscillation were used to identify the FTF.

5.2.2 Flame Transfer Function

The FTF obtained with AVBP is compared to measurements and OpenFoam results for the frequencies f = 53, 115, 182, 258 and 323 Hz in Fig. 5.11. No data for OpenFoam is available at 53 Hz. All simulation results agree well. Compared to measurements, LES under predicts the gain as well as the phase of the FTF for the frequency of 115 Hz. Nevertheless the gain overshoot at this frequency is captured. The low amplitude at 53 Hz is over predicted but the tendency is captured. Saturation of the gain for higher frequencies is also captured with both codes for 258 Hz and 323 Hz. Over prediction for the phase can be observed for both codes

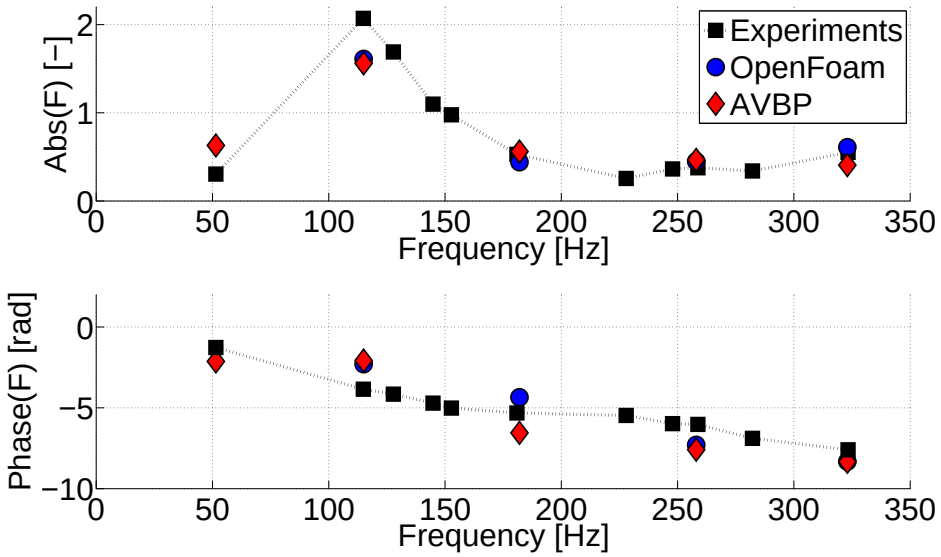

Figure 5.11: Comparison of Flame Transfer Function obtained with AVBP, OpenFoam and measurements.

at high frequencies. OpenFoam and AVBP give similar results for all frequencies comforting the LES modeling strategy for such problems and showing that the uncertainty associated to LES remains reasonable compared to the difference between experimental data and LES. In other words, when both LES solvers agree but do not match experimental data, this may indicate that the experiment has a problem or that something is missing in both LES.

5.2.3 Mechanisms affecting the FTF

Figure 5.12 displays the temperature field with an iso-line of the mean heat release ($2 \cdot 10^7 J/m^3/s$) for different phase angles of the heat release oscillation cycle for the forcing frequency 115 Hz. The flame is stabilized inside the injection tube and the position oscillates in phase. While pulsating the ingoing acoustic wave, the mass

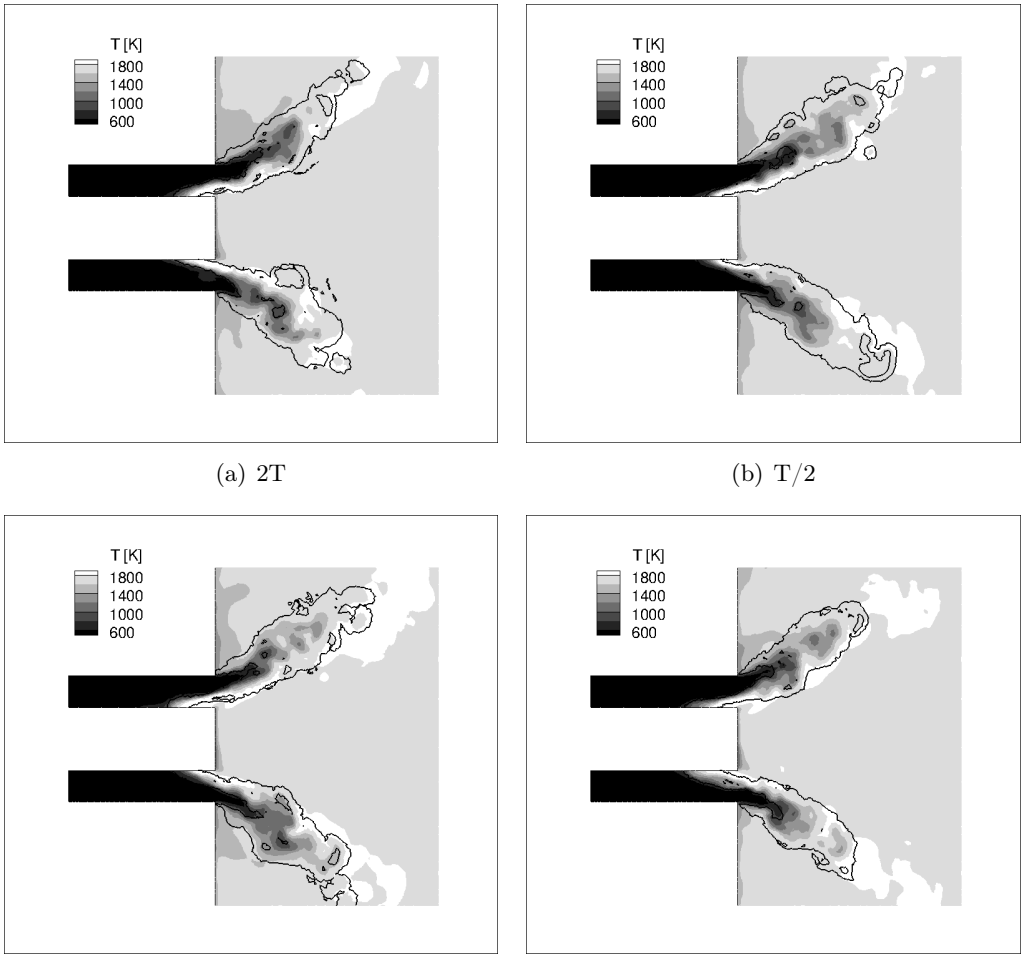

(a) 2T (b) T/2

(c) T (d) 3T/2

Figure 5.12: Phase averaged temperature field for 115 Hz and iso-line of heat release (the level of the isoline corresponds to the mean heat release over the whole cycle).

flow rate oscillates sinusoidally and the flame reacts to this perturbation after a certain time lag (compare Fig. 5.11).

When acoustic perturbations impinge the swirler, axial and transverse velocity fluctuations are created travelling with the speed of sound and the convective velocity respectively. This leads to a phase difference between both velocity components resulting in swirl number fluctuations. This is illustrated in Fig. 5.13. At the trailing edge of the swirler vanes (plane 1), the axial u_{ax} and azimuthal u_θ velocities are in phase. Within the passage, since the axial signal is propagating at $u + c$ while the azimuthal perturbations move at u, the phase at plane 2 between both components can take any value depending on L. This phase is one of the parameters which control swirl variation at the chamber inlet. According to Palies et al. [117] this mechanisms has a strong impact on the flame response. As the vortex breakdown changes with the swirl number, the size and position of the recirculation zones change and affect thus the flame angle. Palies et al. [117] state that an overshoot occurs when axial and azimuthal velocity are in phase when impinging the flame front and low amplitude when both components are out of phase.

Figure 5.14 and Figure 5.15 show the relative axial ($u'_{ax}/\bar{u}_{ax}$) and transverse velocity ($v'_\theta/\bar{v}_\theta$) components at the reference plane (Fig. 5.5) over the normalized time for two cycles of axial velocity fluctuation for the two distinct frequencies 53 Hz and 115 Hz. Axial and transverse velocities are almost in phase at 53 Hz and in quadrature at 115 Hz. Here, in phase variations of u'_{ax} and u'_θ lead to smaller swirl variations and reduced flame angle fluctuations. At 53 Hz, this leads to a small value of the gain n (Fig. 5.11). Inversely, at 115 Hz, the swirl variations will be larger, leading to larger values of n. This result does not support Palies model, suggesting that more complex phenomena (in addition to u'_{ax} and u'_θ) determine the

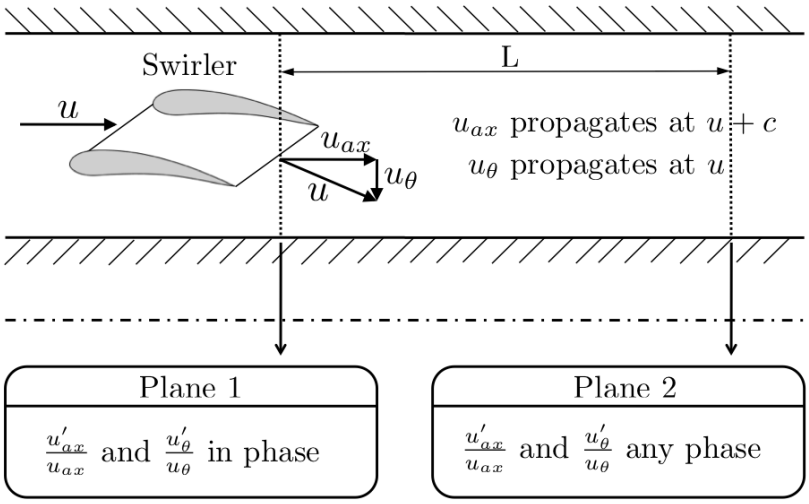

Figure 5.13: Illustration of the creation of swirl number perturbations.

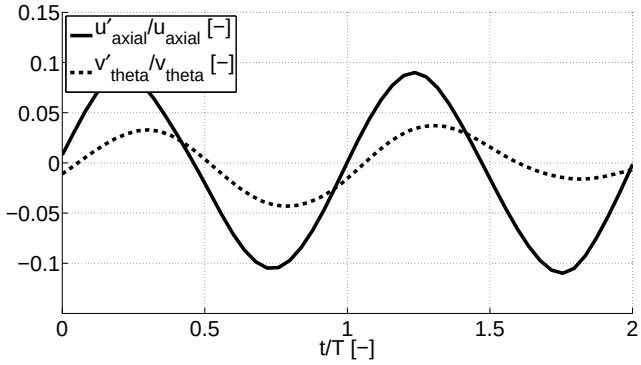

Figure 5.14: Normalised axial, transverse velocity and swirl fluctuation at the reference plane for a forcing frequency of 53 Hz.

flame transfer function of Fig. 5.11 in this case.

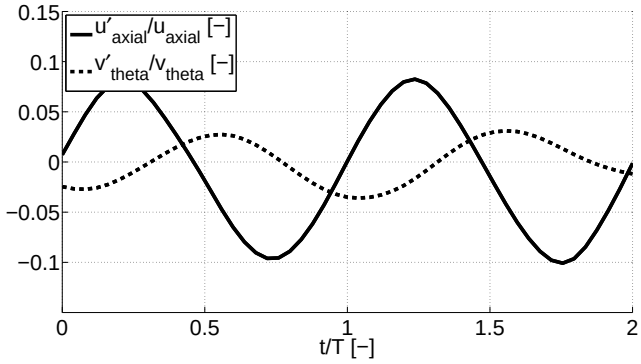

Figure 5.15: Normalised axial, transverse velocity and swirl fluctuation at the reference plane for a forcing frequency of 115 Hz.

5.3 Conclusions

PIV measurements have been compared to Large-Eddy Simulation performed with two different codes (AVBP and OpenFoam). Both AVBP and OpenFoam show good agreement for the averaged flow field compared in terms of temperature and velocity components in axial, radial and tangential direction. The averaged temperature field shows very good agreement between both simulations. When compared to velocity measurements the simulations generally show good agreement. For all velocity components the location of the extrema are well represented as well as the magnitude and the extent of the inner recirculation zone. The outer recirculation zone is over predicted by both simulations compared to experiments. Following [89] measurement errors might be present due to window contamination in this region.

For the forced reactive flow field AVBP and OpenFoam show good agreement for

the considered forcing frequencies. The overshoot in gain is predicted as well as the decreasing gain for higher frequencies. Compared to experiments, the gain at 53 Hz is over predicted and at 115 Hz under predicted while the higher frequencies show better agreement. Both codes under predict the phase for 115 Hz and over predict it for the higher frequencies. The general shape however corresponds to the PIV measurements.

The flame which is stabilised inside the flame-tube changes its position with the oscillating flow rate. Swirl number fluctuations due to different propagating mechanisms of axial and azimuthal velocity lead to different FTF amplitude responses. Both velocity components are in quadrature when impinging the flame front leading to a higher response of the flame at 115 Hz and in phase at 53 Hz where a low amplitude response occurs. This result does not support Palies model, suggesting that more complex phenomena determine the flame transfer function amplitude in this case.

The goal of this part was to validate the modeling for a lean premixed swirled burner against experiments and against OpenFoam LES simulations [89]. The LES code AVBP presented in chapter 3 captures the phenomena appearing during thermoacoustic instabilities. The next part is dedicated to the simulation of the thermoacoustic behaviour of a complex real gas turbine application.

Part IV

Application to an industrial combustor: A Double Swirler Technically Premixed Burner

Chapter 6

Target configuration

Contents

Chapter 1 and 2 in part 1 presented the LES solver and the specificities of annular combustors. Part 2 validated the LES solver against experiments for a single premixed turbulent swirling flame at atmospheric pressure and identified mechanisms acting on the dynamics of the flame. LES was shown to provide good evaluation of the FTF (Flame Transfer Function). The goal of this part is to extend the methodology to an industrial gas turbine where additional mechanisms come into play when air and fuel are injected separately and mixing takes place. These mechanisms have been studied for simple laboratory flames but much less information is available for real gas turbines. This point is investigated here for a real burner corresponding to an industrial gas turbine. Thanks to this fully unsteady numerical approach, effects of mass flow rate perturbation, mixture fluctuation and swirl number perturbation can be studied.

In the first chapter the configuration will be described and the simulation domain, mesh, boundary conditions and numerical parameters are specified. In chapter 7 the numerical results will be validated against experiments on an atmospheric test rig and the unforced flame is analyzed in detail for different operating conditions and burner outlets. In chapter 8 acoustic perturbations are introduced and the linear dynamic response of the flames for the different cases is analyzed in detail. Finally, chapter 10 discusses the non-linear flame response to study the flame dynamics when limit cycles in real machines occur.

6.1 Geometries

During this work, two configurations have been computed. The first one is a single sector of the real gas turbine (Section 6.1.1) and the second one is a specific

laboratory experiment used for cold flow measurements (Section 6.1.2).

6.1.1 Real gas turbine

The combustion chamber considered throughout this part is of annular type (24 burners) shown in Fig. 6.1 on which a Siemens/Ansaldo hybrid burner is mounted on each 15 degree section. The burner is operated at high pressure and possesses multiple air and fuel inlets (Fig. 6.2). Air is injected through two coaxial swirlers (diagonal and axial) with the main air mass flow rate passing through the diagonal passage. The diagonal and axial swirlers of each burner contain 24 and 8 vanes respectively. Methane is injected through small holes in the vanes of the diagonal passage and is mixed with air while reaching the combustion chamber. This mixing is supposed to be fast and an almost premixed lean flow is expected to exit the diagonal passage. Swirl induces a vortex breakdown [106, 167] leading to flame stabilization. The location of the heat release is predominantly determined by the aerodynamics and the size of the recirculation zones which can be modified by changing the burner outlet. To investigate this effect, two burner outlets are considered in this part (Fig. 6.3): a long Cylindrical Burner Outlet (CBO) and a short Normal Burner Outlet (NBO). The existence of this small geometry change, introduced by Siemens to modify flame stability, is a very interesting fundamental issue. CBOs do modify the characteristics of the FTF and affect the engine stability. It is shown here how this is obtained by comparing cases with and without CBO.

In addition to CBO, this real burner also exhibits other specificities. For exam-

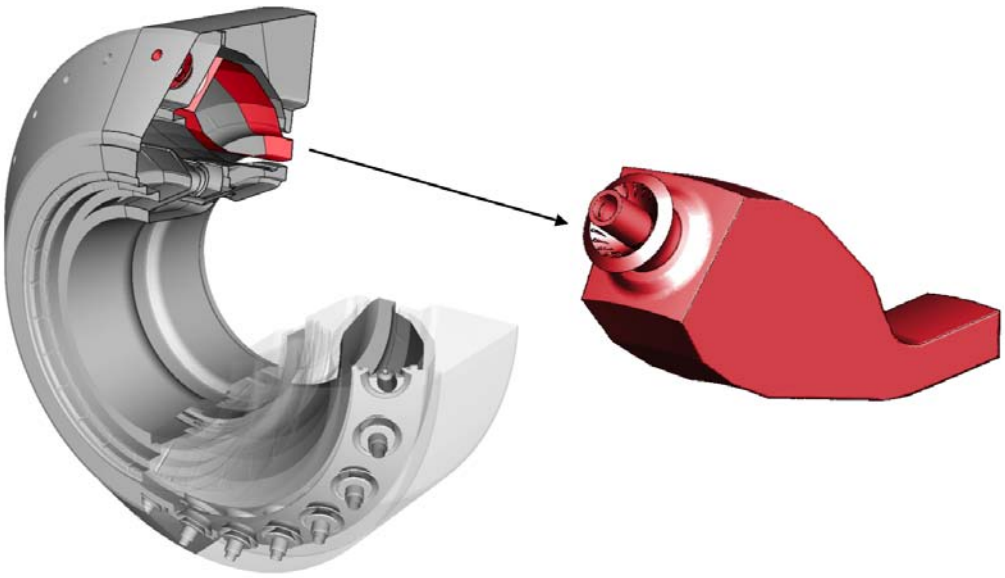

Figure 6.1: 3D view (left) of the annular combustion chamber. One sector (right) will be used for LES here.

ple, to help flame stabilization a pilot methane injection is added in the axial part. Cooling air inlets are also present to shield the burner outlet (CBO and NBO) and the lance seen on Fig. 6.2. In the real gas turbine, NBO and CBO are sometimes mixed (4 NBO and 20 CBO) to control instabilities. The computational domain retained for our computations is one section of the annular combustion chamber and is highlighted in Fig. 6.1.

Today, most LES simulations of annular combustion chambers are for computa-

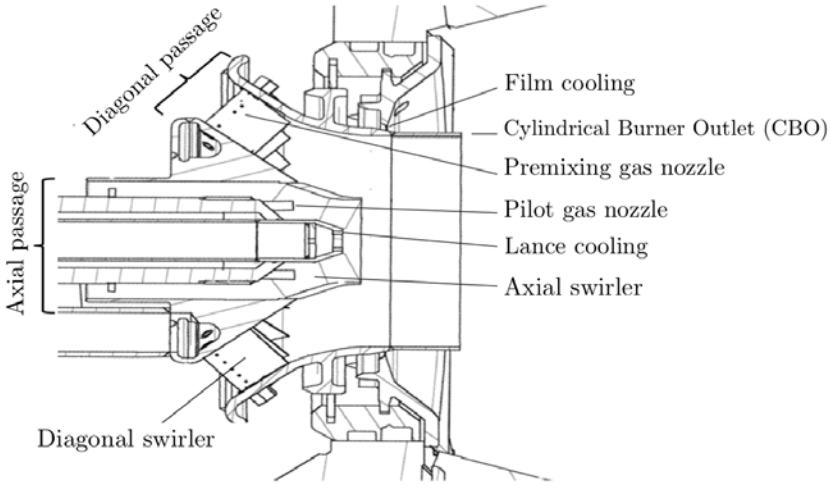

Figure 6.2: Burner details

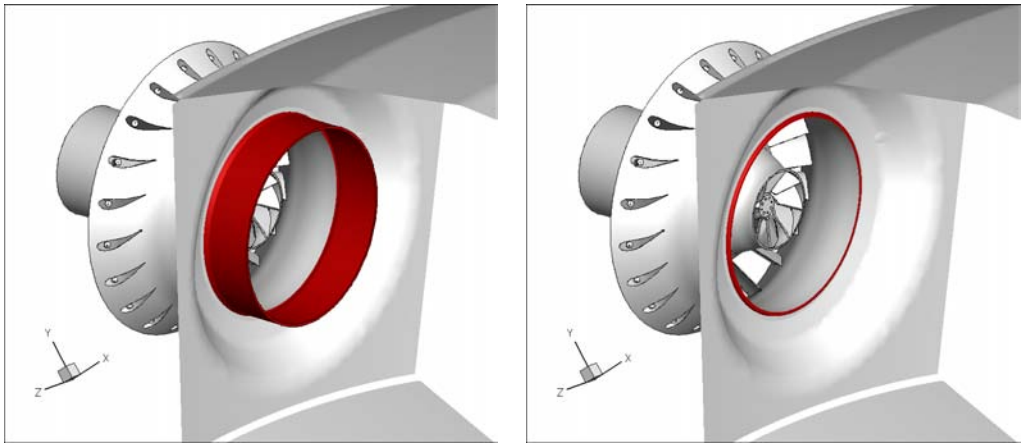

(a) CBO (b) NBO

Figure 6.3: Burner outlet details.

tional cost reasons performed on only one sector of the combustion chamber except for the recent studies of Staffelbach [165], Wolf [188] or Fureby [48]. Such 360° simulations are still impossible for the present turbine where the Reynolds number

exceeds 1.000.000 (based on the machine diameter) and thus this work is limited to single sector computations. These LES in a single sector can be used to study unstable acoustic modes in the full machine (24 sectors) by using an additional assumption called ISAAC (Independence Sector Assumption in Annular Combustors). This approach was first introduced by Staffelbach et al. [165] and Sensiau et al. [158] and states that the heat release fluctuations in one sector of an annular chamber are only due to fluctuating mass flow rates in the burner of the same sector and that they are not interfering with neighbouring flames. This means that unsteady combustion is only driven by the fluctuating longitudinal velocity through each burner. Although this assumption is not satisfied when flame injectors are close to each other and flame/flame interactions are important[1], the combustion chamber and burner investigated by Staffelbach et al. [165] is of similar type as the configuration considered throughout this part and the ISAAC approach is considered satisfied. The ISAAC assumption is also used implicitly in all network approaches developed recently for combustion instabilities by the Siemens group for example [17, 87, 88] or by Cambridge [169] or EM2C [13, 114].

6.1.2 Experimental test rig for cold flow validation

Large-Eddy Simulation was first validated against experiments performed on a test rig under atmospheric pressure. In this specific laboratory experiment installed in Italy (Ansaldo Genoa), a single sector burner is mounted on a octagonal combustion chamber as shown in Fig. 6.4. Only air is injected through the diagonal and axial swirler and the results are used only here to validate pressure losses and velocity profiles. Tests have only been performed for the configuration with CBO. Measurements provide velocity components just downstream of the CBO and pressure loss through the burner.

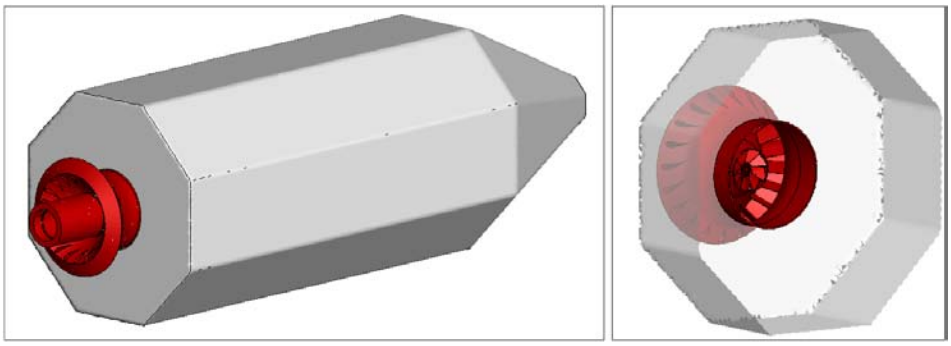

Figure 6.4: The single sector setup is installed in Italy on a laboratory chamber.

[1] There are many examples where the ISAAC assumption is not valid: e.g. rocket engines are known to be dominated by flame/flame interactions [19, 31, 108, 126]

6.2 Description of the numerical setup

6.2.1 Computational mesh

6.2.1.1 Real gas turbine

The grid for the experimental test rig is three-dimensional and fully unstructured with 1.921.370 nodes and 10.472.070 tetrahedral elements for the CBO case and of 1.918.679 nodes and 10.485.031 tetrahedral elements of the NBO case respectively. The time step is approx. $9 \cdot 10^{-8} s$ with the acoustic CFL number being fixed at 0.7 for both cases. The mesh is refined in the flame region and in the vicinity of the fuel injection and progressively coarsened up to the chamber exit. Figure 6.5 shows the meshes on the middle cut plane for both cases and Table 6.1 summarizes its main parameters.

Parameter	CBO case	NBO case
Number of cells	10.472.070	10.485.031
Number of nodes	1.921.370	1.918.679
Smallest cell volume	$2.52071 \cdot 10^{-13} m^3$	$8.31987 \cdot 10^{-13} m^3$
Time step (CFL=0.7)	$8.702 \cdot 10^{-8} s$	$8.742 \cdot 10^{-8} s$

Table 6.1: Parameters describing the mesh for the real gas turbine.

6.2.1.2 Experimental test rig of Genoa

LES were performed on a three-dimensional fully unstructured mesh composed of 895.196 nodes and 4.655.880 tetrahedral elements. The time step is approx. $1.2 \cdot 10^{-7} s$ with the acoustic CFL number also being fixed at 0.7. The mesh is kept similar in the burner for the real gas turbine and the experimental test rig in order to validate it in terms of pressure loss and velocity components. Figure 6.6 shows the mesh on the middle cut plane for the whole domain and a zoom into the burner region in 2D. Table 6.2 summarizes its main parameters.

Parameter	CBO case
Number of cells	4.655.880
Number of nodes	895.196
Smallest cell volume	$4.918 \cdot 10^{-13} m^3$
Time step (CFL=0.7)	$1.18 \cdot 10^{-7} s$

Table 6.2: Parameters describing the grid for the experimental test rig.

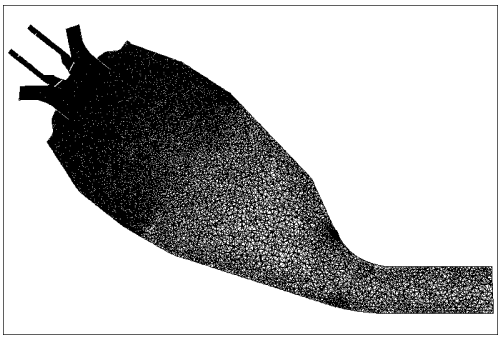

(a) CBO: Full view

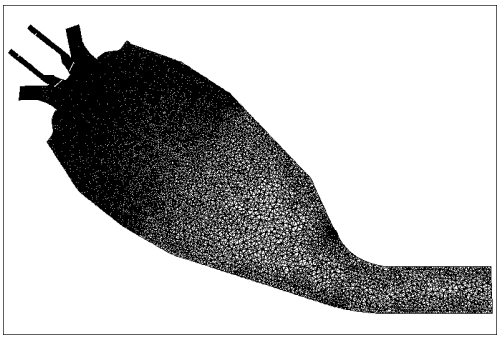

(b) NBO: Full view

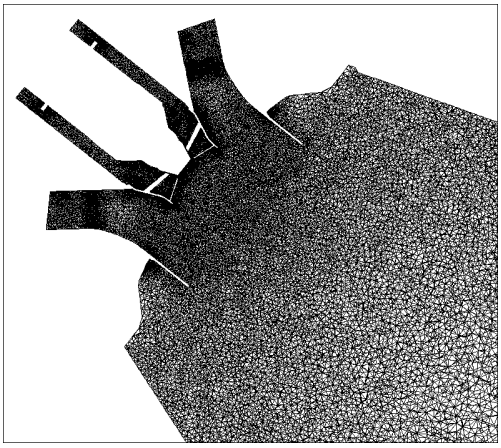

(c) CBO: Zoom

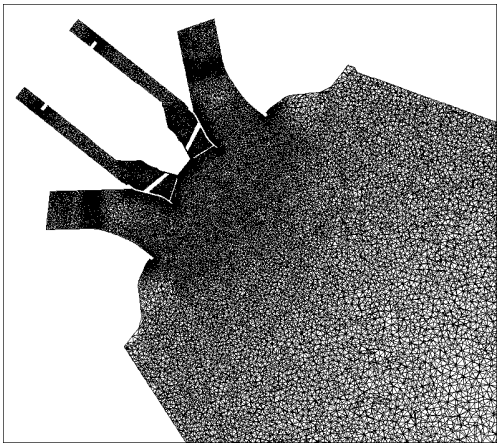

(d) NBO: Zoom

Figure 6.5: Mesh used for the real gas turbine.

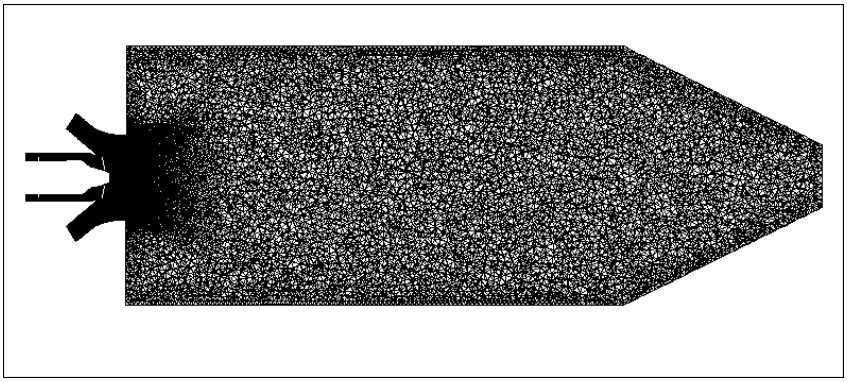

(a) Full view

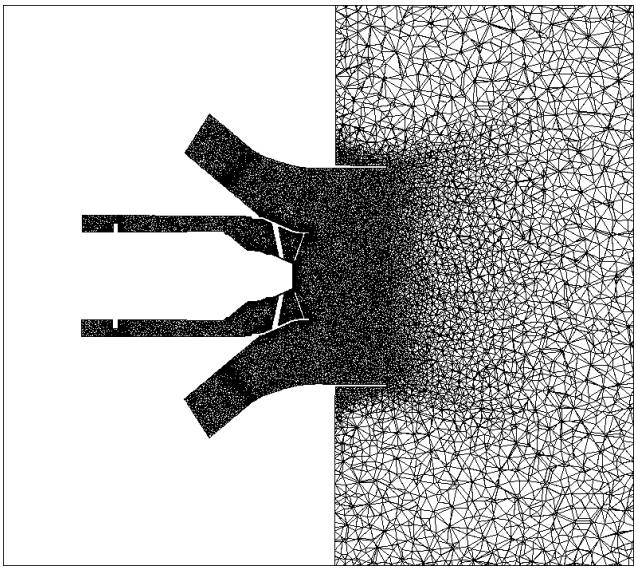

(b) Zoom

Figure 6.6: Mesh used for the experimental test rig.

6.2.2 Boundary conditions

6.2.2.1 Real gas turbine

In addition to the investigation of the CBOs influence on flame dynamics and stabilisation, two different operating points (corresponding to two different powers) are analyzed as well. The first case corresponds to an ambient temperature of +15° C, whereas the second case (-15° C) is at ambient conditions of -15° C. The four investigated cases and the abbreviations used in the following are listed in Table 6.4. Note that for confidentiality reasons, no further detail of the operating points is given. Inlet and outlet boundary conditions are imposed through the non-reflecting Navier-

	Operating mode	Geometry
+15CBO	Ambient temperature: +15° C	Cylindrical Burner Outlet (CBO)
+15NBO	Ambient temperature: +15° C	Normal Burner Outlet (NBO)
-15CBO	Ambient temperature: -15° C	Cylindrical Burner Outlet (CBO)
-15NBO	Ambient temperature: -15° C	Normal Burner Outlet (NBO)

Table 6.3: Investigated cases

Stokes Characteristic Boundary Condition (NSCBC) formulation [125] to control acoustic reflection. At the inlet, the velocity component normal to the boundary patch is imposed and a pressure outlet is used. The outlet of the computational domain is elongated compared to the original geometry to avoid recirculation at the outlet patch, Fig. 6.5. All walls are modeled using a logarithmic wall-law condition and side boundaries of the combustion chamber are considered axi-periodic. The Reynolds number of the two passages are 1.500.000 for the diagonal and 100.000 for the axial swirler.

Pulsation procedure The present burner offers several possibilities to introduce velocity fluctuations. Here a harmonic perturbation is introduced through the diagonal inlet using the inlet wave modulation method proposed by Kaufmann [78] and the perturbation of the heat release rate is measured. An amplitude of 6 percent of the mean inlet velocity is chosen, to be in the linear regime. Both harmonic and broadband forcing will be used (Section 3.5). Note that tests have been performed to investigate the effect of pulsating the diagonal or axial passages separately. Pulsating only the diagonal swirler results in the same flame response as pulsating both axial and diagonal passages, so only the latter is discussed here.

6.2.2.2 Experimental test rig

The inlet and outlet boundary conditions follow the NSCBC formulation [125]. At both inlets the mass flow rate normal to the patch is imposed and a pressure outlet

is used. All wall boundaries are modeled through a logarithmic wall-law condition. The Reynolds numbers are 250.000 for the diagonal and 25.000 for the axial passage.

6.2.3 Numerical parameters

6.2.3.1 Real gas turbine

The numerical parameters used for the simulations are shortly described in this section as they were already discussed in chapter 3. A second-order finite element scheme (Lax-Wendroff) is used for both time and space advancement [57, 94]. The Sub-grid stress tensor is modeled by a classical Smagorinsky approach [161]. The artificial viscosity is detected using the Colin sensor [25, 27].

Finding a proper chemical scheme for these flames is difficult because two flame zones are expected: (1) stoichiometric diffusion flames in front of the lance and (2) lean premixed flames for the mixture provided by the diagonal swirler (Fig. 6.2). For the latter flames, combustion of mixtures around $\phi = 0.4$ to 0.6 and $T = 700$ K are expected. For such flames, large uncertainties exist both in experimental and kinetics data. Figure 6.7 shows recent results for the laminar flame speed of CH_4/air flames at $T = 300$ K and 1 bar [12, 28, 47, 52, 137, 155, 180, 181]. Most data converge to similar values for stoichiometric flames, but larger discrepancies occur for leaner mixtures. This means that even under atmospheric conditions uncertainties for chemical schemes exist. These uncertainties increase with pressure. In the present work, chemistry is modelled using a two-step mechanism

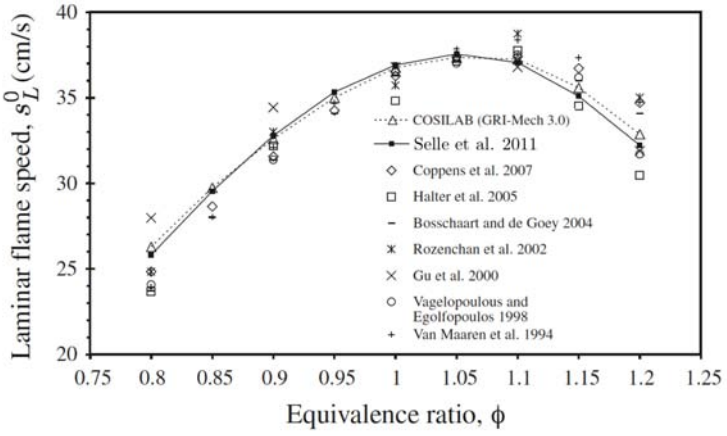

Figure 6.7: Laminar flame speed s_L^0 vs. equivalence ratio ϕ at 300 K and 1 bar [155].

for methane/air flames (BFER) [44–46] with two reactions and six species (CH_4, O_2, CO_2, CO, H_2O and N_2). The first reaction is irreversible and controls the oxydation of CH_4 while the second reaction is reversible leading to an equilibrium between CO and CO_2 [153]. The considered combustor operates at high pressure: the laminar flame speed decreases compared to atmospheric conditions as shown in Fig. 6.8a for BFER and GRI-mech [47]. Furthermore, the compressor outlet

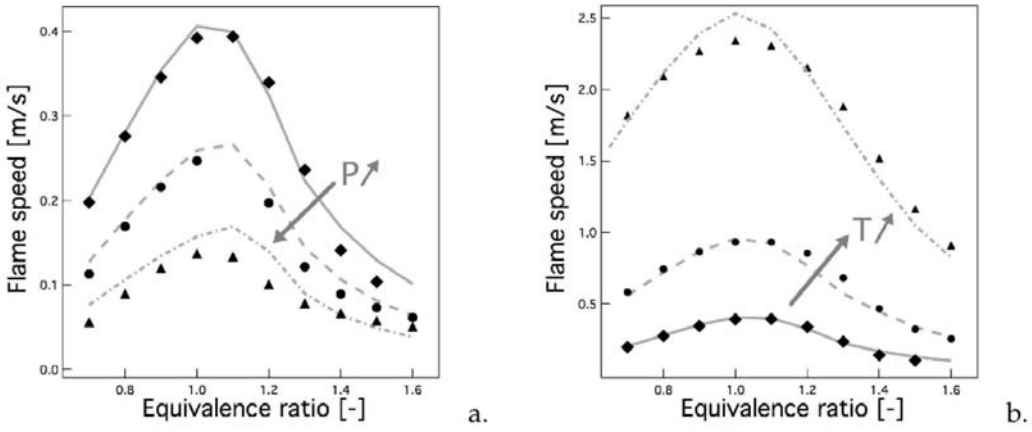

Figure 6.8: Comparison between GRI-meach and BFER scheme for (a) different pressures $p = 1, 3, 10atm$ at $T = 300K$ and (b)different temperatures $T = 300, 500, 700K$ at $p = 1atm$ [45].

temperature is higher than at atmospheric conditions leading to an increase of the laminar flame speed (Fig. 6.8b). However, measurements of the laminar flame speed at elevated pressure (and temperature) are difficult: premixed laminar flames become susceptible to thermal and hydrodynamic instabilities [23, 83] so that up to now just a few measurements have been performed in the range of the operating conditions considered here [182]. A comparison between GRI-mech and the BFER scheme is shown in Fig. 6.9 and Fig. 6.10 for maximum temperature and laminar flame speed respectively over equivalence ratio at the gas turbine operating point (approx. $T > 500$K and $p > 15$ bar). The temperatures correspond well between both mechanisms in the lean regime, slight differences occur around stoichiometry and the results diverge at high equivalence ratios. Since such rich flames are not expected here, this is not a problem. Laminar flame speeds are predicted by BFER to be higher as in the GRI-mech scheme for lean mixtures (until $\phi = 0.7$), whereas for $\phi > 0.7$ GRI-mech predicts higher flame speeds. Latest results of Varea [182] indicate that GRI-Mech underpredicts the laminar flame speed at high pressure in the lean regime. Since the mixture in the considered configuration is predominantly lean and in the absence of detailed experimental data which also show significant discrepancies even at atmospheric conditions (Fig. 6.7), the BFER scheme is the better choice here and is used for the following computations without modifications. It is important to remember however that the lack of reliable kinetics and experimental data for lean CH_4/air flames at high pressure could be a weak point of the present LES.

To capture flame/turbulence interactions, the dynamic thickened flame model is used [25, 27, 98]. Sub-gridscale wrinkling and interactions are modeled using an efficiency function [25, 27, 98] which is well suited for all flames studied here which all correspond to the premixed or partially premixed regime. The numerical parameters

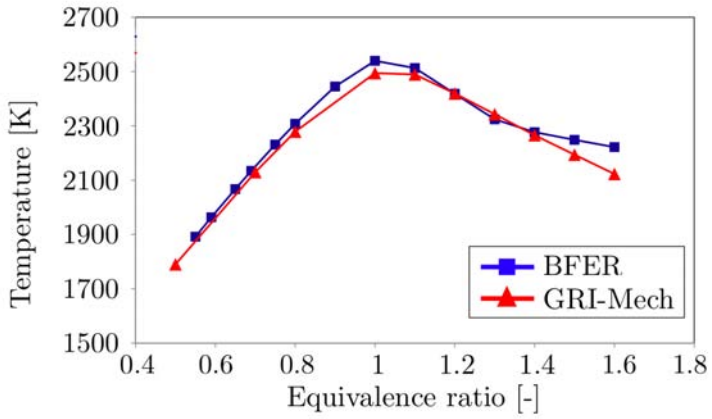

Figure 6.9: Temperature over equivalence ratio for GRI-Mech and BFER for CH_4/air flames at $T = 700$ K and $p = 17$ bar.

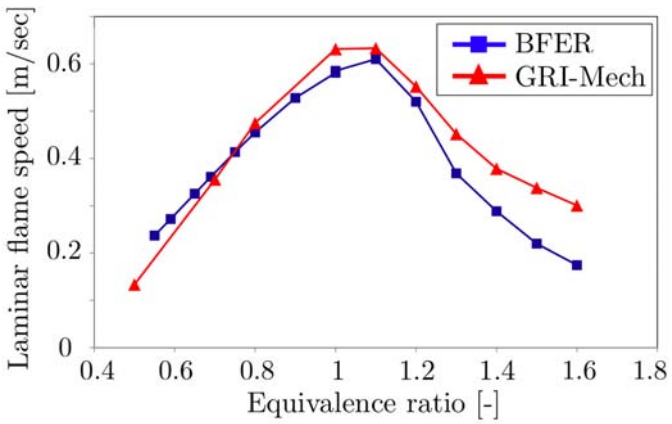

Figure 6.10: Laminar flame speed over equivalence ratio for GRI-Mech and BFER for CH_4/air flames at $T = 700$ K and $p = 17$ bar.

are kept constant for all considered cases to reduce possible sources of variability and facilitate comparisons (Table 6.4).

Numerical scheme	Lax-Wendroff
Sub-grid scale model	Smagorinsky model
Artificial viscosity model	Colin Sensor ($\varepsilon_2 = 0.2$; $\varepsilon_4 = 0.01$)
Chemistry	Two-step BFER
Flame/turbulence interaction	Thickened flame model

Table 6.4: Numerical parameters used for the real gas turbine simulation.

6.2.3.2 Experimental test rig

For the experimental test rig, where only cold flow cases are investigated, the same parameters are used as above to minimize deviations which could be caused by different models. The second order scheme Lax-Wendroff is used for time and space advancement [57, 94] and the Sub-grid stress tensor is modeled by a classical Smagorinsky approach [161]. The artificial viscosity is detected using the Colin sensor [25, 27]. Obviously, no models for chemistry or flame/turbulence interactions are needed since only cold flow cases are computed (Table 6.5).

Numerical scheme	Lax-Wendroff
Sub-grid scale model	Smagorinsky model
Artificial viscosity model	Colin Sensor ($\varepsilon_2 = 0.2$; $\varepsilon_4 = 0.01$)

Table 6.5: Numerical parameters used for the experimental non reacting test rig simulation of Genoa.

Chapter 7

Numerical results for the unforced flame

Contents

In this chapter LES is first validated against experiments on the atmospheric test rig of Ansaldo (Genoa): velocity components and pressure loss through the burner for the non-reacting flow field are compared to experiments (Section 7.1). Then the hot (high pressure) cases are discussed (Section 7.2) and the different operating conditions and burner outlet configurations will be analyzed and their differences will be presented. Furthermore flame anchoring is discussed (Section 7.3 and Section 7.4). Finally, the quality of the LES is analyzed (Section 7.5).

7.1 Non-reacting flow fields

7.1.1 Instantaneous flow characteristics

In the absence of experimental results for the high pressure combustion chamber, LES was validated on the atmospheric test rig where experiments have been carried

out. The Reynolds number in the combustion chamber is of order of 1.000.000. For such high Reynolds number flows, LES is difficult and validation mandatory. Note also that performing experimental measurements is also much more difficult than in lab-scale set-ups. PIV measurements at the cut plane (Fig. 6.4) just downstream of the burner outlet allow the comparison of different velocity components. Furthermore the pressure drop through the burner will be evaluated and compared against pressure measurements obtained in Genoa.

Swirling flows feature several types of vortex breakdown [106] and can lead to the formation of so-called precessing vortex cores (PVC). The PVC is a well known large scale hydrodynamic structure occurring at high Reynolds and swirl number flows [51, 53, 63, 135, 136, 153, 157]. It is characterized by a regular rotation of a spiral structure around the geometrical axis of the combustion chamber and is shown for the considered configuration in Fig. 7.1 for one cycle. The frequency predicted by LES matches the experiments and is 120 Hz corresponding to a Strouhal $St = fD/u_{bulk} = 1.3$ based on the burner diameter D and the bulk velocity u_{bulk}. The present vortex breakdown results from a highly swirled flow and leads in combination with the sudden geometrical expansion at the combustion chamber inlet to a recirculation of the flow. An outer and a inner recirculation zone is formed and interacts with the hydrodynamic instability of the PVC. The resulting averaged mean flow field is shown in the following.

7.1.2 Mean flow fields

The PVC influences the mean axial velocity field shown in Fig. 7.2 on the middle cut plane. For this swirler with multiple passages, the flow topology is more complicated than in usual swirling flows. Here, two recirculation zones are found on the chamber axis. As indicated by the zero velocity iso-lines, negative velocity occurs first close to the lance followed by a region of positive velocity and finally by the main inner recirculation zone. The positive velocity region results form the PVC whose low pressure vortex core sucks the flow in the direction of the geometrical axis and dependent on their position along the axis, either the upper flow of the diagonal swirler is deviated or the lower part so that the inner recirculation zone finally underlies strong variations. In the averaged field this is seen as a positive axial velocity region. Comparison to the PIV experiments in Fig. 7.4 for the axial velocity on the measurement plane (Fig. 7.3) just in front of the burner outlet shows differences: in the center LES predicts low positive values but PIV show low negative axial velocities. From the center to the CBO in radial direction, the axial velocity increases significantly with a similar amplitude between PIV and LES. Note that experiments were not performed in the region radially outside the CBO and are marked as zero velocities. The velocities in y- and z direction are compared in Fig. 7.5 and Fig. 7.6 respectively. Experiments and LES agree: the y-velocity is maximal in magnitude on the upper and lower side with opposite sign. The same behaviour is seen for the z-velocity where the maximal magnitude appears on the

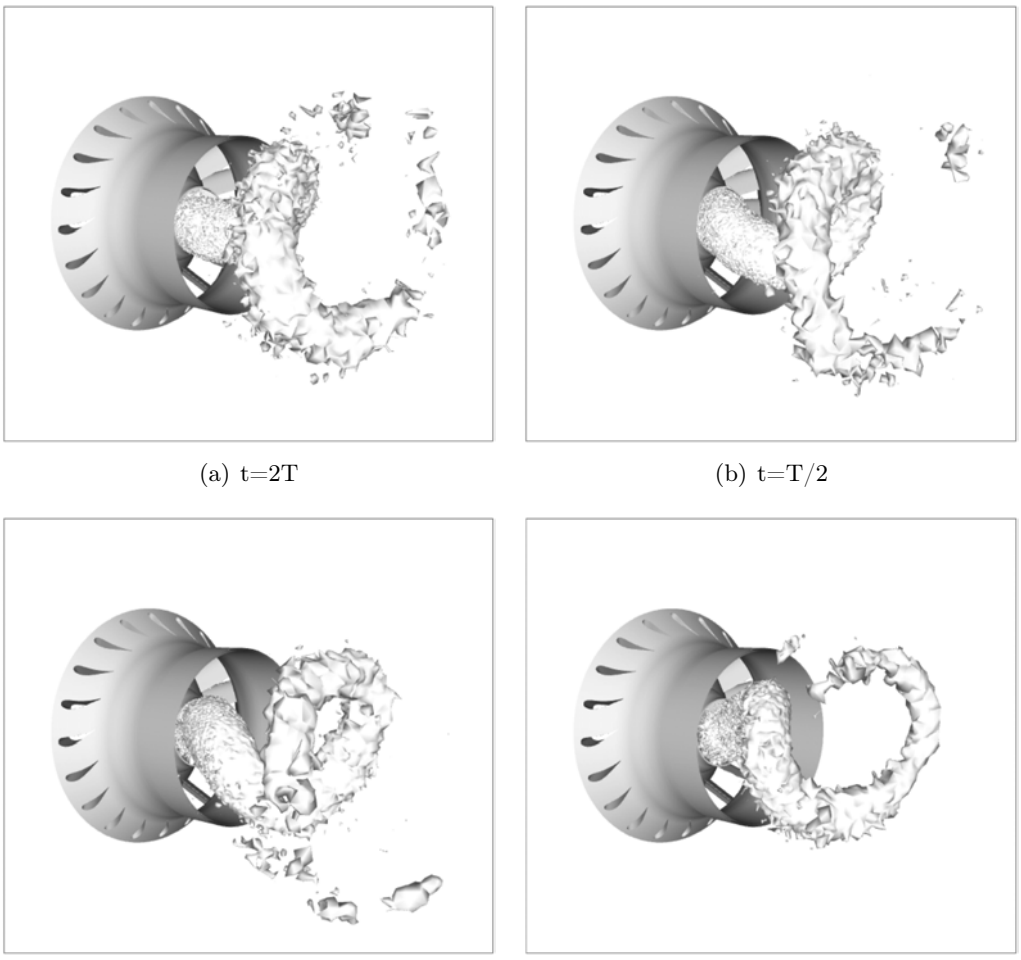

(a) t=2T (b) t=T/2

(c) t=T (d) t=3T/2

Figure 7.1: Precessing vortex core (PVC) in cold flow LES.

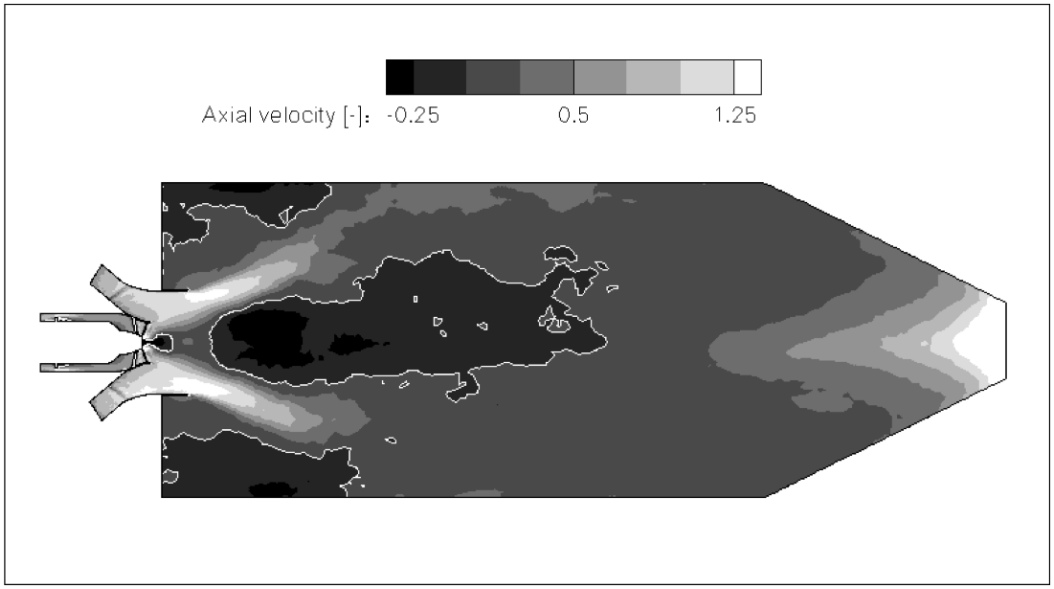

Figure 7.2: Mean axial velocity field on middle cut plane. The white line corresponds to zero axial velocity.

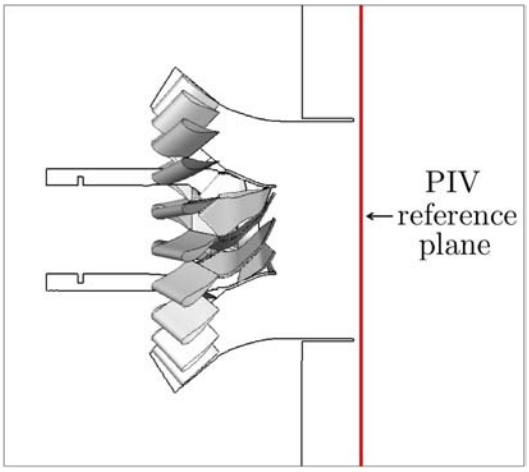

Figure 7.3: Reference plane location.

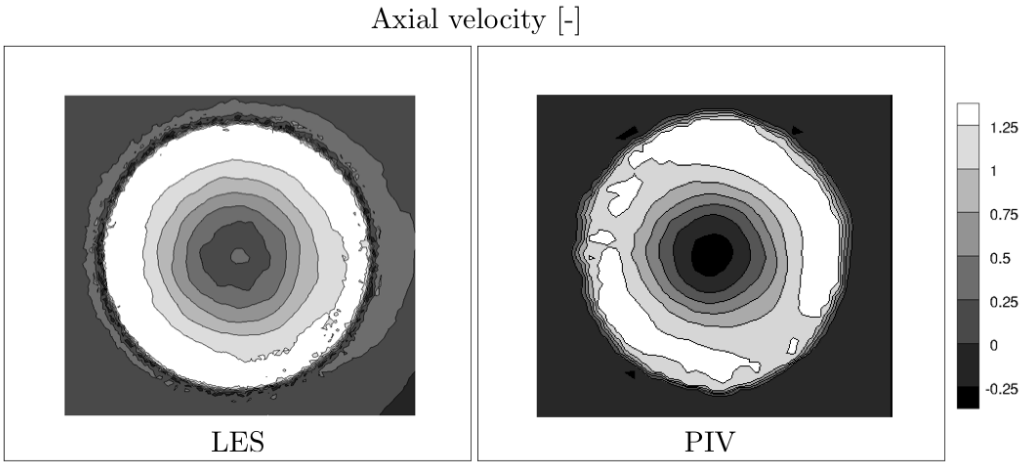

Figure 7.4: Axial-velocity: comparison PIV and LES.

right and left side. The positions of peaks and zero velocities are in good agreement for both velocity components. Furthermore, similar tangential velocity fields are

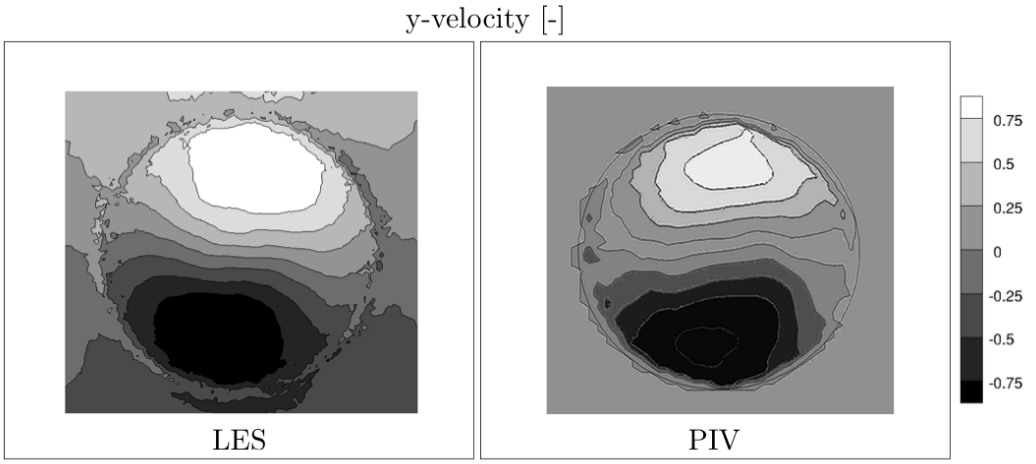

Figure 7.5: y-velocity: comparison PIV and LES.

found (Fig. 7.7). The lowest velocity is found in the center and increases in the radial direction. LES slightly under predicts the magnitude in the outer region and predicts an almost uniform distribution at fixed radius whereas PIV shows a higher velocity magnitude in the top and bottom regions.

7.1.3 Pressure drop

Another possibility to evaluate the quality of LES is to compare the pressure drop through the burner against measurements. A convenient way to quantify pressure

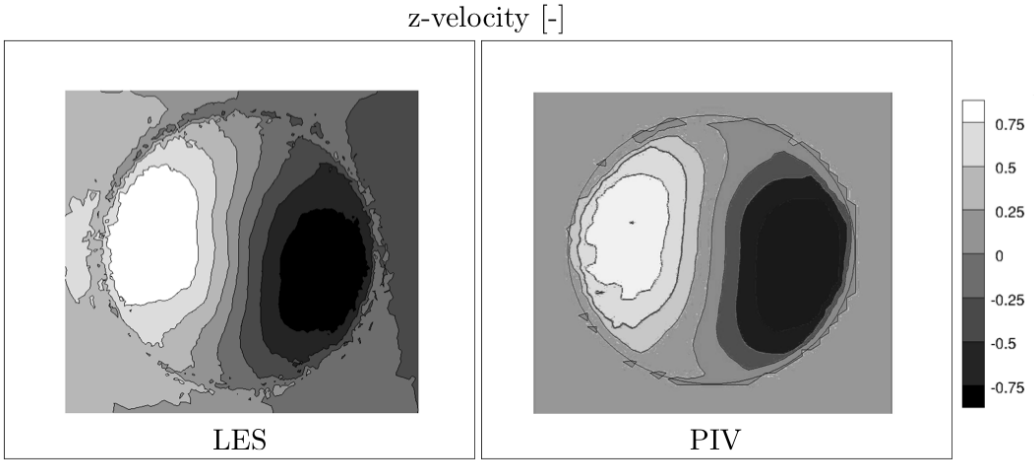

Figure 7.6: z-velocity: comparison PIV and LES.

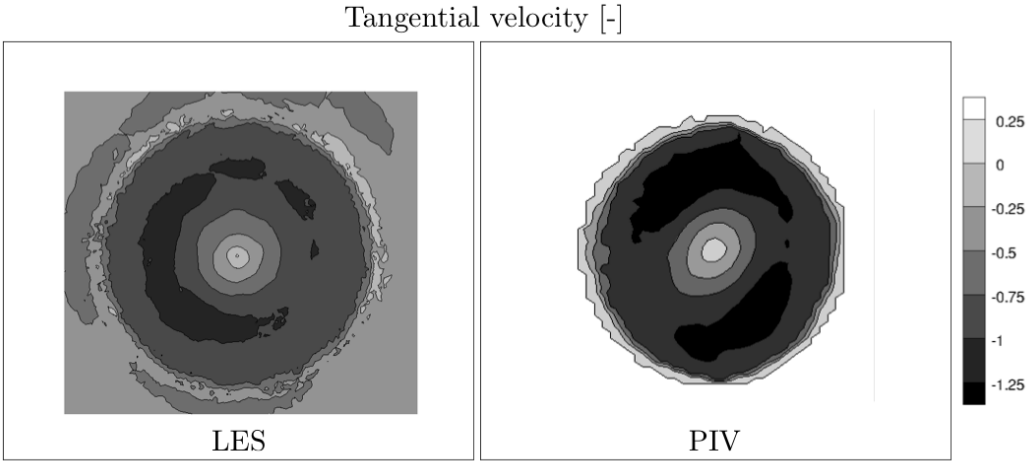

Figure 7.7: Tangential velocity: comparison PIV and LES.

losses is to introduce an equivalent section S_e defined by

$$S_e = \frac{\dot{m}}{\sqrt{2(p_{in} - p_c)\rho}} \tag{7.1}$$

where p_{in} and p_c denote the total pressure at the inlet of the considered passage and in the chamber respectively. The averaged total pressure field (normalized by the mean value in the chamber) is given in Fig. 7.8 and shows a low pressure region in front of the lance due to the rotating PVC. The chamber pressure is taken for three different points: P1 to P3 (Fig. 7.8). For those points the static pressure is almost identical to the total pressure as they are located in low speed zones. The inlet pressure is calculated by mass weighted averaging the corresponding inlet patch for both diagonal and axial swirlers. The deviation of LES results from the experimental values are listed in Table 7.1. The static pressure in the chamber does not change much so that all points give similar results: the equivalent section of the diagonal swirler agrees well with the experiments and only slightly over predicts the experimental results (2.1% to 3.2%). Differences occur in the axial swirler where the LES under predicts S_e by 13% in all points. Note that S_e is not the true geometrical minimum surface in each passage S_g. They differ through a discharge coefficient C_d given by $C_d = S_e/S_g$.

The pressure drop is predominantly caused by the loss of dynamic pressure due to the flow expansion at the burner exit and the friction in the boundary layer. The LES is performed using a logarithmic wall-law model for computational cost reasons and the agreement with experiments is reasonable. The experience of Cerfacs for smaller swirlers is that pressure losses are usually over predicted by 30 to 50 %, showing that the present geometry is somewhat easier than the aero engine swirlers used by Snecma or Turbomeca.

	Point 1	Point 2	Point 3
Diagonal swirler	102.6%	102.1%	103.2%
Axial swirler	87.0%	87.0%	87.0%

Table 7.1: Ratio S_e^{LES}/S_e^{Exp} of the computed equivalent section to the experimental value.

7.1.4 Concluding remarks

In this section the cold flow characteristics obtained by LES were evaluated against experiments under atmospheric conditions and a good agreement was found considering that this is a high Reynolds number flow for which LES as well as measurements are difficult. A PVC appears in both simulation and test rig and the frequency is correctly predicted corresponding to a Strouhal number of 1.3. The

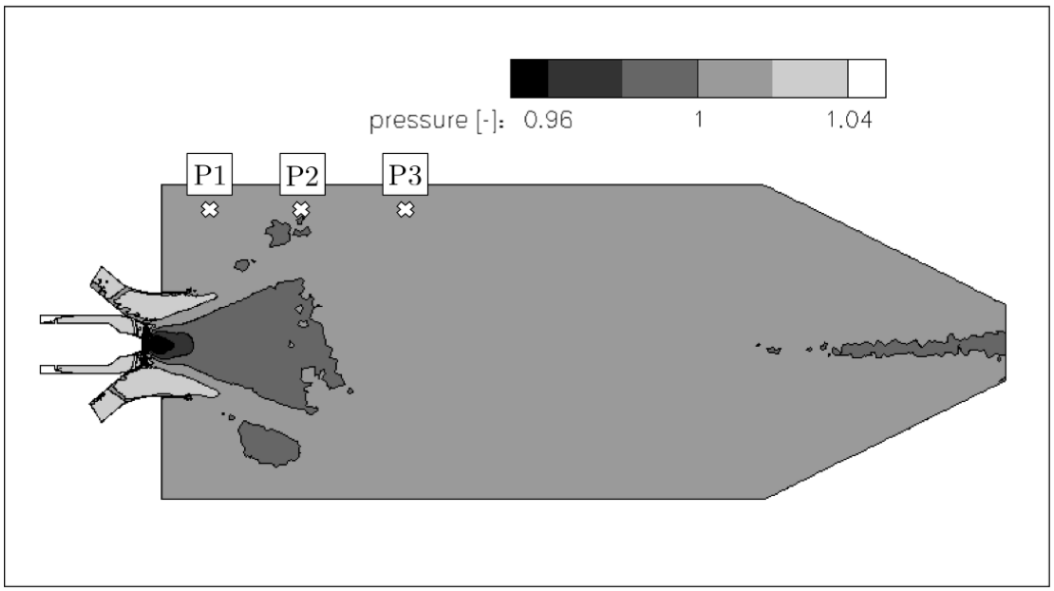

Figure 7.8: Total pressure field on middle cut plane.

mean velocity fields are similar in terms of magnitude and position of extrema, but slight differences are found for the extent of the central recirculation zone in the axial velocities. The differences in radial velocities are explained by errors in the measurements since all other velocities agree well and the radial velocity results from the y- and z-velocity components. Furthermore a reasonable agreement is found for the pressure drop through the axial and diagonal swirler although the wall boundary layer is not resolved and a logarithmic wall-law model is used in the LES. It is concluded that the LES is of good quality and represents the flow field dynamics correctly. It can therefore be used to evaluate the reactive flow fields which are discussed in the following.

7.2 Reacting flow fields

To analyse the influence of the operating condition and of the burner outlet geometry on the flame, the averaged reacting flow fields are compared in a first step. Averaged solutions are obtained by time averaging a converged simulation over the time corresponding to five convective timescales. The convective timescale is here defined as the time the flow needs to go from the inlet to the flame front based on the bulk velocity at the entrance of the chamber. The configuration corresponds to the real gas turbine at high pressure. Four cases are studied (Table 7.2): with or without CBO (change of geometry), for inlet temperatures of −15°C and 15°C (change of operating condition).

	Operating condition	
Geometry	+15°C	−15°C
CBO	$+15CBO$	$+15NBO$
NBO	$-15CBO$	$-15NBO$

Table 7.2: Denomination of investigated cases.

7.2.1 Instantaneous flow characteristics

The rotational motion imposed by the swirler provides fuel and air mixing due to the creation of turbulence. In combination with the sudden expansion at the entrance of the combustion chamber it also leads to an increased opening of the gaseous flow compared to the cold flow of Section 7.1. Velocity gradients inside the chamber lead to a strong shear creating supplementary turbulence which is then gradually dissipated downstream. Furthermore, the rotational swirling motion from the axial swirler also causes strong shear when the flow of the diagonal passage meets the axial one and this creates additional turbulence.

Figure 7.9 shows an iso-surface of Q-criterion [68] representing vortical structures in the flow for +15CBO and +15NBO. The operating conditions at −15°C show similar behaviour and are not shown here. Highly vortical structures are present at the lance and at the entrance of the combustion chamber showing a spiral shape due to the rotating motion imposed by the swirler for both cases. In contrast to the cold flow, no PVC was detected in the reactive simulations.

7.2.2 Mean flow field

The high swirling motion of the flow is evidenced in Fig. 7.10 on the middle cut plane of the chamber in terms of normalized averaged axial velocity and zero axial velocity iso-lines for the four considered cases (Table 7.2). The velocity is normalized by the mean bulk velocity at the entrance of the chamber. The inner recirculation zone

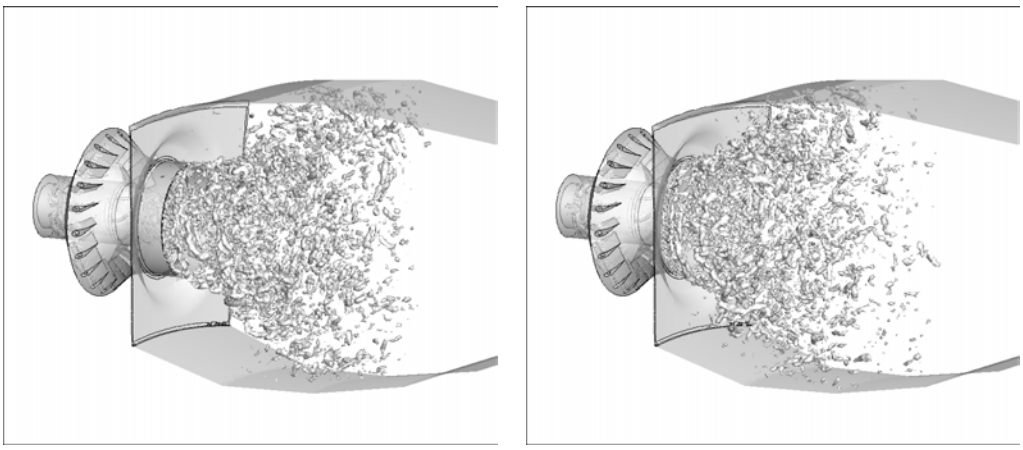

(a) +15CBO (b) +15NBO

Figure 7.9: Instantaneous iso-surface of Q-criterion ($Q = 3.4 \cdot 10^8$) in the chamber. Case +15CBO and +15NBO.

appears at the center of the chamber and is smaller in the CBO than in the NBO cases. The outer recirculation zone is present in the upper and lower corners of the combustion chamber. As observed on the cut plane in axial direction 3 (Fig. 7.11), the outer recirculation zones are not closed on the side walls where periodic boundaries are applied and are bigger for the CBO cases (Fig. 7.12): the CBO pushes the flow outwards and in axial direction. Furthermore the flow is more accelerated at the burner outlet and a higher axial velocity is observed in the CBO cases. Since the recirculation zones are responsible for the stabilization of the flames, these results suggest that the CBO which diminishes the recirculation zone, may also affect flame stabilization.

A closer look at the velocities forming the recirculation zones and acting on flame stabilization can be obtained by plotting the velocity profiles along cuts (Fig. 7.11). Axial velocity profiles are analyzed in Fig. 7.12 along the different cuts. At location 1 the position and magnitude of the inner recirculation zone are similar for all cases. At 2 the CBO prevents the flow from pushing outwards whereas the NBO flow can move unobstructed. From 3 on, the CBO leads to an acceleration of the flow (compare with Fig. 7.10). Here, the NBO flame is already located at a significantly outer position than the CBO flame. The outer recirculation zone is of lower magnitude from 5 on in the NBO case and is shorter in its extend as it vanishes earlier as seen an cut 7. The inner recirculation zones are similar for all cases and the different operating conditions behave similarly.

The magnitude of the radial velocity is defined as the dot product of the velocity vector in the radial direction:

$$U_{rad} = \frac{v \cdot r}{|r|} \tag{7.2}$$

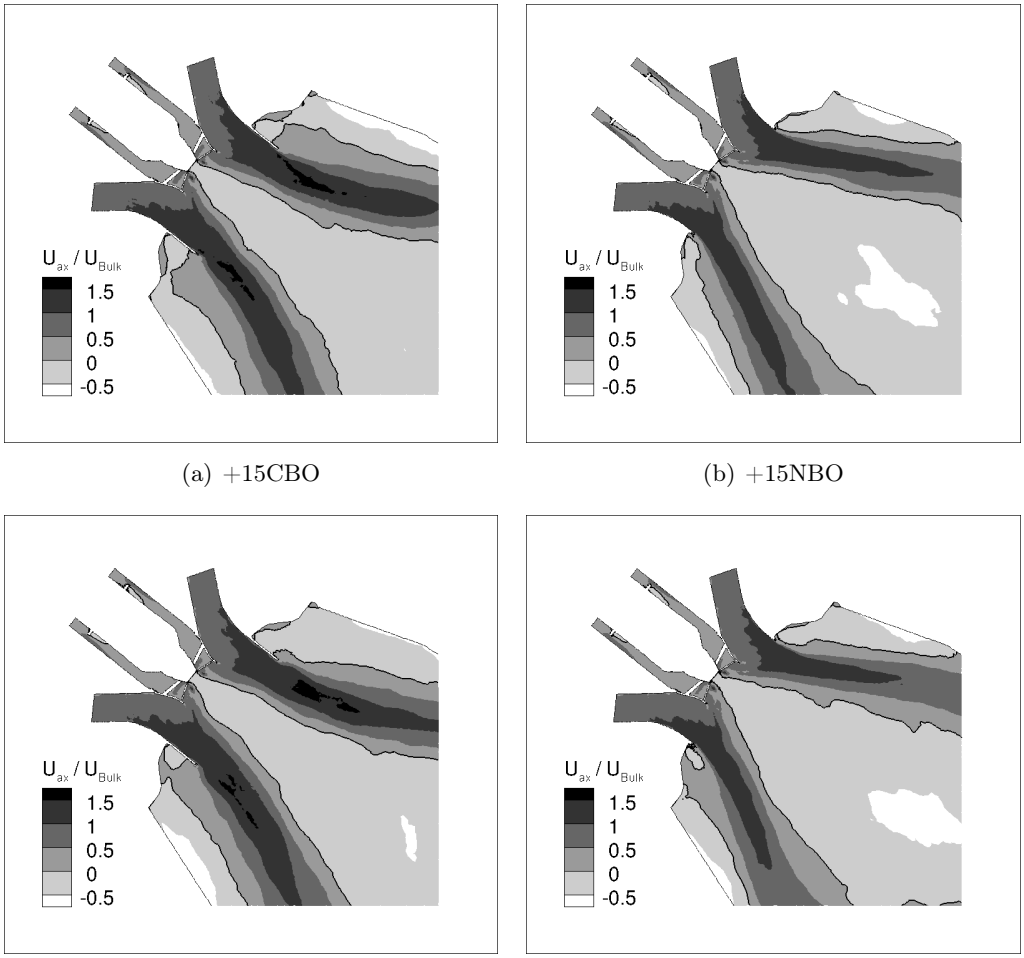

(a) +15CBO (b) +15NBO

(c) -15CBO (d) -15NBO

Figure 7.10: Normalized axial velocity field on middle cut plane and iso-line of zero axial velocity (solid black line).

and is shown in Fig. 7.13. It is normalized by the mean bulk velocity. Again a difference between the operating conditions (-15°C and +15°C) is hardly visible. The magnitude of the peaks is slightly higher in the NBO cases at cut 1 with the positions being similar. At 2 the NBO cases develop a distinct peak at the height of the burner outlet and with about twice the velocity of the CBO cases. The CBO geometries develop a peak further in the inner region at cut 3.

Tangential velocity fields allow a further insight into the rotational motion of the fluid and its magnitude is shown in Fig. 7.14. It is calculated as the cross product of the velocity vector in the radial direction:

$$U_{tang} = \frac{v \times r}{|r|}. \tag{7.3}$$

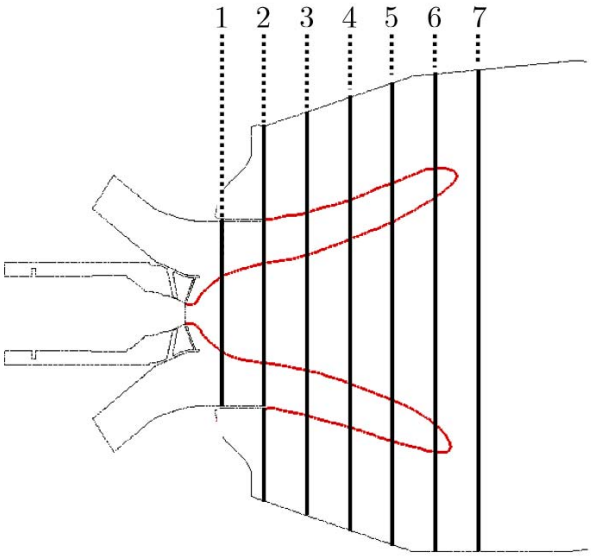

Figure 7.11: Planes for profile extraction

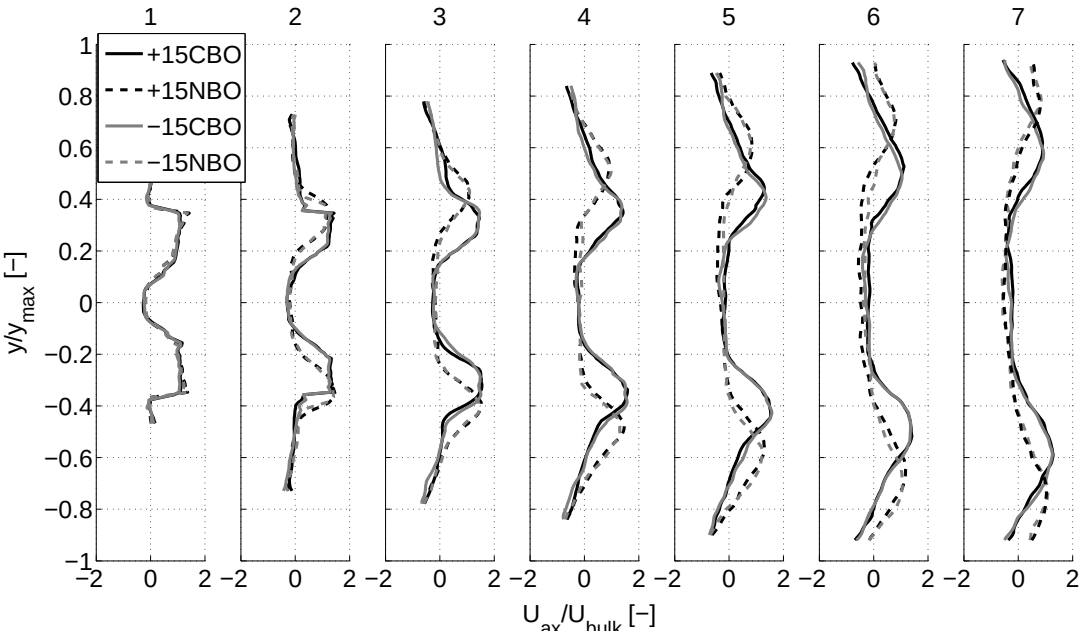

Figure 7.12: Axial velocity profiles for +15CBO, +15NBO, -15CBO, -15NBO

All flames behave similarly in terms of tangential velocity close to the lance where the peak shows a only slightly decreasing magnitude to outer direction. As the flame opens in the NBO cases, the peaks is further away from the axis but with similar magnitude compared to the CBO cases. No distinctive differences can be found between the operating conditions +15 and -15. The interaction of those different velocity components control the flame and are directly responsible for its stabilization and dynamics.

Figure 7.15 shows the three-dimensional flame surface obtained with a temperature iso-surface ($T/T_{mean} = 1.3$) and coloured by the axial velocity for the four investigated cases. The negative axial velocities from the inner recirculation zones (Fig. 7.10) anchor all flames at the lance and in combination with the outer recirculation zones the flames attach at the burner outlet. Nevertheless, the different shapes of the recirculation zones and the associated velocity profiles affect the flames directly. The CBO elongates and narrows the flame for both operating conditions while the NBO flame is distinctively shorter and more open. Although the outer recirculation zones are only present in the upper and lower walls of the combustion chamber, the flames are closed and completely attached to the burner outlet. In all cases the lowest velocity appears at the burner outlet with increasing velocities up to the flame tip. The temperature field on the middle cut plane (Fig. 7.16) reveals that the highest temperature occurs at the lance where pure methane stabilizes the flame through the pilot injection. The averaged flame shapes and axial velocity fields are similar for the two operating conditions.

The temperature profiles reveal more details about the flame shapes (Fig. 7.17). Similar normalized temperature profiles between the operating conditions are found. The burner outlet geometry has a great impact: close to the lance (profile 1) all four profiles are similar and show the highest temperature being twice the mean value which is due to the pilot injection where a high local equivalence ratio is present. At cut 2 the NBO flame is significantly more open showing the same temperature magnitude as the CBO case. Downstream of location 3, minima have a higher temperature for the NBO geometry because the flame is shorter. All cases reach a similar temperature in the burnt gases and are axi-symmetric.

To obtain further insight on the mechanisms at play insuring flame stabilization, the fluctuations of temperature in Fig. 7.18 are investigated. Both operating conditions (-15°C and +15°C) show similar fluctuations. In both burner configurations two distinct peaks appear and merge downstream. Since the NBO flame is shorter, the fluctuations vanish earlier and are higher close to the lance at cut 2.

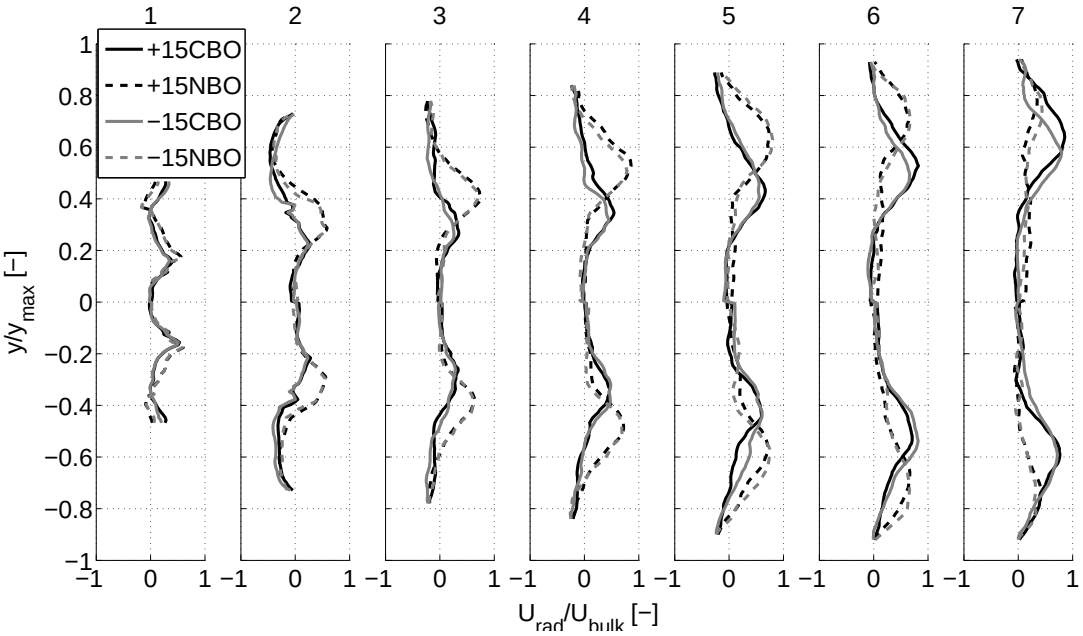

Figure 7.13: Radial velocity profiles for +15CBO, +15NBO, -15CBO, -15NBO

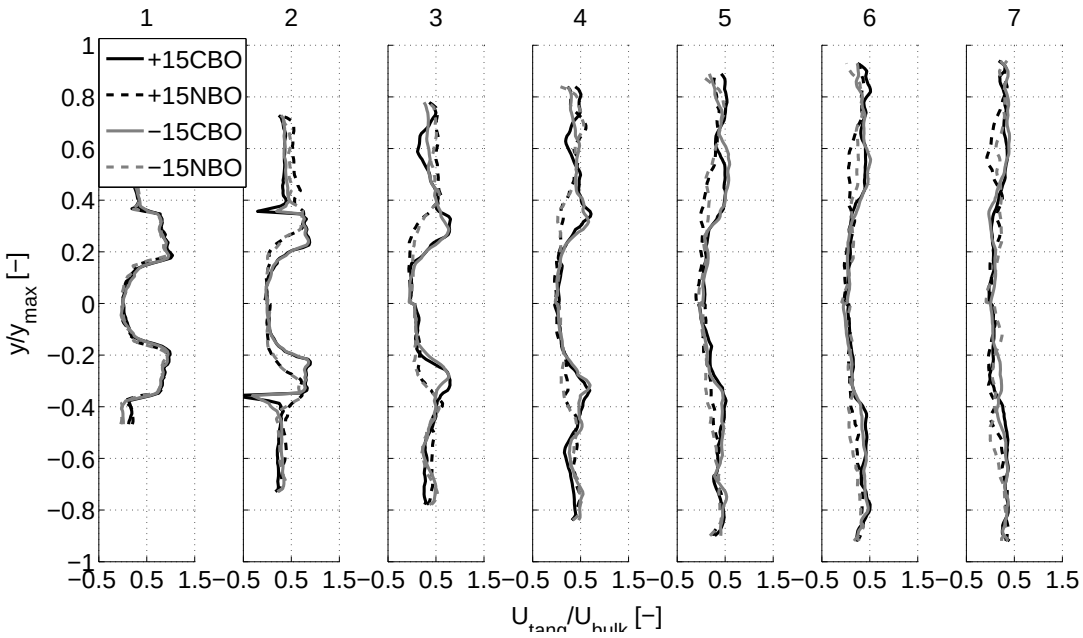

Figure 7.14: Tangential velocity profiles for +15CBO, +15NBO, -15CBO, -15NBO

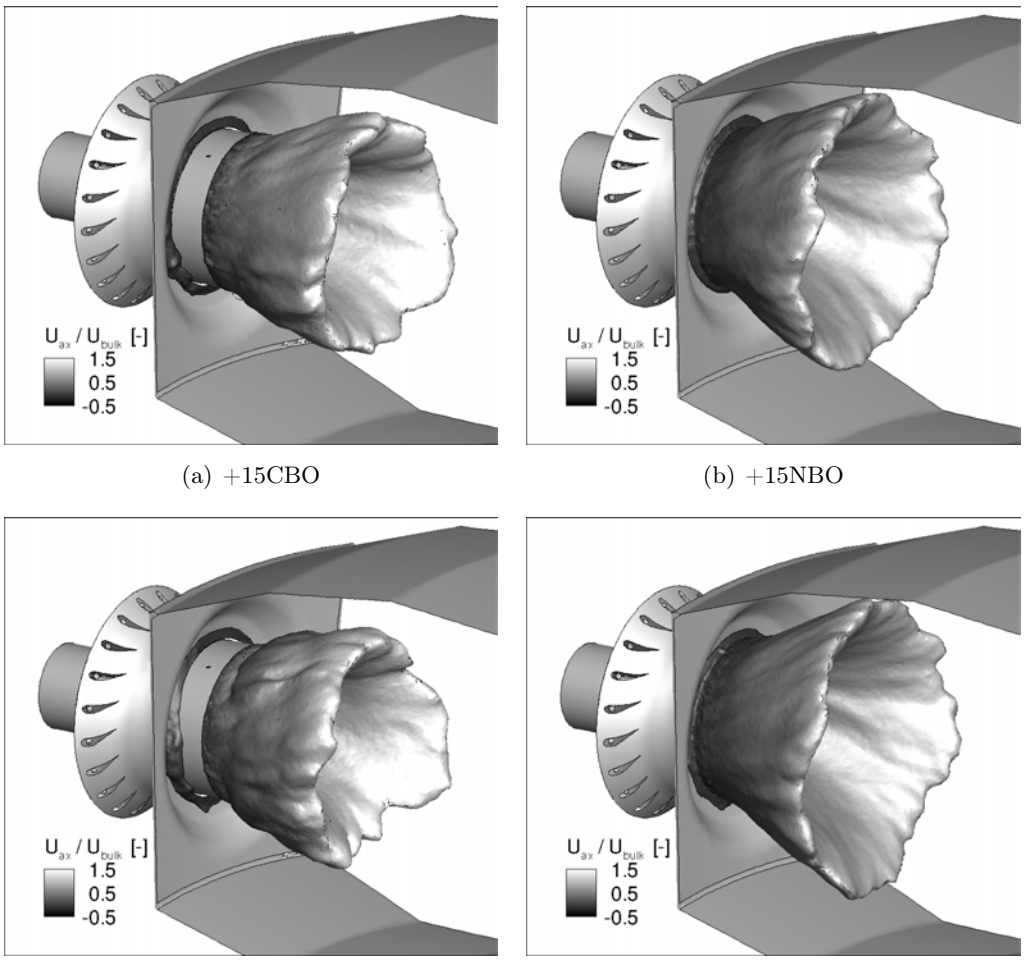

(a) +15CBO (b) +15NBO

(c) -15CBO (d) -15NBO

Figure 7.15: Temperature iso-surface ($T/T_{mean} = 1.3$) coloured by normalized axial velocity.

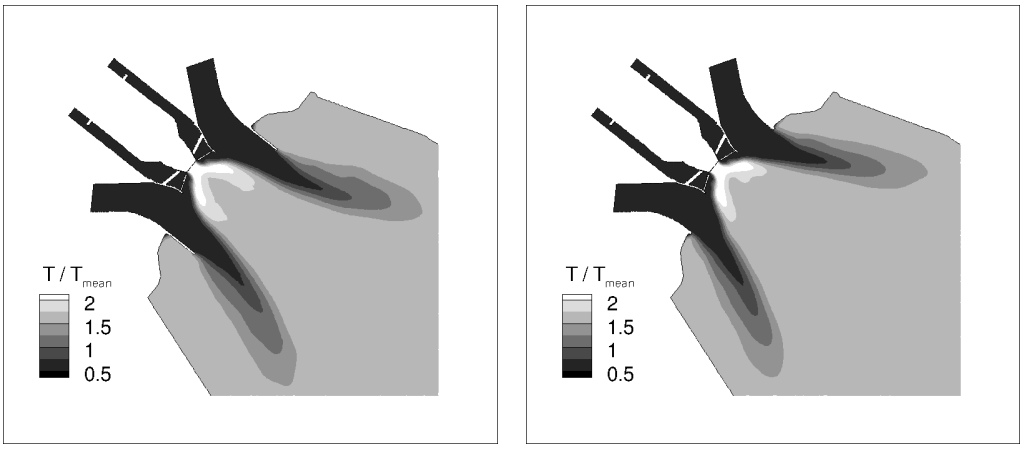

(a) +15CBO (b) +15NBO

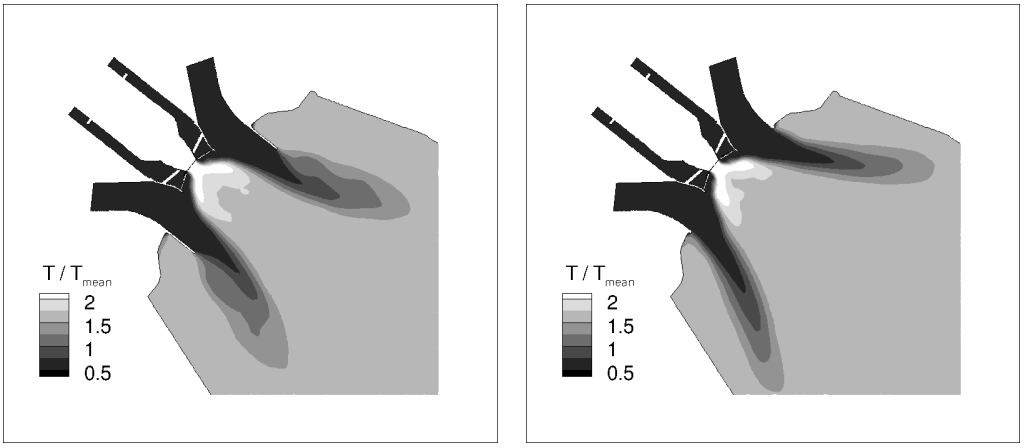

(c) -15CBO (d) -15NBO

Figure 7.16: Normalized temperature field on middle cut plane.

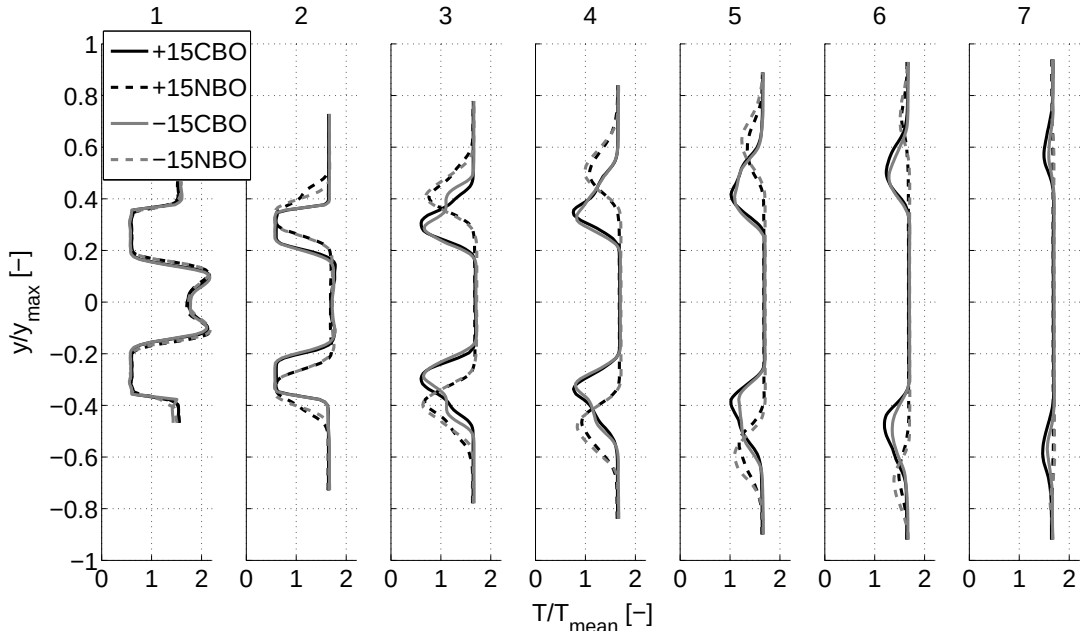

Figure 7.17: Temperature profiles for +15CBO, +15NBO, -15CBO, -15NBO

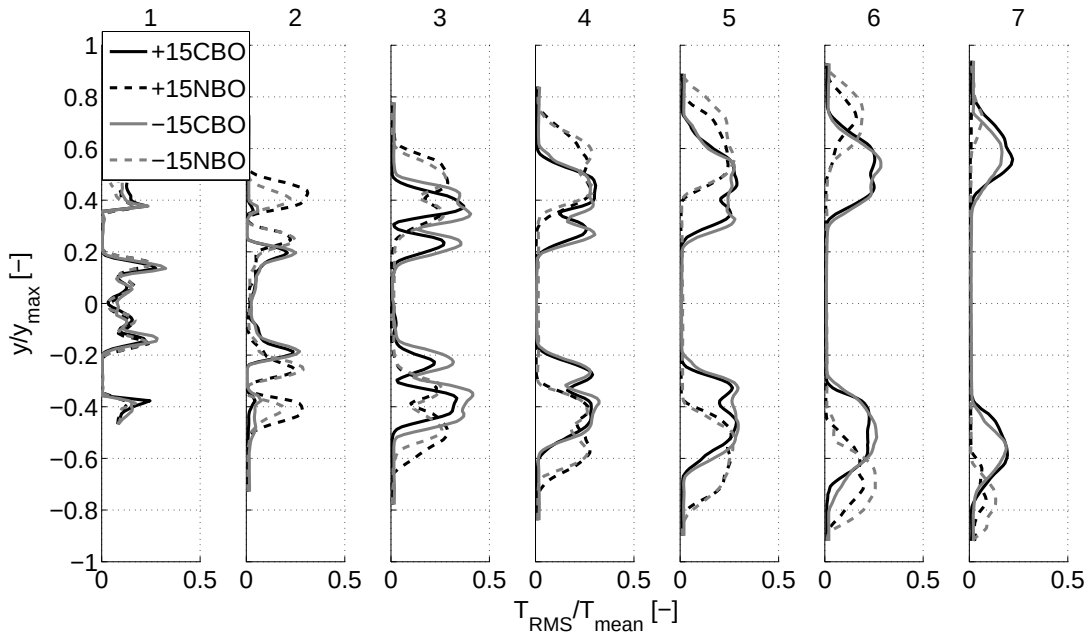

Figure 7.18: RMS temperature profiles for +15CBO, +15NBO, -15CBO, -15NBO

7.2.3 Acoustic characteristics of the chamber

The analysis of the combustion chamber's dynamics reveals fluctuations of pressure in all LES cases as illustrated in Fig. 7.19 on the middle cut plane only for +15CBO. The frequential analysis of this pressure fluctuation allows to determine the frequency at f_{acous} (Fig. 7.20). This high frequency mode is not found experimentally in the full annular chamber and might affect the results of our one sector simulation. To analyze its influence on the flame, the FFT of the heat release signal is superposed in Fig. 7.20: The flame reacts to several different frequencies but only shows a small peak at f_{acous} and has therefore a negligible impact on the overall combustion process. An acoustic analysis with an Helmholtz 3D solver called AVSP [6] using the mean speed of sound reveals that the pressure fluctuations observed in the LES are due to the first transverse eigenmode at a frequency close to that found in the LES and are not a numerical artefact. The eigenmode obtained with AVSP is shown in Fig. 7.21. The fact that AVSP captures correctly the mode appearing in the LES is confirmed by the comparison of the pressure fluctuation in AVBP (dominated by the acoustic mode) and the mode structure in AVSP.

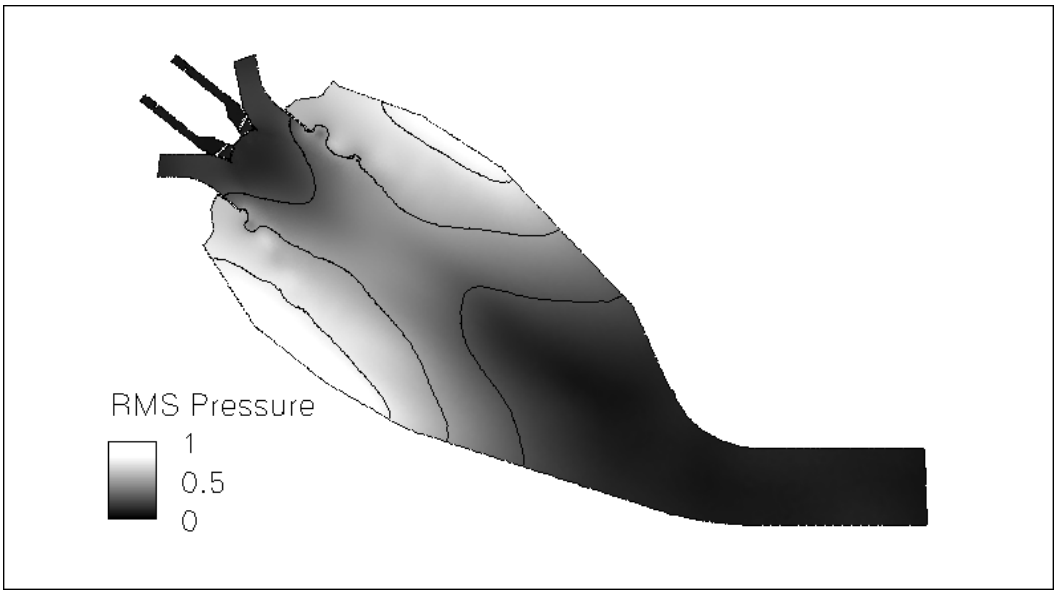

Figure 7.19: Normalized RMS pressure field on middle cut plane obtained from LES data.

7.2.4 Concluding remarks

LES of the real industrial gas turbine combustion chamber for two different operating conditions and burner outlets were performed. The mean flames and instantaneous flow characteristics exhibit no significant difference between the two operating conditions +15°C and -15°C. In both cases the burner outlet changes the velocity field and therefore the flame stabilization. The CBO elongates the flame and pushes it straight downstream, whereas the NBO leads to an opening of the flame in radial

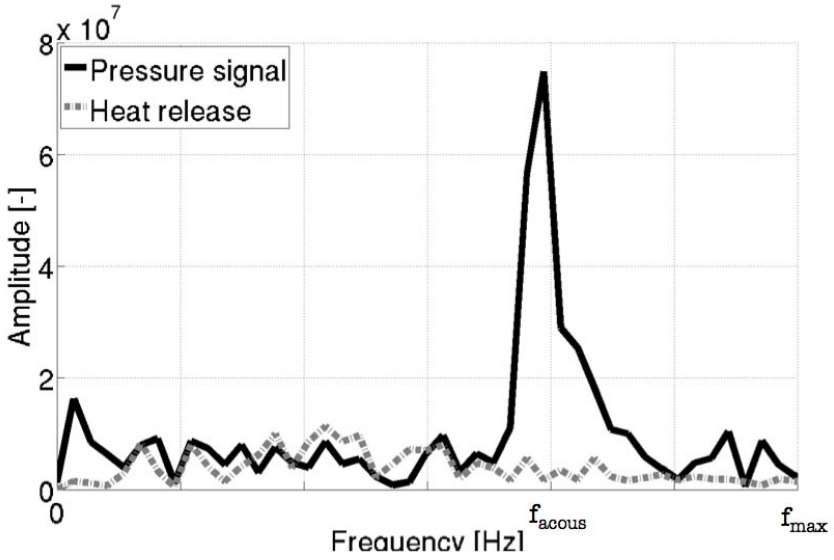

Figure 7.20: FFT of chamber pressure signal and heat release rate obtained from LES data.

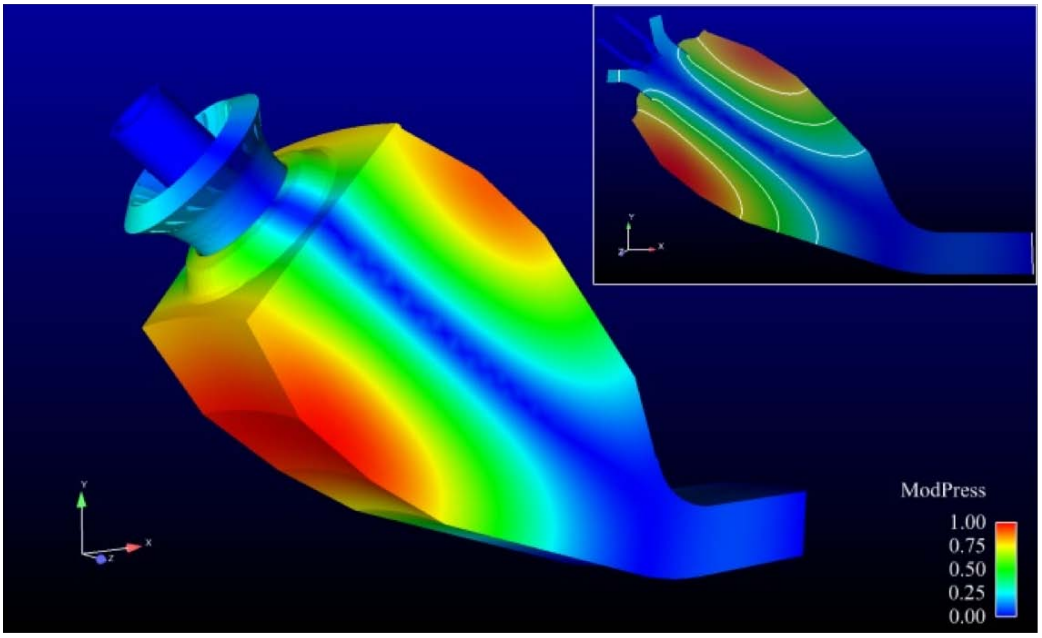

Figure 7.21: Mode shape obtained with the Helmholtz 3D solver AVSP.

direction and its length is slightly shorter. All cases burn at a similar equivalence ratio. Acoustic analysis reveals that the first transverse eigenmode of the chamber appears in the LES while it is not seen in the real full machine. Nevertheless FFT shows that this mode does not affect the flame dynamics so that FTFs can still be measured using LES of a single sector.

7.3 Flame stabilization

In the previous simulations all walls were treated with an adiabatic logarithmic law of the wall. Since the temperatures reached in the combustion chamber and burner parts are higher than their melting temperature, cooling must be applied in a real gas turbine engine to protect them. The temperature difference between the adiabatic walls and the cooled walls (in the real engine) can have an influence on the stabilization of the flame in the computation. The highest temperatures in all cases appear in the pilot flame zone at the lance (Fig. 7.16), where the flame directly attaches. In this section the effects of the wall treatment on the flame is investigated: isothermal and heat loss wall conditions are applied at the lance and results are compared.

To model heat losses through the walls a simple model that follows the linear law

$$q_w = \frac{T_{ref} - T_w}{R_w} \tag{7.4}$$

is used, where q_w describes the heat flux at the wall, T_{ref} a reference temperature and T_w the wall temperature. R_w is the heat resistance of the material by conduction and of the convection outside the wall with $R_w = e/\lambda + 1/h$, where e is the material thickness and the heat resistances $1/\lambda$ and $1/h$ of the material and outside convection respectively. Large variations and incertitudes are expected on e and h so that the heat resistance R_w is an uncertain parameter. If $h = \infty$, a heat resistance of $1/R_w = 1500W/m^2K$ corresponds to the real engine lance resistance. To obtain further insight in the flame stabilization $1/R_w = 150W/m^2K$ and $15000W/m^2K$ are tested as well. The reference temperature T_{ref} is the same for all cases and is the air inlet temperature. Additionally, an iso-thermal boundary condition for the lance is used. The investigated parameters are listed in Table 7.3 and the resulting lance temperature is given in terms of $T_w/T_{w,adiab}$ whereas $T_w/T_{w,adiab} = 0.28$ represents the air inlet temperature. The lance temperature decreases with increasing $1/R_w$ and reaches T_{ref} when using isothermal walls. Although the lance temperature changes significantly, the flame still stabilizes at the wall as shown in Fig. 7.22 for

	Heat Resistance $1/R_w$	Temperature T_{ref}	Wall temperature $T_w/T_{w,adiab}$
Adiabatic treatment	—	—	1.00
Heat transfer model	$150W/m^2K$	Air inlet temp.	0.92
Heat transfer model	$1500W/m^2K$	Air inlet temp.	0.54
Heat transfer model	$15000W/m^2K$	Air inlet temp.	0.32
Isothermal treatment	—	Air inlet temp.	0.28

Table 7.3: Flame stabilization: Wall treatment at the lance

isothermal and heat loss ($1/R_{wall} = 1500W/m^2K$) conditions. In the isothermal case a small cooled layer between the lance and the hot gases is visible, but no effect of heat transfer from the flame to the lance is observed and no local flame quenching appears. This is due to a strong inner recirculation zone transporting back hot gases and thus keeping this zone at high temperature.

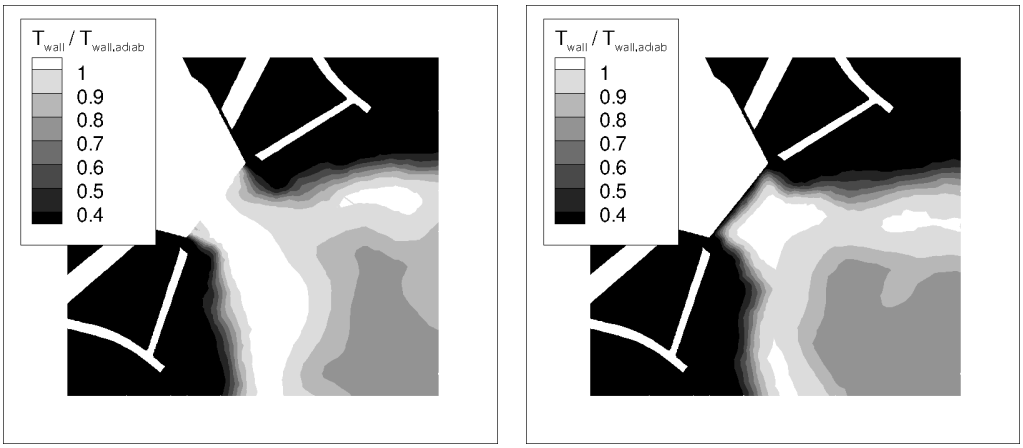

(a) Heat loss at lance ($1/R_{wall} = 1500W/m^2K$) (b) Isothermal lance ($T_{Lance} = 700$ K)

Figure 7.22: Instantaneous temperature field close to the lance.

7.3.1 Concluding remarks

Previous tests have shown that the flame stabilization process at the lance is weakly dependent on the temperature or on the heat flux lost at the lance wall. The gas temperature close to the lance is always high because of the inner recirculation zone carrying back hot burnt gases. The Boundary Condition at the lance does not affect the flame anchoring or the flame dynamics. Therefore, in the following only adiabatic conditions are used on the lance walls.

7.4 Bi-stable behaviour of the reacting flow

During the initialisation of the operating condition at an ambient temperature of −15°C, LES revealed that when the transition between the two states (15°C to -15°C) is applied harshly, the flame detaches from the lance and a PVC develops, preventing the flame to move back to its normal stabilization point. Figure. 7.23(a) and Fig. 7.23(b) use a low pressure iso-surface to represent the PVC and a temperature iso-line of $T/T_{mean} = 1.3$ to track the flame surface in 2D for the attached and detached flame respectively. In the attached case no PVC is present whereas the detached flame features a "finger-like" rotating structure in the inner region around which the PVC is turning (Fig. 7.23). A similar phenomenon was observed by Staffelbach [164] who discovered that the flame detaches with decreasing fuel mass flow rate at the lance. Field tests performed by Ansaldo also showed different pressure oscillation levels depending on transition between different operating conditions, suggesting hysteresis phenomena. The detached flame exhibits stronger pressure levels than the attached one and this is not desirable for flame stabilization and thermo-acoustic stability. In the following section the detached flame is analyzed in detail. For simplicity reasons the nomenclature listed in Table 7.4 is used. Although this arises for both burner outlets, only the CBO case will be investigated since both cases behave similarly.

A first impression is obtained by plotting the three-dimensional surface of the

-15CBO	Attached flame
-15CBO-D	Detached flame

Table 7.4: Nomenclature for attached and detached flame.

averaged flame as shown in Fig. 7.24 where the flame surface is visualized by a temperature iso-surface ($T/T_{mean} = 1.3$) coloured by the axial velocity. The flame finds two different stable positions for the same regime and is therefore bi-stable.

A cut through the middle plane reveals differences in the heat release field between both flames which is shown in Fig. 7.25(b). Since the flame is detached from the lance, the high temperature region around the pilot injection disappears. In this case the inner recirculation zone does not reach the lance (Fig. 7.25(a)) and does not bring the flame back to the lance. Furthermore the attached flame acts like a geometrical contraction at the outlet of the burner accelerating the flow and leading to higher axial velocities than in the case with detached flame. This is illustrated by plotting the axial velocity along the cuts (Fig. 7.11) in Fig. 7.26. Both flames still agree well in terms of position of lows and peaks but the attached flame shows significantly higher velocities in the peaks all along the flame region (cut 2 to 7). The detached flame shows positive axial velocity in the inner region close to the

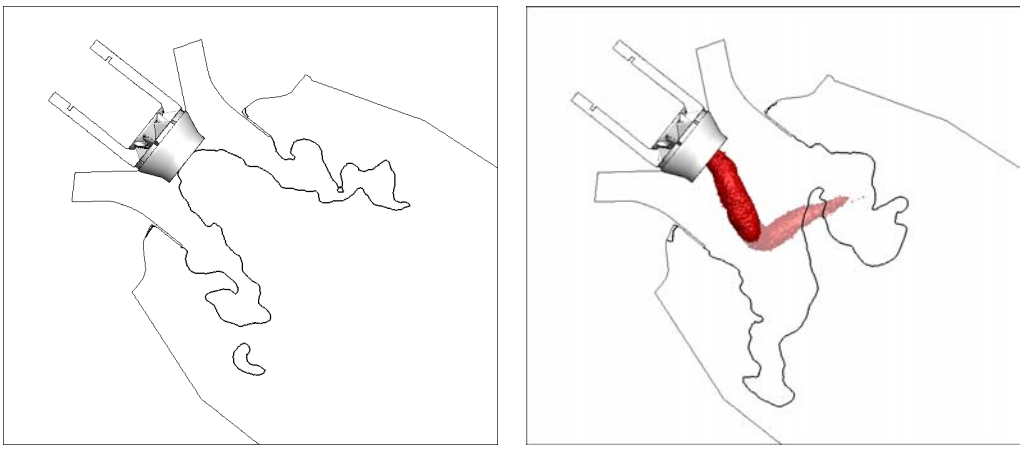

(a) -15CBO: attached flame (b) -15CBO: detached flame

Figure 7.23: Temperature iso-line ($T/T_{mean} = 1.3$) and pressure iso-surface (visualizing the PVC structure) for the -15CBO case: attached (a) and detached (b) flame. The PVC disappears totally for the attached flame.

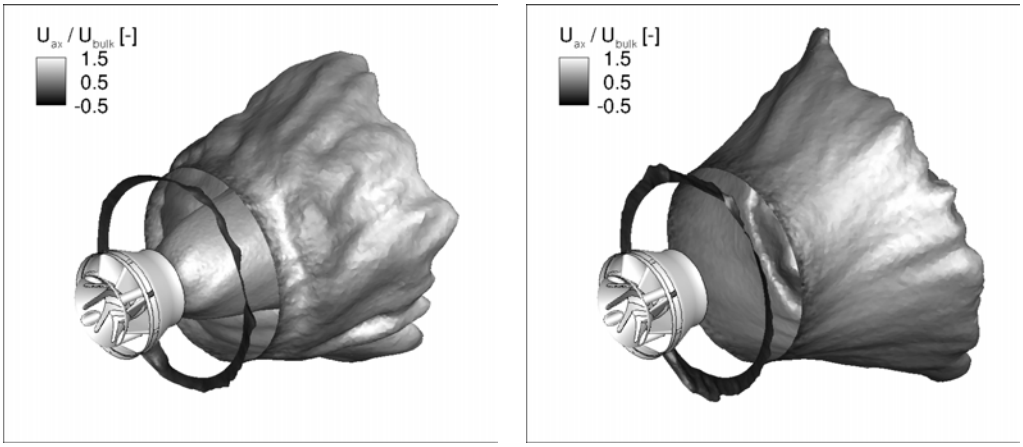

(a) -15CBO: attached flame (b) -15CBO: detached flame

Figure 7.24: Temperature iso-surface ($T/T_{mean} = 1.3$) coloured by normalized axial velocity for the -15CBO case: attached (a) and detached (b) flame.

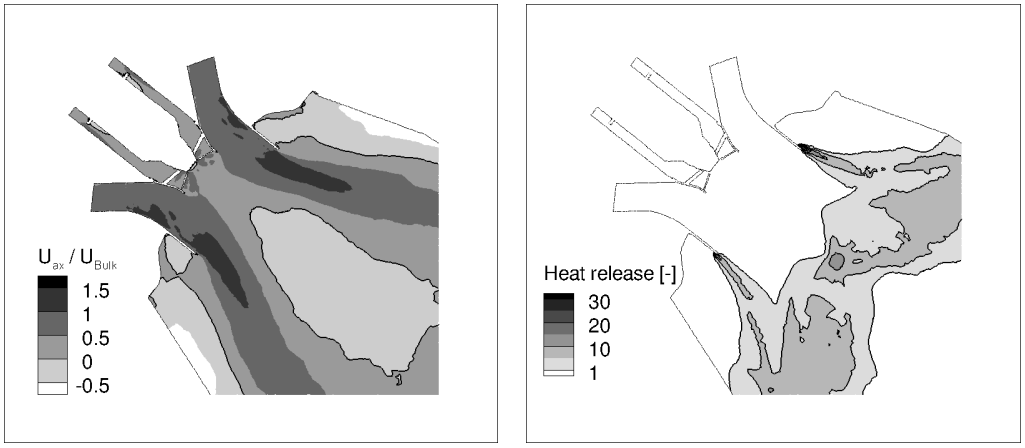

(a) Axial velocity field and zero axial velocity iso-lines on the middle cut plane

(b) Heat release field on the middle cut plane

Figure 7.25: Detached flame (-15CBO-D).

lance (1 to 3) whereas the recirculation zone of the attached case leads to negative velocities. In the inner recirculation zone from cut 4 on, both velocity fields become similar. The radial velocity profiles in Fig. 7.27 reveal further differences: on the first cut 1, low radial velocities appear in -15CBO-D in the inner region where -15CBO shows important peaks. In the outer region both profiles are similar. Up to location 5 both profiles are similar in terms of position and magnitude of extrema. At 6 and 7 the peaks of -15CBO-D are further outwards and lower in magnitude than in -15CBO. Further differences are visible for the tangential velocity profiles in Fig. 7.28. Close to the lance (1 and 2), significantly higher velocities are found in -15CBO-D in the inner region, where the peak has a larger extent than in -15CBO. Further outside the -15CBO-D peak meets the -15CBO one and both cases match in the outer region. The high tangential velocities in the inner region decrease with distance but only reach at 7 the magnitude of the -15CBO case. Nevertheless peaks match in terms of magnitude.

The position of the flame can be also visualized using temperature profiles (Fig. 7.29). The maximum temperature is the same for both flames, but the position of extrema differs. The -15CBO-D flame shows no peak in the central zone for the first profiles (1 to 4) but starts to develop one at 6. The flame length is similar to -15CBO as an almost constant temperature profile is reached at position 7. The -15CBO-D flame is susceptible to temperature fluctuations (Fig. 7.30) over a wider radial range. At location 3 one peak is visible with a similar amplitude and position as the outer peak of -15CBO. At 4 the peak widens significantly and is over a larger radial range than for -15CBO but with a similar amplitude. At 5, 6 and 7 the magnitude is increased compared to -15CBO.

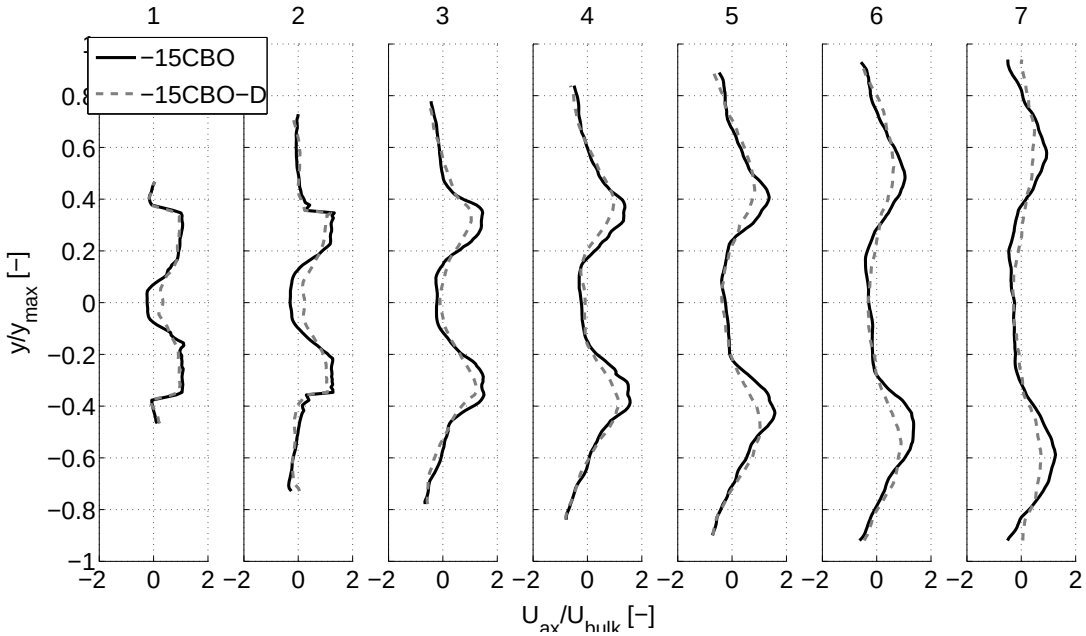

Figure 7.26: Axial velocity profiles for the attached (-15CBO) and detached (-15CBO-D) flame.

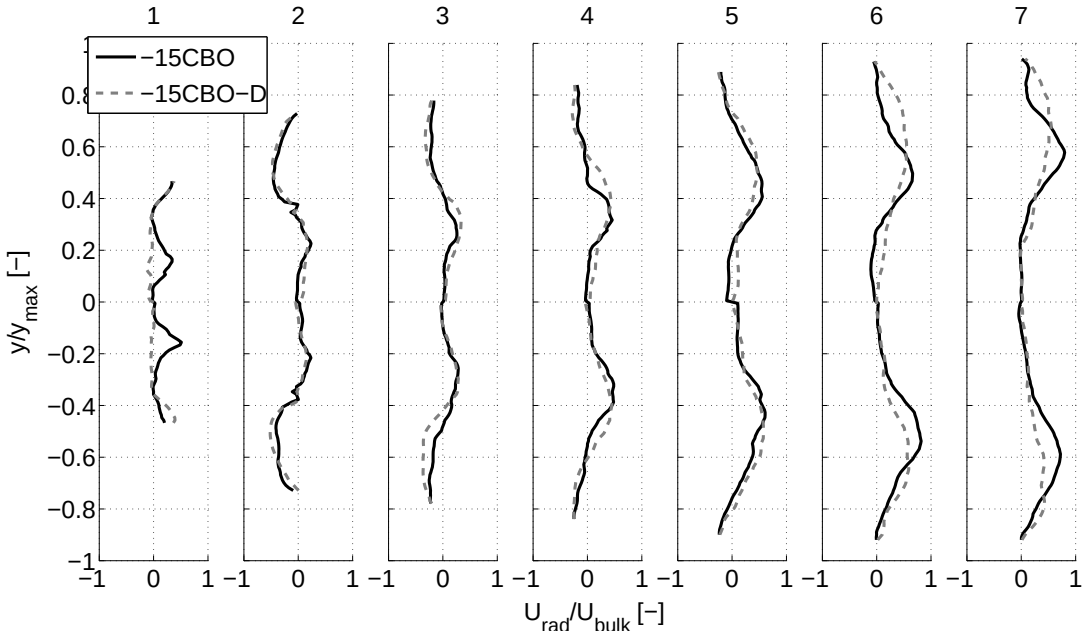

Figure 7.27: Radial velocity profiles for the attached (-15CBO) and detached (-15CBO-D) flame.

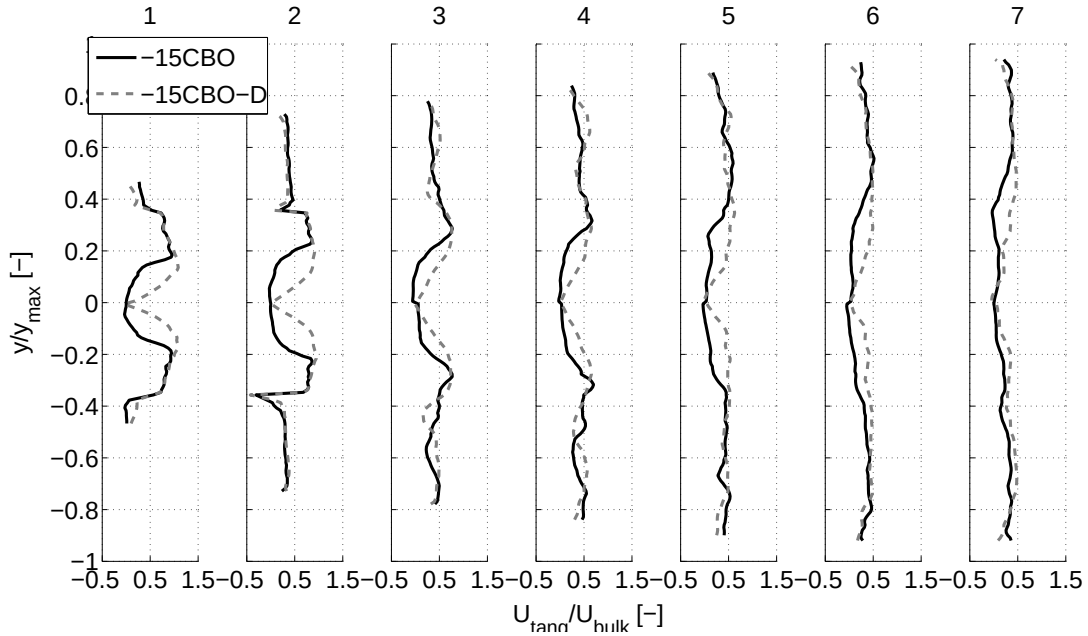

Figure 7.28: Tangential velocity profiles for the attached (-15CBO) and detached (-15CBO-D) flame.

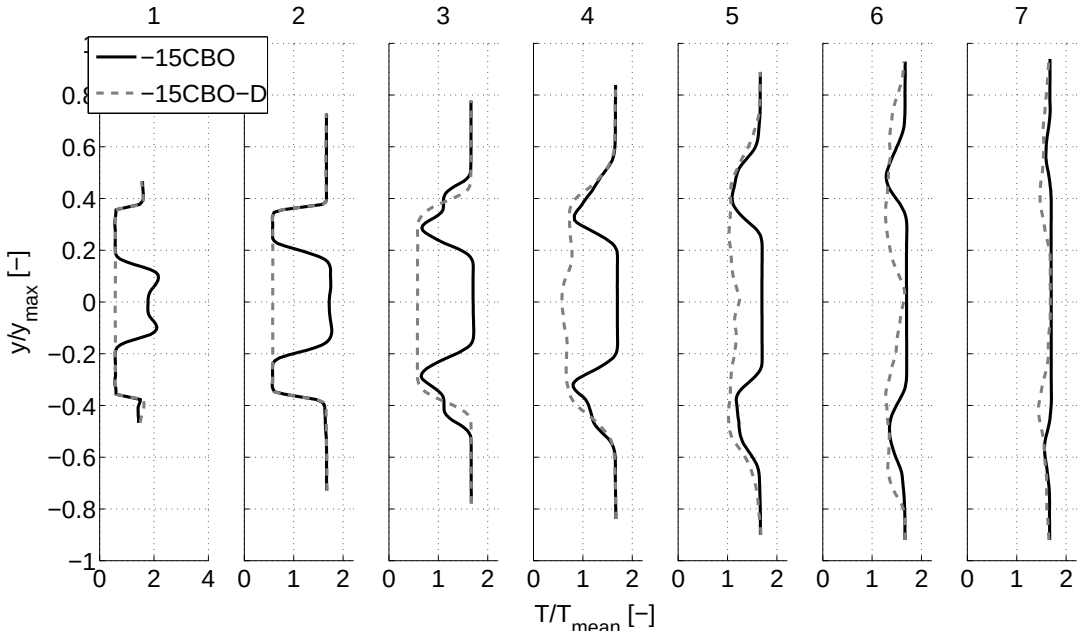

Figure 7.29: Temperature profiles for the attached (-15CBO) and detached (-15CBO-D) flame.

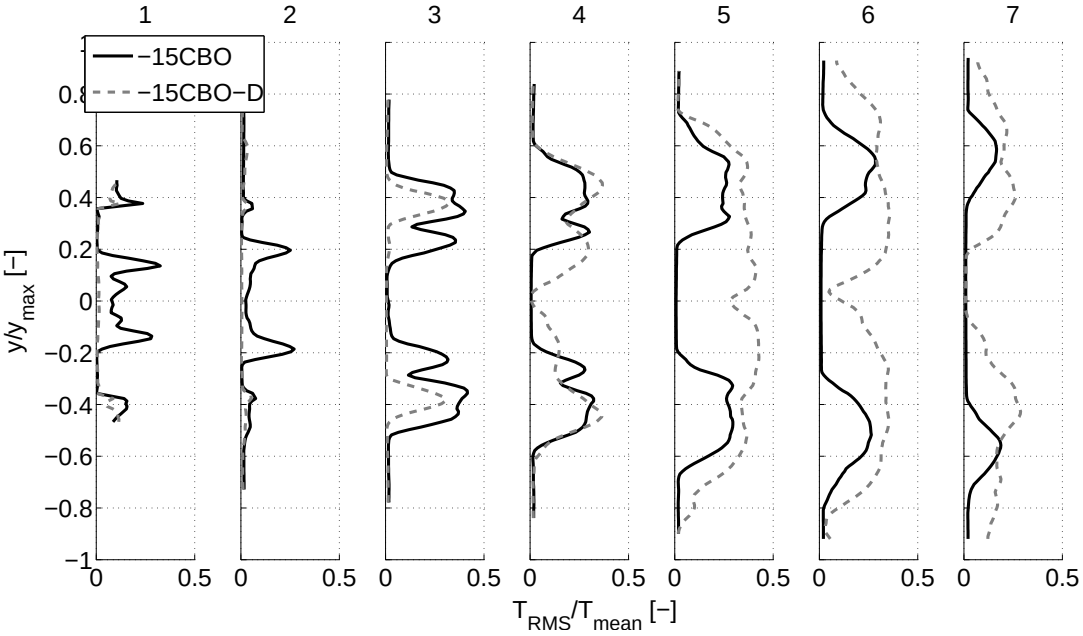

Figure 7.30: RMS temperature profiles for the attached (-15CBO) and detached flame (-15CBO-D)

7.4.1 Concluding remarks

LES suggests that the flame possesses two stable positions depending on the transition from one operating condition to the other. In the first position the flame is attached to the lance whereas in the second one the flame takes a stable position detached from the lance. The detached flame features a "finger-like" rotating structure in the inner region around which the PVC is turning and the flame can not move back. Staffelbach [164] observed this phenomenon and showed that strong pressure levels occur. This is coherent with the results found here where strong temperature fluctuations arise. This flame configuration is not desirable in a real industrial machine. From now on, we assume that the lance-stabilized flame is the relevant configuration. It should be kept in mind, however, that this bistable behaviour may be the source of other problems, which were not studied here.

7.5 Quality of the LES

One goal of the present thesis is to evaluate the quality of LES of complex configurations in an industrial context which requires limited time and computational costs. The quality of the mesh is evaluated in Fig. 7.31 and 7.32 showing the thickening factor for the flame and the turbulent viscosity ratio for +15CBO. The thickening reaches its maximal value at the flame tip and is always less than 300. The PDF of the thickening factor (Fig. 7.33) shows that most of the flame is thickened with a value lower than 10 and only a few points are thickened with values around 300 (Fig. 7.33(b)). Also a reasonable ratio between turbulent and laminar viscosity is reached with maximal values downstream of the burner outlet of 500 where the mesh becomes coarse (Fig. 7.32).

At the operating pressure, the typical flame thickness of a stoechiometric flame

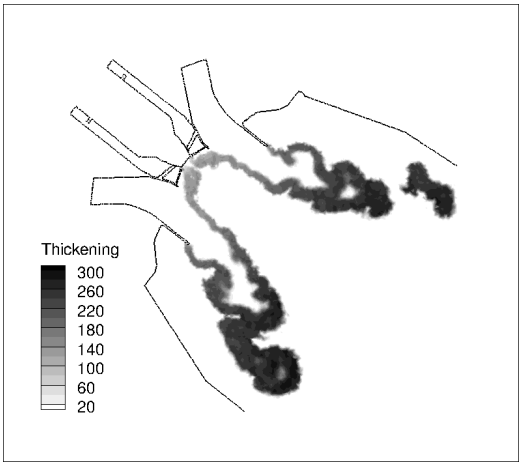

Figure 7.31: Thickening factor on the middle cut plane (+15CBO).

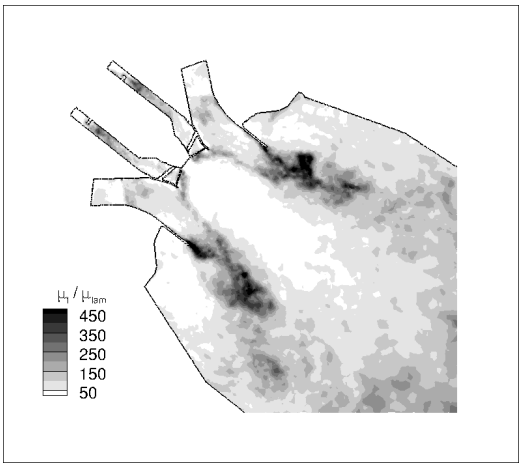

Figure 7.32: Turbulent viscosity ratio on the middle cut plane (+15CBO).

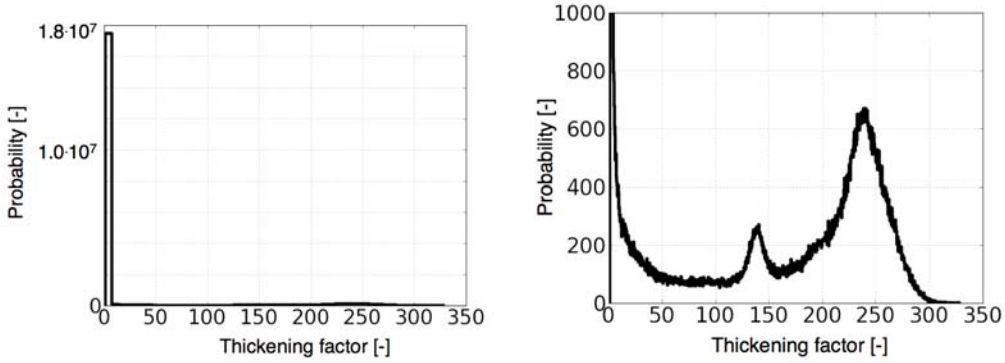

(a) Full range (b) Zoom

Figure 7.33: PDF of thickening factor (+15CBO).

(computed with Cantera for example) is $x = 0.05$ mm. Considering the burner size ($y = 20$ cm in transverse direction), a true DNS using 10 points in the flame thickness would require $10y/x = 40.000$ mesh points in each direction. Thickening using TFLES [25, 27, 98] allows to reduce this constraint. Here, the PDF of thickening shows that most flame zones are thickened by numbers ranging between 1 and 124.

Chapter 8

Acoustically perturbed flame

Contents

Modern regulation policies on pollutant emissions lead to lean (technically) premixed combustion systems [97]. These low-emission gas turbines are known to be particularly susceptible to thermo-acoustic instabilities [126] and their prediction has become an important task today to prevent the appearance of acoustically coupled instabilities at an early design stage [74, 86, 189]. For acoustically compact flames, a common approach can be found in the literature and was first introduced by Crocco [29, 30]. In this approach, the Flame Transfer Function (FTF) is the key parameter and is defined as the ratio of the relative heat release fluctuation ($\hat{q}/\bar{q}$) to the relative inlet velocity perturbation ($\hat{u}/\bar{u}$) issued by the acoustic field. In the frequency domain it writes

$$F(\omega) = \frac{\hat{q}/\bar{q}}{\hat{u}/\bar{u}}. \tag{8.1}$$

with ω being the angular frequency.

The FTF is affected by different mechanisms acting simultaneously on the heat release rate fluctuation and therefore difficult to isolate [178]:

- **The axial velocity perturbation**:
  Flame Transfer Functions have been extensively studied in laminar and turbulent premixed flames where only the axial velocity perturbation is at play. Investigations of laminar conical flames performed by Karimi et al. [76], inverted conical by Durox et al. [38] and multi-slit conical flames studied by Kornilov et al. [85] revealed that the FTF gain shows a low-pass filter behaviour. Schuller et al. [150] observed from laminar flames and Armittage et al. [2] from turbulent V-flames, an overshoot in gain and associated this to vortex roll-up at the flame base. The phase ϕ of the FTF evolves in these cases in an almost linear way with the frequency f indicating that axial velocity perturbations propagate convectively from the burner outlet to the flame, thereby controlling the delay τ of the FTF: $\tau = \phi/(2\pi f)$.

- **The perturbation of swirl**:
  Among the recent contributions towards the understanding of the mechanisms at play for swirled flames, the importance of swirl number fluctuations has been clearly identified. Straub and Richards [173] first noticed a strong impact of the swirler position on the combustion oscillations. Hirsch et al. [59] hence investigated the effect of swirler designs and found that an additional time lag is responsible for changes in the FTF. Komarek et al. [84] investigated the influence of several swirler positions on the FTF and concluded that disturbances propagate at a convective and an acoustic speed downstream of the swirler position. Finally, Palies et al. [117, 119] have shown that the acoustic perturbations reaching the swirler generate transverse velocity fluctuations which are convected by the flow.

- **The perturbation of mixture**:
  Since most gas turbines are partially premixed, fluctuations of equivalence ratio may also modify their flame response [104]. Schuermans et al. [148] compared the measured transfer matrix of a turbulent flame for a technically premixed and a fully premixed system and found the maximal value in amplitude to increase for the technically premixed case where equivalence ratio perturbations are present. Kim et al. [82] found a phase difference between equivalence ratio and velocity at the combustor inlet suggesting that this phase determines if both effects cancel out or amplify the dynamic flame response. Furthermore, they showed that this phase difference is a function of frequency, fuel injection location, fuel injector impedance and the mean velocity in the nozzle.

These mechanisms have been studied for simple laboratory premixed flames but much less information is available for real gas turbines. This point is investigated here using LES of a real burner. Thanks to this fully unsteady numerical approach, effects of mass flow rate perturbation, mixture fluctuation and swirl number perturbation can be studied.

This chapter is organized as follows: first (section 8.1) the specific information for the pulsation of the different cases are given and the methodology is shortly summarized (see chapter 3 for more a detailed description). Then the Flame Transfer Functions of the cases with different operating conditions and burner outlets are given and differences are discussed (section 8.2). Then the specifications of the FTFs are analyzed in detail for the single forcing frequency which allows to obtain further insight into the mechanisms influencing the dynamic response of the flame . Therefore the differences due to operating conditions and burner outlets are further evaluated at one specific frequency (section 8.3) and one case is analyzed for several frequencies (section 8.4). Further effects such as axial velocity perturbation, swirl fluctuation and mixing inhomogeneities are considered. Finally, additional LES are performed separating the effect of mixing inhomogeneities (section 9.1) and of velocity perturbation (section 9.2) on the FTF.

8.1 Pulsation procedure and system identification

8.1.1 Pulsation procedure

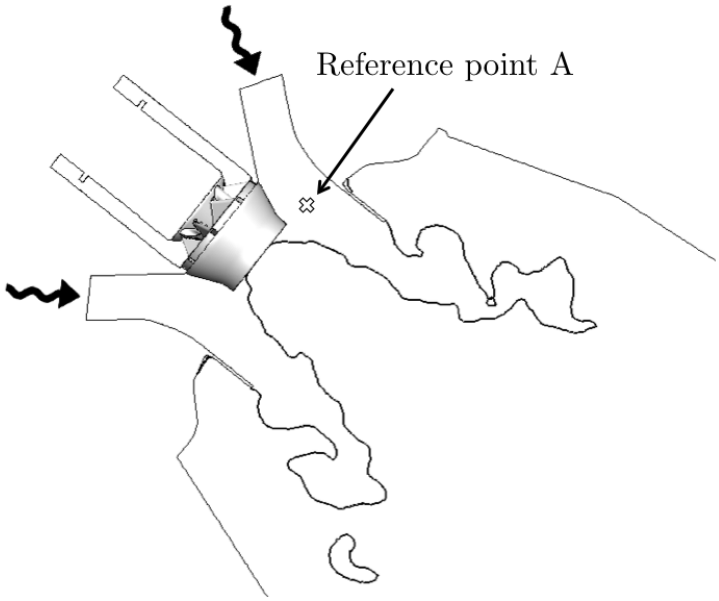

Figure 8.1: Reference point location for FTF measurement and pulsation procedure.

Forcing is introduced by generating a harmonic acoustic perturbation at the diagonal inlet using the inlet wave modulation method [78] as illustrated in Fig. 8.1. Tests have been performed to investigate the effect of pulsating the diagonal or axial passages separately. Pulsation amplitudes between both passages were chosen to lead to the same pressure fluctuations at the swirler exit. Pulsating only the diagonal swirler results in the same flame response as pulsating both axial and diagonal passages, so only the latter is discussed here. The response of the flame is quantified by measuring the perturbation of the heat release rate. An amplitude of 6 percent of the mean inlet velocity is chosen, to be in the linear regime. The velocity perturbation is measured at reference point A (Fig. 8.1).

Two different methods are used to obtain the FTF. Their methodology is described in detail in chapter 3 and will here only be summarized shortly:

- **Single Frequency Forcing and Fast Fourier Transformation**:
  A sinusoidal perturbation is introduced at the diagonal swirler. One obtains the flame response in one LES for each frequency so that several simulations are needed to cover the frequency range. In this study four frequencies are chosen which are known from measurements to be present in the real gas turbine. For confidentiality reasons they are only given in terms of $f_1 < ... < f_4$. This

method is less sensitive to errors and will be used to validate the following second method.

- **Broadband excitation and Wiener-Hopf Inversion (WHI) [64]**:
  This method allows the determination of the whole FTF in one single LES. A Discrete Random Binary Signal (DBRS) is used to perturb the flame. This signal is first low-pass filtered to excite only the frequency range of interest and to achieve a higher power spectrum density [64]. It is also high-pass filtered to avoid reflection on the NSCBC boundaries.

NSCBC boundary conditions show a high-pass filter behaviour. The cut-off frequency is determined by the reflection coefficient. To avoid reflection on the boundaries in the frequency range of interest, the reflection coefficients have been adapted to the lowest forcing frequency.

8.1.2 System identification

One goal of this thesis is to evaluate the capabilities of LES to perform thermoacoustic analysis in an industrial context with limited computational time and cost. The sinusoidal pulsation is performed for six cycles of each frequency and the broad band excitation for six cycles of the lowest frequency of interest f_1. Furthermore the reference velocity signal as well as the heat release response are low pass filtered to exclude effects of the transverse pressure mode discussed in Section 7.2.3. A fixed time step $\delta t = 9 \cdot 10^{-8}$s is used which corresponds to a CFL of 0.7.
A typical evolution of reference velocity and global heat release for a forced case is given in Fig. 8.2 with the corresponding FTF values in Table 8.1. It shows that the forced response of the burner is established after 1 or 2 cycles justifying that six cycles are enough to obtain FTFs.

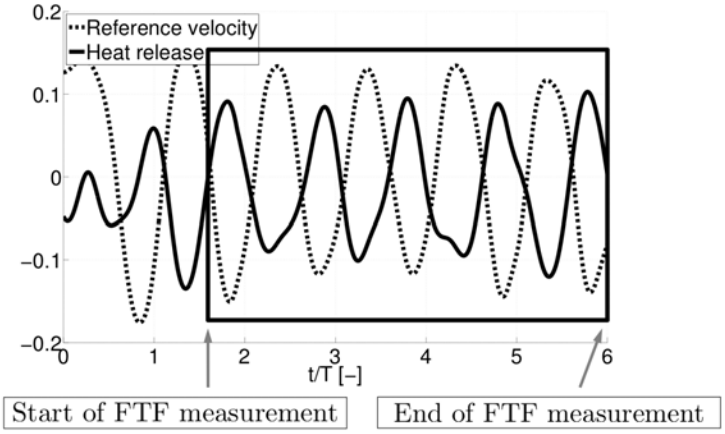

Figure 8.2: Typical time evolution of heat release rate and velocity fluctuation at the reference point A (Fig. 8.1).

n [-]	0.63
Phase [-]	2.96

Table 8.1: FTF determination: amplitude n and phase θ.

8.2 Flame Transfer Function

FTFs for swirled flames often exhibit typical shapes in gain with a decrease at low frequencies followed by a second peak at higher frequencies [40, 85, 117, 119]. Similar behaviours are observed here: Figure 8.3 shows the FTF results for the +15CBO case. The gain in this frequency range is slightly increasing to f_2 for WHI whereas the gain for single frequency forcing decreases already at f_1. From frequency f_4 on the gain again and both show a similar behaviour. The gain at f_1 differs slightly as the single frequency forcing predicts an overshoot in gain whereas the other frequencies agree well for both methods. The phase is constantly decreasing with frequency and especially in the higher frequency range a good agreement is found for both methods.

The +15NBO case is investigated in Fig. 8.4 and behaves differently: the gain

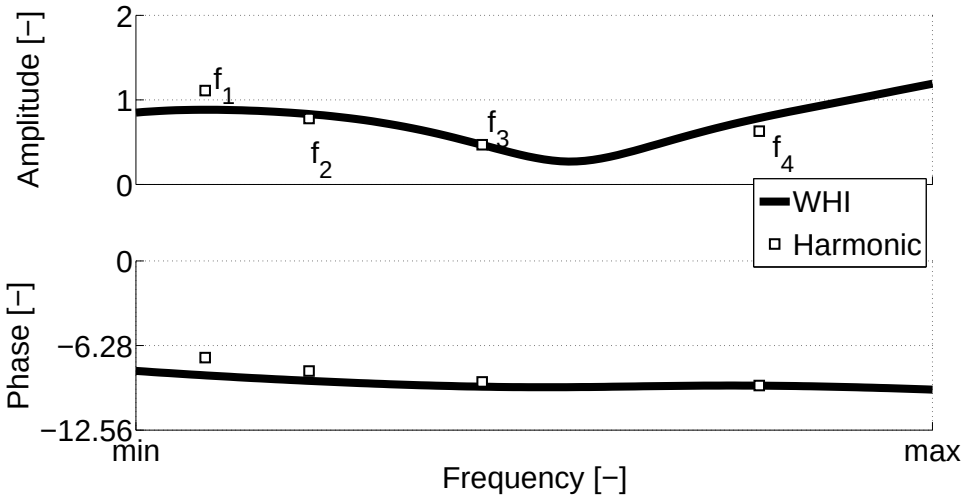

Figure 8.3: Flame Transfer Function for +15CBO.

is decreasing from f_1 to f_3 and increasing again up to f_4. This behaviour is similar to the +15CBO case. WHI predicts in general lower gain except at $f3$ where both methods match. As in +15CBO the phase decreases continuously and WHI gives higher values. Both methods show an overshoot in gain at f_1 in the -15CBO case (Fig. 8.5). Here the gain is slightly higher with WHI but a reasonable agreement is found. The phase matches well for both methods from f_1 to f_3 but decreases faster in the WHI method and a difference of π is found for f_4 showing a major problem

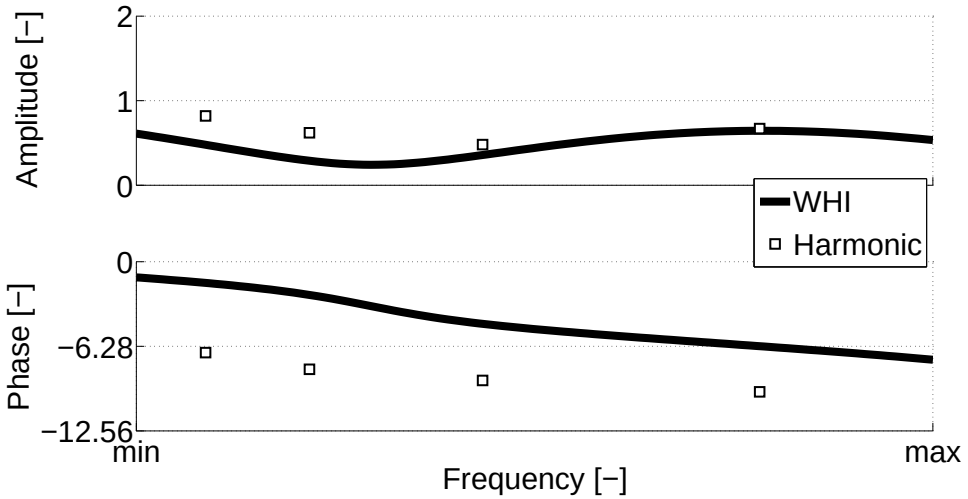

Figure 8.4: Flame Transfer Function for +15NBO.

for WHI at this frequency. The -15NBO case in Fig. 8.6 shows as all cases a peak

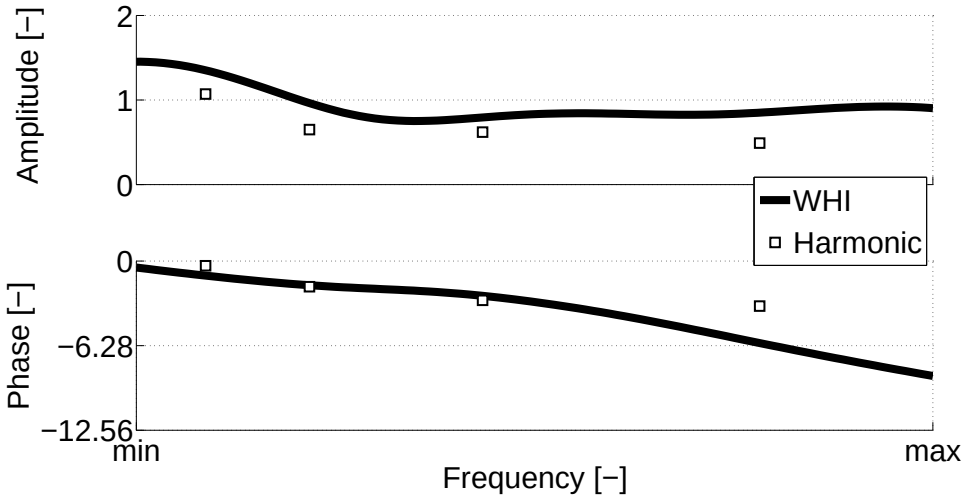

Figure 8.5: Flame Transfer Function for -15CBO.

at f_1, decreases until f_3 and increases again for the harmonic forcing. The phase decreases with frequency and corresponds to the other cases. The gain agrees well between WHI and harmonic forcing, whereas WHI predicts a higher phase.

Note that for all cases the minimal frequency shown here do not correspond to $f_{min} = 0$ since the multi-frequential signal has also been high-pass filtered in order to avoid reflections at the boundaries for low frequencies and results for $f < f_{min}$ are not physical. Following [127] an amplitude $n(f = 0) = 1$ is expected. The Flame Transfer Functions exhibit typical behaviour in all cases. The phase decreases with

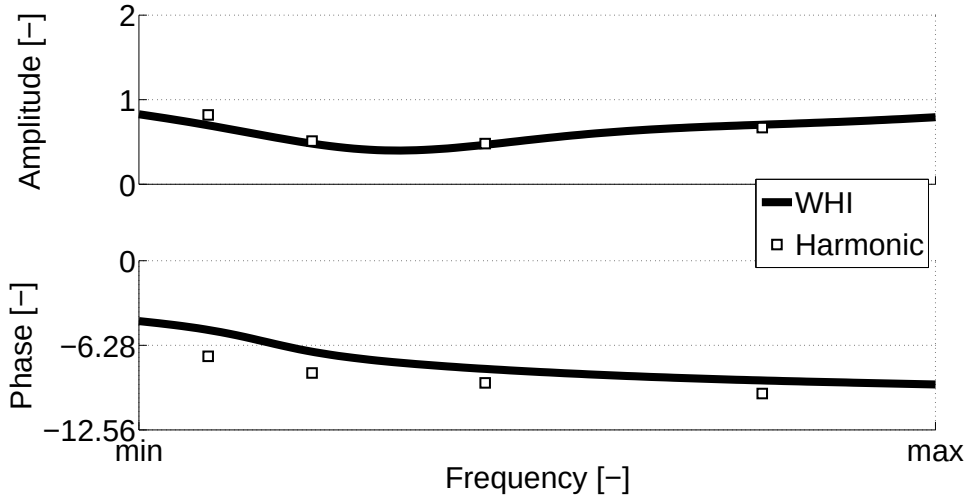

Figure 8.6: Flame Transfer Function for -15NBO.

increasing frequency and the gain is characterized by at least two zones of larger amplification. Concerning the gain, both CBO cases show an overshoot in gain at f_1, decreasing to f_3 and increasing again. The NBO cases agree as well in terms of gain with a peak at f_1 which is below 1 and a similar behaviour as the CBO cases with decreasing and increasing gain. The phase is generally decreasing but a variable time lag is found in all cases. Comparing the CBO cases with the NBO cases shows that most frequencies lead to a shorter time delay for the CBO case. This result is contradictory to what is found in literature: Krebs et al. state in [103] that the time lag increases when adding a CBO compared to the case with no CBO. Their result has been obtained by postprocessing CFD RANS data and the application of the Rayleigh criterion showed an improvement of thermoacoustic stability which has been validated against field tests [8]. This stands in contradiction to what is found here: the CBO cases show shorter time lags at both operating conditions.

8.2.1 Comparison of the identification methods

For all cases a reasonable agreement is found between the two methods WHI and Harmonic but some differences occur especially at high frequencies. They can partly be explained by the complexity of the WHI method and its sensitivity to errors. Another source of error is that the velocity signal is taken at a reference point (see Fig. 8.1) where turbulent fluctuations can have an influence. This is easy to recognize and to filter for an harmonic excitation but it becomes more complicated with a random signal. Furthermore, Huber [64] states that even with a low signal to noise ratio of $S/N = 4$ the quality of the identification process is 90% when having a total simulation time of ten times the longest time lag considered. Below ten times the quality decreases drastically. Here, the WHI simulation was performed to be in the quality range of $> 90\%$ but this means also that some errors are expected.

Generally, the Fast Fourier Transformation is less sensitive to errors in the system identification process than the WHI method. Additionally it allows to easily separate turbulence effects from those coming from the excitation. Although WHI is supposed to minimize the error in a least mean square sense, which means to separate effects from turbulence and excitation, a long time series is needed to reach statistical convergence.

To study the dynamic flame response more in detail, in the following the FTFs obtained by harmonic excitation are analysed in order to determine which mechanisms are at play. In a first step the two operating conditions and burner outlets will be compared to obtain insight into the mechanisms leading to a shorter time lag for the CBO cases. Second, the response to different excitation signals will be evaluated to study the differences in gain and time delay at several frequencies.

8.3 Influence of operating conditions and burner outlets

Constructing stability maps of a given combustor as a function of operating conditions (air flow rate and equivalence ratio) is a classical problem in combustion. For swirled flows, the influence of operating conditions on the stability of a lean premixed swirl-stabilized burner has been studied experimentally for example by Broda et al. [15] and Seo [159]. They found instabilities to increase for increased inlet air temperatures, equivalence ratios from 0.5 to 0.7 and an increase in instability intensity for decreasing swirler angles. Increasing inlet velocity was found by Venkataraman et al. [183] to increase unstable behaviour on a bluff-body stabilized combustor. Instability occurred for low equivalence ratios of 0.55 and around stoichiometry. Increasing swirl stabilizes the combustor at high equivalence ratios. Bernier et al. [7] investigated the instability mechanisms in a premixed prevaporized combustor. Co- and counter-rotating swirlers were used and instabilities occurred for the first when the fuel injection velocity was less than a critical value whereas the counter-swirl configuration triggered instability for higher injection velocities. Additionally, instabilities arised for equivalence ratios higher a threshold value which is in contrast to the observations made in [183].

The geometry of a combustion chamber is of great importance to the stability of the gas turbine since it determines the flow and flame characteristics as well as the acoustic properties of the system [63]. The geometry of the combustion chamber is amongst others characterized by its dimensions in length and diameter, the fuel injection system, inlet and exit conditions and the flame stabilization setup. Several duct geometries were tested by Katsuki et al. [77] on a bluff-body stabilized burner and only one configuration showed stable combustion. Straub and Richards [172] changed the fuel nozzle location along the burner axis of a lean premixed configuration and altered the interaction between heat release and pressure oscillations since the distance and thus the time lag changed.

This small literature review suggests that geometry and operating conditions changes must affect the FTF. In this section, we investigate how a change of geometry (CBO or no CBO) or a change in regime ($-15°$C or $+15°$C) changes FTF in our computations. The analysis between the two different operating conditions and burner outlets is performed by means of the averaged pulsated flow fields and the dynamics of the flame.

8.3.1 Mean pulsated flow fields

An interesting issue to study combustion instabilities is to know whether mean fields with forcing remain similar to unforced mean fields since this is an assumption used to linearize equations in almost all approaches [31]. This point was tested here: averaged pulsated flow fields behave similarly in both operating conditions (-15°C and $+15°$C) compared to their averaged non-pulsated ones, so that only the

cases +15CBO and +15NBO are shown here. The temperature profiles along the cuts match very well for the pulsated and non-pulsated averaged flame of +15CBO (Fig. 8.7) in terms of position and magnitude extrema, meaning that both flames are in the same averaged position. Since the stabilization of the flame is determined by the recirculation zones, the velocity profiles agree also very well for both cases as shown in Fig. 8.8 on the axial velocity. Nevertheless, differences occur in the RMS temperature profiles (Fig. 8.9): The fluctuations are higher close to the lance (1) and reach almost the double of the non-pulsated case at cut 2. A similar behaviour is observed for the +15NBO case. Both temperature profiles agree (Fig. 8.10) as well as velocity profiles (not shown). The fluctuations of temperature in Fig. 8.11 reveal also differences in this case: compared to the non-pulsated case, RMS fluctuations are about doubled in the pulsated one on the first profiles. These pulsations decrease with downstream distance showing that the effect of forcing remains limited to the near-swirler zone. After cut 4 typically, the flow is almost unaffected by forcing and even RMS values are similar for forced and unforced cases.

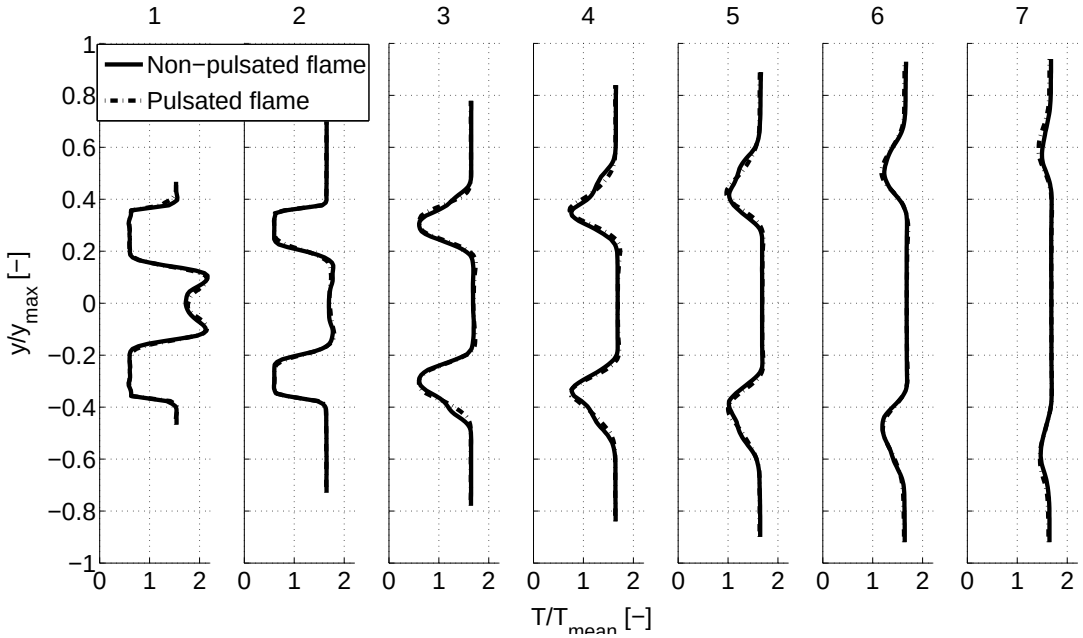

Figure 8.7: +15CBO: Temperature profiles for the averaged pulsated and non-pulsated flame at f_4.

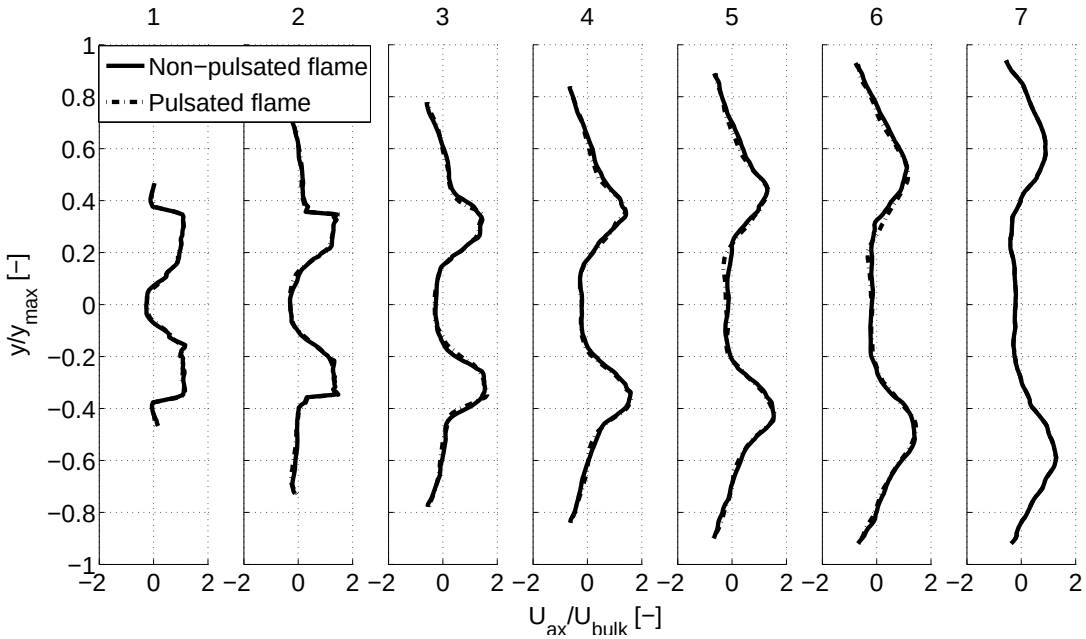

Figure 8.8: +15CBO: Axial velocity profiles for the averaged pulsated and non-pulsated flame at f_4.

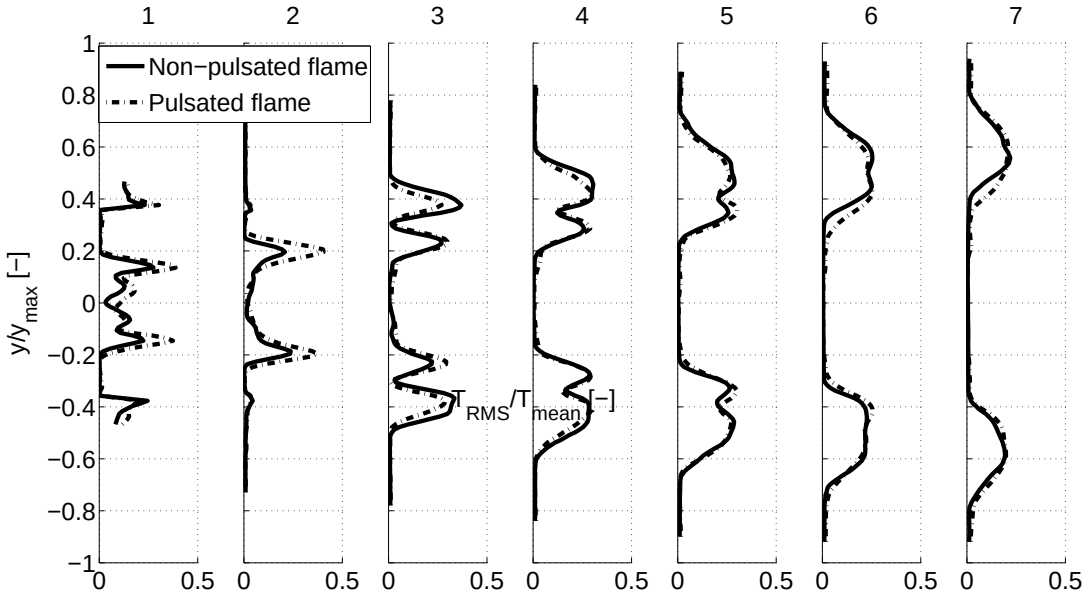

Figure 8.9: +15CBO: RMS temperature profiles for the averaged pulsated and non-pulsated flame at f_4.

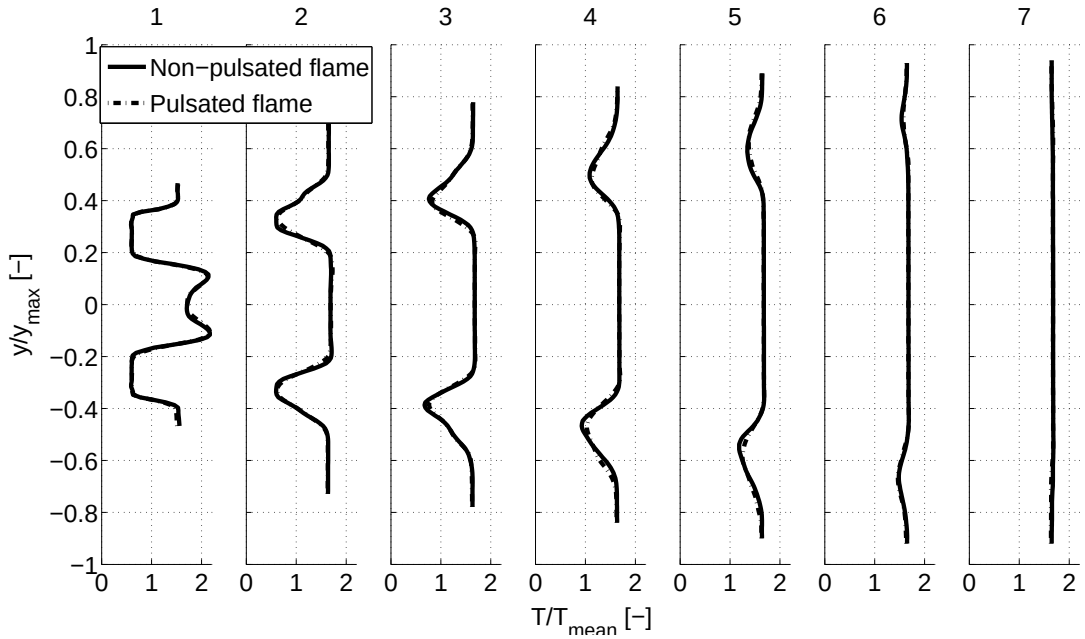

Figure 8.10: +15NBO: Temperature profiles for the averaged pulsated and non-pulsated flame at f_4.

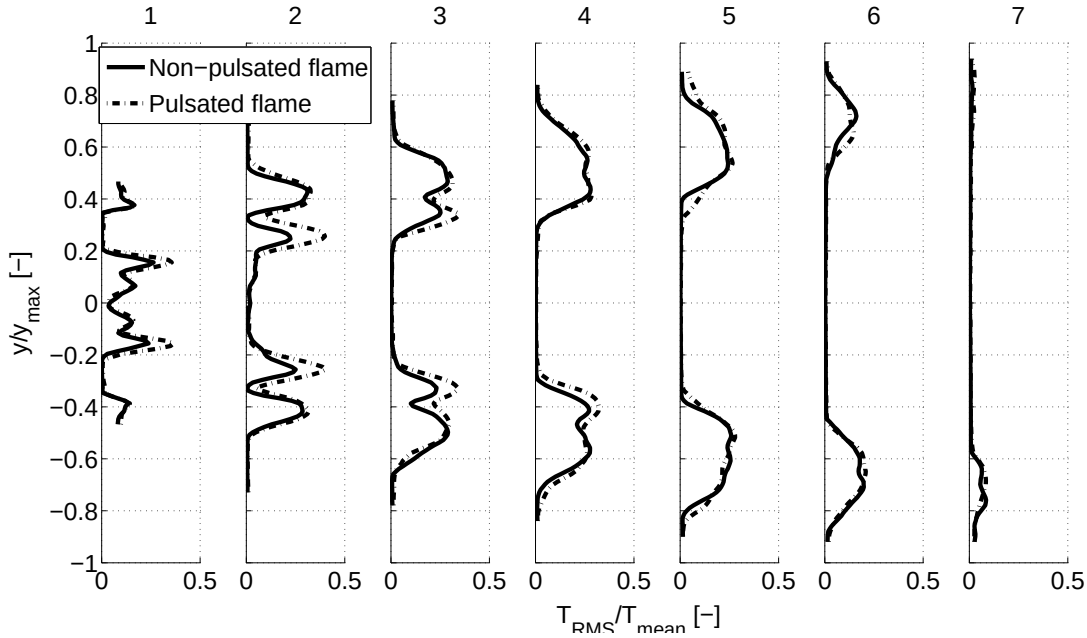

Figure 8.11: +15NBO: RMS temperature profiles for the averaged pulsated and non-pulsated flame at f_4 (+15NBO).

8.3.2 Dynamic flame response

The global flame response for frequency f_4 is shown in Fig. 8.12 with the corresponding reference velocity signal (at reference point A in Fig. 8.1) for both operating conditions and burner outlets and corresponding values for the amplitude and the time delay are given in Table 8.2. The amplitude of both +15 cases is similar whereas a small difference is found between -15CBO and -15NBO with the latter value being slightly higher. As previously mentioned the CBO cases show a shorter time delay whereas the difference in +15 cases is larger than in the -15 operating condition. Following Krebs et al. [103] the time lag increases when adding a CBO compared to the case with no CBO whereas in this study the CBO cases show at both operating conditions a change to shorter time lags. The reason for this apparent discrepancy is investigated in the following.

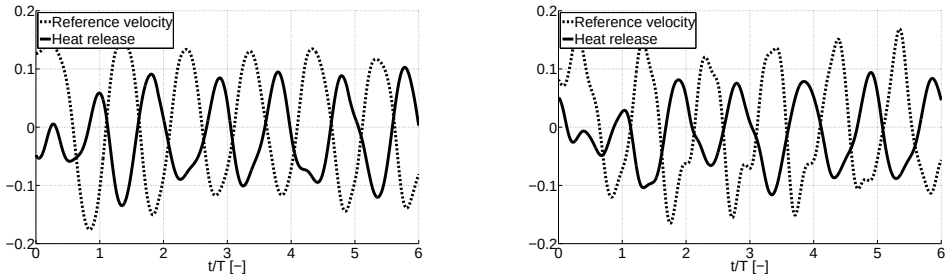

(a) +15CBO

(b) +15NBO

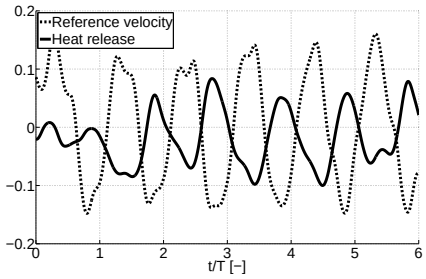

(c) -15CBO

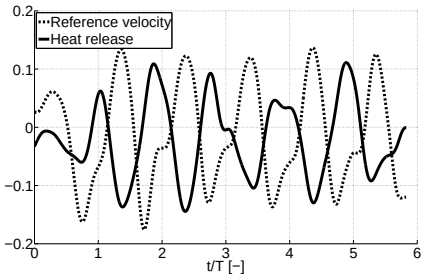

(d) -15NBO

Figure 8.12: Flame response and velocity signal for +15CBO, +15NBO, -15CBO and -15NBO at f_4.

8.3.3 Local comparison of FTF

Experimental studies are usually limited to measurements of global FTFs: the transfer functions between fluctuating velocity at the reference points and the global heat release as discussed in section 8.3.2. With LES, it is also possible to quantify local FTFs giving the transfer function between velocity and local heat release at every point in the burner.

Local FTFs for the four cases of Table 7.2 are shown on longitudinal cuts coloured by the local amplitude and phase in Fig. 8.13 and 8.14 respectively. All flames exhibit maximum response zones in the vicinity of the pilot flame. Both configurations (CBO and NBO) show high gain along the inner flame and low gain along the outer flame. High gain in the CBO geometry occurs over a longer distance in the inner flame whereas the low gain on the outer flame surface is slightly lower in the NBO cases. Globally, a similar local amplitude field occurs for the two geometries and operating conditions. The time delay fields (Fig. 8.14) are plotted in terms of their phase (note that the phase is wrapped and might be shifted by 2π) and show that the flame is not reacting in a compact way for all cases: the phase jumps observed for almost all cases show that at the same instant certain parts of the flame damp the excitation while others feed it. Even flame regions which are located right next to each other exhibit significant differences in delay. Both NBO cases are comparable: the flame tip is reacting with a phase close to 2π to the velocity fluctuation. The CBO cases both show a phase close to π to the velocity fluctuation at the flame tip, whereas -15CBO shows a slightly higher phase.

There is a link between local and global FTF: obviously the overall response of the burner must be the integral of the local response. A consistency equation corresponding to this statement is that

$$n(\omega)e^{-i\omega\tau(\omega)} = \iiint_V n_l(\omega,\vec{x})e^{-i\omega\tau_l(\omega,\vec{x})} \tag{8.2}$$

where the global n and τ are given by Table 8.2 and the local n_l and τ_l are given by Fig. 8.13 and Fig. 8.14. This consistency property is verified in Table 8.3. The global n and τ obtained by Eq. 8.2 and the n and τ obtained from global heat release signals agree reasonably for both amplitude n and phase θ. The flame exhibits local variations in amplitude and time delay response for all cases. It is known that mixture [82, 104, 148] and swirl fluctuations [59, 84, 117, 119, 173] have an strong impact on the flame dynamics. This point is therefore investigated in the following.

8.3.4 Effect of mixture and swirl perturbation

The effect of mixture perturbation on the flame can be analyzed by phase averaging solutions over the heat release oscillation cycle and are shown for the two distinct

	+15CBO	+15NBO	-15CBO	-15NBO
n [-]	0.63	0.67	0.49	0.74
Phase [-]	2.96	3.37	3.34	3.58

Table 8.2: Global FTF: amplitude n and phase θ for +15CBO, +15NBO, -15CBO and -15NBO at f_4.

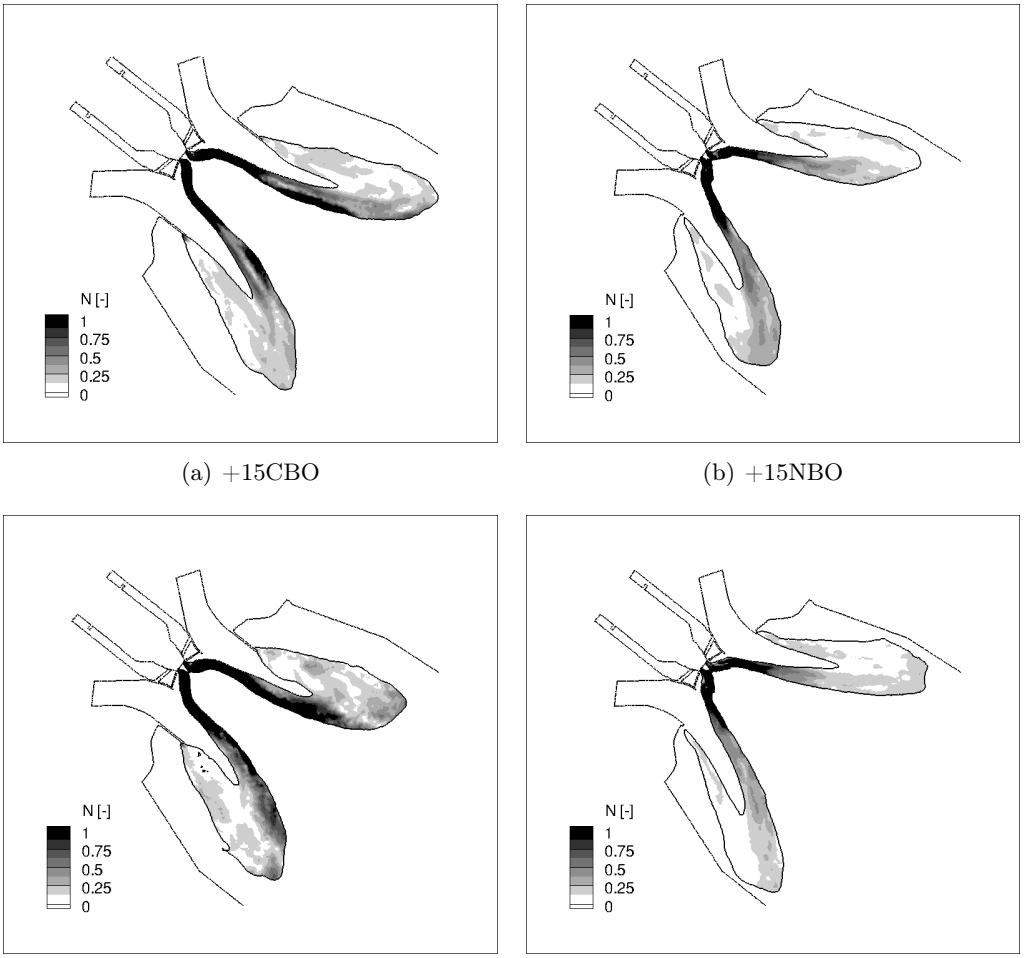

(a) +15CBO (b) +15NBO

(c) -15CBO (d) -15NBO

Figure 8.13: Local amplitude response for the cases +15CBO, +15NBO, -15CBO and -15NBO at frequency f_4.

		+15CBO	+15NBO	-15CBO	-15NBO
global FTF	n [-]	0.63	0.67	0.49	0.74
	Phase [-]	2.96	3.37	3.34	3.58
local FTF	n [-]	0.44	0.55	0.49	0.75
	Phase [-]	2.73	3.18	4.08	3.59

Table 8.3: Comparison between local (obtained by Eq. 8.2) and global FTF (obtained by Eq. 10.1).

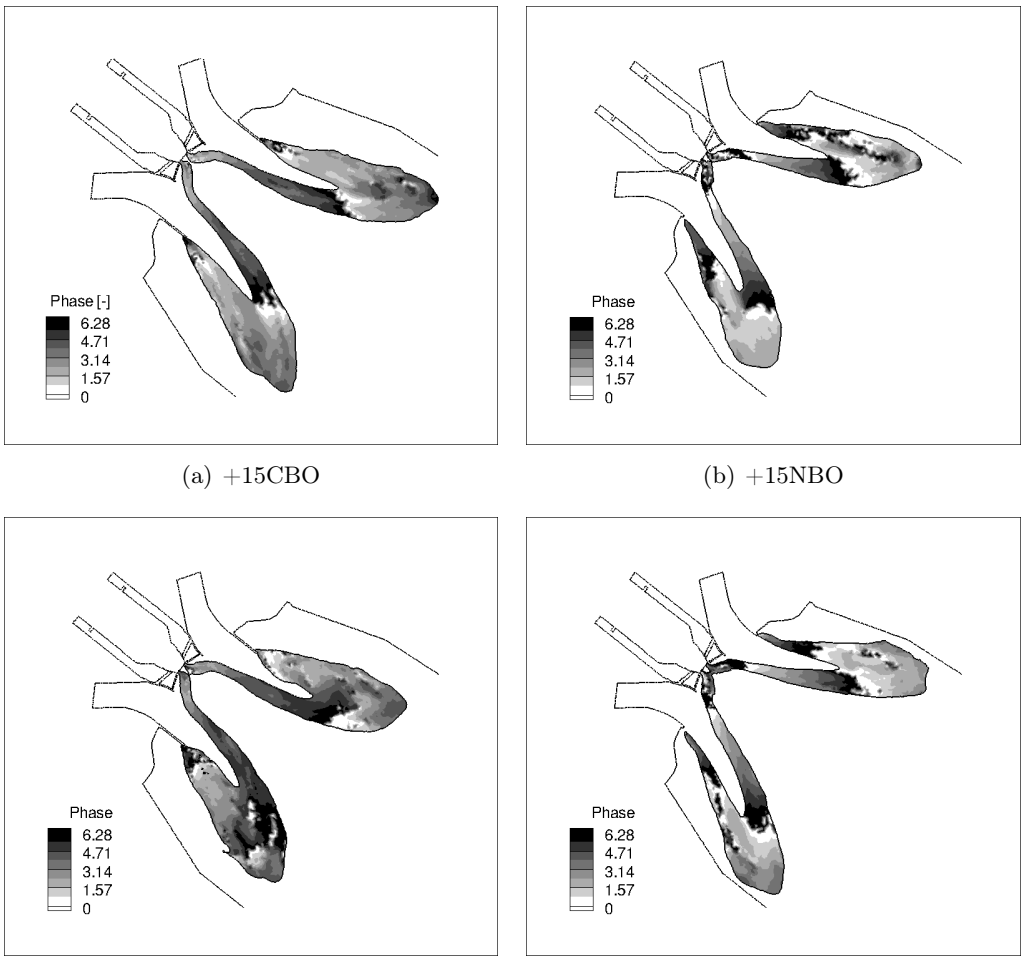

(a) +15CBO (b) +15NBO

(c) -15CBO (d) -15NBO

Figure 8.14: Local phase response for the cases +15CBO, +15NBO, -15CBO and -15NBO at frequency f_4.

oscillation cycles $T/2$ and $3T/2$ in Fig. 8.15 on the middle cut plane coloured by the normalized equivalence ratio and iso-line of the heat release rate. This is only given for +15CBO and +15NBO since -15CBO and -15NBO behave similarly.

First, both configurations show a longer flame at $T/2$ than at $3T/2$. Second, fluctuating mixture during the oscillation cycle appears over a large flame surface area. Along the inner flame region (close to the burner center line), both cases show a strongly rich mixture at $T/2$, which becomes leaner at $3T/2$ explaining the strong amplitude response in this region (Fig. 8.13). In the CBO configurations this rich mixture is present over a longer distance of the burner axis which is also seen on the extent of the strong local amplitude response in Fig. 8.13. Along the outer flame region (close to the chamber walls) the mixture is for both configurations and oscillation cycles predominantly leaner than the global equivalence ratio in the diagonal swirler resulting in a low local gain (Fig. 8.13).

Fluctuations of equivalence ratio ϕ or mixture fraction Z'[1] can be considered as one dimensional waves propagating at the convective speed u_{conv}:

$$\frac{Z'}{\bar{Z}} = A_Z e^{i(\omega x/u_{conv} - \omega t)} \tag{8.3}$$

They can couple with the axial velocity fluctuations u'_{ax}

$$\frac{u'_{ax}}{\bar{u_{ax}}} = A_u e^{i(\omega x/c - \omega t)} \tag{8.4}$$

which travels at the speed of sound c and affect the FTF [82, 104, 148]. The phase difference between both components is of crucial importance. Since the four configurations (+/- CBO/NBO) are forced with the same frequency here, the phase between axial velocity fluctuation and mixture fraction fluctuation is the same until reaching the diagonal swirler outlet. Figure 8.15 shows that both flames exhibit similar equivalence ratio fluctuations along the flame front which results in similar local FTF fields (Fig. 8.13). Considering the additional size of the burner outlet in the CBO case, the convective velocity and the sound speed, the phase between Z' and u'_{ax} changes only slightly between CBO and NBO before reaching the flame. This effect is therefore not considered to be the driving mechanisms being responsible for the differences in FTF. Swirl fluctuations can also have an important effect on FTF [59, 84, 117, 119, 173] but are for the same reason not considered to be responsible for the differences.

8.3.5 Concluding remarks

This section compared the dynamic flame response to an acoustic perturbation for two operating conditions and two burner outlets. The averaged velocity and temperature profiles between pulsated and non-pulsated cases agree well for all cases.

[1] The equivalence ratio ϕ is linked to Z by $\phi = Z/(1-Z) \cdot (1-Z_{st})/Z_{st}$

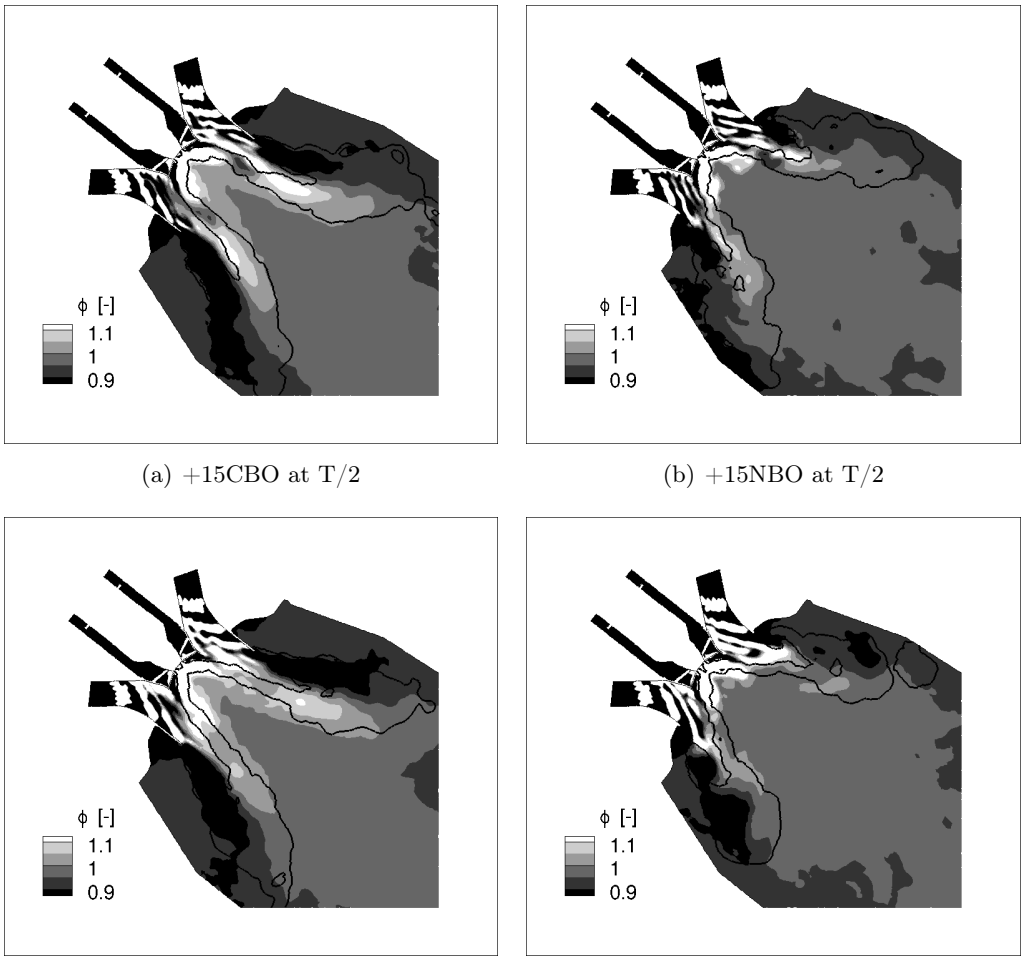

(a) +15CBO at T/2

(b) +15NBO at T/2

(c) +15CBO at 3T/2

(d) +15NBO at 3T/2

Figure 8.15: Normalized equivalence ratio field and iso-line of heat release rate on the middle cut plane for +15CBO and +15NBO at T/2 and 3T/2 phase averaged over the heat release oscillation cycle.

RMS temperature profiles reveal that the NBO cases undergo slightly stronger fluctuations than the CBO cases. Distinct equivalence ratio fields of the oscillation cycle reveal that mixture perturbations propagate similarly to and on the flame surface for both configurations.

The global flame response in terms of n and tau shows that the CBO cases have a slightly shorter time lag than the NBO cases although the flame is slightly longer. This result is contradictory to Krebs et al. [103] who states that the time lag increases when adding a CBO compared to the case with no CBO. Although an uncertainty exists regarding the values of amplitude and time delay found in this work, the shorter CBO delay is explained as follows: first, the length of the averaged flame is only slightly shorter in the NBO case as found in chapter 7. Second, even though hypothetically the time delay values could be shifted by 2π, a significantly higher time delay for the NBO case is less probable. To support this, the length of the flame is additionally evaluated defined as the distance from the lance to the flame tip. It is found that the CBO flame is about 1.15 times longer. The acoustic fluctuation perturbs the flame front which is convectively transported to the flame tip and the time needed even for a convective perturbation to reach this additional part is only of $1/5T$ based on the bulk velocity. This means that a different mechanism is at play causing the NBO flame to react slightly later. The mean velocity profiles in Fig. 7.10 to 7.14 show that the CBO cases possess a higher axial velocity at the burner outlet. Vortices are formed due to shear at the burner outlet in the outer flame region and in the inner region where the mass flow of axial and diagonal meet. These vortices convect along the flame front and control the dynamic flame response. Since the convective velocity is higher in the CBO cases this can lead to a lower time delay as the differences in flame length are small. Sensiau et al. [158] noticed that even small changes in time delay can lead to important effects on the stability and found the transition between amplification and damping to be at half the period T with damping occurring at $\tau < T/2$. The time lags found for this frequency f_4 correspond to this. One can state furthermore, that a simple model taking only into account the flight time is not appropriate [51]: as shown by [150], even though FTF delay scales to first-order like the flame length divided by the bulk velocity for very simple flames, additional mechanisms in real chambers make flight time estimates of the delay doubtful in complex combustors. The amplitude of the global FTF varies only slightly for all cases. Local FTFs of all cases revealed that +15NBO and -15NBO behave similarly in terms of n and tau whereas differences between +15CBO and -15CBO occur slightly for the amplitude in the inner flame region and especially for the time delay.

8.4 Effects of forcing frequencies

The aim of this section is to analyze the differences of the global FTF when the forcing frequency changes. Only one case (+15CBO) is considered and analyzed at the different forcing frequencies f_1 to f_4. Note that also here the averaged non-pulsated and pulsated flames agree very well for all frequencies and confirm hence the assumption used to linearize equations [31]. The RMS fluctuations behave for all cases similarly to +15CBO at f_4. This point shall not be discussed in detail here.

8.4.1 Dynamic flame response

The FTF of the +15CBO case with single frequency forcing is summarized in Table 8.4 in terms of n and τ. At frequency f_1 an overshoot in amplitude arises and the time delay is lower than at the other frequencies. Time lags are similar at f_2 and f_3 but f_2 shows a slightly higher amplitude. The time lag of f_4 is higher than for f_1 but still lower than for f_2 and f_3 with an amplitude between the latter.

8.4.2 Local comparison of FTF

The local FTFs allow a further insight into flame responses. The gain in Fig. 8.16 reveals that the flame reacts strongly close to the lance at all frequencies. This zone is important but note that it is also very small and may not control the overall flame response of the burner. The global overshoot at frequency f_1 is caused by high local responses all along the inner flame region and the flame tip. Between frequencies f_2 to f_4 the differences in local gain occur mainly in the flame tip region. High local values there, lead also to a higher global amplitude response suggesting that the flame tip is responsible for the amplitude response change in this configuration. In all cases the local gain is low at the outer flame region, whereas it is slightly higher at f_1. The local phase at frequency f_1 is close to 2π at the flame tip and around $\pi/2$ at the swirler outlets (Fig. 8.17). The global phase of 0.89, is clearly formed out of the different local responses. The phase at f_2 and f_3 is more uniformly distributed, whereas non-uniformities are stronger again at f_4. The flame is not compact even at the lowest frequency f_1.

	f_1	f_2	f_3	f_4
n [-]	1.11	0.78	0.47	0.63
Phase [-]	0.89	1.89	2.70	2.96

Table 8.4: Global FTF: amplitude n and phase θ for +15CBO at f_1, f_2, f_3 and f_4.

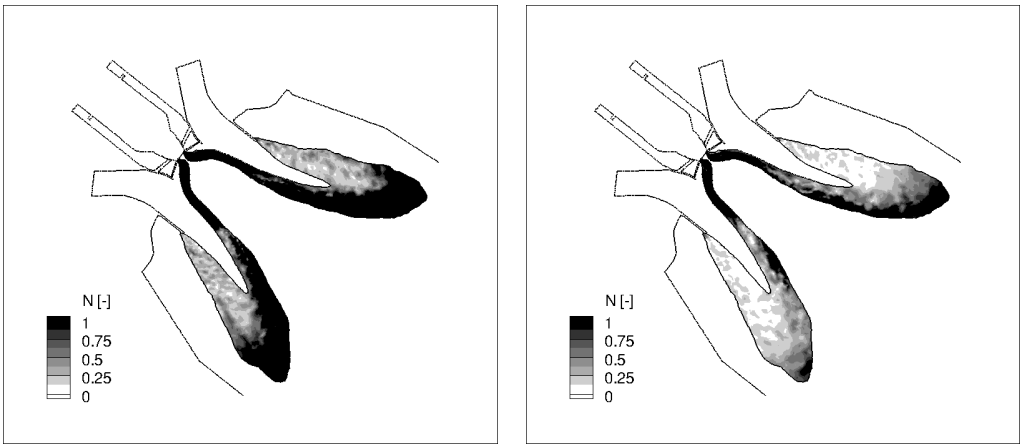

(a) f_1 (b) f_2

(c) f_3 (d) f_4

Figure 8.16: Local amplitude response for +15CBO at frequencies f_1, f_2, f_3 and f_4.

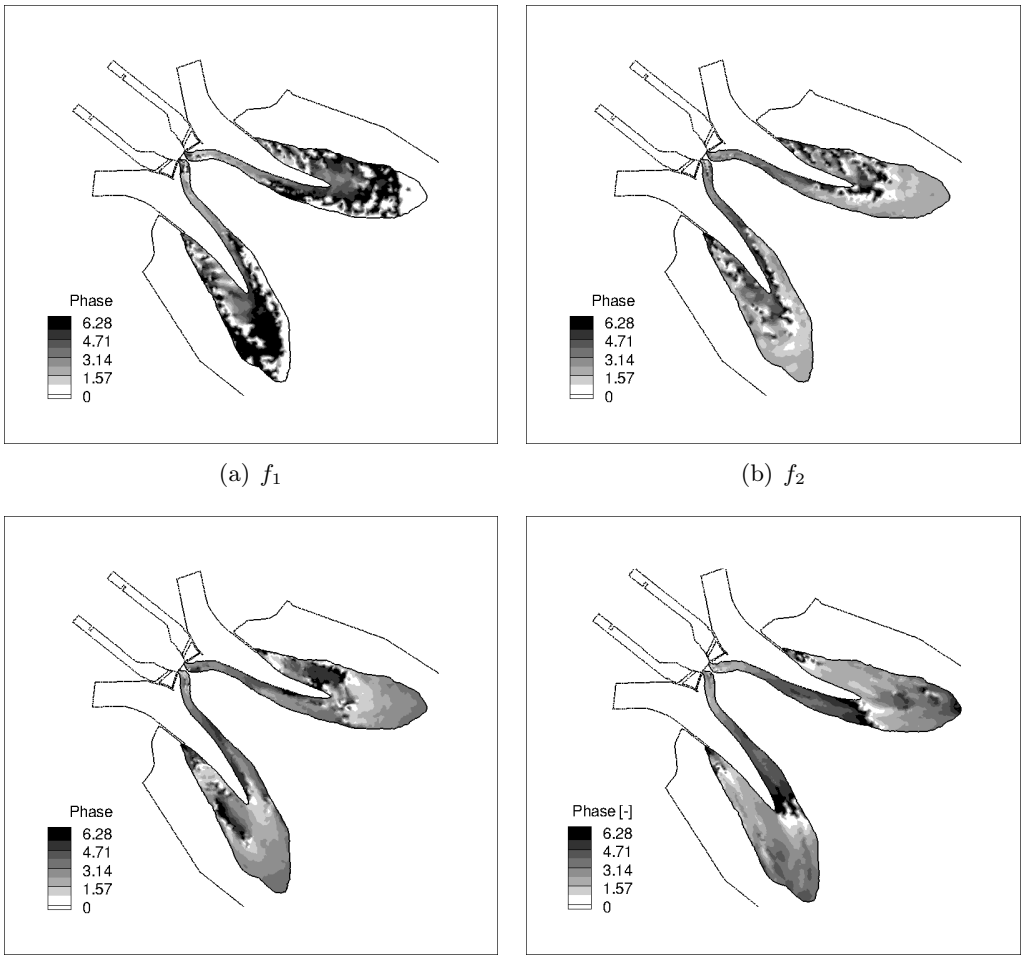

(a) f_1 (b) f_2

(c) f_3 (d) f_4

Figure 8.17: Local phase response for +15CBO at frequencies f_1, f_2, f_3 and f_4.

8.4.3 Effects of fuel heterogeneities and swirl perturbation

In this section, the effects of mixing for pulsated regimes are investigated. Since pure fuel is injected in the vanes of the diagonal swirler, two phenomena take place during forcing:

- fuel and air have to mix in the diagonal passage before they enter the chamber. Even if the injected air and fuel flow rates are constant, this local phenomenon may be too slow to ensure perfect mixing in the chamber inlet plane (plane A in Fig. 8.18).
- in addition, fuel and air flow rates both fluctuate, changing the mean equivalence ratio of the injected gases and creating unmixedness.

These two effects combine to lead to a mixture in reference plane A at the combustor inlet (Fig. 8.18) which has an oscillating mean equivalence ratio (averaged over the section of the passage) but also an oscillating spatial distribution. To analyze this question, this section focusses on the analysis of LES results between the diagonal passage inlet and the combustor inlet for +15CBO. The analysis does not include what is taking place at the axial swirler: most of the fuel and air enters the chamber through the diagonal swirler and in a first approach, it is assumed that this is the most important part of the burner.

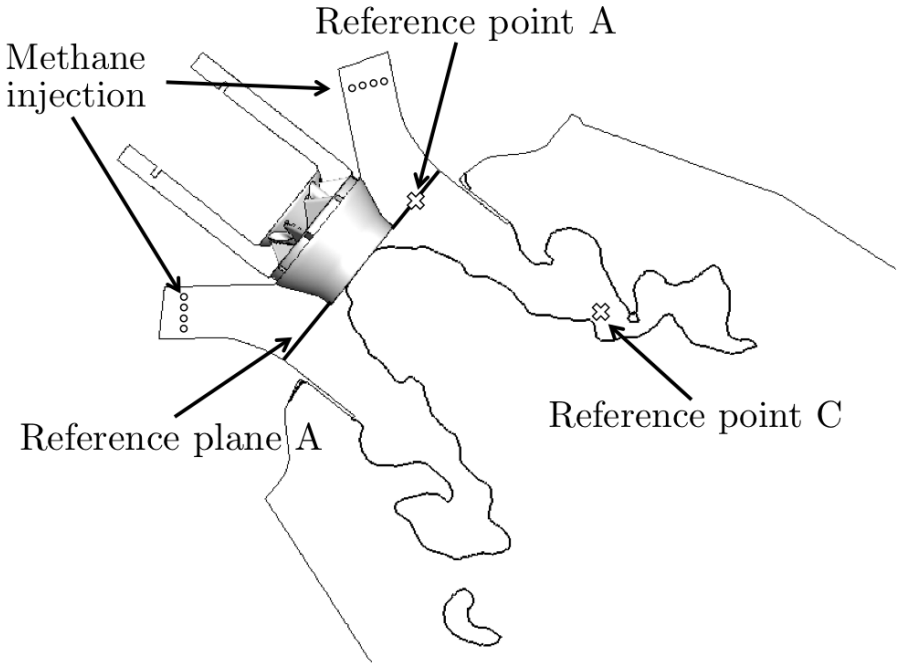

Figure 8.18: Location of reference point A, plane A and reference point C.

The global mixture fraction Z through the diagonal passage is calculated with:

$$Z = \frac{\dot{m}_{CH4}}{\dot{m}_{Air} + \dot{m}_{CH4}} \tag{8.5}$$

and results from the fluctuating air mass flow rate at the diagonal inlet $\dot{m}_{Air}$ (Fig. 8.19) and the fuel mass flow rate through the premixing nozzle $\dot{m}_{CH4}$ (Fig. 8.20). Both flow rates are shown as normalized fluctuations $\dot{m}'/\dot{m}$ over the forcing period.

The velocity perturbation introduced at the inlet of the diagonal swirler leads to

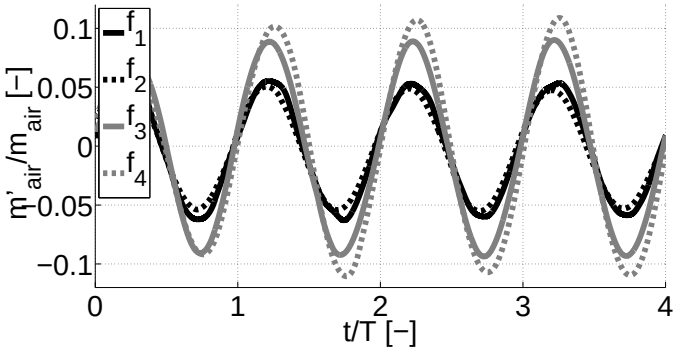

Figure 8.19: Relative variations of the air mass flow rate at diagonal inlet at frequencies f_1, f_2, f_3 and f_4.

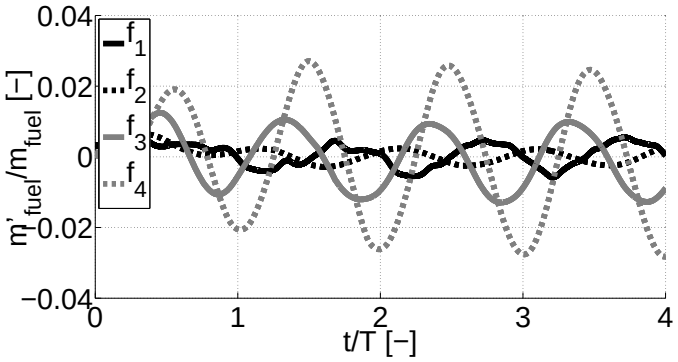

Figure 8.20: Relative variations of the fuel mass flow rate at diagonal inlet at frequencies f_1, f_2, f_3 and f_4.

a perturbation of the air mass flow rate of the order of 5 to 10%. The fuel fluctuations result from the oscillating pressure perturbations at the injection holes: they depend on the stiffness of the boundary condition imposed at the fuel inlet. Here, they lead to a relative modification of the fuel flow rate which is much less than for the air. Typically, the fuel flow rate varies by 1 to 2 % at most (Fig. 8.20) and a phase difference is visible. Since the air mass flow rate is fluctuating at much higher amplitude, this has only small effects on the global mixture fluctuation (Fig. 8.21) which fluctuates by 8 to 10 %. Fluctuations of mixture propagate at the

convective speed to the flame front and are damped through the swirler as shown by the time variation of the mixture fraction averaged over the reference plane A in Fig. 8.22. First the mixing fluctuations introduced at the diagonal inlet (Fig. 8.21) do not disappear in the passage: at the combustor inlet section (reference plane A in Fig. 8.18) Z still changes by ±5%, compared to + or - 8 to 10 % at the diagonal inlet. The diagonal passage is not long enough to damp fuel heterogeneities introduced by the fluctuations. Second, as expected, higher frequencies (f_4) are damped more than low frequency fluctuations (f_1).

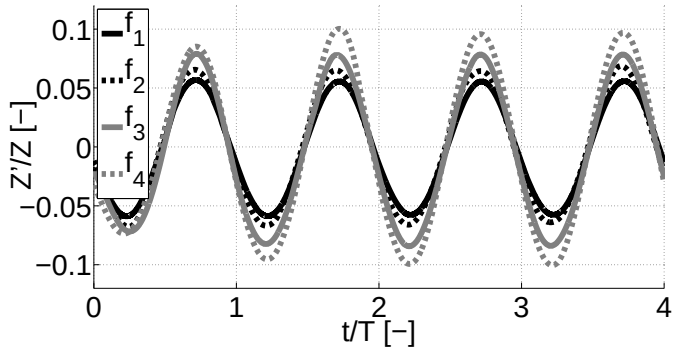

Figure 8.21: Global mixture fraction (Eq. 8.5) at diagonal inlet for frequencies f_1, f_2, f_3 and f_4.

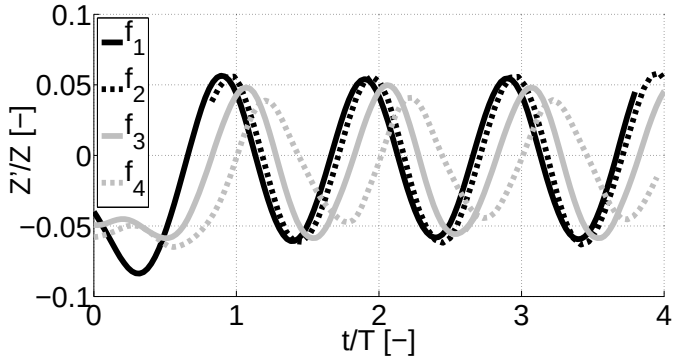

Figure 8.22: Global mixture fraction averaged over reference plane A for frequencies f_1, f_2, f_3 and f_4.

A phase difference appears for the different frequencies indicating a different phase between axial velocity perturbation and mixture fraction oscillation. Following Kim et al. [82] this has an impact on the amplitude response of the flame: When the two perturbations are out of phase richer mixtures enter the combustion chamber with low velocity, and mixtures with lower equivalence ratio reach the flame front with high velocity. The flame sees nearly the same amount of fuel during a cycle

of oscillation. Therefore, the heat release rate does not vary significantly and a low amplitude response results.

In a first step, to see the impact of mixture fraction fluctuations over the heat release oscillation cycle, phase averaged solutions are shown in Fig. 8.23 and 8.24 at $T/2$ and $3T/2$ respectively. Although the global FTF response is different (table 8.4), significant similarities are found: for all frequencies, the normalized equivalence ratio is the highest at the maximum of the global heat release and a richer mixture reaches the highest flame surface (on the inner flame in axial direction) for all oscillation cycles. Note that phase averaged solutions are taken for $2T$, $T/2$, T and $3T/2$ whereas only $T/2$ and $3T/2$ are shown here. At $3T/2$, the phase corresponding to the lowest global heat release, equivalence ratio fluctuations meeting the flame front

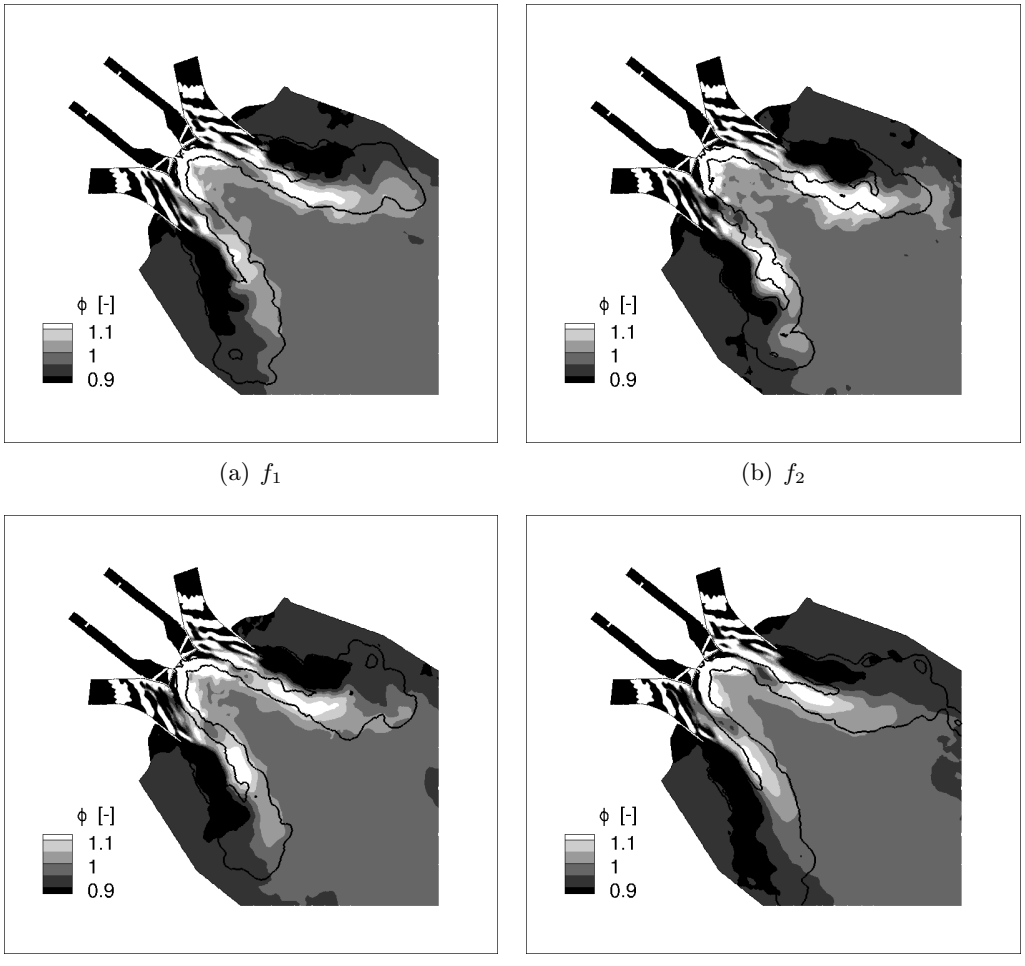

(a) f_1 (b) f_2

(c) f_3 (d) f_4

Figure 8.23: Normalized equivalence ratio field and iso-line of heat release rate on the middle cut plane for +15CBO phase averaged at the maximum of the heat release oscillation cycle for frequencies f_1, f_2, f_3 and f_4.

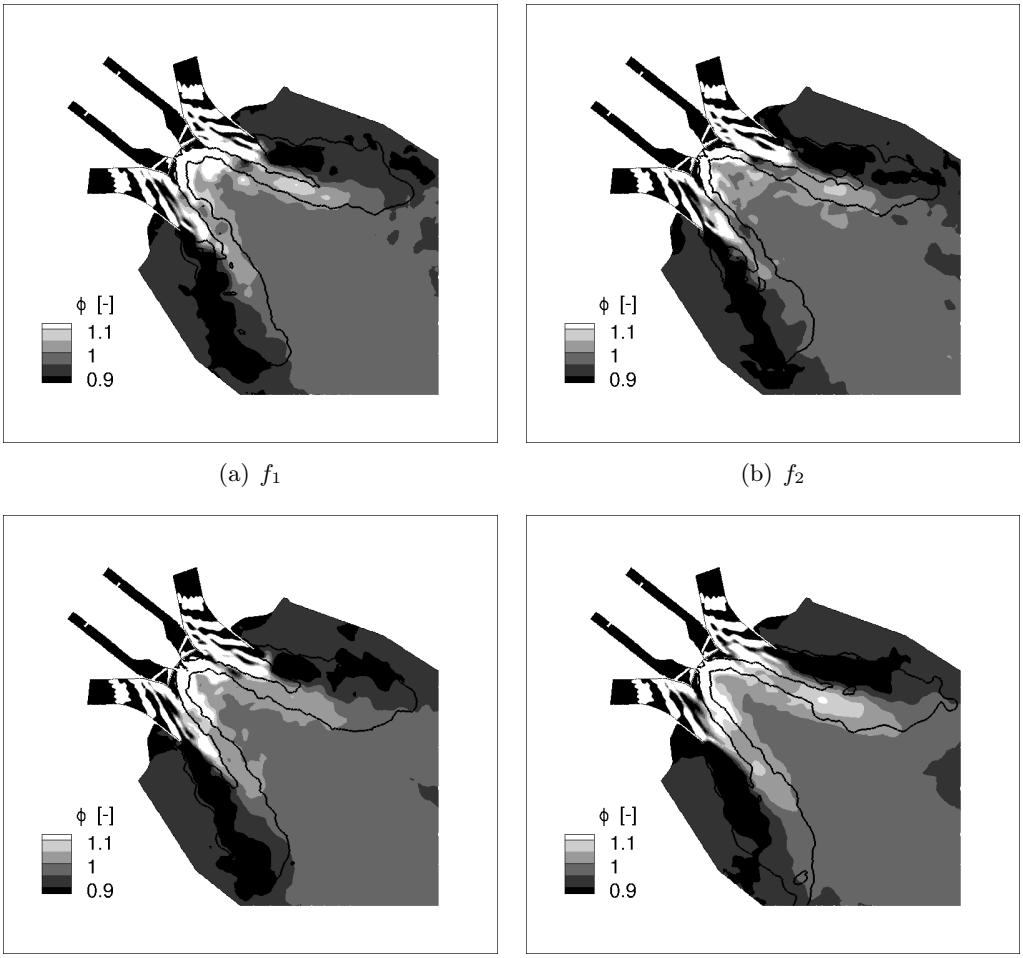

(a) f_1 (b) f_2

(c) f_3 (d) f_4

Figure 8.24: Normalized equivalence ratio field and iso-line of heat release rate on the middle cut plane for +15CBO phase averaged at the minimum of the heat release oscillation cycle for frequencies f_1, f_2, f_3 and f_4.

are also lowest for all cases (Fig. 8.24). Nevertheless, high equivalence ratios are still present near the lance due to pilot injection.

The equivalence ratio field is similar for the four frequencies with respect to the heat release oscillation cycle: Fig. 8.23 and 8.24 suggest that the rich mixture region in the inner flame region close to the flame tip is responsible for this since it is the most significant difference occurring during the different oscillation cycles. Furthermore, local FTF delay fields (Fig. 8.17) prove the that differences in phase are mainly due to differences in the flame tip region. Here, also the local FTF amplitude (Fig. 8.16) shows the highest differences between the forcing frequencies. To address this issue, it is useful to plot Z, u' and Q' near the flame tip. This can be done using Eq. 8.3 and 8.4: the mixture fraction and axial velocity fluctuation measured at reference

plane A is shifted to a reference point C shown in Fig. 8.18. The mixture fraction fluctuation is transported with the convective velocity for which the bulk velocity is taken. The axial velocity fluctuation propagates with the speed of sound which is given through the inlet temperature. For simplicity reasons, damping effects on the fluctuations are not accounted for. The resulting relative axial velocity, mixture fraction and heat release fluctuation at reference point C are shown in Fig. 8.25 to 8.28 for frequencies f_1 to f_4 leading to an interesting observation (Table 8.5). At point C, the phase between mixture fraction Z' and heat release Q' fluctuation is the same for all frequencies while the phase between velocity perturbation u' and Q' changes significantly (it increases with frequency). This result suggests that the heat release is synchronized with the fluctuation of mixing and not with the velocity for this regime.

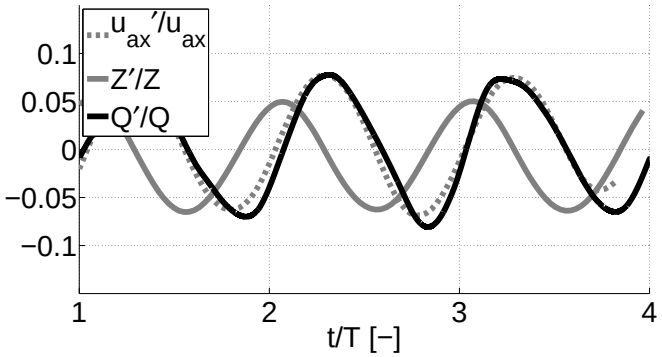

Figure 8.25: Relative axial velocity, mixture fraction and heat release fluctuation at reference point C for frequency f_1.

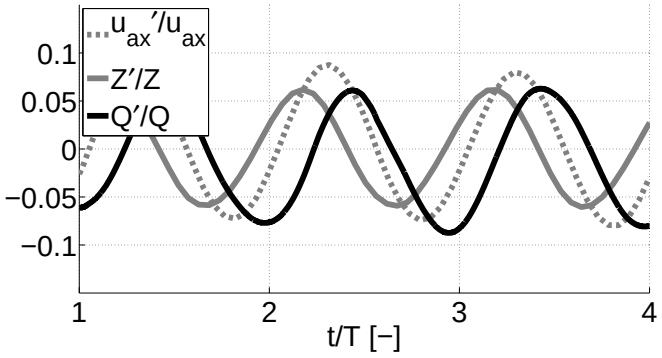

Figure 8.26: Relative axial velocity, mixture fraction and heat release fluctuation at reference point C for frequency f_2.

A third effect of the ingoing acoustic wave besides the acoustic perturbation normal to the flame front and the convectively transported mixture fluctuation is the effect of swirl number perturbations [59, 84, 173]. When acoustic perturbations impinge the swirler, an axial and azimuthal velocity fluctuation is created travelling with

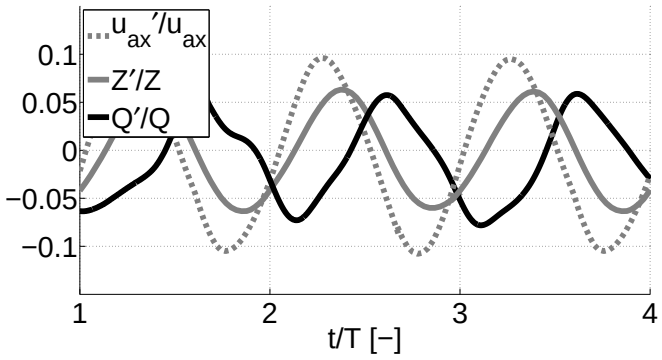

Figure 8.27: Relative axial velocity, mixture fraction and heat release fluctuation at reference point C for frequency f_3.

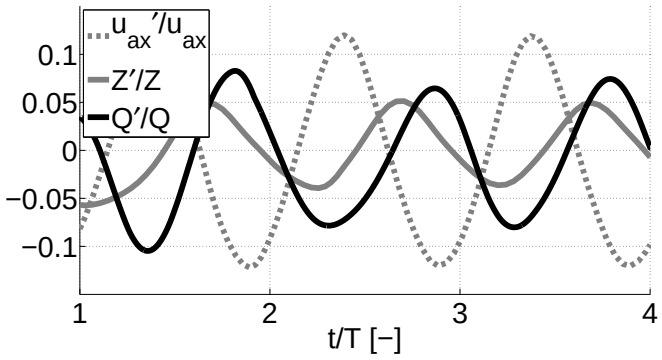

Figure 8.28: Relative axial velocity, mixture fraction and heat release fluctuation at reference point C for frequency f_4.

	f_1	f_2	f_3	f_4
Phase between Z' and Q' [-]	1.69	1.64	1.52	1.26
Phase between u' and Q' [-]	0.27	0.77	2.21	2.91

Table 8.5: Phase angle (radian) of mixture fraction and axial velocity to the heat release rate oscillation at reference point C for f_1, f_2, f_3 and f_4.

the speed of sound and the convective velocity respectively [117, 119]. This is illustrated in Fig. 8.29. At the trailing edge of the swirler vanes (plane 1), the axial u_{ax} and azimuthal u_θ velocities are in phase. Since both components are propagating with different velocities, their phase at plane 2 can take any value depending on the length L. This phase is one of the parameters which control swirl variation at the chamber inlet. As the vortex breakdown changes with the swirl number, the size and position of the recirculation zones change and affect thus the flame angle. Palies et al. [117] state that an overshoot occurs when axial and azimuthal velocity are in phase when impinging the flame front and low amplitude when both components are out of phase. However, an increasing air mass flow rate at the fuel injection leads to a decrease of mixture fraction Z (Fig. 8.19 and 8.21) so that u_{ax} and Z are out of phase at plane 1 (supposing that the distance from the fuel injection to the vane trailing edge is small). This means that u_θ and Z are out of phase at plane 1 and since they are propagating at the same convective velocity they are also out of phase at plane 2.

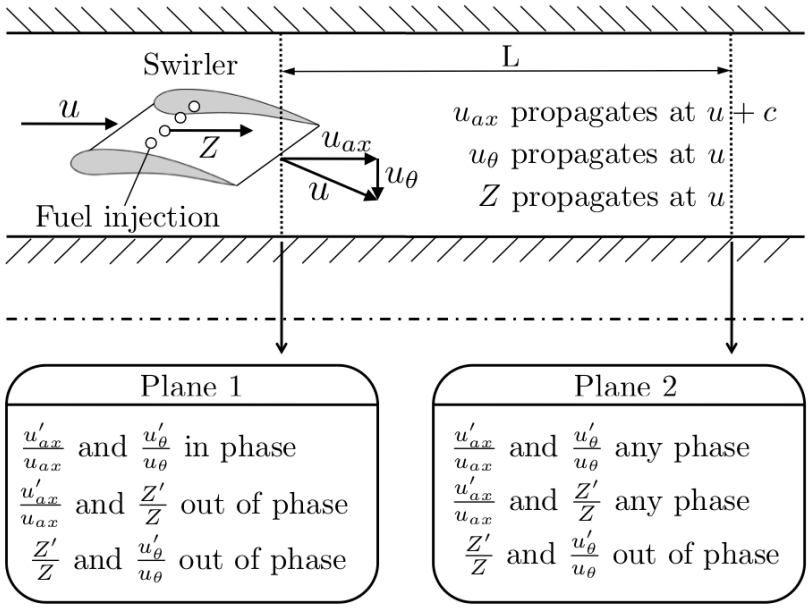

Figure 8.29: Illustration of the propagation of swirl number and mixture perturbations.

Figure 8.30 to 8.33 show the relative axial ($u'_{ax}/\bar{u_{ax}}$), the azimuthal velocity ($u'_\theta/\bar{u_\theta}$) components and the relative mixture fraction fluctuation $Z'/\bar{Z}$ at the reference plane A as a function of normalized time for the frequencies f_1 to f_4. Mixture fraction and azimuthal velocity are fluctuating nearly out of phase for all frequencies. The phase angle between u'_θ and Z' is constant over the geometry (in the cold gases) since both are propagating at the same convective velocity so that u'_θ and Z' are both acting on the flame with opposite effects on the amplitude response. Here, the flame is long and anchored at two different positions (lance and CBO) so that it is

not clear where both components act most importantly on the flame.

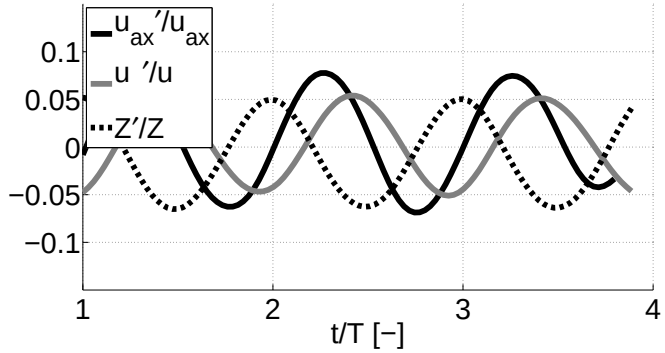

Figure 8.30: Relative fluctuation of axial velocity $u'_{ax}/\bar{u_{ax}}$, azimuthal velocity $u'_\theta/\bar{u_\theta}$ and mixture fraction $Z'/\bar{Z}$ at reference plane A for frequency f_1.

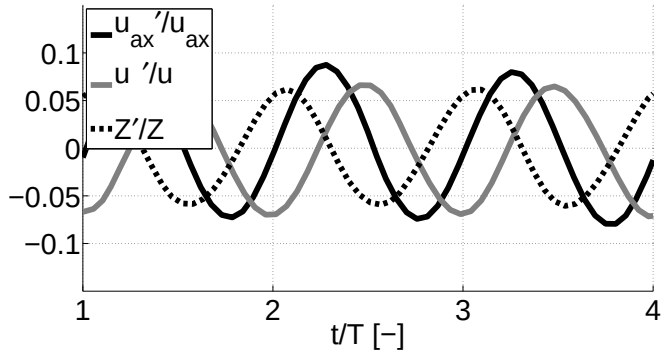

Figure 8.31: Relative fluctuation of axial velocity $u'_{ax}/\bar{u_{ax}}$, azimuthal velocity $u'_\theta/\bar{u_\theta}$ and mixture fraction $Z'/\bar{Z}$ at reference plane A for frequency f_2.

8.4.4 Concluding remarks

The dynamic flame response for one case (+15CBO) at four frequencies showed differences in the global FTF for the amplitude as well as the time delay. The local FTF gain fields reveal that these differences are due to different responses at the flame tip and along the inner flame region. The flame is not compact as evidenced by the local FTF delay fields. Phase averaged solutions over the heat release oscillation cycle show strong similarities between the equivalence ratio field at the different frequencies. Rich mixture enters the region close to the flame tip in all cases. Mixture fraction perturbation at the tip have a similar phase to the heat release oscillation for the four frequencies suggesting that the mixture fraction fluctuation at least partially controls the FTF delay. Since the mixture fraction propagates at the convective speed, the changes in global time delay can be explained. Although this is the important mechanism in this configuration, the effect of axial velocity on the

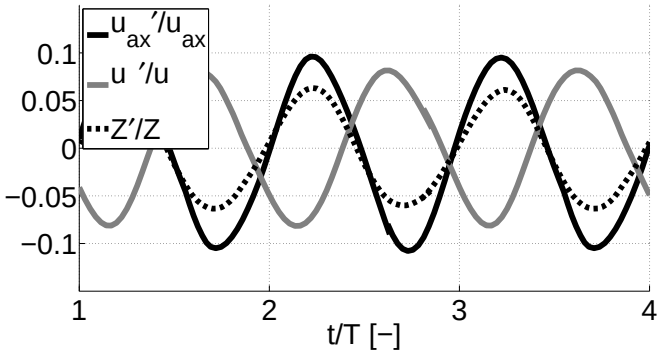

Figure 8.32: Relative fluctuation of axial velocity $u'_{ax}/\bar{u_{ax}}$, azimuthal velocity $u'_\theta/\bar{u_\theta}$ and mixture fraction $Z'/\bar{Z}$ at reference plane A for frequency f_3.

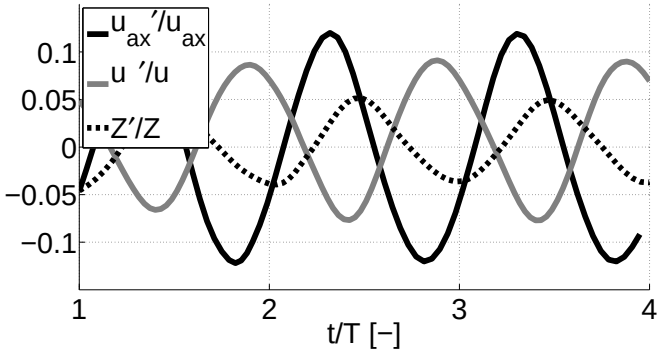

Figure 8.33: Relative fluctuation of axial velocity $u'_{ax}/\bar{u_{ax}}$, azimuthal velocity $u'_\theta/\bar{u_\theta}$ and mixture fraction $Z'/\bar{Z}$ at reference plane A for frequency f_4.

global FTF is still present. Furthermore, azimuthal velocity fluctuations are propagating out of phase with the mixture fraction oscillations. Its impact (and also of the mixture fraction oscillation) on the global FTF gain still remains a matter of investigation.

Obviously, the present analysis fails to clearly identify individual mechanisms controlling FTFs because they all play a role at the same time. In the next chapter, a new strategy will be utilized: additional LES are performed to isolate mechanisms and study their effects separately. In a first simulation a fully premixed flow is injected in the diagonal passage in order to investigate only the effect of axial velocity perturbation. Then, only fuel is pulsated at the diagonal inlet to analyze only the effect of mixture fraction fluctuation decoupled from the axial velocity perturbation.

Chapter 9

Identification of mechanisms controlling FTFs

Contents

The mechanisms controlling FTF have been studied extensively for simple laboratory flames but much less information is available for real gas turbines. Previous chapters have shown that one of the specificities of gas turbine chambers is that several mechanisms control the flame dynamics (Fig. 9.1). The fluctuating air and fuel inlet mass flow rates in the diagonal swirler cause oscillations of mixture fraction, axial velocity and swirl number which combine and act on the flame. When LES of FTF are performed, they integrate these three mechanisms and the LES results are certainly valid. However, understanding what controls FTF and how they can be modified requires to be able to isolate mechanisms. Additional LES are performed here to reach this goal.

This chapters' goal is to exclude one mechanism after the other to study separately its effect on this complex flame. Therefore the +15CBO case will be considered at one frequency f_4 and compared against two additional LES of the same geometry:

- For the first one, a fully premixed flow is passing through the diagonal swirler (Section 9.1) thereby cancelling any potential effect on the FTF due to modulated mixing and focussing on the effect of mass flow rate perturbation.
- A second simulation is performed in Section 9.2 where only the fuel at the diagonal swirler is fluctuated and the main air mass flow rate through the

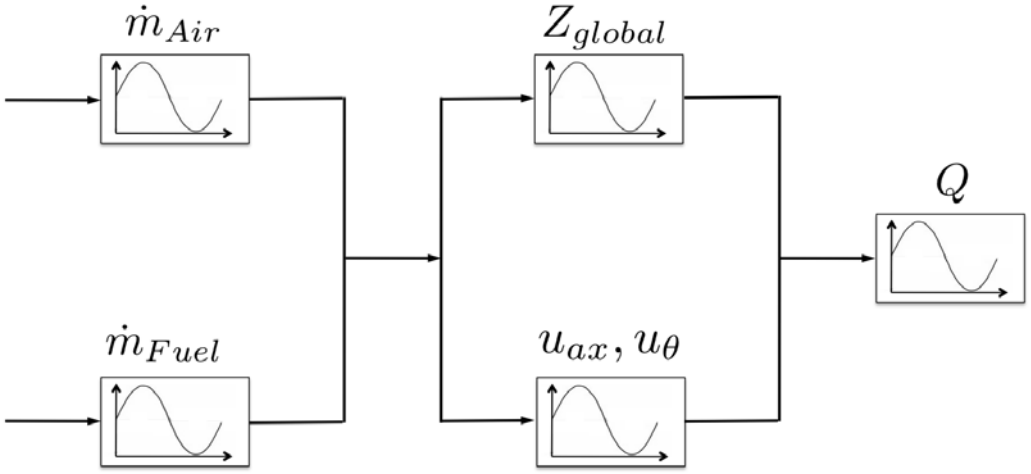

Figure 9.1: Schematic description of the pulsation mechanisms in the gas turbine. In previous chapters, $\dot{m}_{Air}$ and $\dot{m}_{Fuel}$ were both pulsated. Here, only one will be pulsated for each case.

diagonal swirler is kept constant in order to cancel out the effect of fluctuating mass flow rate and to study only the influence of mixture fluctuation.

At the end of the chapter, a FTF based on a relation between Q' and (u', Z') is proposed (following Huber [64]) and tested to replace the usual Q' versus u' FTF used up to now in this thesis. This evolution from SISO (Single Input Single Output) models to a MISO (Multiple Inlet Single Output) model is a promising path to describe combustion instabilities in gas turbines.

9.1 Effects of mass flow rate perturbation

To analyze the effect of mass flow rate fluctuation separately, an additional LES is performed with a fully premixed flow passing through the diagonal swirler thereby cancelling any potential effect on the FTF due to modulated mixing (Fig. 9.2). This will be performed for the +15CBO case at forcing frequency f_4. Table 9.1 gives the nomenclature used here. The pilot flame injection in the axial swirler is not changed.

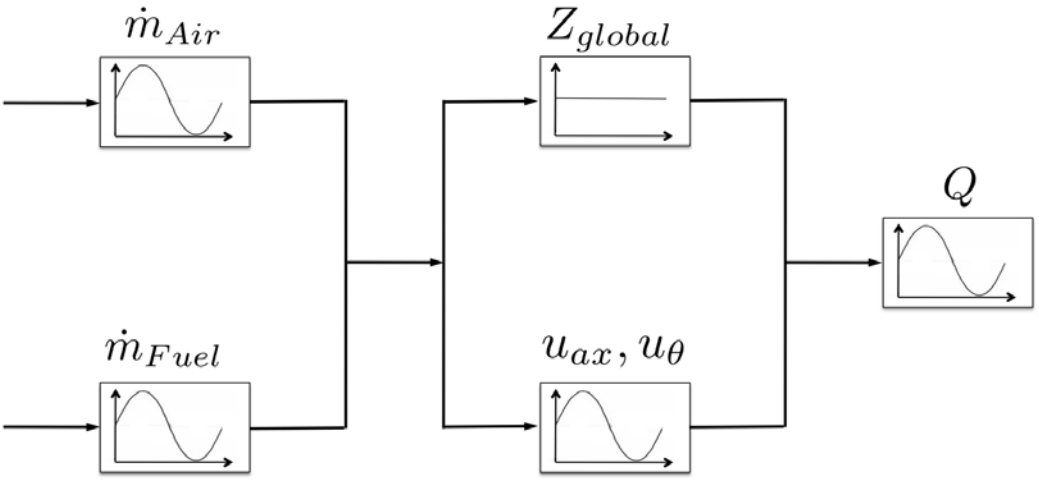

Figure 9.2: Schematic description of the pulsation mechanisms in the gas turbine with a fully premixed diagonal swirler. Only the inlet velocity u changes.

Case	Fuel injection in diagonal swirler	Fuel injection in axial swirler
TECH	By holes located in the vanes	Pilot flames (pure CH_4)
FULL	Fully premixed	Pilot flames (pure CH_4)

Table 9.1: Description of investigated cases: TECH and FULL. Both cases correspond to +15CBO.

9.1.1 Mean reacting flow fields

In a first step, both cases (TECH and FULL) are compared by analyzing their averaged flow fields.
The normalized equivalence ratio $\bar{\phi}$ and an iso-line of temperature are shown in Fig. 9.3 for the mean flows. The equivalence ratio is normalized by its value at the inlet of the diagonal swirler for the FULL case. In the TECH case the non-uniformity of mixture in the diagonal swirler is clearly visible. However, mixing takes place due to the rotational fluid motion and a quasi-uniform mixture reaches

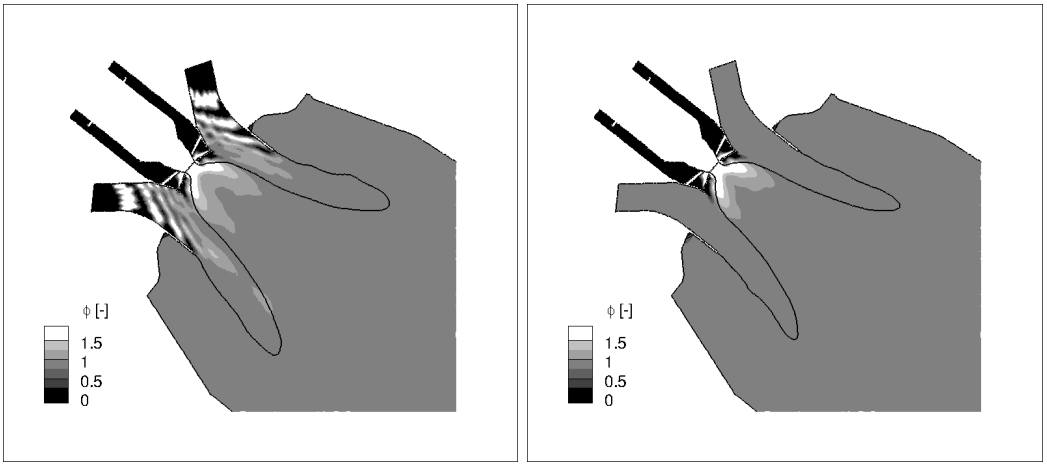

Figure 9.3: Normalized averaged equivalence ratio field and temperature iso-line for the TECH (left) and the FULL (right) case.

the flame front. Of course, for the FULL case, the mixture in the diagonal swirler has a constant equivalence ratio ($\bar{\phi} = 1$). Figure 9.3 shows that the two flames are very similar in terms of shapes. The mean fields of both configurations are similar and remain similar with the forced fields (not shown): the assumption used to linearize equations [31] is fulfilled here too. For the sake of completeness, the flames of the technically premixed and fully premixed case are only shortly compared in terms of averaged pulsated solutions in Fig. 9.4 and 9.5 showing profiles in terms of mean and RMS temperature respectively. Very good agreement is found for both flames for the location and magnitude of extrema in all flame regions. RMS temperature profiles also agree well for both flames.

Mixing can be analyzed by plotting the probability density functions (PDF) of normalized heat release versus local equivalence ratio $\bar{\phi}$ (Fig. 9.6). While the overall heat release is constant for both cases, a different heat release distribution over $\bar{\phi}$ is found. The TECH flame produces slightly less heat around $\bar{\phi} = 1$ and more at $\bar{\phi} = 0.8$ than the FULL case but differences between the two cases for the mean flow are limited. The next step consists of analyzing the influence of these differences on the forced flame.

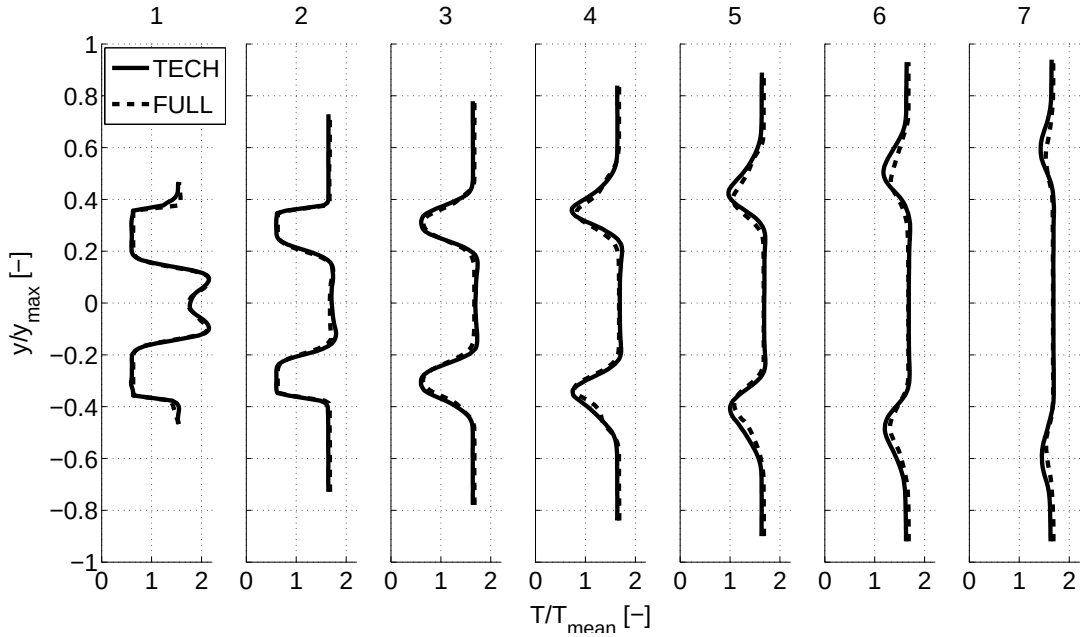

Figure 9.4: Profiles of temperature for the pulsated mean technically (TECH) and fully premixed flame (FULL).

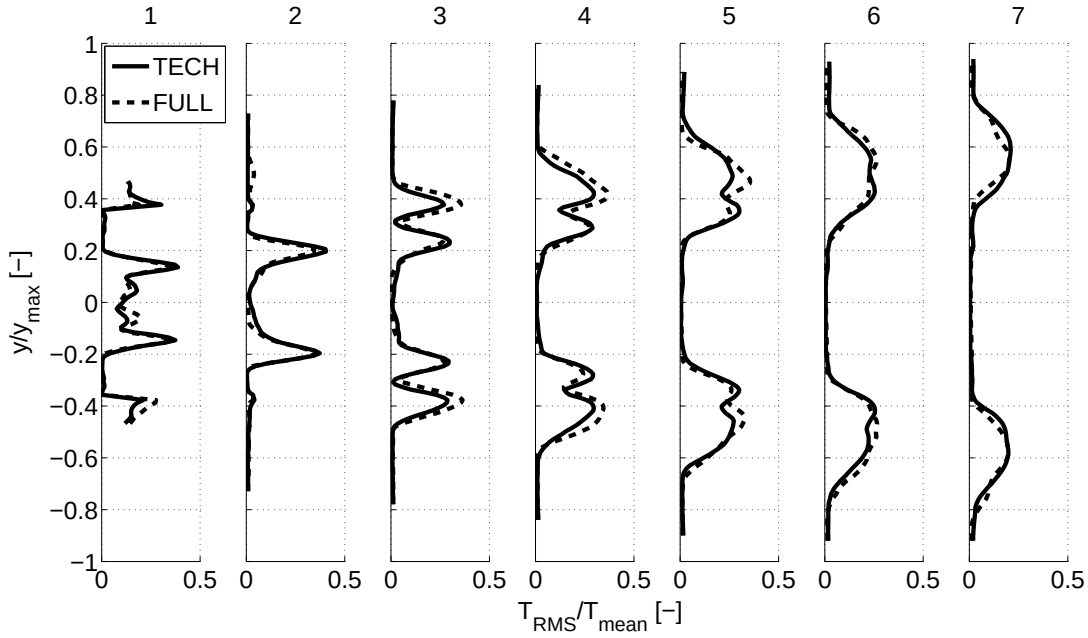

Figure 9.5: Profiles of RMS temperature for the pulsated mean technically (TECH) and fully premixed flame (FULL).

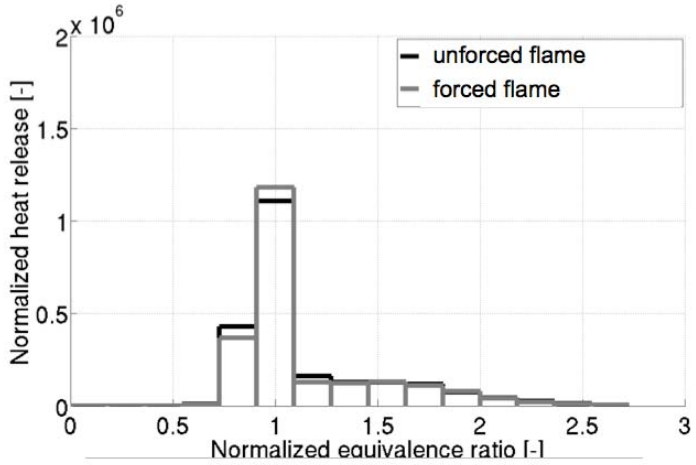

(a) TECH

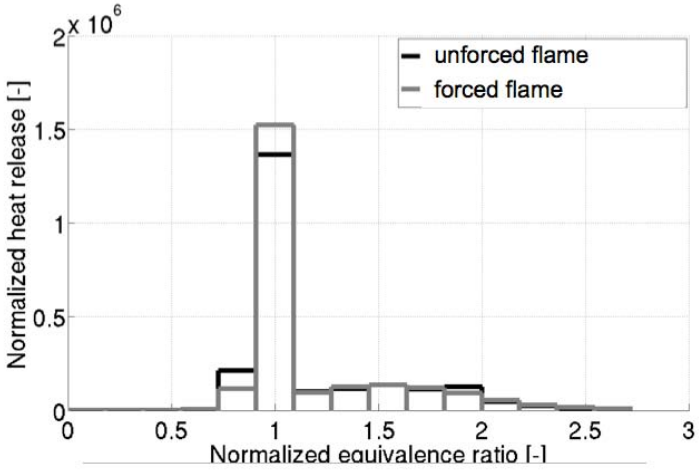

(b) FULL

Figure 9.6: PDF of the TECH and the FULL case for the averaged and the pulsated averaged flame (the equivalence ratio is normalized by its value in the diagonal passage).

9.1.2 Dynamics of the reacting flow fields

The previous section has shown that both cases exhibit similar mean pulsated and non-pulsated flame shapes but show slight differences for the equivalence ratios at which combustion occurs. It is worth investigating how this affects the dynamics of the flame.

The time variations of global heat release rate and velocity fluctuation at the reference point A (Fig. 8.1) are given in Fig. 9.7. Time is normalized by the acoustic forcing period T. Since the reference velocity signal is identical for both simulations, only the reference signal for the TECH case is shown. A phase difference between the relative heat release signals is clearly visible and the amplitudes differ slightly. The global FTF is given in table 9.2 in terms of amplitude n and phase θ. Although the

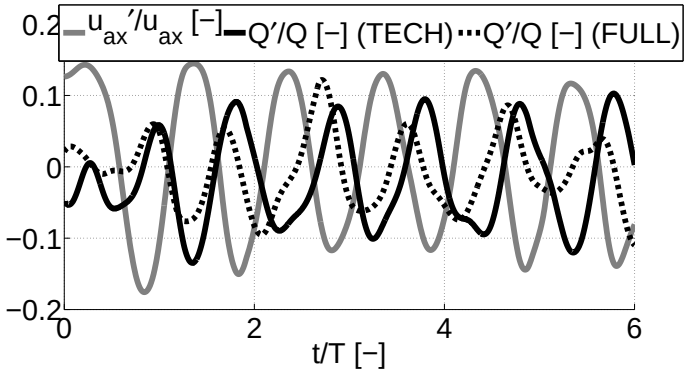

Figure 9.7: Relative velocity perturbation at the reference point A and relative heat release fluctuation for the TECH and the FULL cases (frequency f_4).

	n [-]	θ [-]
TECH	0.63	2.98
FULL	0.74	2.05

Table 9.2: Global FTF: amplitude n and phase θ for TECH and FULL.

mean flame shape is not influenced by mixing heterogeneities, the dynamic response of the flame is changed especially in terms of time delay: the delay of the TECH case is 1.5 times the FULL case delay, showing that mixture fraction fluctuations in the diagonal swirler do modify the FTF: when the flow is fully premixed (FULL) and fluctuations of Z are excluded, the delay decreases significantly compared to the TECH case studied up to now in this thesis.

Figure 9.7 shows that the global response of the system is highly affected by mixing heterogeneities. It is therefore interesting to focus on the local response of the flame: longitudinal cuts coloured by the local amplitude and time delay are shown

in Fig. 9.8 and Fig. 9.9 respectively. The amplitude response of the TECH case is intense near the lance and in the inner flame region. At the flame tip the amplitude varies strongly and is non-uniform with higher values on the inner side and lower at the outer flame. The FULL case shows less intense amplitude near the lance than the TECH case but behaves similarly in the inner flame region where a shear layer separates the flows of the axial and diagonal swirlers. Close to the flame tip and in the outer flame region, the amplitude is almost uniformly distributed but at slightly lower values than the TECH case. Although the global amplitude of both cases is similar, the local FTF fields reveal significant differences. The mixture fluctuations in the TECH case are phased with the velocity perturbations and propagate along the flame front affecting the local amplitude of the flame to higher and lower values whereas the FULL case shows a more uniformly distributed amplitude along the flame. The phase (Fig. 9.9) is in the FULL case similar to TECH in the vicinity of the lance. Differences are found at the flame tip underlying the importance of the flame tip reaction on the global time delay. In TECH, the reaction of the flame tip is predominantly determined by its phase to the mixture fraction fluctuation close to it (section 8.4).

9.1.3 Concluding remarks

LES reveals that both cases, the fully premixed (FULL) and the technically premixed (TECH), exhibit similar mean pulsated and non-pulsated flame shapes but PDFs show slight differences for the equivalence ratio distribution participating in heat release production. Mixture perturbations have an important effect on the global FTFs: the FTF delay for the TECH case is 1.5 times larger than for the FULL case and the interactive index slightly lower. Local FTF fields show that mixture heterogeneities propagating in the diagonal swirler lead to locally different responses over the flame region, whereas the FULL flame shows similar values of amplitude and time delay over the whole flame. The following section gives a deeper investigation on the effect of mixture heterogeneities while only forcing the fuel in the diagonal swirler and hence excluding the effect of air mass flow rate perturbations.

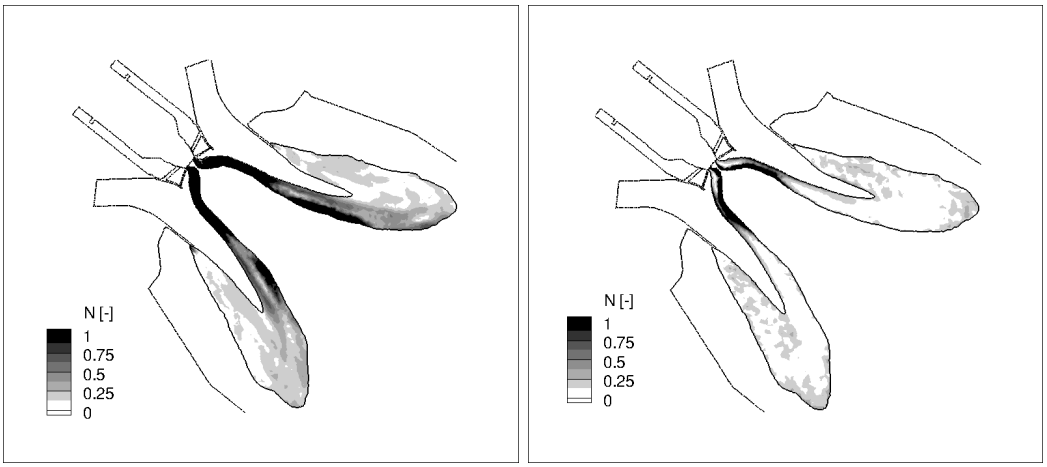

Figure 9.8: Amplitude of the local FTF for the TECH (left) and the FULL case (right).

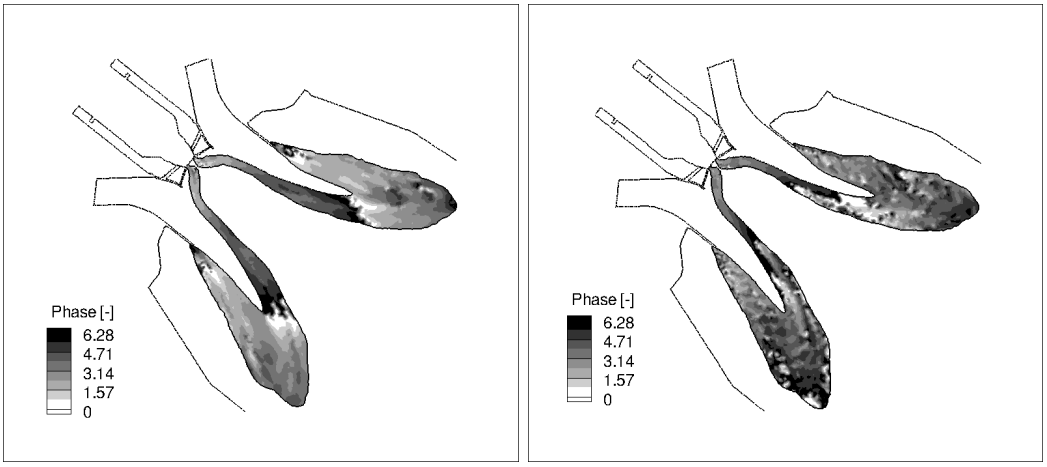

Figure 9.9: Time delay of the local FTF for the TECH (left) and the FULL case (right).

9.2 Effects of mixture fluctuation

To isolate the effects of mixture fluctuations on the flame response, another LES (called TECH-F, table 9.3) is performed where forcing is introduced only at the diagonal fuel inlet in order to exclude the effects of fluctuating air velocity perturbation (Fig. 9.10). It is compared to the "original" case +15CBO (called TECH). Although the fuel flow rate fluctuates, its effects on the global mass flow rate and thus the velocity fluctuation are negligible because the total fuel flow rate represents only 2 to 3 % of the total flow rate in the engine. Note that the absence of axial velocity fluctuation also excludes the fluctuation of azimuthal velocity and thus of swirl number.

The FTF in a system with fluctuating mixture fraction can be captured by an-

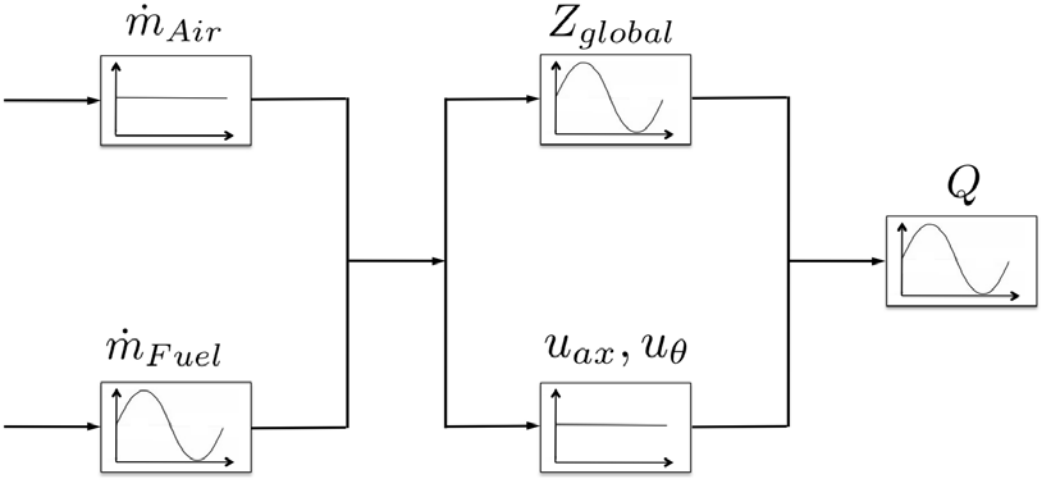

Figure 9.10: Schematic description of the pulsation mechanisms in the gas turbine with only fuel fluctuation. Only the inlet mixture fraction changes (TECH-F).

Case	Pulsation
TECH	Air injection in diagonal swirler
TECH-F	Fuel injection in diagonal swirler

Table 9.3: Description of investigated cases: TECH and TECH-F

other transfer function, which describes the impact of mixture fraction variation Z' to heat release rate fluctuations:

$$F(\omega) = \frac{\hat{q}/\bar{q}}{\hat{Z}/\bar{Z}}. \tag{9.1}$$

The fuel pulsation amplitude in TECH-F is 10% of the fuel injection velocity and has been chosen to reach the same global mixture fraction oscillation at the diagonal

inlet as in TECH. Note that even if Z' levels are the same, they are obtained in very different ways. In TECH, Z fluctuates because the air flow rate varies. In TECH-F, Z fluctuates because the fuel flow rate varies (the air flow rate is constant). The forcing frequency is f_4. In a first step, the mechanisms leading to mixture fraction fluctuations are studied in section 9.2.1 and the FTF response is analyzed in section 9.2.2.

9.2.1 Dynamic flame response

The heat release rate response of the flame to the mixture fraction perturbation at the reference plane A (Fig. 8.18) are given in Fig. 9.11 and Fig. 9.12 for TECH and TECH-F respectively. In both cases, the heat release fluctuates with 10% of its mean value. However the FTF amplitude is almost double for TECH (table 9.4). The FTF phase for TECH (3.93) is significantly shorter than in TECH-F (4.46) and the amplitude in TECH-F is almost doubled (based on the mixture fraction fluctuation).

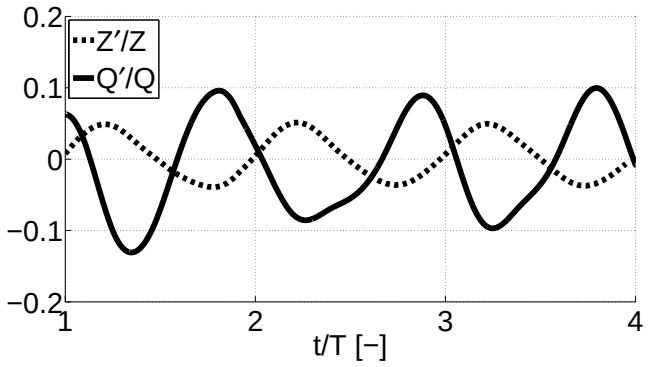

Figure 9.11: Normalized mixture fraction at the reference plane A (Fig. 8.18) and heat release rate for TECH.

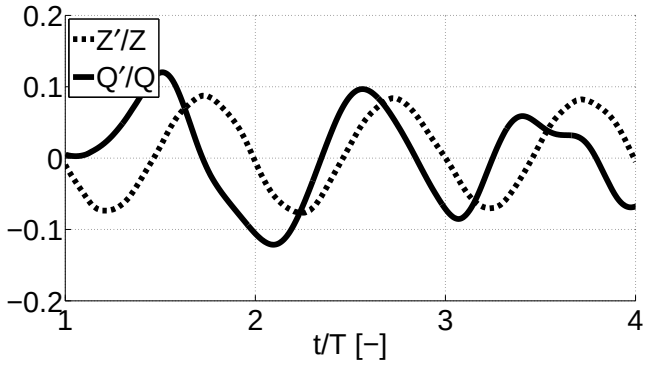

Figure 9.12: Normalized mixture fraction at the reference plane A (Fig. 8.18) and heat release rate for TECH-F.

	n [-]	θ [-]
TECH	1.97	3.93
TECH-F	1.12	4.46

Table 9.4: Global FTF: amplitude n and phase θ for TECH and TECH-F based on reference plane A (Fig. 8.18) and mixture fraction fluctuation (Eq. 9.1).

Although in section 8.4 a relation between the phase of the flame and the mixture fraction fluctuation was demonstrated, this is not the only mechanism determining the FTF delay. Furthermore, although the same mixture fraction oscillation was imposed through the boundary condition, a different amplitude occurs at reference plane A for Z'/Z. It is therefore interesting to investigate how mixing heterogeneities are transported between the vanes of the swirler and the chamber. Note that two mechanisms control mixing in such a regime: (1) the fuel jets created at the vanes must mix with the air of the diagonal passage and (2) the flow rate of the fuel jet is oscillating leading to an unsteady mixing problem.

9.2.2 Propagation of mixing heterogeneities

Figure 9.13 shows that the global instantaneous inlet mixture fraction of the diagonal passage (defined as the ratio of the fuel flow rate to the total flow rate) oscillates at the forcing frequency between 0.025 and 0.035 which is about 10% of the mean value for both cases. At the inlet of the chamber (reference plane A) in Fig. 9.14, after convection and mixing through the diagonal swirler, the mixture fraction fluctuations have been damped. The TECH case shows fluctuations between 0.029 and 0.032 and TECH-F between 0.027 and 0.032. The spatially averaged fluctuations are more damped, when the air and fuel are oscillating at the same time (TECH). Nevertheless, looking at the local mixture fraction at reference point A (Fig. 9.15) shows that locally, even higher fluctuations can occur in TECH than in TECH-F. With the mixture fraction fluctuating between 0.01 and 0.045 (TECH) and 0.02 and 0.045 (TECH-F), pockets of leaner and richer mixture reach the flame. The local mixture fraction shows larger fluctuations than the global mixture fraction, demonstrating that the heterogeneities created at the chamber inlet are not only due to flow rate fluctuations but also to unsteady mixing in the swirler. This point is analyzed next.

Forcing the diagonal air inlet (TECH) causes not only an acoustic perturbation normal to the flame but also pressure fluctuations at the fuel injection holes. This results in two effects: 1) the injected fuel flow rate pulsates and 2) the trajectory of the fuel jet fluctuates. Figure 9.17 and Fig. 9.18 show the fuel and air flow rate perturbation at the reference point B (Fig. 9.16) for TECH and TECH-F respectively. The air flow rate perturbation at this point is 12% of the mean axial

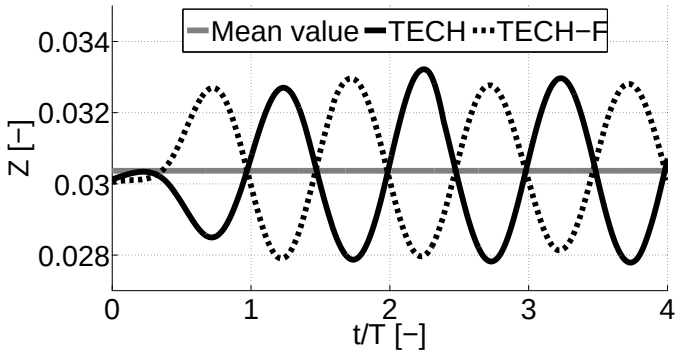

Figure 9.13: Global mixture fraction at diagonal swirler inlet for TECH, TECH-F and mean diagonal mixture fraction.

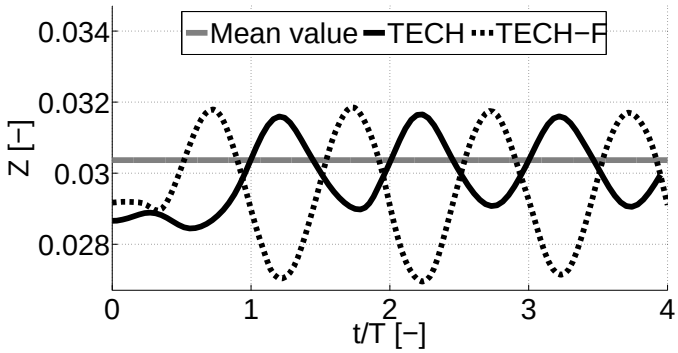

Figure 9.14: Spatially averaged mixture fraction at reference plane A (Fig. 8.18) for TECH, TECH-F and mean diagonal mixture fraction.

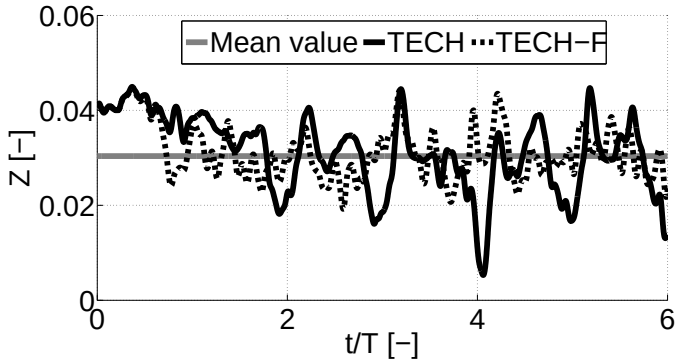

Figure 9.15: Local mixture fraction at the reference point A (Fig. 8.18) for TECH, TECH-F and mean diagonal mixture fraction.

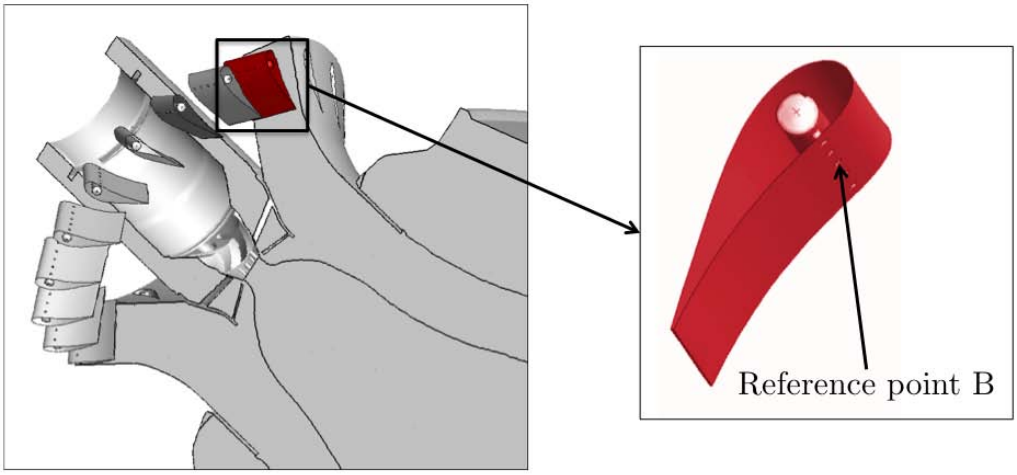

Figure 9.16: Relative fuel and air velocity at reference point B.

component and the fuel flow rate fluctuation 5% in the TECH case whereas for TECH-F 7% of air and 10% of fuel flow rate perturbation are present. Compared to TECH the fuel flow rate perturbation is higher and the air perturbation is less pronounced. Note that the small fuel injection holes are fed by a plenum (Fig. 9.16) where the most important pressure drop occurs through the holes. This means that even when a non-reflecting boundary condition is imposed at the plenum, the impedance and therefore the fluctuations of fuel flow rate are captured realistically in TECH by the LES set-up used here.

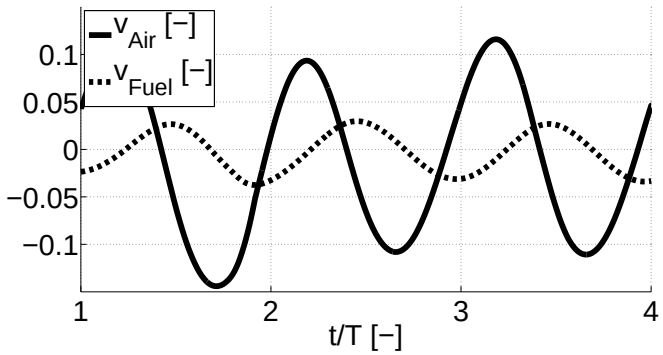

Figure 9.17: TECH: Relative fuel and air velocity perturbation at reference point B (Fig. 9.16).

The fuel velocity perturbation causes a variation of the fuel jet trajectory as well as a perturbation in mixture illustrated by two snapshots from LES in Fig. 9.19 showing an iso-surface of methane mass fraction, the normalized equivalence ratio field and a temperature iso-surface ($T/T_{mean} = 1.3$) for TECH. The oscillations of

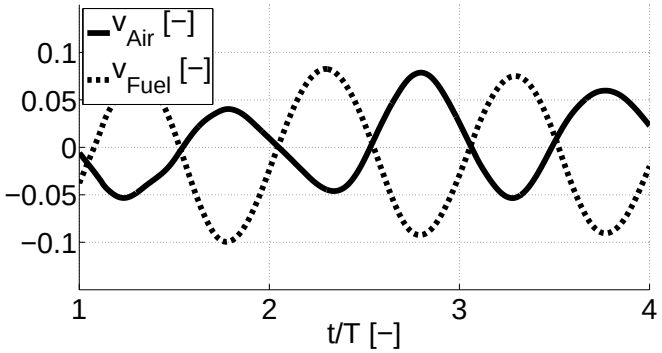

Figure 9.18: TECH-F: Relative fuel and air velocity perturbation at reference point B (Fig. 9.16).

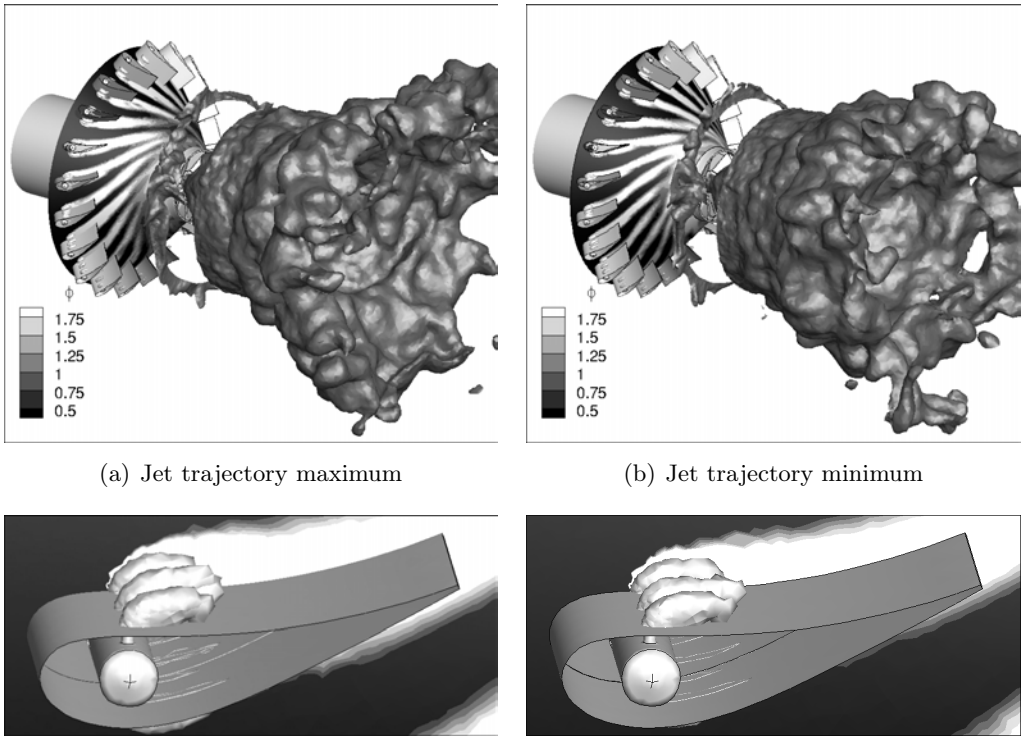

(a) Jet trajectory maximum

(b) Jet trajectory minimum

(c) Jet trajectory maximum (zoom)

(d) Jet trajectory minimum (zoom)

Figure 9.19: Jet trajectory visualized as Y_{CH4} iso-surface and normalized equivalence ratio field for two distinct snapshots (TECH case).

the fuel jet observed in the LES can be confirmed by literature data on jet in cross flows. Since fuel and air jets oscillate with different phases at the injection point, the resulting velocity ratio, which determines the trajectory of the jet and therefore the mixing, oscillates with another phase. The corresponding momentum flux ratio J [186] is shown in Fig. 9.20 as a function of time and is defined as follows:

$$J = \frac{\rho_{Jet} U_{Jet}^2}{\rho_\infty U_\infty^2} \tag{9.2}$$

To describe the jet trajectory several analytical models can be found in the literature. Following Priere [133] the empirical relation given by Ivanov [70] reads:

$$\frac{x}{d} = \left(\frac{U_\infty}{U_{Jet}}\right)^{2.6} \left(\frac{y}{d}\right)^3 + \frac{y}{d} cot(\delta) \tag{9.3}$$

and allows to track the jet trajectory envelope resulting from an oscillating J. Figure 9.21 shows that J fluctuates from 120 to 200 in the TECH case whereas it only varies half of this from 60 to 120 in TECH-F. This leads to large trajectory fluctua-

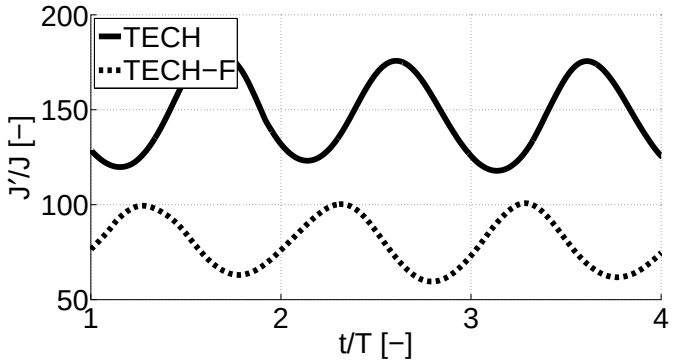

Figure 9.20: TECH: Momentum flux ratio at reference point B (Fig. 9.16).

tions in TECH (Fig. 9.21) and less in TECH-F (Fig. 9.22), as observed in the LES. Twenty diameters downstream of the vanes, Eq. 9.3 shows that in both cases the variations in J lead to lateral displacements of the jet of the order of ten diameters and obviously to fluctuations of local mixing. Both effects, the pulsating injected fuel flow rate and the fluctuating trajectory of the fuel jet have an impact on mixing close to the injection (Fig. 9.19). Generally, the diagonal swirler is designed to provide good mixing and to damp those effects. Nevertheless, Fig. 9.15 shows that pockets of leaner and richer mixture reach the flame (here at point A of Fig. 8.18). The local mixture fraction shows larger fluctuations than the global mixture fraction, demonstrating that the heterogeneities created at the chamber inlet are not only due to flow rate fluctuations but also to unsteady mixing in the swirler induced by the unsteady movements of the methane jets.

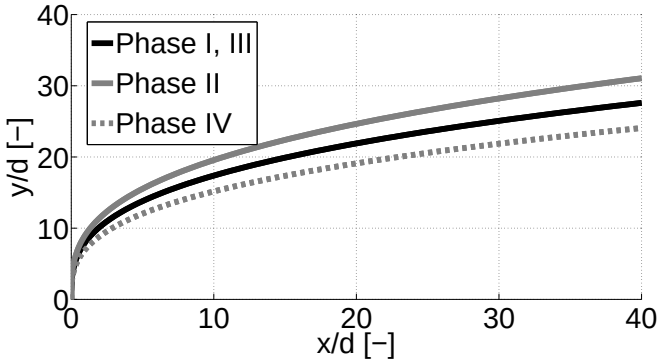

Figure 9.21: TECH: Jet trajectory envelope.

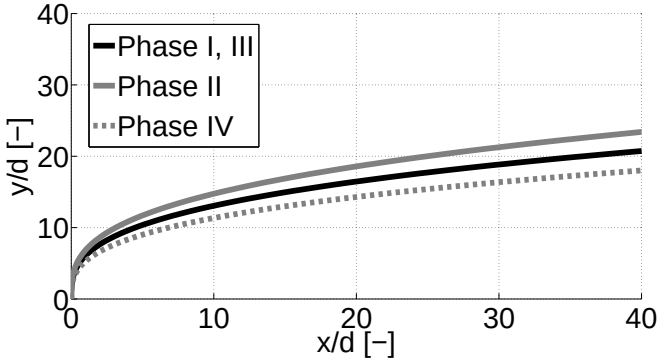

Figure 9.22: TECH-F: Jet trajectory envelope.

9.2.3 Swirl number perturbation

Since velocity perturbations are not introduced in TECH-F, the azimuthal velocity component does not fluctuate as shown in Fig. 9.23. It is known that swirl number fluctuations can also have an impact not only on the FTF gain but also on the FTF delay [84]. Here this effect is totally avoided so that the flame response is due only to fluctuation of mixture fraction.

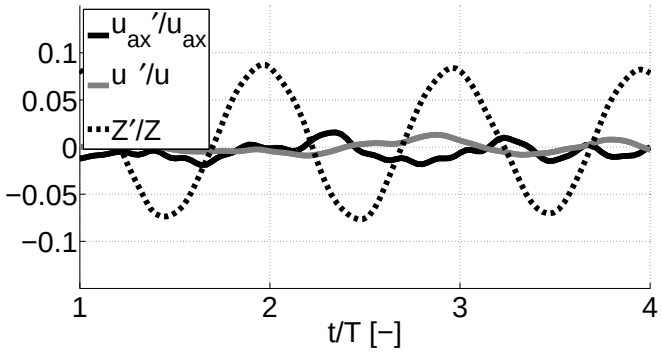

Figure 9.23: TECH-F: Axial, azimuthal velocity and mixture fraction fluctuation at reference plane A.

9.2.4 Concluding remarks

Two mechanisms are responsible for the perturbation of mixture during forced operation of the chamber: 1) the pulsating injected fuel flow rate and 2) the fluctuating trajectory of the fuel jets. Even though mixing takes place in the diagonal swirler, mixture fluctuations are not damped at the combustion chamber inlet. They are phased with velocity (and hence with swirl) fluctuations and combine with them to lead to different FTF results. The global FTF delay for the TECH case is smaller than for TECH-F and the interactive index is almost doubled. Note that the FTF links mixture fraction fluctuation to heat release response. This shows that although fuel injection in this turbine was designed to produce good mixing, this is true only for steady flames. As soon as the flames are pulsated, LES reveals that the fuel injection system produces a response which is not the same as a fully premixed system.

9.3 Combined Flame Transfer Function approach

All results obtained so far show that pulsating air or fuel flow rates in the present chamber triggers fluctuations of multiple parameters: inlet velocity, inlet mixture fraction and swirl. The evolution of delays or interaction indices when parameters such as geometry (CBO or NBO) change is not necessary intuitive because all these mechanisms interact. A possibility to clarify the modeling is to use a MISO model as suggested by Huber [64–66]: instead of linking heat release to velocity fluctuation only (or to air flow rates), expressing Q' as a function of inlet velocity and mixture fraction fluctuation may be a better physical formulation. As shown in Fig. 9.24, u' and Z can be created by fluctuations of $\dot{m}_{Air}$ or $\dot{m}_{Fuel}$ but the right parameters controlling Q' should be u' and Z' (and not $\dot{m}_{Air}$ or $\dot{m}_{Fuel}$). This path is investigated here.

The response of a flame as a MISO (**M**ultiple-**I**nput-**S**ingle-**O**utput) element in-

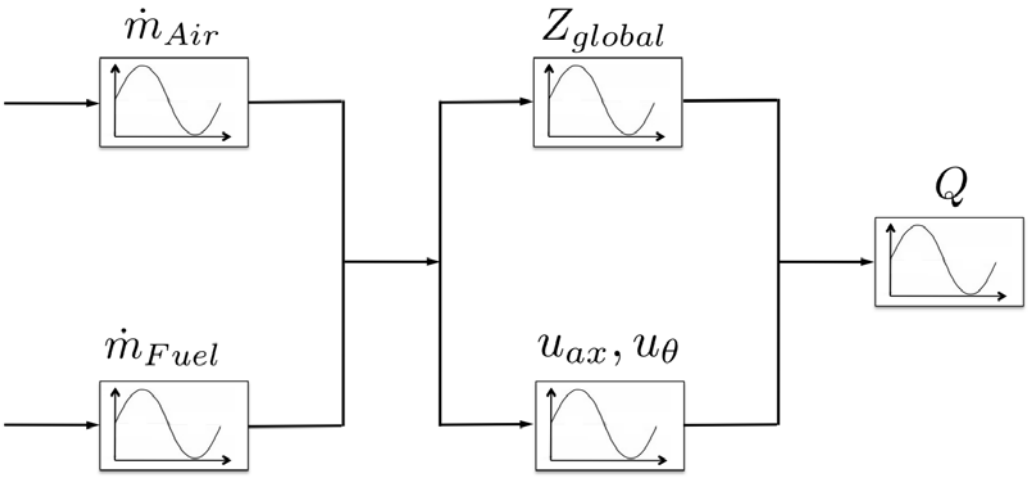

Figure 9.24: Schematic description of the pulsation mechanisms in the gas turbine.

stead of the SISO (**S**ingle-**I**nput-**S**ingle-**O**utput) element (which was used until now) can be expressed as:

$$\frac{Q'}{\bar{Q}} = n_u \frac{u'}{\bar{u}} e^{-i\omega\tau_u} + n_Z \frac{Z'}{\bar{Z}} e^{-i\omega\tau_Z} \tag{9.4}$$

This model takes into account the fluctuations of axial velocity perturbation and mixture fraction in terms of two amplitude response indices n_u and n_Z and two delay response τ_u and τ_Z. The analyses performed in section 9.1 and 9.2 can theoretically be combined since the response is in the linear regime. Table 9.5 gives the results and shows that with both SISO (TECH) and MISO (FULL+TECH-F) approach, similar values for n and τ can be found. Table 9.5 shows that a MISO model combining the effects of u' and Z' could be a good solution to model FTF in the present gas turbine. This would require measuring n_u, n_Z, τ_u and τ_Z for all geometries (CBO/NBO),

		Effects of velocity		Effects of mixture			Global effects	
		n_u [-]	θ_u [-]	n_Z [-]	θ_Z [-]		n [-]	θ [-]
SISO	TECH	-	-	-	-		0.63	2.98
MISO	FULL	0.74	2.05	-	-	$\Longrightarrow$	0.49	2.55
	TECH-F	-	-	1.12	4.46			

Table 9.5: Global FTF: comparison between SISO and MISO approach.

regimes (-15°C or 15°C) and frequencies to compare the results of the MISO model to the direct measurements performed with the SISO approach. This will be the topic of future work at Cerfacs.

Chapter 10

Nonlinear analysis

Contents

In the previous chapter, a possible extension of usual SISO (Single Input Single Output) models to MISO (Multiple Input Single Output) approaches have been discussed. Another limitation of usual models is the existence of nonlinearities. This issue is investigated here for the gas turbine chamber.

For acoustically compact flames the linear analysis of combustion instabilities is generally performed with the Flame Transfer Function (FTF) introduced by Crocco [29, 30] presented in the previous chapters. In this approach the FTF is defined as the relative heat release fluctuation $(\hat{q}/\bar{q})$ to the relative inlet velocity perturbation $(\hat{u}/\bar{u})$ issued by the acoustic field and writes $F(\omega) = (\hat{q}/\bar{q})/(\hat{u}/\bar{u})$. Nevertheless it is well known that in real gas turbine engines limit cycle oscillations can occur where non-linear effects play a dominant role. Figure 10.1 shows energy gain and losses as a function of the perturbation in terms of the square of the acoustic velocity: the energy gain of the flame is linear for low perturbation amplitudes (region I) and saturates for larger perturbation levels (region II). The acoustic losses, e.g. due to turbulence and the boundaries, are assumed to be linearly increasing with the perturbation level [35]. A limit cycle is reached when the losses and gain balance. This limit cycle is controlled by non-linear effects due to heat release [2, 3, 101]. The flame is observed to saturate in the presence of high perturbation amplitudes when the acoustic velocity reaches a magnitude of the order of the mean flow velocity [2, 3, 101, 118]. Since the flame response is not only a function of the frequency any more but also of the perturbation amplitude, the classical FTF approach is not able to describe the flame behaviour correctly. Therefore an extended version of the linear FTF approach is introduced [35, 118]: The so-called Flame Describing Function (FDF) is defined as

$$F(\omega, \hat{u}) = \frac{\hat{q}/\bar{q}}{\hat{u}/\bar{u}} \tag{10.1}$$

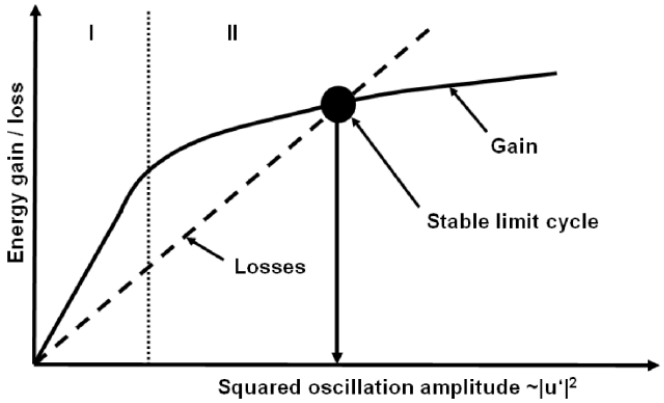

Figure 10.1: Interaction between between energy losses and gain with unsteady heat addition [101].

and accounts for the perturbation amplitude dependence $\hat{u}$.

The saturation mechanism has been investigated by several reviewers. Studies on V-flames and swirling flames [3, 40, 118] showed that the flame sheet and the vortices shed from the injector interact non-linearly and that the flame surface area evolves non-linearly with increasing excitation amplitude. Durox et al. [40] found experimentally that the response is dependent on the amplitude. Lieuwen et al. [101] state from investigations on a swirled flame that vortex roll-up and unsteady flame lift-off decrease the flame surface area and lead therefore to saturation at higher amplitudes. Thumuluru et al. [178] showed that the flame shape is strongly influenced by the excitation level as well as the position and strength of the vortex breakdown region. Schimek et al. [142, 143] found that the flame saturation mechanisms were flame quenching due to local extinction and re-ignition. Kim et al. [81] investigated the effects of equivalence ratio fluctuations in a swirled flame and showed that the response of the flame depends on the phase difference between velocity and equivalence ratio fluctuations and can be either linear or non-linear.

Recent publications often deal with the experimental determination of the Flame Describing Functions and the analysis of mechanisms at play in the saturation mechanisms. Nevertheless, only a few publications deal with the numerical investigation of non-linear effects. Armitage et al. [2] investigated in a 2D-URANS approach the FDF for a bluff body flame and Krediet el al. [89] detemined the FDF of the FVV case (chapter 4). An analysis of non-linear effects in real gas turbine engines has not been performed so far. The goal of this chapter is investigate this topic for an industrial configuration. The aim is not to determine the FDF over the whole frequency range for computational cost reasons, but to analyze one frequency in detail. Therefore the +15CBO case is chosen and the ingoing acoustic wave is pulsated sinusoidally at a frequency f_4 with an amplitude reaching 45% of the mean

inlet velocity. Table 10.1 summarizes the linear and non-linear cases. The following

Case	Pulsation amplitude
TECH	6 %
TECH-NL	45 %

Table 10.1: Description of investigated cases.

section compares the simulations TECH and TECH-NL in terms of mean pulsated flow fields and flow field dynamics.

10.1 Mean pulsated flow fields

For low pulsation amplitudes, Section 8.3.1 showed that averaged fields were not significantly affected by forcing. Here, the situation is different: averaged pulsated temperature fields are compared in Fig. 10.2. The TECH-NL mean fields are affected by the strong forcing. The flame arrives at the diagonal swirler outlet and the hot temperature region of the pilot flame penetrates more into the combustion chamber. This shows that high pulsation amplitudes change the mean pulsated flow fields compared to non-pulsated ones and the assumption used to linearize equations [31] is not valid any more. These observations agree with Thumuluru et al. [178] stating that the flame shape is strongly influenced by the excitation level. RMS temperature fluctuations are almost doubled at the near-lance profiles (Cut 1 to 4) in Fig. 10.3 and the location of the extrema change significantly. At the flame tip from cut 6 on, both cases behave similarly in terms of mean values. Figure 10.4

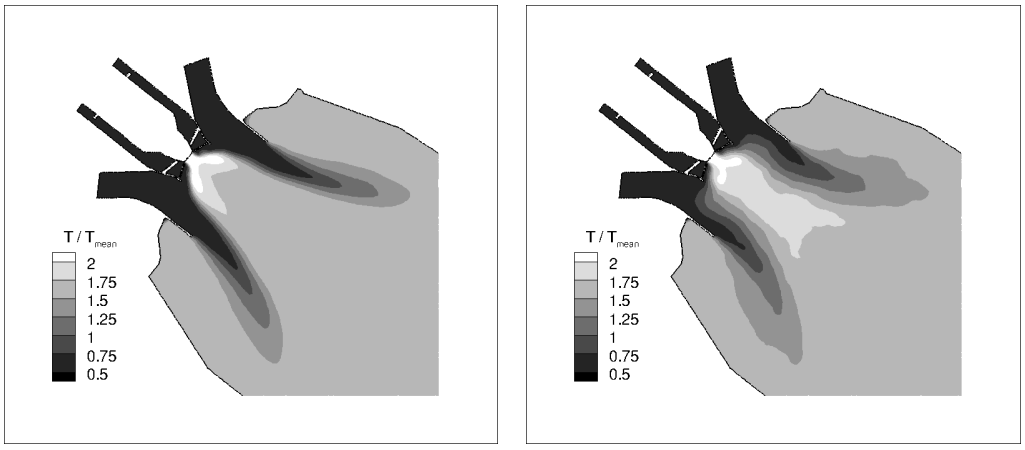

(a) TECH (b) TECH-NL

Figure 10.2: Averaged pulsated temperature field on middle cut plane for TECH and TECH-NL at frequency f_4.

shows the probability density functions (PDF) for the TECH and the TECH-NL flame in comparison to the unforced flame. Forcing has a strong influence on the equivalence ratio at which combustion takes place. For strong forcing (TECH-NL), the PDF of heat release versus equivalence ratio is flatter, indicating that more flamelets are formed at equivalence ratios which differ from the mean value in the diagonal swirler. This shows that mixing is less efficient in the diagonal swirler for TECH-NL: strong forcing leads to less efficient mixing.

Phase averaging the PDF during the heat release oscillation cycle shows that significant fluctuations of equivalence ratio occur (Fig. 10.5) for high forcing amplitudes which are much less in the linear case. The phase averaged heat release rate shows that the TECH-NL flame shape undergoes strong oscillation during the oscillation cycle, whereas the TECH flame shape is only slightly changing (Fig. 10.6 to 10.9 for $2T$ to $3T/2$). In TECH-NL at $2T$, the flame rolls up at the lance and a "ball-like" structure with strong heat release rate appears along the inner flame. This structure grows within the oscillation cycle and decreases from T on. The maximum of heat release along the inner flame is at $T/2$. At time T, the flame rolls-up at the tip and forms a characteristic "mushroom" shape. In TECH, the flame close to the pilot injection is also characterized by a strong heat release but opens and closes only slightly during T. A slightly higher heat release is also present along the inner flame front at $T/2$ which is due to a richer mixture entering this region. The flame tip does not change significantly.

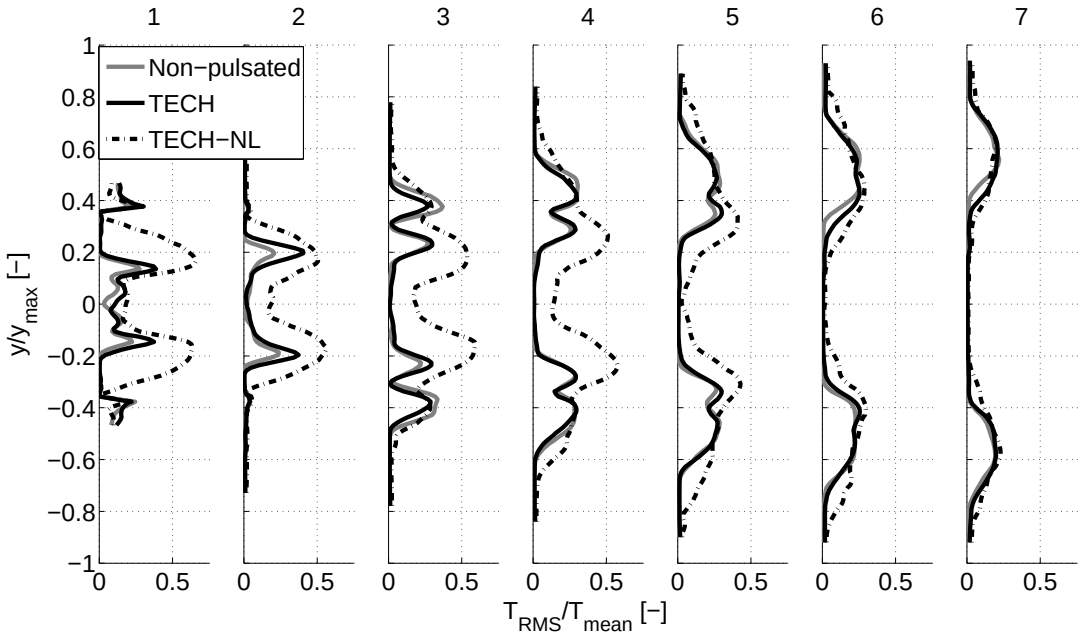

Figure 10.3: Averaged RMS temperature profiles for the non-pulsated flame, TECH and TECH-NL.

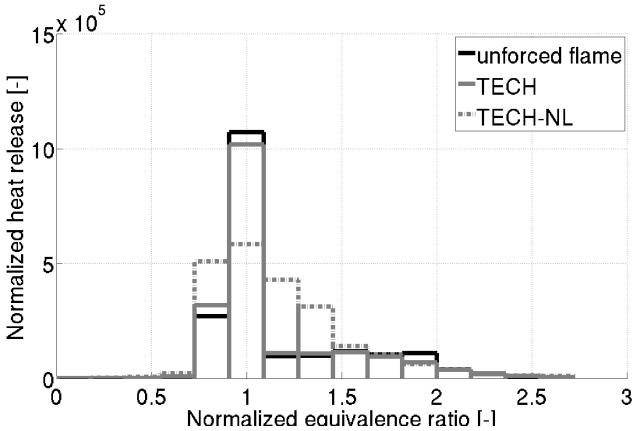

Figure 10.4: PDF of the unforced, TECH and TECH-NL cases (the equivalence ratio is normalized by its value in the diagonal passage).

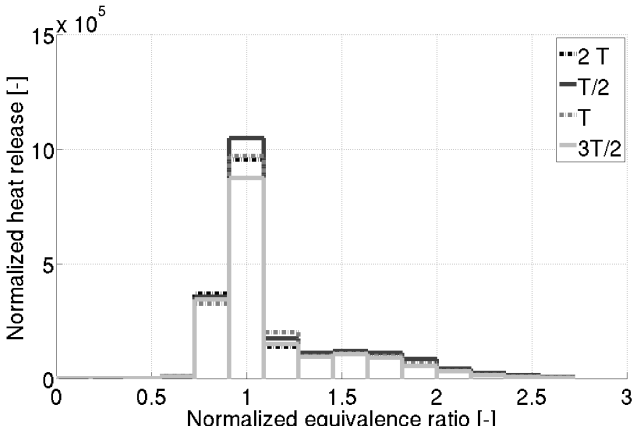

(a) TECH

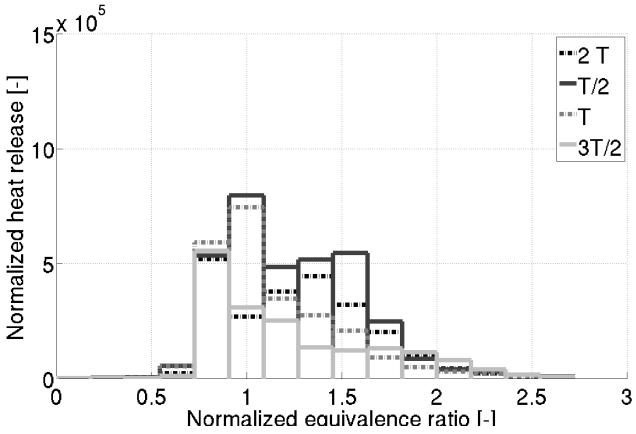

(b) TECH-NL

Figure 10.5: Phase averaged PDF for TECH and TECH-NL at frequency f_4 (the equivalence ratio is normalized by its value in the diagonal passage).

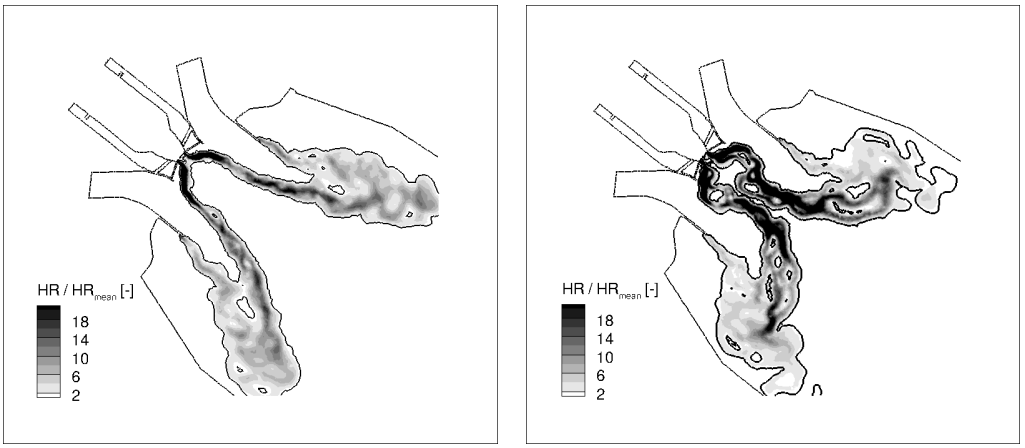

(a) TECH (b) TECH-NL

Figure 10.6: Phase averaged pulsated heat release field on middle cut plane for TECH and TECH-NL at frequency f_4 for $2T$.

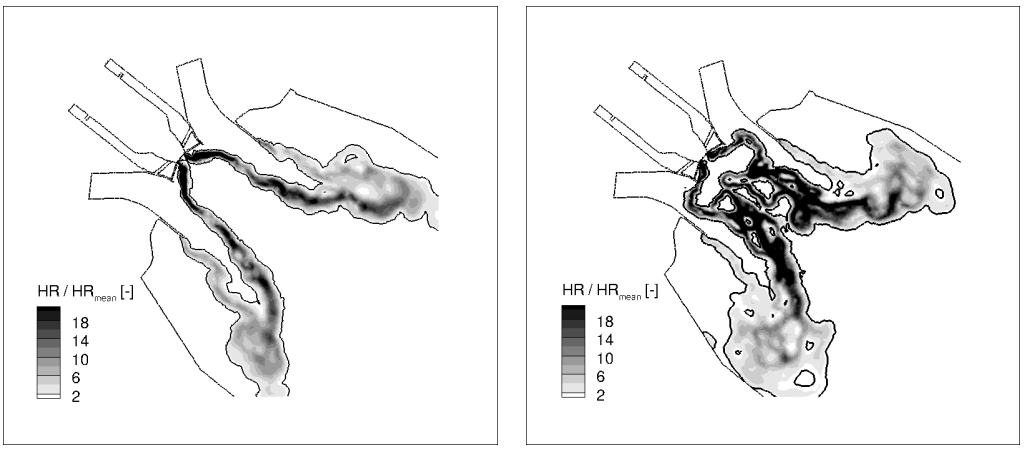

(a) TECH (b) TECH-NL

Figure 10.7: Phase averaged pulsated heat release field on middle cut plane for TECH and TECH-NL at frequency f_4 for $T/2$.

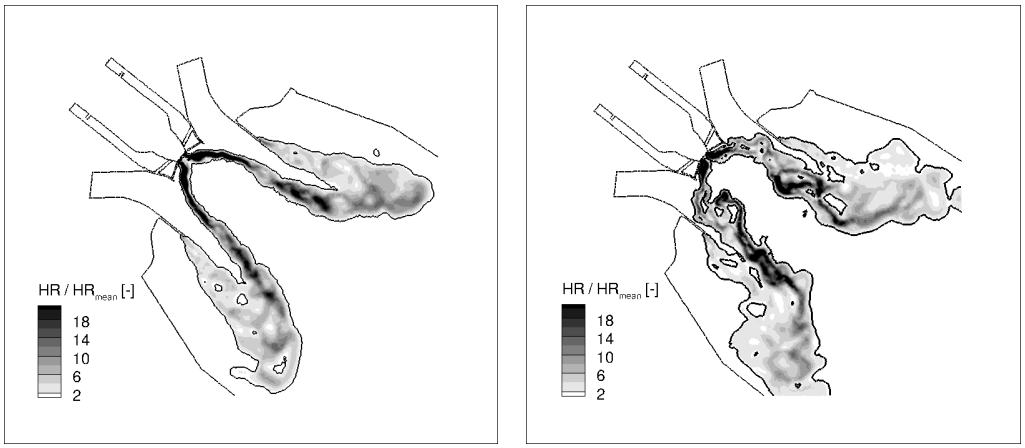

(a) TECH (b) TECH-NL

Figure 10.8: Phase averaged pulsated heat release field on middle cut plane for TECH and TECH-NL at frequency f_4 for T.

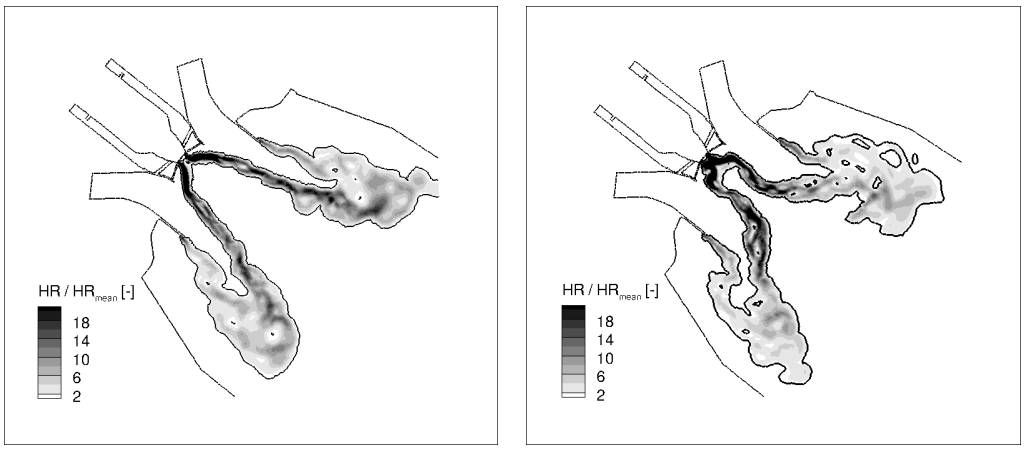

(a) TECH (b) TECH-NL

Figure 10.9: Phase averaged pulsated heat release field on middle cut plane for TECH and TECH-NL at frequency f_4 for $3T/2$.

10.2 Effect of pulsation amplitude on FDF

The dynamic flame response is shown in Fig. 10.10 for the TECH and the TECH-NL case and the values of the FTF/FDF are given in Table 10.2. Both flames react similarly in terms of gain: the TECH case shows an amplitude of 0.63 and 0.75 for the TECH-NL case. All signals in TECH are harmonic, whereas TECH-NL exhibit clear nonlinearities. At this pulsation frequency a saturation (which would lead to a decrease of n) does not appear: the gain for TECH-NL is 0.75 while it is 0.63 for TECH. A larger difference is found for the phase: TECH-NL has (with a phase of 3.78) a longer time delay than TECH (2.96).

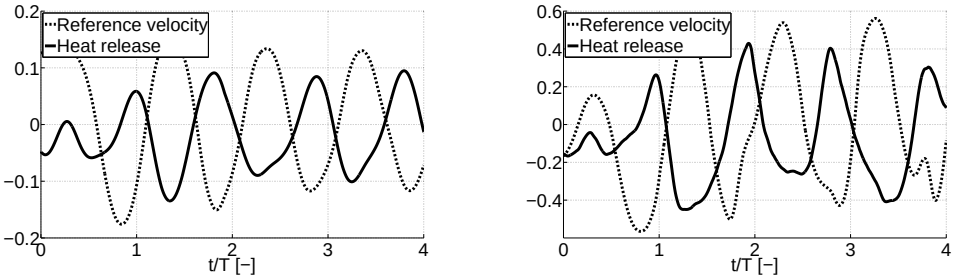

(a) TECH (b) TECH-NL

Figure 10.10: Relative velocity and heat release fluctuations at reference point A for TECH and TECH-NL.

	TECH	TECH-NL
n [-]	0.63	0.75
Phase [-]	2.96	3.78

Table 10.2: Global FTF/FDF: amplitude and phase response for the TECH and TECH-NL case.

10.2.1 Local Flame Transfer Function

Since the global response is strongly affected by mixing inhomogeneities it useful to look at the local response of the flame. The local amplitudes and time delays are given in Fig. 10.11 and Fig. 10.11 respectively on longitudinal cuts and show very large differences. The local amplitude is in the TECH-NL case significantly higher along the inner flame region but slightly different at the flame tip. The phase is in the inner flame region higher in TECH than in TECH-NL. TECH-NL shows low time delays close to the lance which are increasing constantly to the flame tip where the maximum value occurs. The phase at the flame tip is lower in TECH compared to TECH-NL.

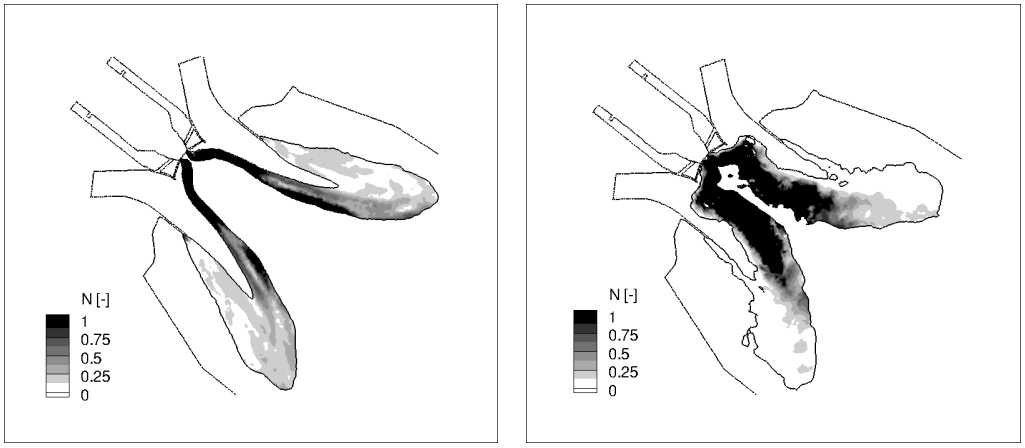

(a) TECH (b) TECH-NL

Figure 10.11: Local Flame Transfer Function amplitude for TECH and TECH-NL at frequency f_4.

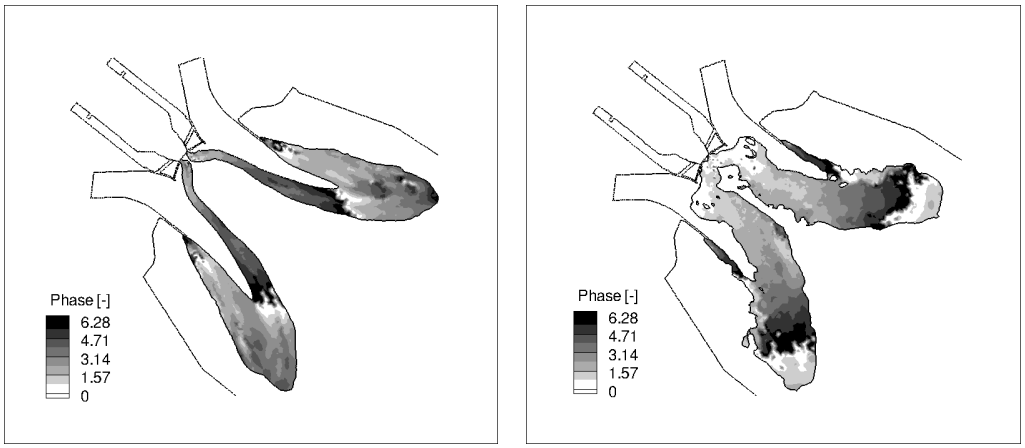

(a) TECH (b) TECH-NL

Figure 10.12: Local Flame Transfer Function phase for TECH and TECH-NL at frequency f_4.

These results also confirm that the flame is not compact: Fig. 10.11 shows much larger values of the local interaction n for TECH-NL than for TECH. These high values do not lead to a much larger value of the global amplitude response given in Table 10.2 because the time delay is not homogeneous (the flame is not compact).

The link between the global amplitude n and the local field $n_l(\vec{x})$ is:

$$ne^{-i\omega\tau} = \iiint_V n_l(\vec{x}) e^{-i\omega\tau_l(\vec{x})} \tag{10.2}$$

This relation is satisfied and it explains why n is not very different for TECH-NL compared to TECH: local values of n_l are larger for TECH-NL but since the flame is not compact, these large n_l values have opposite effects in regions where τ_l changes rapidly. In other words, at high pulsation amplitudes, the flame reacts locally more strongly but this does not mean that the global amplification increases. The absence of saturation observed at high amplitudes of the flame is only true for the global FTF. Locally, the gain increases with increasing velocity perturbation.

10.2.2 Mixture perturbation

The perturbation of mixture results from the fluctuating inlet air mass flow rate (Fig. 10.13) which causes the fuel flow rate to oscillate (20%) in TECH-NL. The global mixture fraction fluctuation is much larger for TECH-NL ($Z'/\bar{Z}$ between -0.4 and 3.8) compared to TECH ($Z'/\bar{Z} = \pm 0.1$) as shown by Fig. 10.14 which also shows nonlinear variations of Z' for TECH-NL. Further downstream at the reference plane A (Fig. 10.15), the fluctuations in TECH-NL are damped to about 10% (between -0.33 and 0.4), whereas TECH fluctuates with 50% of the inlet fluctuations ($Z'/\bar{Z} = \pm 0.05$). Higher mixture fraction fluctuation are also stronger damped in the swirler. The nonlinear oscillation in TECH-NL explains also the nonlinear heat release fluctuation. At strong forcing levels the fluctuations of equivalence ratio at the chamber inlet are very strong: it is likely for example that when $Z'/\bar{Z}$ reaches -0.3, the mixture gets out of flammability limits and must mix downstream of the chamber inlet before burning.

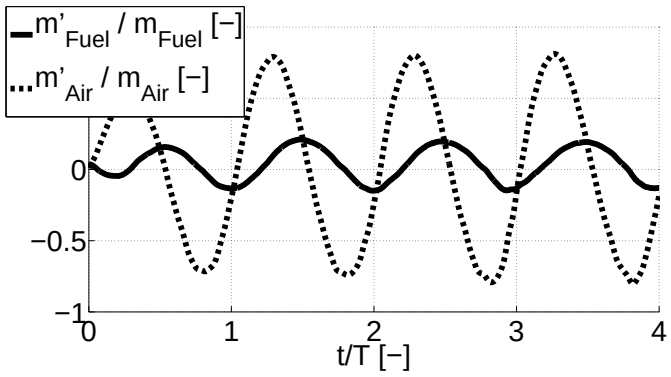

Figure 10.13: Air and fuel mass flow rate fluctuation at the diagonal swirler inlet for TECH-NL.

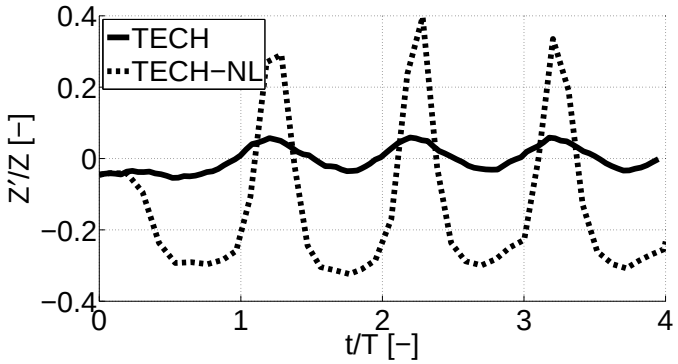

Figure 10.14: Relative mixture fraction fluctuation at the diagonal swirler inlet for TECH and TECH-NL.

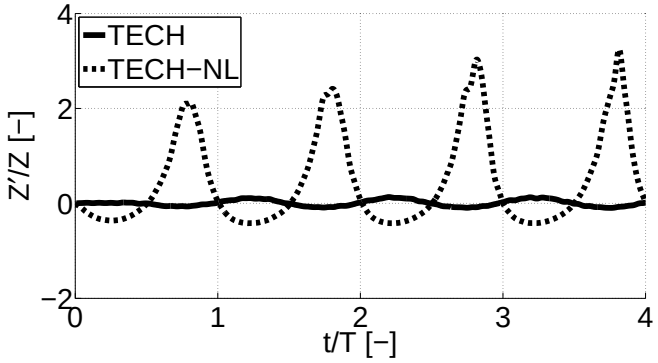

Figure 10.15: Relative mixture fraction fluctuation at the reference plane A for TECH and TECH-NL.

10.3 Conclusion

The pulsation with high excitation level created for the TECH-NL run causes a non-linear response of the flame. The averaged flame shape changes significantly compared to the linear behaviour. During the oscillation cycle the flame undergoes strong variations in shape, with a typical roll-up in mushroom shape [123]. The global FTF shows that the forcing amplitude does not only lead to a saturation of the flame [2, 3, 101, 118] but also changes the delay response. The heat release oscillation shows sharp peaks at its maximum which could be related to the mixture fraction fluctuation. Strong fluctuations of equivalence ratio during the oscillation cycle are shown by PDFs. Local FTF fields reveal that the local interaction index increases significantly with increasing forcing amplitude. Nevertheless the global gain remains similar between the linear and non-linear case since the flame is not compact. This means that high local gain values have opposite effects in regions where the local time delay changes rapidly. To conclude, forcing amplitudes do have an influence on the FTF when they reach large values. Whether this point must be included now in the analysis of instabilities in this gas turbine is an open question: the forcing amplitude used in TECH-NL was very large and should not be reached in the real engine. Moreover, ensuring linear stability (for which linear FTFs are sufficient) is a priority for engineering purposes. However, moving from FTF to FDF formulation is clearly an interesting path which will be investigated in the future.

Conclusion and perspectives

"The machine does not isolate man from the great problems of nature but plunges him more deeply into them." **Antoine de Saint-Exupery** (1900-1944).

Modern pollutant regulations have led to lean (technically) premixed combustion systems which are prone to thermo-acoustic instabilities. In this work, compressible reactive Large Eddy Simulation (LES) has been applied to an academic single burner and a heavy-duty industrial gas turbine combustion chamber. The coupling between acoustic and combustion has been modeled with the Flame Transfer Function approach. The LES of the academic burner has been successfully validated against measurements and against OpenFoam LES simulations. The large-scale industrial gas turbine has been analyzed for two different burner geometries and operating conditions. The assumption used to linearize equations is valid in the linear regime as mean flow fields with forcing remained similar to the unforced mean fields which is not valid for high pulsation amplitudes in the nonlinear regime. The FTF was only slightly influenced for the two operating points considered here. Burner outlets did modify the characteristics of the FTF with the Cylindrical Burner Outlet (CBO) cases having a slightly shorter time lag than the cases without elongated burner outlet (NBO) whereas the CBO flames were slightly longer. This means that a simple model taking only into account the flight time from the reference point to the flame is not appropriate and additional mechanisms are at play.

Results showed that pulsating air or fuel flow rates trigger fluctuations of the inlet velocity, swirl and the inlet mixture fraction whereas the latter is caused by two mechanisms: 1) the pulsating injected fuel flow rate and 2) the fluctuating trajectory of the fuel jets. The diagonal swirler, although designed to provide good mixing, did not damp those effects at the combustion chamber inlet. Mixing inhomogeneities showed to partially control the FTF delay which gets shorter in their absence when a fully premixed flow passes the diagonal swirler instead. Mixture perturbations are phased with velocity (and hence with swirl) fluctuations and combine with them to lead to different FTF results. Another possibility to clarify modeling of FTFs is linking heat release to inlet velocity and mixture fraction fluctuation (MISO model) which showed to be a promising solution. The nonlinear analysis showed that the forcing amplitude not only leads to a saturation of the flame but also to changes of the delay response. All flames studied here were not compact: flame regions located right next to each other exhibited significant differences in delay meaning that at the same instant certain parts of the flame damp the excitation while others feed it.

The ability of LES to handle complex unsteady phenomena in gas turbines has been evidenced during this thesis work. LES has shown its ability to give important insight in the mechanisms dominating the dynamic flame behaviour. Embedding

LES solvers at an early design stage is recommended to help understanding and changing flame dynamics in order to finally construct stable combustors.

Thermo-acoustic instabilities are mainly controlled by the complex interaction between acoustics and combustion. Future work includes further evaluating the effects of combustion modeling and chemical kinetics on the dynamic flame behaviour. Also the influence of a more detailed chemical reaction scheme should be evaluated in order to predict pollutant emissions. Furthermore, the influence of cooling of the chamber walls has not been investigated in this work and should be considered for the future. Including further details in the LES is a logical step since computational power is increasing continuously.

List of Figures

List of Tables

List of symbols

Roman letters

$\dot{m}$	mass flow rate, $kg.s^{-1}$
$\dot{Q}$	global heat release rate, W
$\dot{q}$	heat release rate, $W.m^{-3}$
$\mathcal{E}$	efficiency function
$\mathcal{F}$	thickening factor
A	pre-exponentional factor, $c.g.s$
c	speed of sound, $m.s^{-1}$
C_p	specific heat at constant pressure, $J.kg^{-1}.K^{-1}$
C_r	crest factor
c_{ij}	cross-correlation vector
E	total energy, $J.kg^{-1}$
E_a	activation energy, $J.mol^{-1}$
e_n	noise term
F	Flame Transfer Function
f	frequency, Hz
H	total enthalpy, $J.kg^{-1}$
h_k	unit impulse response, s
h_s	sensible enthalpy, $J.kg^{-1}$
i	the standard imaginary unit ($i^2 = -1$)
$J_{j,k}$	j-th component of the diffusive molecular flux for species k, $mol.s^{-1}.m^{-2}$
K_f	forward reaction constant
K_r	reverse reaction constant
K_{eq}	equilibrium constant
L	Length, m

M	number of reactions
m	downsampling factor
N	number of species
n	amplitude delay response
p	pressure, Pa
q_1,q_2	rate of first and second reaction, $-$
q_i	i-th component of the diffusive heat flux, $W.m^{-2}$
r	response
R^0	universal gas constant, $J.kg^{-1}.K^{-1}$
R_w	heat resistance, m^2K/W
s	signal
S_{ij}	strain rate tensor, s^{-1}
$s_{l,0}$	laminar flame speed, $m.s^{-1}$
T	temperature, K
t	time, s
u	velocity component in x-direction, $m.s^{-1}$
u_i	i-th component of the velocity vector, $m.s^{-1}$
v	velocity component in y-direction, $m.s^{-1}$
V_i^c	correction velocity, $m.s^{-1}$
W	molecular weight, $kg.mol^{-1}$
w	velocity component in z-direction, $m.s^{-1}$
X	molar fraction
x	space coordinate in x-direction, m
Y	mass fraction
y	space coordinate in x-direction, m
Z	mixture fraction
z	space coordinate in x-direction, m

Greek letters

δ	Dirac delta distribution
δ_{ij}	Kronecker's delta
δ_l	laminar flame thickness, m
$\dot{\omega}_T$	chemical heat release rate, $W.m^{-3}$
$\dot{\omega}_k$	production rate of species k, $kg.m^{-3}.s^{-1}$
γ	specific heat ratio
Γ_{ij}	auto-correlation matrix
λ	heat conduction coefficient, $W.m^{-1}.K^{-1}$
μ	dynamic viscosity, $N.m^2.s$
ν	kinematic viscosity, $m^2.s^{-1}$
ν''_{kj}	reverse stochiometric coefficient
ν'_{kj}	forward stochiometric coefficient
ν_t	kinematic turbulent sub-grid scale viscosity, $m^2.s^{-1}$
ω	angular frequency, $rad.s^{-1}$
ϕ	equivalence ratio
ρ	mass density, $kg.m^{-3}$
τ	time delay response, s
τ_{ij}	component i, j of the stress tensor, Pa
θ	phase response

Dimensionless numbers

Ma	Mach number
Pr	Prandtl number
Re	Reynolds number
Sc	Schmidt number

Operators

$\overline{f}$	Reynolds average

$\widetilde{f}$	Favre filtering

Subscripts

∞	quantity taken at infinity
F	related to the fuel
i	i-th component
j	related to the j-th reaction
k	related to species k
O	related to the oxidizer
ref	quantity taken at the reference point

Superscripts

$'$	related to the temporal fluctuation
t	turbulent sub-grid scale contribution

Abbreviations

CBO	Cylindrical Burner Outlet
CFD	Computational Fluid Dynamics
CFL	Courant-Friedrichs-Lewy
DBRS	Discrete Random Binary Signal
DNS	Direct Numerical Simulation
FDF	Flame Describing Function
FFT	Fast Fourier Transformation
FTF	Flame Transfer Function
LES	Large-Eddy Simulation
LW	Lax-Wendroff
NBO	No Burner Outlet
NSCBC	Navier-Stokes Characteristic BC
PVC	Precessing Vortex Core
RANS	Reynolds Averaged Navier-Stokes
RMS	Root Mean Square
WHI	Wiener-Hopf Inversion

Bibliography

[1] *http://www.openfoam.org/.* (Cited on pages 11 and 47.)

[2] Armitage, C. A., Balachandran, R., Mastorakos, E., and Cant, R. Investigation of the non-linear response of turbulent premixed flames to imposed inlet velocity oscillations. *Combust. Flame 146* (2006), 419–436. (Cited on pages 10, 21, 24, 110, 163, 164 and 174.)

[3] Balachandran, R., Ayoola, B., Kaminski, C., Dowling, A., and Mastorakos, E. Experimental investigation of the non-linear response of turbulent premixed flames to imposed inlet velocity oscillations. *Combust. Flame 143* (2005), 37–55. (Cited on pages 10, 24, 163, 164 and 174.)

[4] Balasubramanian, K., and Sujith, R. Nonnormality and nonlinearity in combustion-acoustic interaction in diffusion flames. *J. Fluid Mech. 594* (2008), 29–57. (Cited on page 25.)

[5] Balasubramanian, K., and Sujith, R. Thermoacoustic instability in a rijke tube: non-normality and nonlinearity. *Phys. Fluids 20* (2008), 044103. (Cited on page 25.)

[6] Benoit, L. *Prédiction des instabilités thermo-acoustiques dans les turbines à gaz.* Phd thesis, University Montpellier II, 2005. (Cited on page 96.)

[7] Bernier, D., Lacas, F., and Candel, S. Instability mechanisms in a premixed prevaporized combustor. *Journal of Propulsion and Power 20* (2004), 648–656. (Cited on page 118.)

[8] Bethke, S., Krebs, W., Flohr, P., and Prade, B. Thermoacoustic properties of can annular combustors. *Am. Inst. Aeronaut. Astronaut. J.* (May 2002), 2002–2570. (Cited on page 116.)

[9] Billoud, G., Galland, M., Huynh, C., and Candel, S. Adaptive active control of combustion instabilities. *Combust. Sci. Tech. 81* (1992), 257–283. (Cited on page 19.)

[10] Bird, R. B., Stewart, W. E., and Lighfoot, E. N. *Transport phenomena.* John Wiley, New York, 1960. (Cited on page 31.)

[11] Bloxsidge, G., Dowling, A., Hooper, N., and Langhorne, P. Active control of reheat buzz. *AIAA Journal26* (1988), 783–790. (Cited on page 19.)

[12] Bosschaart, K., and de Goey, L. The laminar burning velocity of flames propagating in mixtures of hydrocarbons and air measured with the heat flux method. *Combust. Flame* , 136 (2004), 261–269. (Cited on page 75.)

[13] Boudy, F., Durox, D., Schuller, T., and Candel, S. Nonlinear mode triggering in a multiple flame combustor. In *Proceedings of the Combustion Institute* (2011), vol. 33, pp. 1121–1128. (Cited on pages 25 and 70.)

[14] Boussinesq, J. Essai sur la théorie des eaux courantes. *26ème édn. Acad. Sci. Paris* (1877). (Cited on page 34.)

[15] Broda, J., Seo, S., Santoro, R., Shirhattikar, G., and Yang, V. An experimental study of combustion dynamics of a premixed swirl injector. In *Proceedings of the Combustion Institute* (1998), vol. 27, pp. 1849–1856. (Cited on page 118.)

[16] Buschmann, M. H., and el Hak, M. G. Generalized logarithmic law and its consequences. *AIAA Journal41*, 1 (January 2003), 40–48. (Cited on page 38.)

[17] Campa, G., Camporeale, S., Guaus, A., Favier, J., Bargiacchi, M., Bottaro, A., Cosatto, E., and Mori, G. A quantitative comparison between a low order model and a 3d fem code for the study of thermoacoustic combustion instabilities. In *ASME Turbo Expo, GT2011-45969, Vancouver* (2011), Combustion instabilities. (Cited on page 70.)

[18] Candel, S., Durox, D., Ducruix, S., Birbaud, A., Noiray, N., and Schuller, T. Flame dynamics and combustion noise : progress and challenges. *International Journal of Aeroacoustics 8* (2009), 1–56. (Cited on page 25.)

[19] Candel, S., Durox, D., and Schuller, T. Flame interactions as a source of noise and combustion instabilities. In *10th AIAA/CEAS Aeroacoustics Conference - AIAA 2004-2928* (2004). (Cited on page 70.)

[20] Charlette, F., Veynante, D., and Meneveau, C. A power-law wrinkling model for LES of premixed turbulent combustion: Part i - non-dynamic formulation and initial tests. *Combust. Flame 131* (2002), 159–180. (Cited on page 35.)

[21] Chassaing, P. *Turbulence en mécanique des fluides, analyse du phénomène en vue de sa modélisation à l'usage de l'ingénieur.* Cépaduès-éditions, Toulouse, France, 2000. (Cited on page 32.)

[22] Chatterjee, P., Vandsburger, U., Saunders, W., Khanna, V., and Baumann, W. On the spectral characteristics of a self-excited rijke tube combustor - numerical simulation and experimental measurements. *Journal of Sound and Vibration 283* (2005), 573–588. (Cited on page 25.)

[23] Chen, Z. Effects of radiation and compression on propagating spherical flames of methane/air mixtures near the lean flammability limit. *Combust. Flame 157* (2010), 2267–2276. (Cited on page 76.)

[24] Chu, B. T. On the energy transfer to small disturbances in fluid flow (part i). *Acta Mechanica* (1965), 215–234. (Cited on pages 17 and 19.)

[25] Colin, O., Ducros, F., Veynante, D., and Poinsot, T. A thickened flame model for large eddy simulations of turbulent premixed combustion. *Phys. Fluids 12*, 7 (2000), 1843–1863. (Cited on pages 52, 75, 76, 78 and 108.)

[26] Colin, O., and Rudgyard, M. Taylor-galerkin schemes in avbp. Tech. Rep. TR/CFD/98/56, CERFACS, 1998. (Cited on page 29.)

[27] Colin, O., and Rudgyard, M. Development of high-order taylor-galerkin schemes for unsteady calculations. *J. Comput. Phys. 162*, 2 (2000), 338–371. (Cited on pages 52, 75, 76, 78 and 108.)

[28] Coppens, F., De Ruyck, J., and Konnov, A. Effects of hydrogen enrichment on adiabatic burning velocity and no formation in methane + air flames. *Experimental Thermal and Fluid Science*, 31 (2007), 437–444. (Cited on page 75.)

[29] Crocco, L. Aspects of combustion instability in liquid propellant rocket motors. part i. *J. American Rocket Society 21* (1951), 163–178. (Cited on pages 20, 109 and 163.)

[30] Crocco, L. Aspects of combustion instability in liquid propellant rocket motors. part ii. *J. American Rocket Society 22* (1952), 7–16. (Cited on pages 20, 109 and 163.)

[31] Culick, F. E. C. Combustion instabilities in liquid-fueled propulsion systems- an overview. In *AGARD 72B PEP meeting* (1987). (Cited on pages 23, 70, 118, 129, 146 and 165.)

[32] Culick, F. E. C. Some recent results for nonlinear acoustic in combustion chambers. *AIAA Journal32*, 1 (1994), 146–169. (Cited on page 17.)

[33] Culick, F. E. C. Unsteady motions in combustion chambers for propulsion systems. In *AGARDogrpah* (2006). (Cited on page 23.)

[34] Dowling, A. P. The calculation of thermoacoustic oscillations. *J. Sound Vib.180*, 4 (1995), 557–581. (Cited on page 16.)

[35] Dowling, A. P. Nonlinear self-exited oscillations of a ducted flame. *J. Fluid Mech. 346* (1997), 271–290. (Cited on pages 17, 24, 25 and 163.)

[36] Dowling, A. P., and Stow, S. R. Acoustic analysis of gas turbine combustors. *Journal of Propulsion and Power 19(5)* (2003), 751–763. (Cited on page 23.)

[37] Ducruix, S., Durox, D., and Candel, S. Theoretical and experimental determinations of the transfer function of a laminar premixed flame. In *Proceedings of the Combustion Institute* (2000), vol. 28, pp. 765–773. (Cited on pages 22 and 23.)

[38] Durox, D., Schuller, T., and Candel, S. Combustion dynamics of inverted conical flames. In *Proceedings of the Combustion Institute* (2005), vol. 30, pp. 1717–1724. (Cited on pages 21 and 110.)

[39] Durox, D., Schuller, T., Noiray, N., Birbaud, A., and Candel, S. Rayleigh criterion and acoustic energy balance in unconfined self-sustained oscillating flames. *Combust. Flame 155*, 3 (2008), 416–429. (Cited on page 25.)

[40] Durox, D., Schuller, T., Noiray, N., and Candel, S. Experimental analysis of flame transfer functions nonlinearities. In *Proceedings of the Combustion Institute* (2009), vol. 32, pp. 1391–1398. (Cited on pages 24, 114 and 164.)

[41] Ern, A., and Giovangigli, V. *Multicomponent Transport Algorithms*. Lecture Notes in Physics. Springer Verlag, Heidelberg, 1994. (Cited on page 31.)

[42] Fleifil, M., Annaswamy, A., Ghoneim, Z., and Ghoniem, A. Response of a laminar premixed flame to flow oscillations: A kinematic model and thermoacoustic instability results. *Combustion and Flame 106(4)*, 487-510 (1996). (Cited on page 22.)

[43] Foeller, S., and Polifke, W. Determination of acoustic transfer matrices via large eddy simulation and system identification. In *16th AIAA/CEAS Aeroacoustics Conference (31th AIAA Aeroacoustics Conference)* (Stockholm, Sweden, 2010), no. AIAA-2010-3998. (Cited on pages 39 and 40.)

[44] Franzelli, B. *Impact of the chemical description on Direct Numerical simulations and Large Eddy simulations of turbulent combustion in indutrial aeroengines*. Phd thesis, CERFACS, 2011. (Cited on pages 51 and 75.)

[45] Franzelli, B., Riber, E., Gicquel, L., and Poinsot, T. Large-eddy simulation of combustion instabilities in a lean partially premixed swirled flame. *Combustion and Flame Submitted* (2011). (Cited on pages 52, 76 and 178.)

[46] Franzelli, B., Riber, E., Sanjosé, M., and Poinsot, T. A two-step chemical scheme for large eddy simulation of kerosene-air flames. *Combustion and Flame 157*, 7 (2010), 1364–1373. (Cited on pages 51, 52 and 75.)

[47] Frenklach, M., Wang, H., Goldenberg, M., Smith, G. P., Golden, D. M., Bowman, C. T., Hanson, R. K., Gardiner, W. C., and Lissianki, V. Gri-mech: an optimized detailed chemical reaction mechanism

for methane combustion. Tech. Rep. GRI-Report GRI-95/0058, Gas Research Institute, 1995. (Cited on page 75.)

[48] Fureby, C. Les of a multi-burner annular gas turbine combustor. *Flow, Turbulence and Combustion 84 (3)* (2010), 543–564. (Cited on page 69.)

[49] Gentemann, A. *Identifikation von akustischen Transfermatrizen und Flammenfrequenzgaengen mittels Stroemungssimulation.* Phd thesis, Technische Universitaet Muenchen, 2006. (Cited on pages 42 and 43.)

[50] Gentemann, A., Fischer, A., Evesque, S., and Polifke, W. Acoustic transfer matrix reconstruction and analysis for ducts with sudden change of area. In *9th AIAA/CEAS Aeroacoustics Confrence and Exhibit* (Hilton Head, SC, USA, 2003), no. AIAA-2003-3142. (Cited on pages 23, 39, 40 and 42.)

[51] Giauque, A., Selle, L., Poinsot, T., Buechner, H., Kaufmann, P., and Krebs, W. System identification of a large-scale swirled partially premixed combustor using LES and measurements. *J. Turb. 6*, 21 (2005), 1–20. (Cited on pages 23, 80 and 128.)

[52] Gu, X. J., Haq, M. Z., Lawes, M., and Woolley, R. Laminar burning velocity and markstein lengths of methane-air mixtures. *Combust. Flame 121* (2000), 41–58. (Cited on page 75.)

[53] Hall, M. G. Vortex breakdown. *Ann. Rev. Fluid Mech.4* (1972), 195–217. (Cited on page 80.)

[54] Hantschk, C.-C., and Vortmeyer, D. Numerical simulation of self-excited thermoacoustic instabilities in a rijke tube. *Journal of Sound and Vibration 227*, 3 (1999), 511–522. (Cited on page 25.)

[55] Hernandez-Vera, I. *Modelisation des Suies et Simulations aux Grandes Echelles des Instabilites thermo-acoustiques.* Phd thesis, CERFACS, 2011. (Cited on page 25.)

[56] Hield, P., Brear, M., and Jin, S. Thermoacoustic limit cycles in a premixed laboratory combustor with open and choked exits. *Combust. Flame* (2009), 1683–1697. (Cited on page 25.)

[57] Hirsch, C. *Numerical Computation of Internal and External Flows*, vol. 2. John Wiley & Sons, New York, 1990. (Cited on pages 51, 75 and 78.)

[58] Hirsch, C. Finite volume method and conservative discretization with an introduction to finite element method. In *Numerical Computation of internal & external flows: Fundamentals of Computational Fluid Dynamics, second edition.* John Wiley & Sons, New York, 2007, ch. 5, pp. 203–248. (Cited on page 36.)

[59] Hirsch, C., Franca, D., Reddy, P., Polifke, W., and Sattelmayer, T. Influence of the swirler design on the flame transfer function of premixed flames. *ASME Paper GT2005-68195* (2005). (Cited on pages 21, 110, 123, 126 and 137.)

[60] Hirschfelder, J. O., Curtiss, C. F., and Bird, R. B. *Molecular theory of gases and liquids.* John Wiley & Sons, New York, 1969. (Cited on page 31.)

[61] Hockstad, L., and Cook, B. Draft inventory of u.s. greenhouse gas emissions and sinks: 1990-2010. Tech. rep., U.S. Environmental Protection Agency, 2012. (Cited on page 5.)

[62] Huang, P. G., and Bradshaw, P. Law of the wall for turbulent flows in pressure gradients. *AIAA Journal33*, 4 (April 1995), 624–632. (Cited on page 38.)

[63] Huang, Y., and Yang, V. Dynamics and stability of lean-premixed swirl-stabilized combustion. *Progress in Energy and Combustion Science 35* (2009), 293–364. (Cited on pages 22, 80 and 118.)

[64] Huber, A. *Impact of fuel supply impedance and fuel staging on gas turbine combustion stability.* Phd thesis, Technische Universitaet Muenchen, 2009. (Cited on pages 22, 23, 39, 40, 113, 116, 144 and 161.)

[65] Huber, A., and Polifke, W. Dynamics of practical premixed flames, part i: model structure and identification. *International Journal of Spray and Combustion Dynamic 2* (2009), 199–228. (Cited on page 42.)

[66] Huber, A., and Polifke, W. Dynamics of practical premixed flames, part ii: identification and interpretation of cfd data. *International Journal of Spray and Combustion Dynamic 2* (2009), 229–250. (Cited on pages 39, 40, 42 and 161.)

[67] Hurle, I. R., Price, R. B., Sugden, T. M., and Thomas, A. Sound emission from open turbulent premixed flames. *Proc. R. Soc. Lond. A 303*, 409 (1968). (Cited on page 16.)

[68] Hussain, F., and Jeong, J. On the identification of a vortex. *J. Fluid Mech. 285* (1995), 69–94. (Cited on page 87.)

[69] Iacona, E., Taine, J., and Tamain, B. *Les enjeux de l'energie.* Dunod, 2009. (Cited on page 3.)

[70] Ivanov, Y. V. Shape of the centerline of an axisymmetric fan type jet in a cross flow. *Izv. VUZ Aviotsionnaya Teknika 4* (1963). (Cited on page 158.)

[71] Jameson, A., Schmidt, W., and Turkel, E. Numerical solution of the euler equations by finite volume methods using runge-kutta time stepping

schemes. In *14th Fluid and Plasma Dynamic Conference* (Palo Alto, 1981), A. paper 81-1259, Ed. (Cited on page 36.)

[72] Jones, P., and Mann, M. Climate over past millennia. *Rev. Geophys. 42 42, RG2002.* (2004). (Cited on pages 5, 6 and 177.)

[73] Juniper, M. Triggering in the horizontal rijke tube: non-normality, transient growth and bypass transition. *J. Fluid Mech. 667* (2011), 272–308. (Cited on page 25.)

[74] Kaess, R., Polifke, W., Poinsot, T., Noiray, N., Durox, D., Schuller, T., and Candel, S. Cfd-based mapping of the thermo-acoustic stability of a laminar premix burner. In *Proc. of the Summer Program* (Center for Turbulence Research, NASA AMES, Stanford University, USA, 2008), pp. 289–302. (Cited on pages 23, 27 and 109.)

[75] Kailasanath, K., Gardner, J. H., Oran, E. S., and Boris, J. P. Numerical simulations of unsteady reactive flows in a combustion chamber. *Combust. Flame 86* (1991), 115–134. (Cited on page 25.)

[76] Karimi, N., Brear, M., Jin, S.-H., and Monty, J. Linear and non-linear forced response of a conical, ducted, laminar premixed flame. *Combust. Flame* (2009), 2201–2212. (Cited on pages 21 and 110.)

[77] Katsuki, M., and Whitelaw, J. The influence of duct geometry on unsteady premixed flames. *Combust. Flame 63* (1986), 87–94. (Cited on page 118.)

[78] Kaufmann, A., Nicoud, F., and Poinsot, T. Flow forcing techniques for numerical simulation of combustion instabilities. *Combust. Flame 131* (2002), 371–385. (Cited on pages 27, 38, 51, 74 and 112.)

[79] Kim, D., Lee, J., Quay, B., Santavicca, D., Kim, K., and Srinivasan, S. Effect of flame structure on the flame transfer function in a premixed gas turbine combustor. *Journal of Engineering for Gas Turbines and Power 132(2)* (2010), 757–765. (Cited on page 21.)

[80] Kim, K., Lee, H., Lee, J., Quay, B., and Santavicca, D. Flame transfer function measurement and instability frequency prediction using a thermo acoustic model. In *ASME Turbo Expo, GT2009-60026, Orlando* (2009), Combustion instabilities. (Cited on page 23.)

[81] Kim, K., Lee, J., Quay, B., and Santavicca, D. Experimental investigation of the nonlinear response of swirl stabilized flames to equivalence ratio oscillations. In *ASME Turbo Expo, GT2010-23023, Glasgow* (2010), Combustion instabilities. (Cited on pages 24 and 164.)

[82] Kim, K., Lee, J., Quay, B., and Santavicca, D. Response of partially premixed flames to acoustic velocity and equivalence ratio perturbations. *Combust. Flame 157* (2010), 1731–1744. (Cited on pages 21, 110, 123, 126 and 134.)

[83] Kochar, Y., Seitzman, J., Lieuwen, T., Metcalfe, W., Burke, S., Curran, H., Krejici, M., Lowry, W., Petersen, E., and Bourque, G. Laminar flame speed measurements and modeling of alkane blends at elefated pressures with various dilutents. In *Procceedings of ASME Turbo Expo 2011. GT2011-45122* (2011). (Cited on page 76.)

[84] Komarek, T., and Polifke, W. Impact of swirl fluctuations on the flame response of a perfectly premixed swirl burner. *Journal of Engineering for Gas Turbines and Power 132* (2010). (Cited on pages 21, 23, 110, 123, 126, 137 and 160.)

[85] Kornilov, V., Rook, R., ten Thije Boonkkamp, J., and de Goey, L. Experimental and numerical investigation of the acoustic response of multi-slit bunsen burners. *Combust. Flame* (2009), 1957–1970. (Cited on pages 21, 23, 110 and 114.)

[86] Krebs, W., Flohr, P., Prade, B., and Hoffmann, S. Thermoacoustic stability chart for high intense gas turbine combustion systems. *Combust. Sci. Tech. 174* (2002), 99–128. (Cited on page 109.)

[87] Krebs, W., Krediet, H., Portillo, E., Hermeth, S., Poinsot, T., Schimek, S., and Paschereit, C. Comparison of nonlinear to linear thermoacoustic stability analysis of a gas turbine combustion system. In *Procceedings of ASME Turbo Expo 2012. GT2012-69477* (2012). (Cited on pages 25 and 70.)

[88] Krebs, W., Walz, G., and Hoffmann, S. Thermoacoustic analysis of annular combustor. In *5th AIAA Aeroacoustics Conference* (1999), A. P. 99-1971, Ed. (Cited on pages 23 and 70.)

[89] Krediet, H., Beck, C., Krebs, W., Schimek, S., and Paschereit, C. Identification of the flame describing function of a premixed swirl flame from les. In *Proceedings of the Seventh Mediterranean Combustion Symposium (MCS-7)* (2011). (Cited on pages 11, 47, 53, 56, 63, 64 and 164.)

[90] Kuo, K. K. *Principles of combustion*, 2nd ed. John Wiley & Sons, Inc., Hoboken, New Jersey, 2005. (Cited on page 32.)

[91] Lamarque, N. *Schémas numériques et conditions limites pour la simulation aux grandes échelles de la combustion diphasique dans les foyers d'hélicoptère.* Phd thesis, INP Toulouse, 2007. (Cited on pages 36 and 37.)

[92] Lang, W., Poinsot, T., and Candel, S. Active control of combustion instability. *Combust. Flame 70* (1987), 281–289. (Cited on page 19.)

[93] Lartigue, G., Meier, U., and Berat, C. Experimental and numerical investigation of self-excited combustion oscillations in a scaled gas turbine combustor. *Applied Thermal Engineering 24* (2004), 1583–1592. (Cited on page 25.)

[94] Lax, P. D., and Wendroff, B. Systems of conservation laws. *Commun. Pure Appl. Math. 13* (1960), 217–237. (Cited on pages 51, 75 and 78.)

[95] Lax, P. D., and Wendroff, B. Difference schemes for hyperbolic equations with high order of accuracy. *Commun. Pure Appl. Math. 17* (1964), 381–398. (Cited on page 36.)

[96] LeConte, J. On the influence of musical sounds on the flame of a jet of coal gas. *American Journal of Science and Arts 23(2)* (1858), 62–67. (Cited on page 15.)

[97] Lefebvre, A. H. *Gas Turbines Combustion.* Taylor & Francis, 1999. (Cited on pages 8, 10 and 109.)

[98] Légier, J.-P., Poinsot, T., and Veynante, D. Dynamically thickened flame LES model for premixed and non-premixed turbulent combustion. In *Proc. of the Summer Program* (2000), Center for Turbulence Research, NASA Ames/Stanford Univ., pp. 157–168. (Cited on pages 35, 52, 76 and 108.)

[99] Lewis, N. Powering the planet. *Engineering and Science 70 (2)* (2007), 12–23. (Cited on pages 3, 4 and 177.)

[100] Lieuwen, T. Modeling premixed combustion-acoustic wave interactions: A review. *J. Prop. Power 19*, 5 (2003), 765–781. (Cited on page 23.)

[101] Lieuwen, T., Bellows, B., Bobba, M., and Seitzman, J. Nonlinear flame transfer function characteristics in a swirl stabilized combustor. *Journal of Engineering for Gas Turbines and Power 132* (2007), 954–961. (Cited on pages 10, 18, 24, 163, 164, 174, 177 and 182.)

[102] Lieuwen, T., and Neumeier, Y. Nonlinear pressure-heat release transfer function measurements in a premixed combustor. In *Proc. Combust. Inst.* (2002), vol. 29, pp. 99–105. (Cited on page 25.)

[103] Lieuwen, T., and Yang, V. Combustion instabilities in gas turbine engines. operational experience, fundamental mechanisms and modeling. In *Prog. in Astronautics and Aeronautics AIAA* (2005), vol. 210. (Cited on pages 16, 19, 22, 116, 122, 128 and 177.)

[104] Lieuwen, T., and Zinn, B. T. The role of equivalence ratio oscillations in driving combustion instabilities in low nox gas turbines. *Proc. Combust. Inst. 27* (1998), 1809–1816. (Cited on pages 21, 110, 123 and 126.)

[105] Ljung, L. *System Identification. Thoery for the user.* Prentice Hall PTR, 2nd edition, 2009. (Cited on pages 23, 40, 41 and 42.)

[106] Lucca-Negro, O., and O'Doherty, T. Vortex breakdown: a review. *Prog. Energy Comb. Sci. 27* (2001), 431–481. (Cited on pages 21, 68 and 80.)

[107] McManus, K., Poinsot, T., and Candel, S. A review of active control of combustion instabilities. *Prog. Energy Comb. Sci. 19* (1993), 1–29. (Cited on page 19.)

[108] Mery, Y., Ducruix, S., Scouflaire, P., and Candel, S. Injection coupling with high amplitude transverse modes: experimentation and simulation. *Comptes Rendus Mécanique 337* (2009), 426–437. (Cited on page 70.)

[109] Moeck, J., Paul, M., and Paschereit, C. Thermoacoustic instabilities in an annular rijke tube. *Proc. ASME Turbo Expo GT2010-23577* (2010), 1219–1232. (Cited on page 25.)

[110] Moureau, V., Lartigue, G., Sommerer, Y., Angelberger, C., Colin, O., and Poinsot, T. Numerical methods for unsteady compressible multi-component reacting flows on fixed and moving grids. *J. Comput. Phys. 202*, 2 (2005), 710–736. (Cited on pages 28 and 29.)

[111] Nations, U. World population prospects: The 2010 revision, highlights and advance tables. esa/p/wp.220. Tech. rep., Department of Economic and Social Affairs, Population Division, 2011. (Cited on pages 3, 4 and 177.)

[112] Nicoud, F., Benoit, L., Sensiau, C., and Poinsot, T. Acoustic modes in combustors with complex impedances and multidimensional active flames. *AIAA Journal45* (2007), 426–441. (Cited on pages 23 and 25.)

[113] Nicoud, F., and Poinsot, T. Thermoacoustic instabilities: should the rayleigh criterion be extended to include entropy changes ? *Combust. Flame 142* (2005), 153–159. (Cited on pages 17 and 19.)

[114] Noiray, N. *Analyse lineaire et non-lineaire des instabilites de combustion, application aux systemes a injection multipoints et strategies de controle.* Phd thesis, Ecole Centrale de Paris, 2007. (Cited on pages 25 and 70.)

[115] Noiray, N., andT. Schuller, D. D., and Candel, S. A unified framework for nonlinear combustion instability analysis based on the flame describing function. *J. Fluid Mech. 615* (2008), 139–167. (Cited on page 25.)

[116] Palies, P. *Dynamique et instabilites de combustion des flammes swirlees.* Phd thesis, Ecole Centrale de Paris, 2010. (Cited on pages 10 and 21.)

[117] Palies, P., Durox, D., Schuller, T., and Candel, S. The combined dynamics of swirler and turbulent premixed swirling flames. *Combust. Flame 157* (2010), 1698–1717. (Cited on pages 21, 62, 110, 114, 123, 126 and 139.)

[118] Palies, P., Durox, D., Schuller, T., and Candel, S. Nonlinear combustion instability analysis based on the flame describing function applied to turbulent premixed swirling flames. *Combust. Flame 158* (2011), 1980–1991. (Cited on pages 24, 25, 163, 164 and 174.)

[119] Palies, P., Schuller, T., Durox, D., and Candel, S. Modeling of premixed swirling flames transfer functions. In *Proceedings of the Combustion Institute* (2011), vol. 33, pp. 2967–2974. (Cited on pages 21, 23, 110, 114, 123, 126 and 139.)

[120] Pankiewitz, C., and Sattelmayer, T. Time domain simulation of combustion instabilities in annular combustors. *ASME Journal of Engineering for Gas Turbines and Power 125*, 3 (2003), 677–685. (Cited on page 24.)

[121] Parry, M., Canziani, O., Palutikof, J., van der Linden, P., and Hanson, C. Contribution of working group ii to the fourth assessment report of the intergovernmental panel on climate change 2007. *Cambridge University Press, Cambridge, United Kingdom and New York, NY, USA* (2007). (Cited on page 5.)

[122] Piomelli, U. Wall-layer models for large-eddy simulations. *Prog. Aerospace Sci. 44*, 6 (2008), 437–446. (Cited on page 38.)

[123] Poinsot, T. *Analyse des instabilités de combustion de foyers turbulents prémélangés.* Thèse d'etat, Université d'Orsay, 1987. (Cited on pages 17 and 174.)

[124] Poinsot, T., and Candel, S. The influence of differencing and cfl number on implicit time dependant non linear calculations. *J. Comput. Phys. 62* (1986), 282–296. (Cited on page 50.)

[125] Poinsot, T., and Lele, S. Boundary conditions for direct simulations of compressible viscous flows. *J. Comput. Phys. 101*, 1 (1992), 104–129. (Cited on pages 37, 51 and 74.)

[126] Poinsot, T., and Veynante, D. *Theoretical and Numerical Combustion.* R.T. Edwards, 2nd edition, 2005. (Cited on pages 10, 18, 19, 20, 26, 31, 32, 35, 70, 109 and 177.)

[127] Polifke, W., and Lawn, C. On the low-frequency limit of flame transfer functions. *Combust. Flame 151* (2007), 437–451. (Cited on pages 21 and 115.)

[128] Polifke, W., and Paschereit, C. O. Determination of thermo-acoustic transfer matrices by experiment and computational fluid dynamics. ERCOFTAC bulletin, p. 38. (Cited on pages 39 and 40.)

[129] Polifke, W., Poncet, A., Paschereit, C. O., and Doebbeling, K. Reconstruction of acoustic transfer matrices by instationnary computational fluid dynamics. *J. Sound Vib.245*, 3 (2001), 483–510. (Cited on pages 23 and 42.)

[130] Pope, S. B. *Turbulent flows*. Cambridge University Press, 2000. (Cited on page 32.)

[131] Porta, M. *Développement, vérification et validation des outils LES pour l'étude du bruit de combustion et de l'interaction combustion/acoustique/turbulence - TH/CFD/07/46*. PhD thesis, Institut National Polytechnique de Toulouse, France - Dynamique des Fluides, CERFACS - CFD Team, Toulouse, 2007. (Cited on page 37.)

[132] Portillo, J., Sisco, J., Anderson, W., and Sankaran, V. Application of a generalized instability model to a longitudinal mode combustion chamber. In *43rd AIAA/ASME/SAE/ASEE Joint Propulsion Conference & Exhibit* (2007). (Cited on page 25.)

[133] Prière, C. *Simulation aux grandes échelles : application au jet transverse*. Phd thesis, INP Toulouse, 2005. (Cited on page 158.)

[134] Raupach, M., Marland, G., Ciais, P., le Quere, C., Canadell, J., Klepper, G., and Field, C. Global and regional drivers of accerlerating co2 emissions. *Proc. Natl. Acad. Sci. ISA 104(24)* (2007), 10288–93. (Cited on page 5.)

[135] Rayleigh, L. The explanation of certain acoustic phenomena. *Nature July 18* (1878), 319–321. (Cited on pages 15, 17 and 80.)

[136] Roux, S., Lartigue, G., Poinsot, T., Meier, U., and Bérat, C. Studies of mean and unsteady flow in a swirled combustor using experiments, acoustic analysis and large eddy simulations. *Combust. Flame 141* (2005), 40–54. (Cited on pages 10 and 80.)

[137] Rozenchan, G., Zhu, D., Law, C., and Tse, S. Outward propagation, burning velocities, and chemical effects of methane flames up to 60 atm. *Proc. Combust. Inst.* , 29 (2002), 1461–1469. (Cited on page 75.)

[138] Rudgyard, M. Cell vertex methods for steady inviscid flow. In *Lectures Series 1993-04*, V. K. I. for Fluid Dynamics, Ed., vol. 1993-04. Von Karman Institute for Fluid Dynamics, 1993. (Cited on page 36.)

[139] Rudgyard, M. Integrated preprocessing tools for unstructured parallel cfd applications. Tech. Rep. TR/CFD/95/08, CERFACS, 1995. (Cited on page 29.)

[140] Rudgyard, M. A. *Cell Vertex methods for compressible gas flows*. Phd thesis, Oxford University Computing Laboratory, 1990. (Cited on page 36.)

[141] Sawyer, R. Science based policy for adressing energy and environmental problems. In *Proceedings of the Combustion Institute* (2009), vol. 32, pp. 45–56. (Cited on page 5.)

[142] Schimek, S., Moeck, J., and Paschereit, C. Design of a combustion test rig with high amplitude forcing capabilities for nonlinear flame transfer function measurements. In *Proc. ICSV 16, Krakow, Poland* (2009). (Cited on pages 11, 24, 47, 49, 53, 164 and 177.)

[143] Schimek, S., Moeck, J., and Paschereit, C. An experimental investigation of the nonlinear response of an atmospheric swirl-stabilized premixed flame. In *Proc. of ASME Turbo Expo, GT2010-2282, Glasgow* (2010). (Cited on pages 24, 25, 48, 49, 164 and 177.)

[144] Schimek, S., Moeck, J., and Paschereit, C. Experimental investigation of high amplitude forcing and swirl fluctuations on the flow field and the transfer function of a swirl-stabilized flame. *AIAA Paper 2011-5702 47nd AIAA/ASME/SAE/ASEE Joint Propulsion Conference & Exhibit* (31 July-03 Aug. 2011). (Cited on pages 11, 47 and 53.)

[145] Schmitt, P. *Simulation aux grandes échelles de la combustion étagée dans les turbines à gaz et son interaction stabilité-polluants-thermique.* Phd thesis, INP Toulouse, 2005. (Cited on pages 28, 29, 35, 38, 39 and 177.)

[146] Schønfeld, T., and Rudgyard, M. A cell-vertex approach to local mesh refinement for the 3-d euler equations. In *32nd Aerospace Sciences Meeting & Exhibit* (Reno, U.S.A., 1994), AIAA-94-0318, Ed., AIAA. (Cited on pages 29 and 36.)

[147] Schønfeld, T., and Rudgyard, M. Steady and unsteady flows simulations using the hybrid flow solver avbp. *AIAA Journal37*, 11 (1999), 1378–1385. (Cited on pages 36 and 51.)

[148] Schuermans, B., Bellucci, V., Guethe, F., Meili, F., Flohr, P., and Paschereit, C. A detailed analysis of thermoacoustic interaction mechanisms in a turbulent premixed flame. In *ASME Turbo Expo 2004-Power for Land Sea and Air* (Vienna, Austria, 2004), vol. GT2004-53831. (Cited on pages 21, 23, 110, 123 and 126.)

[149] Schuermans, B., Bellucci, V., Nowak, D., and Paschereit, C. Modelling of complex thermo-acoustic system: A state-space approach. In *9th International Congress on Sound and Vibration* (2002). (Cited on page 23.)

[150] Schuller, T., Durox, D., and Candel, S. A unified model for the prediction of laminar flame transfer functions: comparisons between conical and v-flames dynamics. *Combust. Flame 134* (2003), 21–34. (Cited on pages 21, 23, 110 and 128.)

[151] Selimefendigil, F., and Polifke, W. A nonlinear frequency domain model for limit cycle thermoacoustic systems with modal coupling. *International Journal of Spray and Combustion Dynamic 3* (2011), 303–330. (Cited on page 24.)

[152] Selle, L. *Simulation aux grandes échelles des interactions flamme-acoustique dans un écoulement vrillé*. Phd thesis, INP Toulouse, 2004. (Cited on page 23.)

[153] Selle, L., Lartigue, G., Poinsot, T., Koch, R., Schildmacher, K.-U., Krebs, W., Prade, B., Kaufmann, P., and Veynante, D. Compressible large-eddy simulation of turbulent combustion in complex geometry on unstructured meshes. *Combust. Flame 137*, 4 (2004), 489–505. (Cited on pages 10, 25, 27, 75 and 80.)

[154] Selle, L., Nicoud, F., and Poinsot, T. The actual impedance of non-reflecting boundary conditions: implications for the computation of resonators. *AIAA Journal42*, 5 (2004), 958–964. (Cited on pages 27 and 37.)

[155] Selle, L., Poinsot, T., and Ferret, B. Experimental and numerical study of the accuracy of flame-speed measurements for methane/air combustion in a slot burner. *Combust. Flame 158* (2011), 146–154. (Cited on pages 75 and 178.)

[156] Sengissen, A. *Simulation aux grandes échelles des instabilités de combustion: vers le couplage fluide/structure - TH/CFD/06/12*. Phd thesis, Université de Montpellier II, 2006. (Cited on pages 35 and 38.)

[157] Sengissen, A., Kampen, J. F. V., Huls, R., Stoffels, G., Kok, J. B. W., and Poinsot, T. Les and experimental studies of cold and reacting flows in a swirled partially premixed burner with and without fuel modulation. *Combust. Flame 150* (2007), 40–53. (Cited on pages 28, 29 and 80.)

[158] Sensiau, C., Nicoud, F., and Poinsot, T. A tool to study azimuthal and spinning modes in annular combustors. *Int. Journal Aeroacoustics 8*, 1 (2009), 57–68. (Cited on pages 70 and 128.)

[159] Seo, S. *Parametric study of lean-premixed combustion instability in a pressurized model gas turbine combustor*. Phd thesis, The Pennsylvania State University, 1999. (Cited on page 118.)

[160] Seume, J., Vortmeyer, N., Krause, W., Hermann, J., Hantschk, C., Zangl, P., Gleis, S., and Vortmeyer, D. Application of active combustion instability control to a heavy duty gas turbine. *ASME Journal of Engineering for Gas Turbines and Power 120* (1998), 721–726. (Cited on page 19.)

[161] Smagorinsky, J. General circulation experiments with the primitive equations: 1. the basic experiment. *Mon. Weather Rev. 91* (1963), 99–164. (Cited on pages 34, 51, 75 and 78.)

[162] Solomon, S., Qin, D., Manning, M., Z.Chen, M.Marquis, K.B.Averyt, M.Tignor, and Miller, H. Technical summary. in: Climate change 2007: The physical science basis. contribution of working group i to the fourth assessment report of the intergovernmental panel on climate change. *Cambridge University Press, Cambridge, United Kingdom and New York, NY, USA* (2007). (Cited on page 5.)

[163] Spalding, D. B. A single formula for the "Law of the Wall". *J. Appl. Mech.* (September 1961), 455–458. (Cited on page 38.)

[164] Staffelbach, G. *Simulation aux grandes échelles des instabilités de combustion dans les configurations multi-brûleurs*. Phd thesis, INP Toulouse, 2006. (Cited on pages 23, 101 and 106.)

[165] Staffelbach, G., Gicquel, L., Boudier, G., and Poinsot, T. Large eddy simulation of self-excited azimuthal modes in annular combustors. *Proc. Combust. Inst. 32* (2009), 2909–2916. (Cited on pages 36, 69 and 70.)

[166] Staffelbach, G., Gicquel, L., and Poinsot, T. Highly parallel Large Eddy Simulations of multiburner configurations in industrial gas turbines. In *Lecture Notes in Computational Science and Engineering - Complex effects in Large Eddy Simulation* (2006), Springer, Ed., vol. 56, pp. 326–336. (Cited on page 27.)

[167] Stein, O., and Kempf, A. Les of the sydney swirl flame series: a study of vortex breakdown in isothermal and reacting flows. *Proc. Combust. Inst. 31* (2007), 1755–1763. (Cited on page 68.)

[168] Steinberg, A., Boxx, I., Stoehr, M., Carter, C., and Meier, W. Flow-flame interactions causing acoustically coupled heat release fluctuations in a thermo-acoustically unstable gas turbine model combustor. *Combust. Flame 157* (2010), 2250–2266. (Cited on page 22.)

[169] Stow, S. R., and Dowling, A. P. A time-domain network model for nonlinear thermoacoustic oscillations. In *ASME Turbo Expo 2008, GT2008-50770* (Berlin, Germany, 2008). (Cited on page 70.)

[170] Strahle, W. Some results in combustion generated noise. *J. Sound Vib.23* (1972), 113–125. (Cited on page 16.)

[171] Strahle, W. Combustion noise. *Prog. Energy Comb. Sci. 4* (1978), 157–176. (Cited on page 16.)

[172] Straub, D., and Richards, G. Effect of fuel nozzle configuration on premixed combustion dynamics. In *ASME Paper 1998-GT-492* (1998). (Cited on page 118.)

[173] Straub, D., and Richards, G. Effect of axial swirl vane location on effect of axial swirl vane location on effect of axial swirl vane location on combustion dynamics. In *ASME Paper 99-GT-109* (1999). (Cited on pages 21, 110, 123, 126 and 137.)

[174] Swaminathan, N., and Bray, K. *Turbulent premixed flames*. Cambridge University Press, 2011. (Cited on pages 10 and 15.)

[175] Tay, L., Bomberg, S., Ulhaq, A., Komarek, T., and Polifke, W. Comparative validation study on identification of premixed flame transfer function. In *ASME Turbo Expo, GT2011-46342, Vancouver* (2011), Combustion instabilities. (Cited on page 23.)

[176] Tay, L., Komarek, T., Kaess, R., Foeller, S., and Polifke, W. Identification of flame transfer functions from les of a premixed swirl burner. In *ASME Turbo Expo, GT2010-22769, Glasgow* (2010), Combustion instabilities. (Cited on pages 10, 27, 38, 43, 51 and 177.)

[177] Thompson, K. W. Time dependent boundary conditions for hyperbolic systems. *J. Comput. Phys. 68* (1987), 1–24. (Cited on page 37.)

[178] Thumuluru, S., Ma, H., and Lieuwen, T. Measurements of the flame response to harmonic excitation in a swirl combustor. In *45th AIAA Aerospace Sciences Meeting and Exhibit* (Reno, USA, 2007), AIAA Paper 2007-0845. (Cited on pages 24, 109, 164 and 165.)

[179] Tyndal, J. *Sound*. D. Appleton and Company, New York, 1897. (Cited on page 15.)

[180] Vagelopoulos, C. M., and Egolfopoulos, F. Direct experimental determination of laminar flame speeds. In *27th Symp. (Int.) on Combustion* (1998), The Combustion Institute, Pittsburgh, pp. 513–519. (Cited on page 75.)

[181] Van Maaren, A., Thung, D. S., and De Goey, L. R. H. Measurement of Flame Temperature and Adiabatic Burning Velocity of Methane/Air Mixtures. *Combust. Sci. Tech. 96*, 4 (1994), 327–344. (Cited on page 75.)

[182] Varea, E., Vandel, A., Modica, V., Corbin, F., Godard, G., and Renou, B. Measurement of laminar flame speed for high pressure and high temperature conditions: validation of the facility and development of new tool for postprocessing. In *15th Int Symp on Applications of Laser Techniques to Fluid Mechanics* (Lisbon, Portugal, 05-08 July 2010). (Cited on page 76.)

[183] Venkataraman, K., Preston, L., Simons, D., Lee, B., Lee, J., and Santavicca, D. Mechanisms of combustion instability in a lean premixed dump combustor. *Journal of Propulsion and Power 15(6)* (1999), 909–18. (Cited on page 118.)

[184] Ward, K., Knight, Z., Robins, N., Spedding, P., and Singh, C. Energy in 2050 - will fuel constraints thwart our growth porjections? *HSBC report* (2011). (Cited on pages 3, 6 and 177.)

[185] Williams, F. A. *Combustion Theory*. Benjamin Cummings, Menlo Park, CA, 1985. (Cited on pages 31 and 35.)

[186] Williams, J., and Wood, M. Aerodynamic interference effects with jet lift schemes on vstol aircraft at forward speeds. *AGARDograph 103, Aerodynamics of power plant installation, 2: 625-351* (Oct. 1965). (Cited on page 158.)

[187] Williamson, J. H. Low-storage Runge-Kutta schemes. *J. Comput. Phys. 35*, 1 (March 1980), 48–56. (Cited on page 36.)

[188] Wolf, P. *Large eddy simulation of thermoacoustic instabilities in annular combustion chambers*. Phd thesis, CERFACS, 2011. (Cited on pages 10 and 69.)

[189] Wolf, P., Staffelbach, G., Roux, A., Gicquel, L., Poinsot, T., and Moureau, V. Massively parallel les of azimuthal thermo-acoustic instabilities in annular gas turbines. *C. R. Acad. Sci. Mécanique 337*, 6-7 (2009), 385–394. (Cited on pages 10, 27 and 109.)

[190] Zinn, B., and Powell, E. Application of the galerkin method in the solution of combustion instability problems. In *Proceedings of the Nineteenth International Astronautical Congress on Propulsion, Re-Entry Physics* (1970), vol. 3, pp. 59–73. (Cited on page 23.)

Acknowledgements

Once upon a time, there was a Basti, who never thought he would ever write the acknowledgements of his thesis. Those words are dedicated to everyone who helped to make the unthinkable happen.

First of all I would like to thank Thierry Poinsot, for giving me the trust to do a PhD at Cerfacs and for many fruitful discussions during my time and especially at the end. My work benefits in big parts of him.

Laurent Gicquel, my supervisor, who always had an open ear and endless motivating suggestions. Up to today, several of his ideas still need to be explored and would probably represent a second PhD thesis.

A lot of thanks to Gabriel Staffelbach, the one who had to suffer the most with me. He was not only an extraordinary help during my time at work, but he also became a friend and I enjoyed having "a few" beers with him.

Likewise, I am grateful to the jury Sebastien Ducruix, Jim Kok, Wolfgang Polifke and Matthew Juniper for dedicating their time to read and comment on my manuscript and for giving me the opportunity to present and defend my work.

I also thank Slava and Carmine for their trust in my work and especially for thousands of questions which helped to prepare for the day of my defence.

The EU Marie Curie project Limousine for financing my thesis and offering me the possibility to meet many great people during the project: I appreciated a lot the secondment at Siemens while working with Werner, Christian, Enrique, Stephan and Harmen. Moreover several Limousine meetings around Europe with helpful discussions and questions as well as nice food and drinks in the evenings with Patrick, Bela, Lukas, Thomas, Lukas, Sebastian, Roel, Juan Carlos, Mehmet, Santosh, Mina, Reddy, Simone, Antonio, Salvo and Can.

All the people I met at Cerfacs: The seniors Ele, Olivier, Antoine for their support whenever needed. CSG for solving all problems dealing with not working things and Marie, Nicole for the help in organising travels etc. Pierre W., Thomas P., Anthony, Marina, Geoff, Jean-Phi, Nacho small and Nacho tall, Matthias, Abdullah, Elsa and Camilo for several activities: having fun in Brussels, discovering Coppa in Corsica, walking around with a donkey, being afraid of bungee jumps and many many more. Also a big thank to JC and l'equipe aero for the never ending Vasco.

One entire page to all my friends:

All the people I met in Toulouse for sharing great moments. Les apéros chez Tonio et Emilie sur le balcon ensoleillé et plein d'autres soirées passées ensemble. Merci également à Frudge, Tutu, Dams, Alice et tous les autres pour tous les supers souvenirs que j'ai avec vous.

Greg, my long time co-bureau. I passed my entire Cerfacs life with him and we shared good and bad moments, supported each other and became good friends.

Fab, I only remember where I met him first, I don't know how but at least I know why we became such good friends.

Last but not least, my German friends from H-Town as well as from Aachen. Diejenigen, die mich jetzt schon seit längerer Zeit durch mein Leben begleiten. Insbesondere Bernardo und Daniel für die vielen Erlebnisse während und nach unserem Studium, die Urlaube sowie dafür mich bei meiner Verteidigung unterstützt und diesen besonderen Tag mit mir geteilt zu haben. Torben und seine Couch dafür während meiner Heimaturlaube und auch sonst für mich Zeit zu haben, sowie die vielen grösseren und kleineren Momente die wir zusammen erlebt haben. Desweiteren die ganze Heiligenhauser und Aachener Bande: Benny, der (formerly known as) Müller, Hoffart, Christoph und alle anderen für viele gemeinsame Erinnerungen.

Special thanks goes to my Family.

And he lived happily ever after.

Sebastian Hermeth
Toulouse, November 2012.